KOMUNIKÁCIE

COMMUNICATIONS

SCIENTIFIC LETTERS OF THE UNIVERSITY OF ŽILINA

Volume 27

UNIVERSITY OF ŽILINA

ISSN 1335-4205

1/2025

UNIVERSITY OF ŽILINA
EDIS-Publishing House
UNIZA

EDIS-Publishing House of the University of Žilina (UZ) is one of the University of Žilina's consituents. The beginning of its existence dates back to 1990. In the course of its work, the publishing house has published more than 5 000 titles of book publications, especially university textbooks, scientific monographs, scripts, prose, but also enriched the book market with titles of regional, children's and popular literature.
Students and professional public have the opportunity to purchase published titles in the „Selling Study Literature" directly on the premises of the University of Žilina, in the EDIS shop or upon order on a „cash on delivery" basis. All published titles are available at: www.edis.uniza.sk.

EDIS-Publishing House of the University of Žilina offers book titles in English

Lenka Černá, Jozef Daniš
APPLICATION OF COST ALCULATIONS IN THE TARIFF POLICY FORMATION IN RAILWAY TRANSPORT
ISBN 978-80-554-1391-4 Price 7.61 €

Eva Nedeliaková, Jana Sekulová
EVALUATION OF QUALITY IN RAILWAY TRANSPORT
ISBN 978-554-1272-6 Price 8.00 €

Martin Bugaj
AEROMECHANICS 1
ISBN 978-80-554-1675-5 Price 14.50 €

Anna Tomová
ECONOMICS OF AIR NAVIGATION SERVICES
ISBN 978-80-554-0905-4 Price 14.30 €

Marica Mazurek
MODELS OF BRANDING AND THEIR APPLICATION
ISBN 978-80-554-1705-9 Price 9.00 €

Jozef Melcer
DYNAMICS OF STRUCTURES
ISBN 978-80-554-1698-4 Price 19.00 €

Jozef Gašparík et al.
RAILWAY TRAFFIC OPERATION
ISBN 978-80-554-1281-8 Price 15.80 €

Tetiana Hovorushchenko et.al.
CD - INTELLIGENT INFORMATION-ANALYTICAL TECHNOLOGIES...
ISBN 978-80-554-1729-5 Price 3.50 €

Karol Matiaško, Michal Kvet, Marek Kvet
CD - PRACTICES FOR DATABASE SYSTEMS
ISBN 978-80-554-1397-6 Price 2.20 €

Michal Kvet, Karol Matiaško, Štefan Toth
USB - PRACTICAL SQL FOR ORACLE CLOUD
ISBN 978-80-554-1880-3 Price: 11,30 €

Veronika Valašková, Daniela Kucharová
USB - STATICS OF STRUCTURES 3
ISBN 978-80-554-1826-1 Price: 8,90 €

Michal Kvet, Karol Matiaško, Marek Kvet
USB - BECOME EXPERT IN MYSQL PRACTICES FOR DATABASE SYSTEMS IN MYSQL
ISBN 978-80-554-1786-8 Price 13.50 €

Michal Kvet, Alenka Baggia, Monika Borkovcová, Diana Mudrinić, Frane Urem
E-book - Environmental Data Analysis
ISBN 978-80-554-2145-2 Price 0,00 €

Michal Kvet
E-book – Become master in SQL
ISBN 978-80-554-2132-2 Price 0,00 €

EDIS-Publishing House UNIZA

Univerzitná 8215/1,
010 26 Žilina,
Slovakia

e-mail: edis_objednavky@uniza.sk, edis@uniza.sk
www.edis.uniza.sk

B - MECHANICAL ENGINEERING IN TRANSPORT

C - ELECTRICAL ENGINEERING IN TRANSPORT

D - CIVIL ENGINEERING IN TRANSPORT

E - MANAGEMENT SCIENCE AND INFORMATICS IN TRANSPORT

MODELLING, SIMULATION AND EXPERIMENTAL VERIFICATION OF A 3 DOF MOVING PLATFORM WITH PARALLEL KINEMATICS AND ELECTRO-HYDRAULIC PROPORTIONAL / SERVO CONTROL SYSTEM

Ezz Eldin Ibrahim*, Ahmed Azouz, Tarek Elnady, Mohamed Saffaa Hassan, Ibrahim Saleh

Military Technical College, Cairo, Egypt

*E-mail of corresponding author: ezzbos@gmail.com

Ezz Eldin Ibrahim 0000-0001-9377-7852,
Tarek Elnady 0000-0003-1060-1742,
Ahmed Azouz 0000-0002-7697-6611,
Mohamed Saffaa Hassan 0000-0002-8557-9706

Resume

Hydraulic motion platforms are widely utilized in various environments due to their capacity to bear heavy loads and provide long actuator strokes. The predominant control system employed for hydraulic motion platforms is the electro-hydraulic servo system (EHSS) due to its high accuracy and robustness. However, compared to other types of hydraulic valves, the electro-hydraulic servo valve (EHSV) is less durable. An alternative system to EHSS is the electro-hydraulic proportional system (EHPS), which employs an electro-hydraulic proportional valve (EHPV) instead of the EHSV. The EHPV resolves the durability issue at the expense of accuracy and system error. The optimization of durability and accuracy is the core of this study. The tracking behavior and response of both Three degrees of freedom (3 DOF) motion platforms using EHSS and EHPS are investigated across different frequency ranges.

Available online: https://doi.org/10.26552/com.C.2025.001

Article info

Received 15 May 2024
Accepted 11 September 2024
Online 7 October 2024

Keywords:

hydraulic valve
electro-proportional valve
servo valve
electro-hydraulic proportional system
electro-hydraulic servo system
position tracking control
motion platform

ISSN 1335-4205 (print version)
ISSN 2585-7878 (online version)

1 Introduction

Motion platforms are devices comprising two platforms, with the lower platform being stationary while the upper platform follows the desired motion. They are widely used in transportation simulators, replicating real-world vehicle movements with high precision. They enhance driver training, vehicle testing, and the development of advanced driving assistance systems. Numerous research works have focused on electro-hydraulic systems, exploring their various aspects. Akers et al. [1] extensively discussed the potential configurations of electro-hydraulic systems, providing insights into the performance analysis of system components and operational methodologies. Additionally, Watton [2] delved into the modelling and simulation of electro-hydraulic systems, exploring mathematical derivations of different hydraulic system structures.

Electro-hydraulic systems have gained significant popularity in numerous industrial applications due to their exceptional capacity to deliver high torque and force while maintaining a favorable power-to-weight ratio. These Hydraulic Servo Systems find applications across a wide range of industries, including aircraft, robotics, mining machinery, manufacturing systems, active suspensions, test machines, paper machines, and injection molding machines.

The primary objective of an electro-hydraulic system is to precisely control the desired displacement. To achieve this goal, advanced techniques have been developed to ensure high response and minimize errors. Typically, displacement control and error reduction involve comparing the position, velocity, pressure, and force of the system's output against the input signal, thereby striving to achieve the desired response as accurately as possible.

Optimal system tuning has been extensively explored by researchers, who have employed various methodologies to achieve the desired results. These include root locus analysis, and the Zeigler-Nichols method [3] that are the most famous techniques used in this field. Genetic Algorithm (GA), Particle Swarm Optimization (PSO), and Adaptive Weighted PSO (AWPSO) are examples of evolutionary techniques that are used for tuning Proportional, Integral, and Derivative (PID) controller. The PID controller is applied in this approach to hydraulic servo system (HSS) simulation model and real-time HSS.

Electro-hydraulic servo systems EHSS have been studied by many researchers due to their great importance in industrial fields. One of the main problems in studying EHSS is the nonlinearity problem of the dynamics of the hydraulic system as stated by Sohl et al. [4]. The friction, non-smooth motion, and valve directional change resulted in system nonlinearities. Many studies dealt with analyzing and controlling the nonlinearity of EHSS. These studies helped in providing system stability for a good position and force tracking.

To ensure accurate tracking of position, acceleration, pressure, and force, the EHSS has been equipped with various automatic controllers. Guan and Pan [5] presented a new control technique based on an adaptive sliding mode method for controlling the electro-hydraulic system. The controlling method is applied experimentally, and the results proved the effectiveness of it in tracking any trajectory by the hydraulic actuator. Niksefat and Sepehri [6-7] used a quantitative feedback theory (QFT) to control the hydraulic actuator displacement by evaluating the force acting on the cylinder. Lichen et al. [8] presented a new control strategy for hydraulic servo systems to obtain more robustness and stability using the PID tuning.

Tian [9] studied the actuator external torque and invented a new control theory. The utilization of a Fuzzy Logic Controller (FLC) has been highlighted for precise position control of electro-hydraulic actuators. Additionally, an (ACO) ant colony optimization technique is employed to optimize the parameters of the fuzzy neural network, ensuring the attainment of optimal values [10].

The enhancement of position-tracking performance is achieved through the application of the invariance principle and feed-forward compensation, utilizing the pole-zero placement theory of the system. This approach allows for the development of improved control strategies to ensure accurate and efficient position tracking, as described in [11].

A hydraulic position servo system control is established by employing a Particle Swarm Optimization (PSO) algorithm to regulate the PID loops. This implementation enables effective optimization of the control parameters, resulting in improved performance and precision of the servo system as presented in [12]. The force control of the hydraulic servo system is achieved through the design and implementation of fuzzy controllers. These controllers are specifically designed to minimize force overshoot and protect the load from potential failure. By employing the fuzzy control techniques, the system ensures precise force regulation and safeguards the overall stability and integrity of the load, as illustrated in [13]. Three control strategies are employed to regulate an electro-pneumatic 3DOF platform by Prieto et al. [14].

Proportional valves demand significantly higher input power typically hundreds of milliamps or more compared to servo valves, which operate on mere tens of milliamps as mentioned by Bin [15]. While proportional valves offer less precise control and can exhibit greater hysteresis, the servo valves excel in accuracy. The performance of EHSV is discussed by MI et al. [16].

In the previous review, focused on controlling stabilization platforms and electro-hydraulic systems, the emphasis was placed on selecting an appropriate control method to address system errors and transient response. However, this study shifts its attention to the key control component of the hydraulic system, namely the electro-hydraulic valve. It delves into examining the impact of valve parameters on platform stability and the potential for improving error reduction within the system.

2 Model description

The 3 DOF motion platform shown in Figure 1 consists of the lower plate, which is fixed, and the upper plate which is moving to track the required position. The two plates are connected via three hydraulic actuators driven by an electro-hydraulic system. The actuators are joined with the two plats by six universal joints. The electro-hydraulic system forces the three actuators to extract or retract to enable the upper plate to track the required motion. The figure shows the orientation of the three axes x, y, and z and two rotations which are roll and pitch.

The overall system of the 3 DOF motion platform is depicted in the block diagram shown in Figure 2. The input signal from the transition motion in the z-direction and the rotation motion in both roll and pitch were transformed to a linear motion by the mean of the rotation matrix block, which are described later. These signals were then analyzed after feeding back from the position sensor and operating the EHSVs/ EHPVs. The three valves were fed by the required flow rate from the hydraulic power block. The three actuators are operated to drive the upper plate with the required input position signal. The lower plate remained stationary as a reference frame, so the motion of the upper plate was referred to concerning it.

3 Modeling of 3 DOF motion platform using EHPS and EHSS

The electro-hydraulic system could be used for motion platforms; it can be either EHSS or EHPS. The mathematical model of the EHPS for one hydraulic

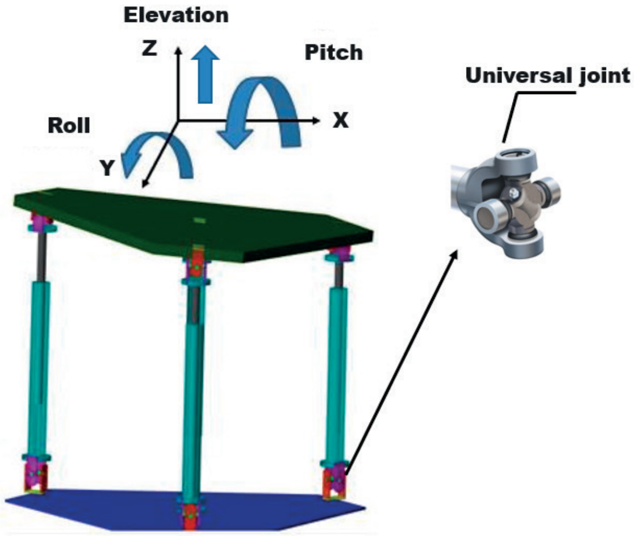

Figure 1 *Motion platform with 3 DOF motion*

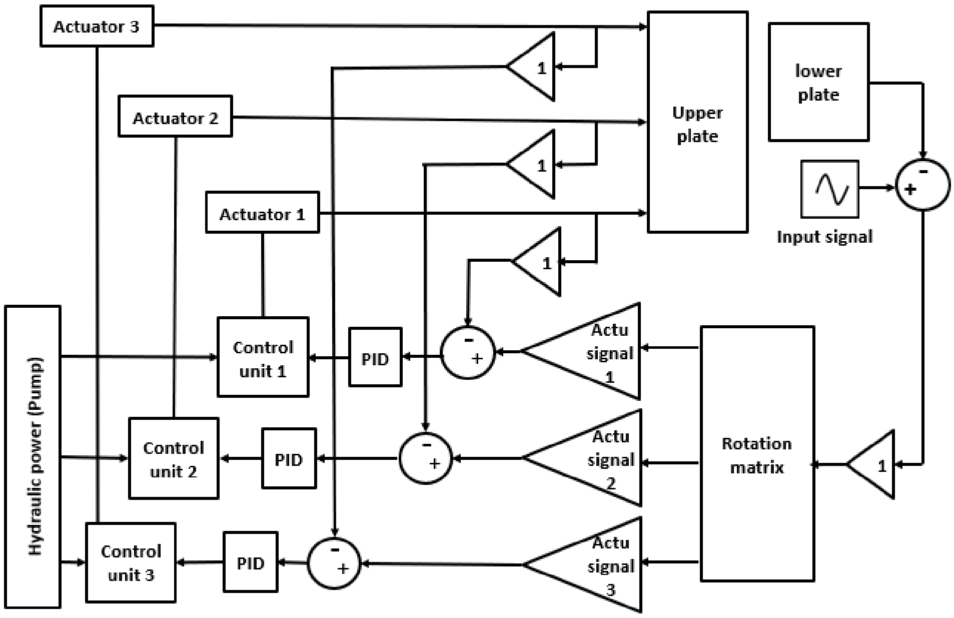

Figure 2 *Hydraulic motion platform with 3 DOF block diagram*

actuator was discussed recently by Yuan in [17] and [18]. The mathematical model is derived in this section. The single hydraulic actuator system is then integrated into the MATLAB Simulink program to model the 3 DOF motion platform. The Q-P mathematical relation of the pump was found in Rabie [19], as follows:

$$Q_P = Q_{th} - cP_G\,, \tag{1}$$

where:
Q_{th} is the theoretical maximum flow rate of the gear pump,
c is a constant equal 7x10^{-3},
P_G is the pump output pressure.

The mathematical equations, which describe the operation of the relief valve, as in Rabie [19], are:

The equation of poppet motion:

$$m_p \frac{d^2 z}{dt^2} + f_r \frac{dz}{dt} + k_r(z + z_0) = pA_p + F_{seat} \tag{2}$$

$$F_{seat} = K_r z_0\,, \tag{3}$$

$$A_p = \pi D^2/4(m^2)\,, \tag{4}$$

where:
m_p is the relief valve poppet mass, kg,
z is the displacement of relief valve poppet, m,
f_r is the pump output pressure,
K_r is the stiffness coefficient of relief valve spring, N/m,
A_p is the poppet area of the relief valve, m^2,

F_{seat} is the seat reaction of the relief valve, N.

The flow-rate equation through the relief valve is:

$$Q_{rv} = C_d A_p \sqrt{\frac{2(P - P_t)}{\rho}}\,, \tag{5}$$

where:
C_d is the discharge coefficient.
P_t is the tank pressure, Pa.

The EHPV is a 4/3 valve hydraulic ring manufactured of type NG6. It is designed with a valve spool that exhibits zero overlap and is regulated by the movement of two electrical proportional solenoids.

The equation of motion of the valve spool could be written as follows:

$$F_s = m_s \frac{d^2x}{dt^2} + f_s \frac{dx}{dt} + k_s x\,, \tag{6}$$

where:
m_s is the mass of spool (kg),
f_s is the EHPV spool damping coefficient [13] (N),
k_s is the EHPV return spring stiffness (N/m),
x is the spool displacement.

The first term on the right-hand side of Equation (6) represents the inertia force of the spool during motion. The second term represents the damping force, while the last term represents the force applied by the return spring. The internal orifices of the valve are shown in Figure 3.

The flow-rate equations throughout the valve orifices are given by the following equations:
from port B to port T,

$$Q_a = C_d A_a(x) \sqrt{\frac{2(P_B - P_t)}{\rho}}\,, \tag{7}$$

from port P to port B,

$$Q_b = C_d A_b(x) \sqrt{\frac{2(P_s - P_B)}{\rho}}\,, \tag{8}$$

from port P to port A,

$$Q_c = C_d A_c(x) \sqrt{\frac{2(P_s - P_A)}{\rho}}\,, \tag{9}$$

from port A to port T,

$$Q_d = C_d A_d(x) \sqrt{\frac{2(P_A - P_t)}{\rho}}\,, \tag{10}$$

where:

$$A_a = A_c = A_r \qquad x \geq 0\,, \tag{11}$$

$$A_b = A_d = \omega\sqrt{(x^2 + c^2)} \qquad x \geq 0\,, \tag{12}$$

$$A_a = A_c = \omega\sqrt{(x^2 + c^2)} \qquad x \leq 0\,, \tag{13}$$

$$A_b = A_d = A_r \qquad x \geq 0\,, \tag{14}$$

where
ω is the width of the port,
c is the spool radial clearance,
x is the valve opening distance,
A_r is the radial clearance area.

To obtain a mathematical model for the cylinder; the internal and external flows of the cylinder are described in the schematic drawing shown in Figure 4.

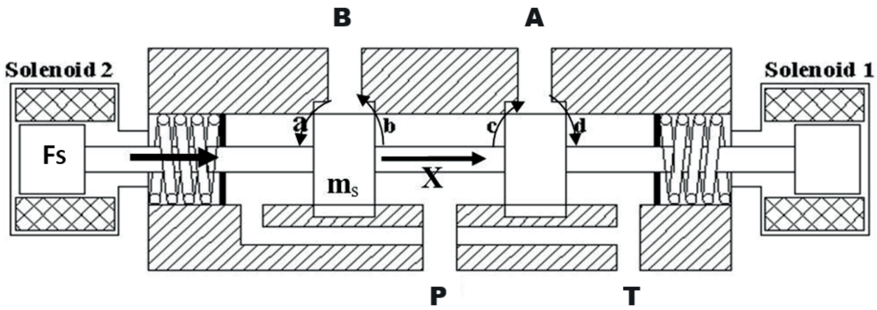

Figure 3 *Internal orifices of proportional-directional valve*

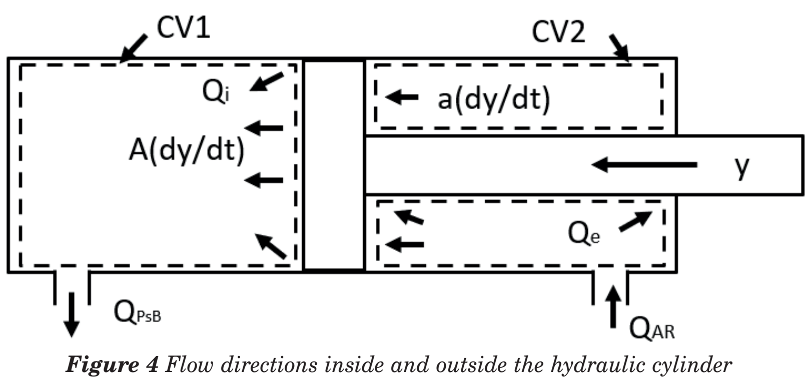

Figure 4 *Flow directions inside and outside the hydraulic cylinder*

The continuity equation, applied on the control volume CV1and CV2, could be written as follows:

$$Q_{AR} - a\frac{dy}{dt} - Q_i - Q_e - \frac{(V_R + ay)}{B} \times \frac{dP_R}{dt} = 0\,, \tag{15}$$

$$A\frac{dy}{dt} - Q_i - Q_{PsB} - \frac{(V_{PS} + Ay)}{B} \times \frac{dP_{Ps}}{dt} = 0\,. \tag{16}$$

The equation of motion, applied for the piston and its rod, could be described as follows:

$$aP_R - AP_{Ps} = m_c\frac{d^2y}{dt^2} + f_c\frac{dy}{dt} + F\,. \tag{17}$$

4 Analysis for kinematics

Much research dealt with the 6DOF parallel manipulator platform and its motion. This study focuses on investigating the design and implementation of a system that incorporates inverse kinematics and motion monitoring for a 3DOF platform. The aim is to explore the execution and effectiveness of this system as done by [20]. The system enables motion along is the three linear translations (x, y, and z directions) and three rotations around the three axes (yaw, pitch, and roll, denoted as ψ, θ, and ϕ, respectively).

In this study, 3 DOF is the main concern which are two rotation pitch θ, roll ϕ, and one translation in the z-direction. These linear and rotation motions are represented in Figure 5, by representing the two frames; one is fixed while the other is moving with respect to the fixed frame. The length vector between the fixed and a moving plate l is determined from the following equation:

$$l_i = \mathbf{t} + \mathbf{P}_i \,.\, \mathbf{R}_P - \mathbf{b}_i \tag{18}$$

where:

l_i is the length of the actuators,

t is the translational position vector of the origin of the moving frame with respect to the reference frame,

$\mathbf{P}_i$ are represents each actuator's position vector about the moving frame,

$\mathbf{b}_i$ are represents each actuator's position vector about the reference frame,

$\mathbf{R}_P$ are represents a mix of rotation matrix stationary and moving frames by knowing input rotation angles in roll and pitch, as discussed in [13].

$$\mathbf{R}_p = \begin{bmatrix} C_\theta & 0 & S_\theta \\ S_\theta S_\phi & C_\phi & -C_\theta S_\phi \\ -S_\theta C_\phi & S_\phi & C_\theta C_\phi \end{bmatrix}, \tag{19}$$

where:

C_θ is cos θ and S_ϕ is sin ϕ, etc.

The design of a 3DOF translational parallel manipulator, utilizing hydraulic actuation, was recently studied by [21].

The mathematical model of the entire hydraulic system could be obtained by integrating all derived mathematical equations with the aim of the MATLAB Simulink program. The system transfer function was identified using the system identification tool as follows:

$$f(s) = \frac{8.468S + 11.05}{S^2 + 8.522S + 11.11}\,. \tag{20}$$

Modelling and validation of the EHSV system are done based on the published work by Ibrahim et al. [22]. The model was utilized in this study to simulate the 3 DOF motion platform using the MATLAB Simulink program.

5 Experimental work

The 3 DOF motion platform test rig was established with EHPS using The Military Technical College laboratory facilities. The test rig was used to investigate the motion of the platform in roll and pitch directions with a maximum inclination angle of 10° and elevation up to 100 mm.

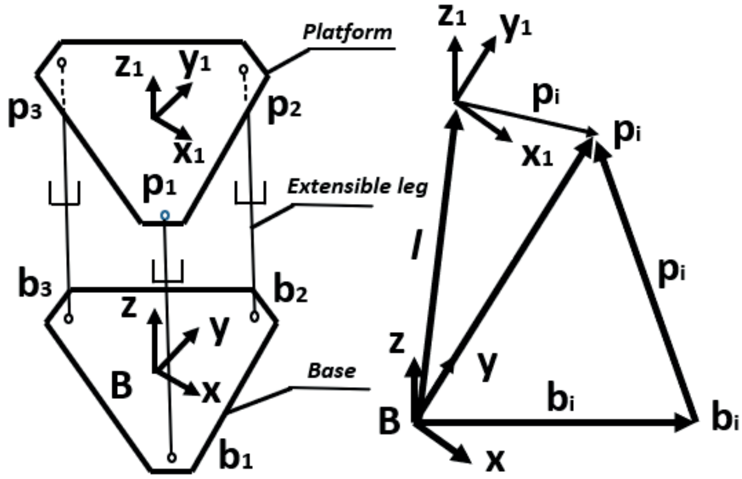

Figure 5 *Coordinates diagram for 3 DOF motion platform*

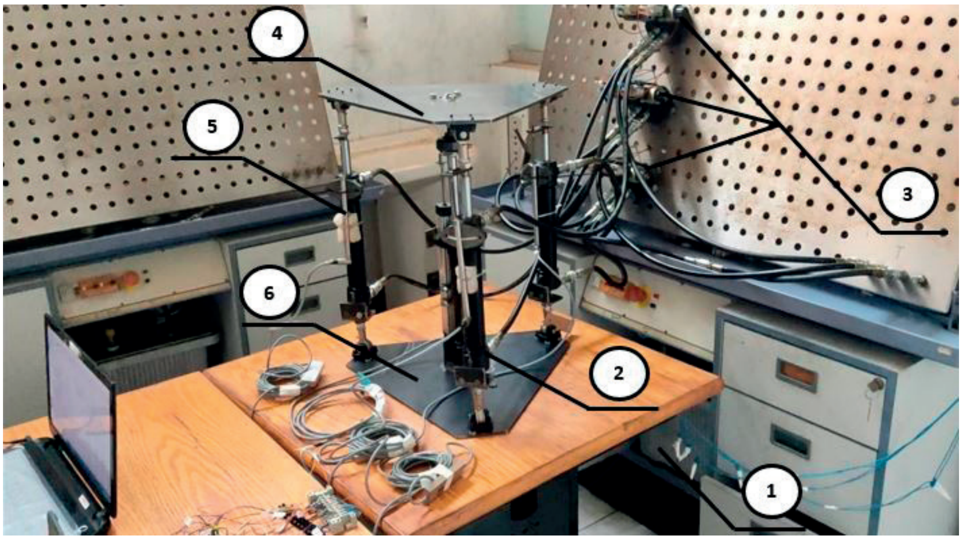

Figure 6 *Experimental test rig for 3DOF hydraulic motion platform*

Table 1 *Hydraulic circuit components description*

Component	Specification
Pump	A fixed displacement gear pump produces up to 6.05 liters per minute at its highest output flow rate, at a nominal speed of 600 rpm
RV.	Relieving pressure at 60 bar
PV.	4/3 EHPV type NG6
Actuator	Cylinder to road ratio 1.6:1 with 32/22 mm area and a max. pressure of 160 bar

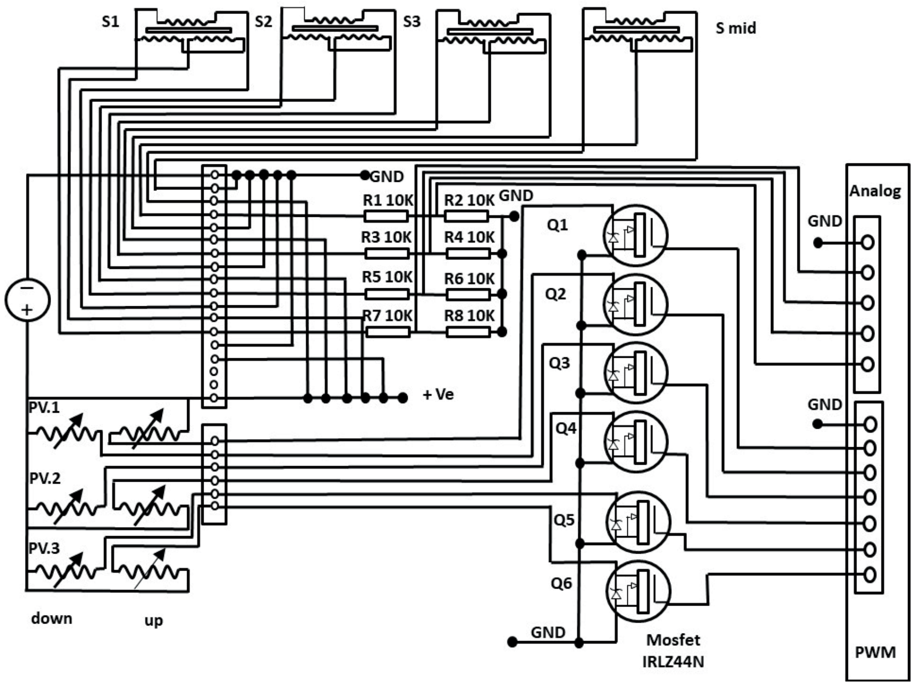

Figure 7 *Electric circuit for controlling 3 DOF hydraulic stabilization platform*

Figure 6 shows the test rig which consists of an oil tank (1) that delivers the circuit with the required hydraulic oil. Three hydraulic actuators (2) were used to perform the required motion by the feeding from three (EHPV) (3), which are the main control unit. Two plates (4) and (6) are used as upper and lower plates, respectively. Three (LVDT) (5) are used to feed the controller with the cylinder's displacement. The hydraulic circuit components are described in Table 1.

The electric circuit used in controlling the proposed motion platform is designed with the aid of the "Proteus 8.8" program [23]. Figure 7 illustrates the block diagram

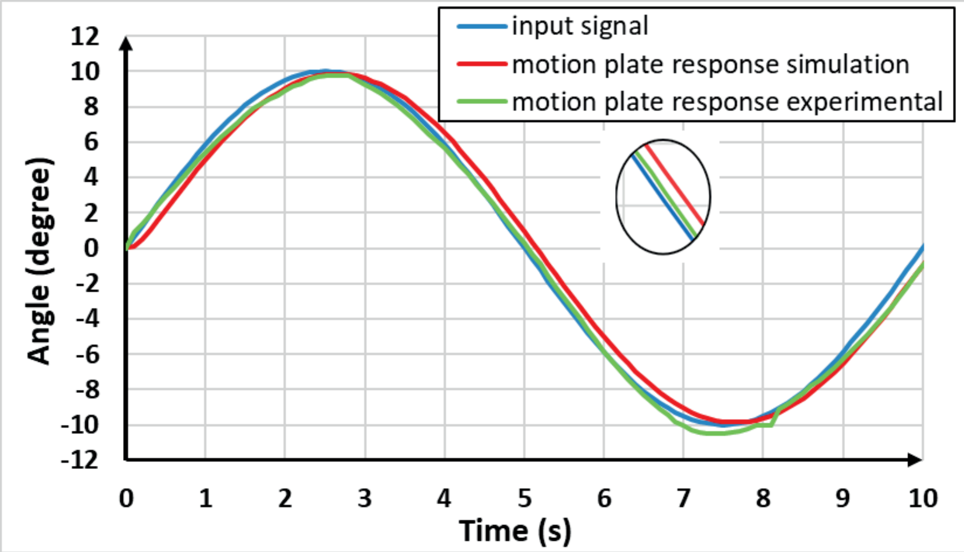

Figure 8 *Experimental and model tracking the behavior of 3DOF motion platform with EHPS to a roll motion*

of this electric circuit. Four LVDT sensors are used in this circuit using a power supply of 24 V DC and its output signal is 10 V DC. The control card is Arduino Mega with input/output volt 5 V DC. Two 10-ohm resistors are used in series to protect the control card from damage. Arduino delivers the sensors signal to the MATLAB Simulink program to adjust the required output to the proportional valve coils. The output voltage of the control card is 5 V DC while the proportional valve coils operate at 24 V DC. Thus, to increase the pulse width modulation from a voltage range of ±5 V DC to ±24 V DC, six MOSFET transistors (IRLZ44) are utilized.

6 System validation

The 3DOF motion plate in this study utilizes an electro-hydraulic proportional valve EHPV instead of EHSV. The outcomes of tracking the motion platform's behavior (experimental vs. model), in response to a sinusoidal input signal with a 10° amplitude and 0.1 Hz frequency, are displayed in Figure 8. When compared to the input signal and the experimental findings, the model shows a good tracking position. There was a recorded 0.038 root-mean-square error between the motion platform model and the input signal. However, there was a 0.046 root-mean-square error between the experimental and model results. The model has a good tracking position with the input signal. The maximum motion platform model tracking angle recorded ±9.86° (i.e., it deviates from its maximum target by 0.14°).

7 Result and discussion

The motion platforms with EHSS and EHPS are examined by applying a sinusoidal input signal with a frequency range (0.1 - 0.5 Hz) to study their tracking behavior. Figure 9 shows the tracking behavior of the motion platform with both systems EHSS and EHPS to a sinusoidal input signal with an amplitude of 10° and frequency of 0.1 Hz. The two models have a good tracking position with the input signal. The root-mean-square error between the input signal and the motion platform with EHPS was recorded at 0.038 and the maximum motion platform tracking angle was recorded at ±9.86° (i.e., it deviates from its maximum target by 0.14°). The root-mean-square error between the input signal and the motion platform with EHSS was recorded at 0.02 and the maximum motion platform tracking angle was recorded at ±9.9° (i.e., it deviates from its maximum target by 0.1°).

Figure 10 shows the motion platform response with EHSS and EHPS to a sinusoidal wave with a frequency of 0.5 Hz and amplitude of 10°. The motion platform with EHPS tracks the input signal with a root-mean-square error of 0.27 and the maximum motion platform tracking angle recorded ±8.67° (i.e., it deviates from its maximum target by 1.33°). The motion platform with EHSS tracks the input signal with a root-mean-square error of 0.11 and the maximum motion platform tracking angle recorded ±9.6° (i.e., it deviates from its maximum target by 0.4°), which agreed with the data plotted in [24].

Figure 11 shows a comparison between the 3DOF motion platform with EHSS and EHPS by applying the input-signal frequencies (0.1, 0.2, 0.3, 0.4, and 0.5 Hz). The results focus on deviation from the maximum target angle. The results show that both systems are affected by high frequency. The results, shown in Figure 12, represent the recorded root-mean-square error with respect to the input signals. Both system's error increases by increasing the input-signal frequency. However, the error resulting from using the EHPS has a major record in comparison to EHSS.

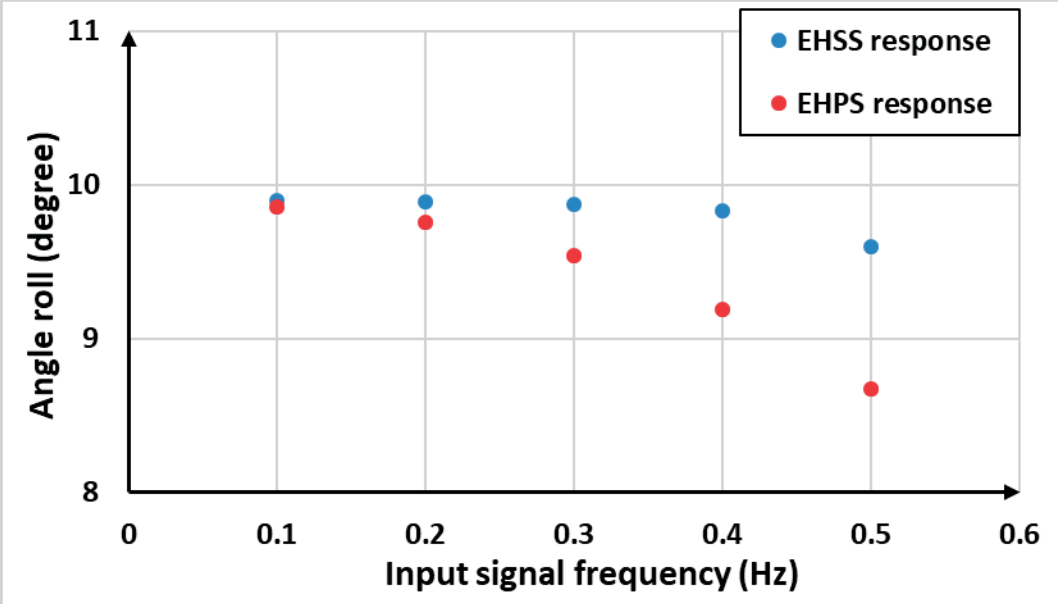

Figure 11 Deviation of the 3 DOF motion platform from the maximum target using EHSS and EHPS

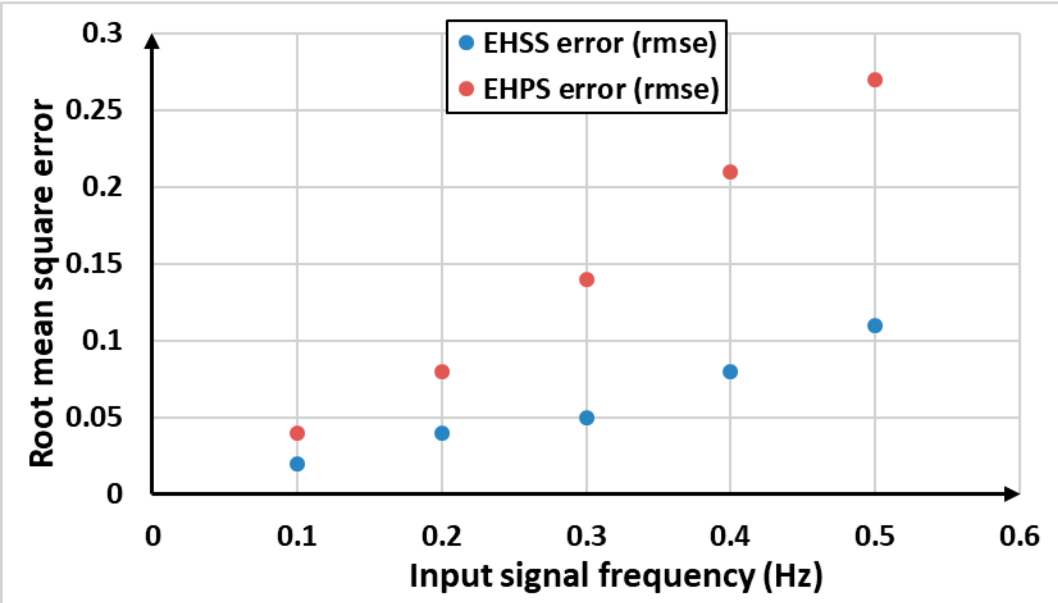

Figure 12 *Root-mean-square error of the 3DOF motion platform using EHSS and EHPS*

Table 2 *EHSS and EHPS tracking behavior by changing input signal frequency*

Input frequency (Hz)	RMSE between the model and input EHSS.	RMSE between the model and input EHPS.	Deviation from target EHSS	Deviation from target EHPS
0.1	0.02	0.038	0.1°	0.14°
0.2	0.04	0.08	0.11°	0.24°
0.3	0.05	0.14	0.13°	0.46°
0.4	0.08	0.21	0.17°	0.81°
0.5	0.11	0.27	0.4°	1.33°

Figure 12 shows the effect of changing the input signal frequency on the platform stability and the deviation achieved from the accurate required inclination using EHSS and EHPS, which is also clarified in Table 2. The platform deviates from its target as the frequency is increased by using both systems; however, by using the EHPS the deviation is larger than by using EHSS. These results confirm the effectiveness of EHPS in low-frequency applications and it is not useful for high frequency up to 0.3 Hz.

8 Conclusion

This study was focused on the design and analysis of 3DOF motion plate models equipped with EHPS and EHSS to investigate their respective frequency ranges.

Firstly, both motion platforms were evaluated, and it was observed that their responses were nearly identical for the low-frequency input signals. This suggests that both systems are capable of effectively handling low-frequency motions.

However, as the input signal frequency increased, both systems exhibited an increase in error. Notably, the EHPS system demonstrated a significant error compared to the EHSS system. This indicates that the EHSS system outperforms the EHPS system in terms of accuracy and precision, especially at higher frequencies.

The suggested motion platform with EHPS, which has been extensively tested and verified over a wide range of frequency ranges, is the best suited for the low-frequency applications, according to the study's findings. This platform can be employed in scenarios where precise motion control is required within a relatively lower frequency range.

In summary, this research contributes to understanding of the frequency capabilities and limitations of the 3DOF motion plate models with EHPS and EHSS. The results highlight the superior performance of the EHSS system, particularly at higher frequencies, while emphasizing the suitability of the EHPS system for the low-frequency applications. These findings can inform the selection and utilization of motion platforms in diverse industrial and research settings. Further research can focus on optimizing the performance of EHPS systems to mitigate their error at higher frequencies and enhance their overall functionality.

Acknowledgment

The authors received no financial support for the research, authorship and/or publication of this article.

Conflicts of interest

The authors declare that they have no known competing financial interests or personal relationships that could have appeared to influence the work reported in this paper.

Reference

[1] AKERS, A., GASSMAN, M., SMITH, R. *Hydraulic power system analysis* [online]. 1. ed. Boca Raton: CRC Press, 2006. eISBN 9780429191176. Available from: https://doi.org/10.1201/9781420014587

[2] WATTON, J. *Fluid power systems: modeling, simulation, analog and microcomputer control*. Prentice-Hall, Inc., 1989. ISBN 978-0133231977.

[3] PUANGDOWNREONG, D., SUKULIN, A. Obtaining an optimum PID controllers for unstable systems using current search. *International Journal of Systems Engineering, Applications and Development*. 2012, **6**(2), p. 188-195. eISSN 2074-1308.

[4] SOHL, G. A., BOBROW, J. E. Experiments and simulations on the nonlinear control of a hydraulic servosystem. *IEEE Transactions on Control Systems Technology* [online]. 1999, **7**(2), p. 238-247. ISSN 1063-6536, eISSN 1558-0865. Available from: https://doi.org/10.1109/87.748150

[5] GUAN, C., PAN, S. Adaptive sliding mode control of electro-hydraulic system with nonlinear unknown parameters. *Control Engineering Practice* [online]. 2008, **16**(11), p. 1275-1284. ISSN 0967-0661, eISSN 1873-6939. Available from: https://doi.org/10.1016/J.CONENGPRAC.2008.02.002

[6] NIKSEFAT, N., SEPEHRI, N. Designing robust force control of hydraulic actuators despite system and environmental uncertainties. *IEEE Control Systems Magazine* [online]. 2001, **21**(2), p. 66-77. ISSN 1066-033X, eISSN 1941-000X. Available from: https://doi.org/10.1109/37.918266

[7] NIKSEFAT, N., SEPEHRI, N. Design and experimental evaluation of a robust force controller for an electro-hydraulic actuator via quantitative feedback theory. *Control Engineering Practice* [online]. 2000, **8**(12), p. 1335-1345. ISSN 0967-0661, eISSN 1873-6939. Available from: https://doi.org/10.1016/S0967-0661(00)00075-7

[8] YU, M., LICHEN, G. Fuzzy immune PID control of hydraulic system based on PSO algorithm. *Telkomnika Indonesian Journal of Electrical Engineering* [online]. 2013, **11**(2), p. 890-895. ISSN 1693-6930, eISSN 2302-9293. Available from: https://doi.org/10.11591/TELKOMNIKA.V11I2.2048

[9] TIAN, J. Study on control strategy of electro-hydraulic servo loading system. *Telkomnika Indonesian Journal of Electrical Engineering* [online]. 2013, **11**(9), p. 5044-5047. ISSN 1693-6930, eISSN 2302-9293. Available from: https://doi.org/10.11591/TELKOMNIKA.V11I9.3246

[10] ROZALI, S. M., RAHMAT, M. F., HUSAIN, A. R., KAMARUDIN, M. N. Design of adaptive backstepping with gravitational search algorithm for nonlinear system. *Journal of Theoretical and Applied Information Technology*. 2014, **59**(2), p. 460-468. ISSN 1992-8645, eISSN 1817-3195.

[11] YAO, J.-J., DI, D.-T., JIANG, G.-L., LIU, S. High precision position control of electro-hydraulic servo system based on feed-forward compensation. *Research Journal of Applied Sciences, Engineering and Technology*. 2012, **4**(4), p. 289-298. ISSN 2040-7459, eISSN 2040-7467.

[12] ROOZBAHANI, H., WU, H., HANDROOS, H. Real-time simulation based robust adaptive control of hydraulic servo system. In: 2011 IEEE International Conference on Mechatronics ICM 2011: proceedings [online]. IEEE. 2011. ISBN 978-1-61284-982-9, eISBN 978-1-61284-985-0, p. 779-784. Available from: https://doi.org/10.1109/ICMECH.2011.5971220

[13] CHEN, H. M., SHEN, C. S., LEE, T. E. Implementation of precision force control for an electro-hydraulic servo press system. In: 2013 3rd International Conference on Intelligent System Design and Engineering Applications ISDEA 2013: proceedings [online]. IEEE. 2013. ISBN 978-1-4673-4893-5, p. 854-857. Available from: https://doi.org/10.1109/ISDEA.2012.202

[14] RUBIO, E., PRIETO, P. J., HERNANDEZ, L., URQUIJO, O. Comparison between three control strategy applied to an electro-pneumatic 3-DOF platform. In: IEEE CHILEAN Conference on Electrical, Electronics Engineering, Information and Communication Technologies CHILECON 2019: proceedings [online]. IEEE. 2019. eISBN 978-1-7281-3185-6. Available from: https://doi.org/10.1109/CHILECON47746.2019.8986866

[15] YU, B. ET AL., Design, mathematical modeling and force control for electro-hydraulic servo system with pump-valve compound drive. *IEEE Access* [online]. 2020, **8**, p. 171988-172005. eISSN 2169-3536. Available from: https://doi.org/10.1109/ACCESS.2020.3012091

[16] MI, J., YU, J., HUANG, G. Direct-drive electro-hydraulic servo valve performance characteristics prediction based on big data and neural networks. *Sensors* [online]. 2023, **23**(16), 7211. eISSN 1424-8220. Available from: https://doi.org/10.3390/S23167211

[17] YUAN, X. J., LING, H. T., CHEN, J. J., FENG, Y., QIU, T. Y., ZHAO, R. CH. A dynamic modelling method for an electro-hydraulic proportional valve combining multi-systems and moving meshes. *Journal of the Brazilian Society of Mechanical Sciences and Engineering* [online]. 2022, **44**(7), p. 1-13. ISSN 1678-5878, eISSN 1806-3691. Available from: https://doi.org/10.1007/s40430-022-03603-x

[18] YUAN, X., SHI, S., WANG, C., WEI, L., LUO, C., CHEN, J. Dynamic modeling method for an electro-hydraulic proportional valve coupled mechanical-electrical-electromagnetic-fluid subsystems. *Journal of Magnetism and Magnetic Materials* [online]. 2023, **587**, 171312. ISSN 0304-8853, eISSN 1873-4766. Available from: https://doi.org/10.1016/J.JMMM.2023.171312

[19] RABIE, M. G. *Fluid power engineering*. New York: McGraw-Hill, 2009. ISBN 9780071626064.

[20] WEI, M. Y. Design and implementation of inverse kinematics and motion monitoring system for 6dof platform. *Applied Sciences* [online]. 2021, **11**(19), 9330. eISSN 2076-3417. Available from: https://doi.org/10.3390/app11199330

[21] DINDORF, R., WOS, P. Design of a hydraulically actuated 3-DoF translational parallel manipulator. *AIP Conference Proceedings* [online]. 2019, **2077**(1), p. 020015-1-020015-12. ISSN 0094-243X, eISSN 1551-7616. Available from: https://doi.org/10.1063/1.5091876

[22] IBRAHIM, E. E., ELNADY, T., HASSAN, M. S., SALEH, I. Modelling, transient response and hydraulic behaviour of 2DOF stabilization platform. *FME Transactions*. 2020, **48**(4), p. 833-840. ISSN 1451-2092, eISSN 2406-128X.

[23] PCB design and circuit simulator software - Proteus [online] Accessed: Aug. 16, 2024. Available from: https://www.labcenter.com

[24] RAD, S. A., TAMIZI, M. G., MIRFAKHAR, A., MASOULEH, M. T., KALHOR, A. Control of a two-DOF parallel robot with unknown parameters using a novel robust adaptive approach. *ISA Transactions* [online]. 2021, **117**, p. 70-84. ISSN 1879-2022, eISSN 0019-0578. Available from: https://doi.org/10.1016/J.ISATRA.2021.02.001

Appendix

***Table A** Nomenclature*

Symbol	Definition
a	Cylinder area rod side, m^2
A	Cylinder area piston side, m^2
A_a	PV. Throttle area (a), m^2
A_b	PV. Throttle area (b), m^2
A_c	PV. Throttle area (c), m^2
A_d	PV. Throttle area (d), m^2
A_p	RV. Poppet area, m^2
B	Hydraulic oil's bulk modulus of elasticity, $N.m^{-2}$
C_d	Coefficient of discharge
C	Radial clearance, m
d	Cylinder rod side diameter, m
D	Cylinder side piston diameter, m
f_r	RV. Poppet damping coefficient, $N.sec.m^{-1}$
f_s	PV. Spool damping coefficient, $N.sec/m^{-1}$
F_s	PV. Solenoid force, N
F_{seat}	RV. Seat reaction, N
k	PV. Spring stiffness, $N.m^{-1}$
m_p	RV. Poppet mass, kg
m_s	PV. Moving parts mass, kg
p	Pressure, Pa
P_A	PV. Pressure port (A), Pa
P_B	PV. Pressure port (B), Pa
P_P	PV. Pressure port (P), Pa
P_t	Tank pressure, Pa
Q	Flow rate, m^3/sec
Q_a	PV. Flow rate through area (a), m^3/sec
Q_{AR}	Flow rate from port A to rod side chamber in the hydraulic cylinder, $m^3.sec^{-1}$
Q_b	PV. Flow rate through area (b), $m^3.sec^{-1}$
Q_c	PV. Flow rate through area (c), $m^3.sec^{-1}$
Q_d	PV. Flow rate through area (d), $m^3.sec^{-1}$
x	PV. Spool displacement, m
y	Displacement of the cylinder rod, m
z	RV. Poppet displacement, m

RESEARCH ON SOIL CUTTING WITH A FLAT CUTTER USING A SIMULATION MODEL

Asset Altynbayev*, Alexandr Ganyukov

Abylkas Saginov Karaganda Technical University NPJSC, Karaganda, Kazakhstan

*E-mail of corresponding author: altynbaev.aset@gmail.com

Alexandr Ganyukov 0000-0002-0651-9781

Resume

The research aims to develop an algorithm for modelling the process of cutting an infinite volume of soil with a flat cutter in the Abaqus software package. The hypothesis of the existence of energy and volume of resistance to cutting is proposed. The analysis of shock wave distribution in the soil volume is performed. Boundary conditions for the soil volume model are determined, as well as for a flat cutter with linear motion. Stress gradients in the soil during its deformation are determined. Confirmation of the hypothesis about the existence of energy and volume of resistance to cutting was obtained. A logarithmic regression equation was derived based on the obtained volume values.

Article info

Received 25 March 2024
Accepted 3 September 2024
Online 9 October 2024

Keywords:

transportation engineering
soil cutting theory
earthmoving machines
soil cutting energy
soil cutting forces
Coulomb-Mohr plastic model
Abaqus software package

Available online: https://doi.org/10.26552/com.C.2025.002

ISSN 1335-4205 (print version)
ISSN 2585-7878 (online version)

1 Introduction

The process of construction is a constant and continuous process that needs accurate calculations. The construction of any object starts with the zero cycle of work. It implies the development and preparation of soil for further safe construction and operation of the object. At this stage of construction, various earthmoving machines are used: excavators, bulldozers, scrapers, motor graders, draglines, and others, Figures 1, 2.

The basic principle of operation of earthmoving machines is cutting the soil with the use of a special cutting device. The soil cutting is the process of separation of soil particles as a result of the mechanical impact of the earthmoving machine's cutting device on the soil, Figure 3. Cutting of the soil is possible on dry and with the use of a clay solution. This technology is used in "wall-in-soil" construction to reinforce the walls of the excavated soil under a layer of clay thixotropic solution, which creates a dense layer and protects the trench walls from collapse.

Depending on the type of work, different working devices are used: ripper teeth, excavator buckets of shovels, dragline, loader, planer, scraper buckets, and bulldozer blades, Figures 4, 5.

For reliable operation of earthmoving machines, the design and operating parameters must be calculated. For this purpose, it is necessary to know the loads and cutting forces that act from the ground on any particular earthmoving machine's cutters and working devices. This is engaged in the theory of soil cutting. Its task is to determine the regularity of changes in the cutting force and loading of the working device of the earthmoving machine under changing conditions of cutting. Research on the loading of working devices of earthmoving machines was carried out by Zhang et al. [1], Stromblad [2], Ha et al. [3], Lee and Chang [4], Goryachkin [5], Dombrovsky [6], Zelenin [7], Vetrov [8], Kadyrov [9] and others.

Zhang et al. [1] investigated the soil-cutting process with a rotary tillage roller and the various problems arising, such as structural buckling, deformation, high energy consumption due to impacts and loads, and difficulty in observing micro changes in soil and tool behavior. They used Finite Element Method (FEM), to model a rotary cultivator with different bending angle parameters and determine the average stresses and deformation of the structure. They also established a linear relationship between the bending angle and rotary cultivator performance.

To simulate the dynamic process of soil cutting by the knife roller of the rotary tillage roller, they developed a contact model, a soil particle model, and a soil interaction model with the knife roller, using the discrete element method (DEM).

Stromblad [2] studied the distribution of loads in a multiphase medium using the finite element method. He described the installation of a tubing string into the seabed. The work presents the Coulomb-Mohr and Drucker-Prager plastic models for sand and clay. Abaqus PC was used as a calculation program.

Modelling of extreme deformations and soil structure interaction for deep-water problems using Abaqus PC was carried out by Mavrodontis [10]. His research

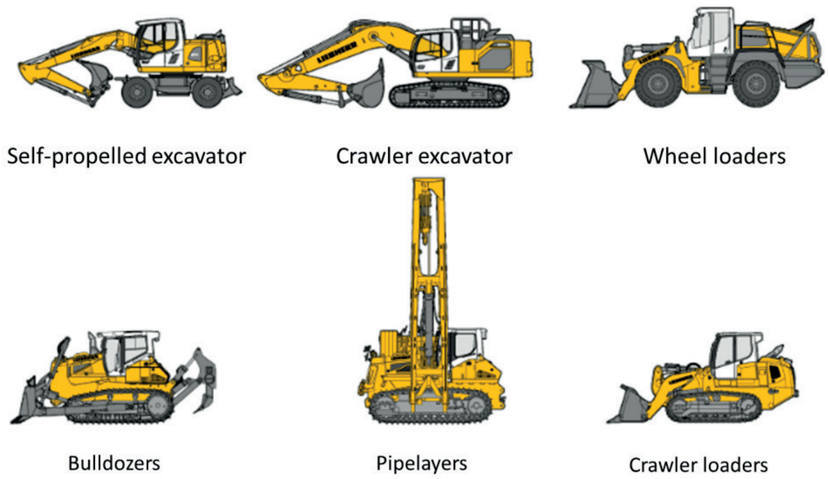

Figure 1 *Various earthmoving machines*

Figure 2 *Types of Liebherr earthmoving machines*

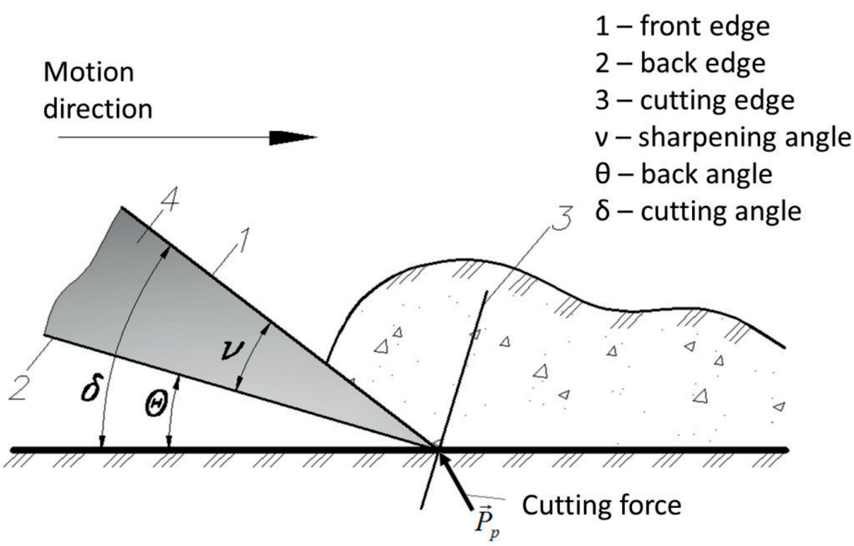

Figure 3 *Schematics of the soil cutting with a wedge-shaped cutter*

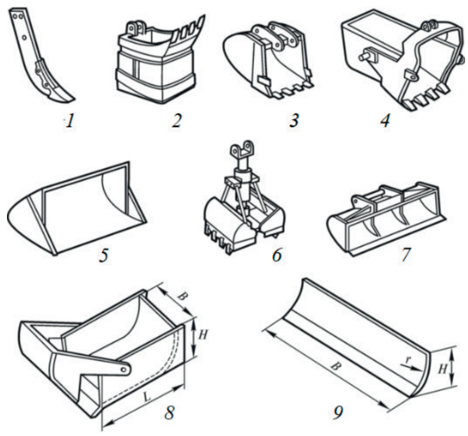

Figure 4 *Types of earthmoving machine working tools*

Figure 5 *Earthmoving with JCB single-bucket crawler excavator*

presents a model of anchor operation when sinking into the seabed. Unlike the model of Stromblad, this model is calculated by taking into account the dynamics of the process in a limited volume. The Coulomb-Mohr model was chosen as the material model.

Vetrov [8] considered the resistance to the cutting of soils as a set of resistances, depending on the cross-sectional area of the cut and the cutting perimeter. The cutting forces of a simple sharp blade, which depend on the cutting angle and thickness of the soil cut, and a complex blade, were considered. The cutting force of a complex knife was investigated as a system of simple knives that interact with each other.

Analyzing the studies on the cutting theory of various scientists, one can came to the conclusion that they use cutting forces in their works to calculate loads. In fact, forces are a physical simplification. Kadyrov [9] assumed that there is some volume that resists cutting.

Our hypothesis is to depart from the concentrated forces in working device calculations, to the mass-energy of the soil volume resisting cutting. For efficient excavation, the mass-energy of the soil volume must be less than the cutting energy. This is a new perspective on the theory of soil cutting, therefore the study could be relevant.

For research, it was decided to use the finite element model in Abaqus because this program gives reliable results and allows the investigation of many variations of cutter shapes.

The purpose of the research was to develop a finite element model, obtain stress distribution in the finite volume of soil, shock wave propagation in the finite volume of soil, and determine the volume of soil involved in the cutting resistance. To reach that purpose, the finite element method in Abaqus software was used, and the following problems were solved:

- an analytical review of methods dedicated to soil development and cutting force calculation was conducted;
- the task was set to apply the Abaqus program complex to realize the research objectives and to verify our hypothesis;
- graphs of soil deformation and stresses occurring in it during the cutting were obtained;
- gradients of strain and stress propagation in the ground during cutting were obtained;
- the volume of soil resisting cutting was obtained;
- a model of cutting of a finite volume of soil was simulated in Abaqus software.

The scientific novelty of this research consists of a new approach to the soil-cutting theory. It is based on the transition from cutting forces to the resistance energy of the soil volume.

In practice, this will avoid excessive loads on cutting

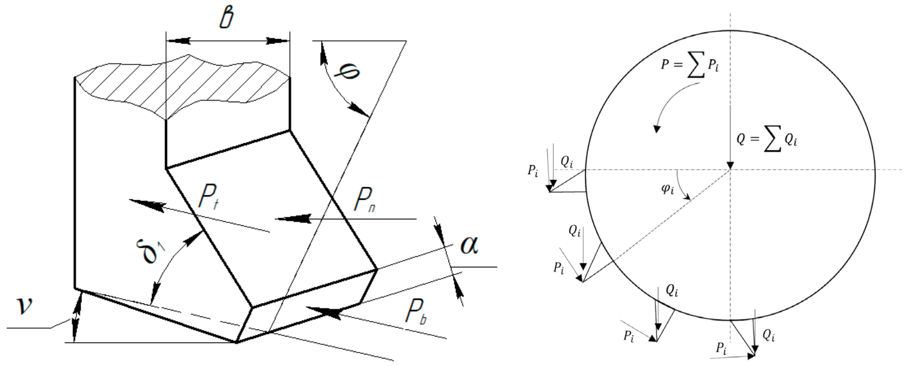

a b

Figure 6 *Effect of cutting forces on the cutter: a) Scheme of forces applied to the cutter; b) Scheme of forces applied to the generalized model of the cutter, the tangential cutting force is labeled as P and the tool feed is labeled as Q*

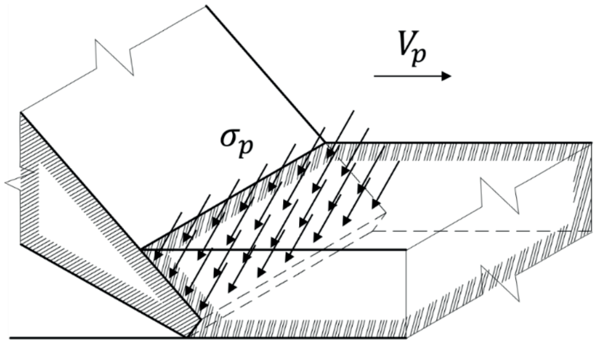

Figure 7 *The action of cutting pressure on the cutter*

tools and mechanisms of earthmoving machines. As a consequence, wear and tear will be reduced and the service life of the equipment will be increased.

2 Material and methods

In the process of cutting the soil, the entire volume of the soil is subjected to pressure from the cutter σ_c. Instead of the cutting force F_{cut}, it is proposed to use the cutting pressure σp distributed over the area of interaction of the cutter with the soil S_{cut}

$$\sigma_c = \frac{F_{cut}}{S_{cut}}. \tag{1}$$

This pressure depends on the volume of soil involved in cutting resistance v_g and its mass m_{res}.

$$m_{res} = \rho \cdot v_g, \tag{2}$$

where ρ is the density of the soil.

To determine this volume of resisting soil, it is necessary to know the deformation and stress damping in the soil (shear σ_{xy}, σ_{xz}, σ_{yz} or axial σ_x, σ_y, σ_z). The stress-damping boundary defines the amount of resistance to cutting.

Mathematical modelling methods were utilized, alongside the creation of a simulation model in Abaqus software and a mathematical experiment.

The calculation of soil-cutting forces with a milling machine was demonstrated by Kadyrov [9]. The forces were projected onto the tangent and normal axes, with respect to the direction of cutting, Figure 6:

$$\{P_t = \varphi bhm_{fr} + 2m_{lat}h + \eta' ahb\varphi m_{fr} P_n = (\varphi bhm_{fr} + 2m_{lat}h)ctg(\delta + \mu) + + \eta' ahb\varphi m_{fr} ctg(\delta_1 + \mu), \tag{3}$$

where P_t - the tangential force, P_n - the normal force, φ - the coefficient accounting for the direction of the cutting angle, m_{fr} - the coefficient characterizing the specific soil resistance to cutting in the front part of the cutter, m_{lat} - the coefficient characterizing the specific force of lateral shearing of the soil by one of the lateral ribs of the cutter. δ - the cutting angle, μ - the angle of external friction between the soil and the blade, b - the cutter width, h - the chip thickness, and η' - a value equal to the coefficient ratio considering the cutter dulling to the wear area.

The lateral expansions of the shear did not take into account the specific force m_{lat}, as the soil was under the clay solution layer, Figure 7.

To calculate the cutting pressure, it is essential to convert the dependencies and coefficients derived by Kadyrov. To achieve this, the deformations and stresses in the soil during the cutting process must be determined.

A non-deformable cutter is simulated that gradually

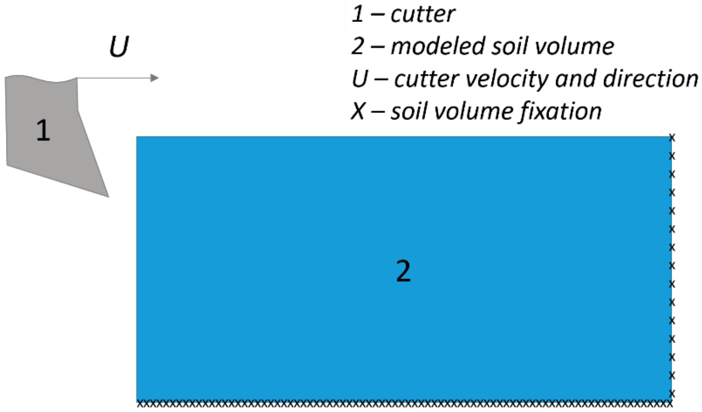

Figure 8 *Schematic diagram of the cutting model with a flat cutter*

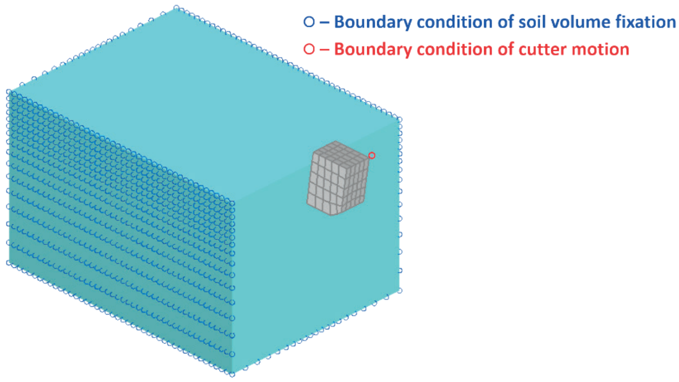

Figure 9 *Simulation model of soil deformation during the cutting with a flat cutter*

moves and eliminates a layer of soil, Figure 8.

The Abaqus software package was chosen to build the model due to its variety of tools and techniques for using the finite element method. It is based on the deformation of volumetric Lagrangian elements with elastic-plastic properties. This model explains the impact of a flat cutter on the soil during translational motion.

To evaluate the stresses, deformations, and attenuation that arise during the cutting process, we analyzed the shearing of a small amount of soil. We used elements of type C3D8R to determine the properties and geometric dimensions of the soil volume and elements of type R3D4 to give the cutter the properties of a rigid body, Figure 9 [11].

Explicit dynamic calculation (DYNAMIC, EXPLICIT) was employed in Abaqus software to model the soil deformation during the cutting with a flat cutter. It is utilized for analyzing displacements and stresses through explicit integration. The explicit integration technique involves dividing the process into many time increments and requires fewer computational resources to perform the calculations. The program automatically determines the process time step and can modify it promptly during the counting process, based on the minimum element size of the computational model, [12].

The element mass change operator (*VARIABLE MASS SCALING) is used to maintain a stable value of the time increment. This operator changes the material density within the deformed element, depending on the given time increment value. Consequently, the equilibrium condition is fulfilled, and the calculation efficiency is preserved.

Following the Abaqus guidelines, the model was constructed within a 2000 x 1500 x 1250 mm box and all the loads and deformations were confined to this volume. The cutter, being much stiffer than the soil, was not considered in the deformations. To model the cutter's geometry, the *RIGID BODY function was used to assign it the properties of a completely solid body, [12].

Boundary conditions are established in Abaqus through the use of the *BOUNDARY function. TYPE=VELOCITY was utilized to establish motion for the working device. This boundary condition specifies the velocity of movement for specific degrees of freedom and a set of nodes. The displacements were restricted using the TYPE=DISPLACEMENT category.

The Coulomb-Mohr plastic model was employed to specify the material properties of the soil. It is specified by using the *MOHR COULOMB function. This model is used to specify the yield properties for elastic-plastic materials.

Our studies are shown for a single cutter. The obtained research will be used in future studies for specific earthmoving machine workpieces.

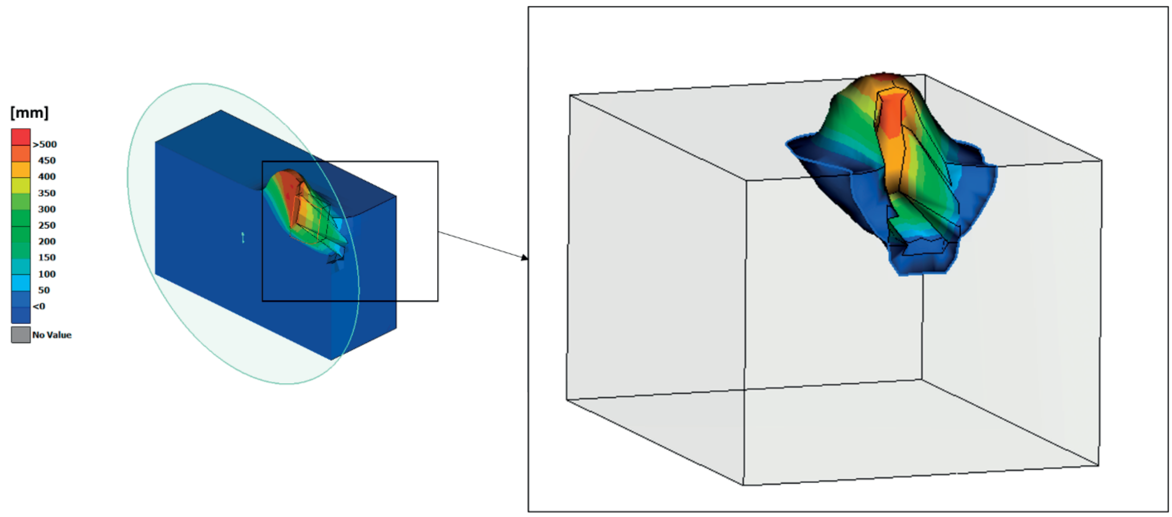

Figure 10 *Soil deformation gradient during the cutting with a flat cutter*

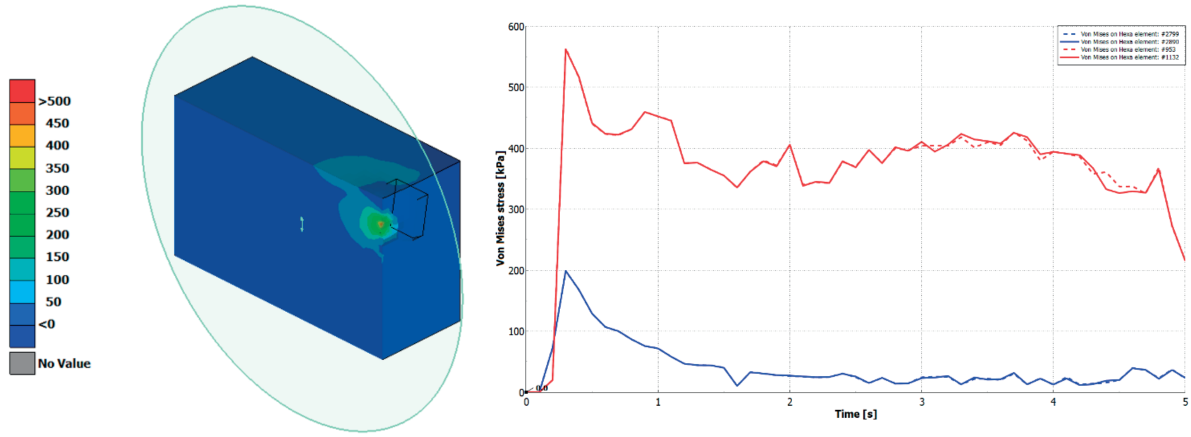

Figure 11 *Gradient and graph of stress propagation in the soil during the cutting with a flat cutter*

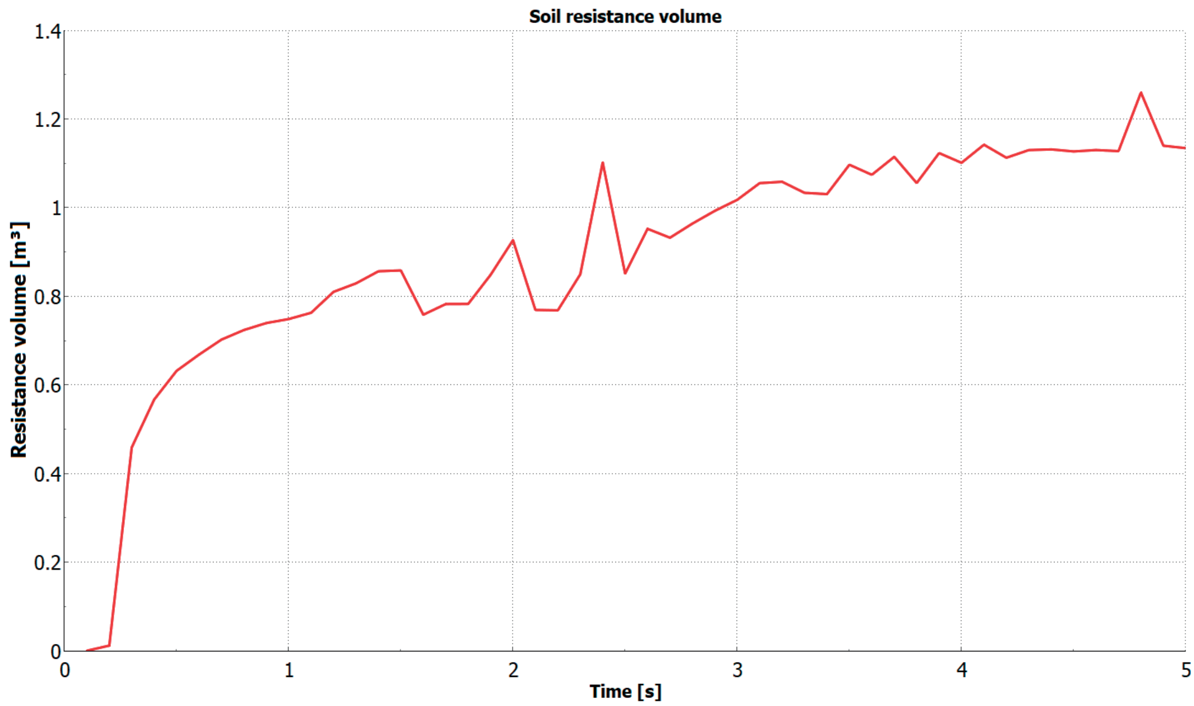

Figure 12 *Graph of the soil volume resisting cutting with a flat cutter*

3 Results

The calculation resulted in gradients and plots of strain and stress. The soil cutting visualization demonstrates a limited deformation distance, which varies based on the physical and mechanical properties of the soil for each type, Figure 10. Note that this distance does not determine the volume of soil involved in the cutting resistance; it can only be determined from the obtained stress values.

As a result of the calculation, gradients and plots of strain and stress were obtained, Figure 11. From visualization of the soil cutting, it can be seen that, the deformation has a limited distance. For each soil type, this distance will vary depending on the physical and mechanical properties of the soil. However, it does not determine the volume of soil involved in the cutting resistance. It can be determined from the stress values obtained, Figure 12.

The stress gradients show that in the process of cutting a compacted core was formed on the surface of the cutter, which negatively impacts efficiency of the soil cutting and reduces the resource of working devices of earthmoving machines, as well.

Based on the stress values obtained, the stress damping range is determined and it can be seen that when the soil is cut with a flat cutter, a much larger volume of soil resists the cutter than the deformed one. The volume can be calculated from the stress values. Therefore, any volume with a stress value less than 5% of the maximum stress value can be ignored as resistance.

The obtained volume can be converted into cutting energy for the efficient operation of the earthmoving machines. For this purpose, the dependence of the volume of resisting soil on the cutter displacement was obtained using the regression equation, Table 1.

According to the obtained auxiliary values, the regression equation is determined, Figure 13:

$$\hat{y} = 711476904.8088 + 277576243.1533 \cdot \ln x \,. \tag{4}$$

4 Conclusion

A simulation model was created using the Coulomb-Mohr model to cut a finite volume of soil with a flat working device. The calculation produced gradients and graphs depicting the soil's deformation and stresses during the cutting. The results revealed that the volume of deformed soil was significantly less than the volume of soil that resisted cutting.

Based on the results obtained, the volume of soil resisting cutting was determined, and a condition for

Table 1 *Table of auxiliary values*

i	x_i	y_i	$\ln x_i$	$\ln^2 x_i$	$y_i \ln x_i$
1	0.1	0	−2.3026	5.3019	0
2	0.2	11600000	−1.6094	2.5903	−18669479.7842
3	0.3	459000000	−1.204	1.4496	−552623517.1856
4	0.4	567000000	−0.9163	0.8396	−519536844.9726
5	0.5	632000000	−0.6931	0.4805	−438069018.1139
6	0.6	668000000	−0.5108	0.2609	−341231516.6757
7	0.7	702000000	−0.3567	0.1272	−250385810.645
8	0.8	724000000	−0.2231	0.0498	−161555931.1515
9	0.9	739000000	−0.1054	0.0111	−77861421.0711
10	1	748000000	0	0	0
			...		
40	4	1100000000	1.3863	1.9218	1524923797.2319
41	4.1	1140000000	1.411	1.9909	1608525150.0297
42	4.2	1110000000	1.4351	2.0595	1592943823.0711
43	4.3	1130000000	1.4586	2.1276	1648234975.6505
44	4.4	1130000000	1.4816	2.1952	1674213131.2444
45	4.5	1130000000	1.5041	2.2622	1699607458.3572
46	4.6	1130000000	1.5261	2.3288	1724443622.9494
47	4.7	1130000000	1.5476	2.3949	1748745634.8491
48	4.8	1260000000	1.5686	2.4606	1976456056.5714
49	4.9	1140000000	1.5892	2.5257	1811728133.8329
50	5	1130000000	1.6094	2.5903	1818664841.0505
Σ	127.5	44830600000	33.3485	60.9821	40653868702.3186

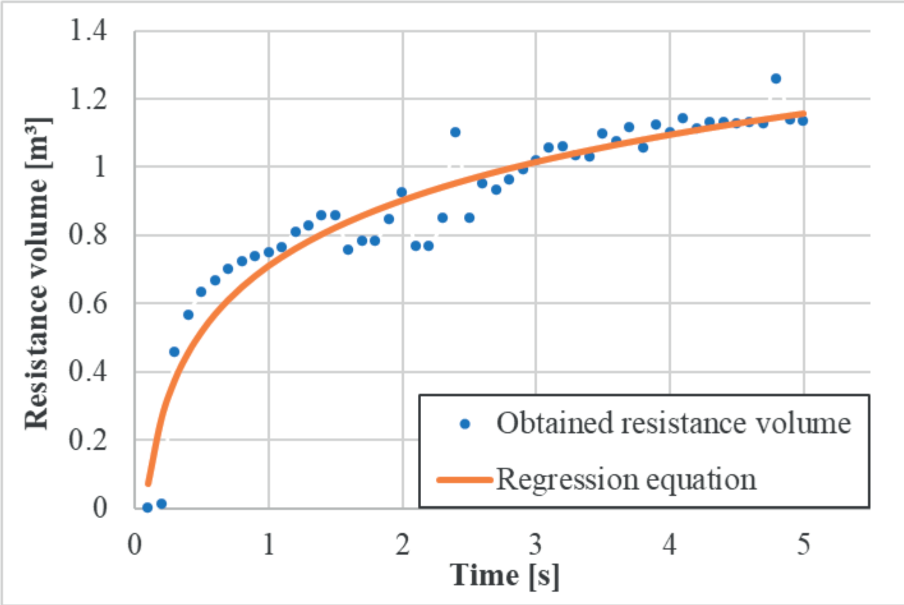

Figure 13 *Scatter diagram and graph of the regression equation*

determining this resisting soil volume was introduced. This work offers a new perspective on the classical theory of soil cutting. The obtained results confirm the hypothesis regarding the existence of a cutting resistance volume and facilitate the determination of cutting energy for the soil. Practically, this advancement will enable more effective operation of earthmoving machines by providing a better understanding of cutting dynamics and optimizing performance.

In terms of modeling specifics, the simulation incorporated a constant cutting speed, which allowed for a controlled analysis of stress distribution and soil behavior. The model also addressed the challenge of accurately representing soil deformation and resistance through calibration of the Coulomb-Mohr parameters for Abaqus Dynamic, Explicit. These considerations were crucial for obtaining reliable results and ensuring that the simulation closely reflects real-world conditions.

Acknowledgment

The authors received no financial support for the research, authorship and/or publication of this article.

Conflicts of interest

The authors declare that they have no known competing financial interests or personal relationships that could have appeared to influence the work reported in this paper.

References

[1] ZHANG, G., ZHANG, Z., XIAO, M., PB, B., BARTOS, P., BOHATA, A. Soil-cutting simulation and parameter optimization of rotary blade's three-axis resistances by response surface method. *Computers and Electronics in Agriculture* [online]. 2019, **164**, 104902. ISSN 0168-1699, eISSN 1872-7107. Available from: https://doi.org/10.1016/j.compag.2019.104902
[2] STROMBLAD, N. Modelling of soil and structure interaction subsea. Master's thesis 2014:09. Goteborg: Chalmers University of Technology, 2014. ISSN 1652-8557.
[3] HA, Q. P., NGUYEN, Q. H., RYE, D. C., DURRANT-WHYTE, H. F. Impedance control of hydraulically actuated robotic excavator. Automation in Construction [online]. 2000, **9**(5-6), p. 421-435. ISSN 0926-5805, eISSN 1872-7891. Available from: https://doi.org/10.1016/S0926-5805(00)00056-X
[4] LEE, S. U., CHANG, P. H. Control of a heavy-duty robotic excavator using time delay control with integral sliding surface. *Control Engineering Practice* [online]. 2002, **10**(7), 697-711. ISSN 0967-0661, eISSN 1873-6939. Available from: https://doi.org/10.1016/S0967-0661(02)00027-8
[5] GORYACHKIN, V. P. *Collected works*. Moscow: Science, 1940.
[6] DOMBROVSKY, M. G. *Excavators*. Moscow: Mechanical Engineering, 1949.
[7] ZELENIN, A. N. *Fundamentals of soil destruction by mechanical methods*. Moscow: Mechanical Engineering, 1968.

[8] VETROV, Y. A. *Machines for earthworks*. 6. ed. Revision and supplement. Kiev: High School, 1980.
[9] KADYROV, A. S., GANYUKOV, A. A. *Loading of milling and drilling machines in relation to the construction method "wall in the ground"*. Novosibirsk: prod. LTD. "SibAK", 2022. ISBN 978-5-6047255-8-0.
[10] Modelling extreme deformations and soil-structure interaction for deep sea applications with Abaqus - Technia [online]. Available from: https://info.simuleon.com/blog/modelling-extreme-deformations-and-soil-structure-interaction-for-deep-sea-applications-with-abaqus
[11] Abaqus 6.14 - Simulia Available from: Available from: http://62.108.178.35:2080/v6.14/index.html
[12] GANYUKOV, A. A., ALTYNBAEV, A. J. Analysis of force methods for calculating the destruction of soil mediums and validation of a new approach to the theory of soil cutting. *Karaganda KSTU University Proceedings* [online]. 2022, **4**(89), p. 274-279. eISSN 2710-3382. Available from: https://doi.org/10.52209/1609-1825_2022_4_274

CLEANING DUSTY AIR FLOW WITH A ROTARY CYCLONE FROM DISPERSED PARTICLES

Oleksandr Kravchenko[1], Oleksiy Bazhynov[2], Ján Dižo[1,*], Yevhen Haiek[3], Miroslav Blatnický[1]

[1]University of Zilina, Zilina, Slovak Republic
[2]Kharkiv National Automobile and Highway University, Kharkiv, Ukraine
[3]State Biotechnological University, Kharkiv, Ukraine

*E-mail of corresponding author: jan.dizo@fstroj.uniza.sk

Oleksandr Kravchenko 0000-0003-4677-2535,
Oleksiy Bazhynov 0000-0002-5755-8553,
Jan Dizo 0000-0001-9433-392X,
Yevhen Haiek 0000-0001-7470-9918,
Miroslav Blatnicky 0000-0003-3936-7507

Resume

The research presented in this article is aimed to show the prospective direction of increasing the efficiency of cleaning dusty air flows from light impurities and dust on mobile grain separators by using a rotary cyclone with a multi-disc after cleaner. An increase in the efficiency of the process of cleaning the dusty air flow in dust collectors is provided by an additional effect on dispersed particles for their intensive redistribution in the working areas. The developed rotary cyclone has two working zones: the main zone and the post-cleaning zone. The rotary cyclone consists of a bladed impeller, a main cylindrical channel, a sedimentation chamber and an after-cleaner. The overall air flow purification coefficient of the rotary cyclone varies between 87.5 to 92.5 %.

Available online: https://doi.org/10.26552/com.C.2025.004

Article info

Received 21 June 2024
Accepted 24 September 2024
Online 10 October 2024

Keywords:

cleaning processes
dusty air flow
cyclone
intensification
performance
cleaning coefficient

ISSN 1335-4205 (print version)
ISSN 2585-7878 (online version)

1 Introduction

The technological process of grain cleaning machines is accompanied by the release of dust, which is dangerous for workers in the service work area, according to the requirements of the ISO 14644-4 standard [1]. The service area is considered to be a space of a height of 2 meters and higher above the floor level, on which the working personnel is located.

To maintain the normalized dustiness, grain cleaning machines are equipped with aspiration systems and dust collectors, which comprise a system of elements removing dispersed particles from the air flow, unloading device, regulating equipment and fan, (EN 481:1993 and ISO 7708:1995 [2-3]).

The further increase in the productivity of grain separators that causes an increase in the concentration of fine particles of impurities and dust, is restrained by the insufficient efficiency of the aspiration systems in cleaning the air flow. The classical improvement of aspiration systems dust collectors, their individual elements, was exhausted and limited by the design features of mobile grain separators.

The conducted review of designs and methods for the efficiency improvement of air flow cleaning of existing devices showed that the most promising way to improve the efficiency of aspiration systems is to combine devices with different operating principles [4-6]. The authors offered the construction of a rotary cyclone with an active rotor on which a bladed impeller is installed. It is designed to give dispersed dust particles a trajectory that takes them away through the blinds from the working area of the device. Dispersed particles remaining in the dusty air stream are also removed through the louvers with the help of a disk pre-cleaner. The cleaned air flow between the discs and the hole inside the discs passes to the outlet nozzle.

Grounding on evaluation and analysis of the research results, a forward-looking direction of increasing the efficiency of cleaning dusty air flows from light impurities and dust on mobile grain separators by using the developed rotary cyclone with a multi-disc after-cleaner, is justified [7-10]. Increasing the efficiency of the dusty air flow cleaning process in dust collectors requires additional influence on dispersed particles to ensure their intensive redistribution in the work zones.

2 Sources review

Despite the sufficient theoretical and experimental material on the study of cleaning processes in devices with swirling dusty flows, a significant part of the phenomena cannot be explained within the framework of the formed ideas, and the task of the efficiency improvement of cleaning the dusty air flow from the dispersed phase, especially on mobile grain separators, remains unresolved. Existing calculation methods do not consider the complexity of the general hydrodynamic picture of separation of a multiphase dusty air flow, as well as the interaction of these flows with each other. This substantiates the necessity to research the main technological parameters of the air flow cleaning process to create high-performance, economical and environmentally friendly rotary cyclones - dust collectors with further forecasting their effectiveness [11].

Unlike experimental studies, numerical modelling allows to vary a number of factors (speed of rotation, viscosity of the air flow, initial properties), which have an important impact on the formation and swirling currents behavior. Changes in mathematical modelling associated with the use of computing technologies and programs, make it possible to implement constructive solutions of individual apparatus modes and to identify optimal hydrodynamic conditions of the process of dusty air flow centrifugal cleaning.

The research of hydrodynamic processes in rotating cyclones is based on a system of Navier-Stokes equations [12-14], supplemented by the equations of non-discontinuity of a symmetric dispersed rotating air flow fixed axis.

Solving the system of Navier-Stokes equations is mathematically difficult, which necessitates the adoption of a number of not quite correct assumptions. This reduces the adequacy of the proposed real hydrodynamic picture analytical descriptions in rotary cyclone devices and, ultimately, leads to significant discrepancies between the results of calculations and experimental data. Regarding this, the physical experiment, as noted in [15], is still the main way of obtaining reliable information about the structure and characteristics of rotating flows. In turn, the most significant drawback of experimental studies of the velocity field is their low accuracy, which is due to the use of probe measurement methods [16]. This explains the obtaining of contradictory results and conclusions by individual authors, which is a restraining factor in the development of analytical, generalizing approaches to the description of the dispersed air flow hydrodynamics in the dust collectors. The use of numerical modelling methods is especially relevant in the problems of mechanics of multiphase flows with the study of related problems of the dusty air flow. It is also necessary to consider statistical approaches for direct numerical modelling dispersed flows and turbulence problems.

An efficient numerical method is a solution of multidimensional purely hyperbolic equations, or equations of a parabolic type containing hyperbolic parts. Mathematical models are used to describe spatially non-stationary problems of the flow of multiphase media; the construction of a computational algorithm for solving similar types of problems in which is quite complex and, as a rule, is solved in stages [17].

One of the most efficient methods of mathematical modelling air flow movement is the use of hydrodynamic equations: the equation of motion continuity and the dynamic equation of an incompressible fluid motion (Navier-Stokes equation) [18-19].

Navier-Stokes equation defines a system of forces acting in a gas (liquid) in the coordinate axes direction [19]. This equation considers the effect of four forces: gravity, pressure, internal friction (viscosity), and the rotating cyclone. The gravitational force is an external factor, and other forces are the result of the environment acting on a selected elementary volume. The equation does not consider external actions on the system and therefore must be supplemented with boundary conditions. Along with the boundary conditions, the initial conditions are given to characterize the system state at the initial moment of the process.

The problem may be solved by computational methods or by experimental methods. As it is described above, the computational methods are usually based on the finite element method. A standard finite element method is applied to strength analysis of many kinds of structures [20-23]. However, the fluid dynamics requires more complicated definition of initial and boundary conditions [24-26].

Analyzing the state of the problem, with regards to improving the productivity of mobile grain cleaning machines and a review of their existing designs of aspiration systems, revealed the following shortcomings: limitation of technological indicators of work (loading the grain cleaning separator); most of the studies were carried out for individual parameters of dust collectors that were subject to optimization; experimental approval is partially or completely absent; the obtained mathematical expressions are complicated or have no further practical use; lack of intermediate removal of captured dispersed particles and dusty air flow additional purification [27-29]. A promising direction of increasing the dusty air flow cleaning process efficiency from light impurities and dust is the creation of a rotary cyclone with a multi-disc after cleaner, enabling to increase the efficiency of dusty air flow cleaning without changing the basic dimensions of serial mobile separators of the OVS-25 and SVS-25 type.

3 Research aim and tasks

The aim of the work implies increasing the efficiency of the of the dusty air flow cleaning process of mobile grain aspiration systems of separators by substantiating the parameters of the developed rotary cyclone with an after-cleaner.

Research objectives:

- to justify the criteria for optimizing the process of cleaning the dusty air flow, to build the objective function and determine the rational design parameters of the proposed rotary cyclone of mobile grain separators;
- to evaluate the impact of the design and technological parameters of the developed rotary cyclone on the particles' velocity field of the dispersed phase in the working zones;
- identify the speed of the air flow and dispersed particles, evaluate the adequacy and effectiveness of the obtained dependencies of dusty air flow cleaning process through the experimental studies and production approval of the rotary cyclone.

4 Theoretical studies of the dynamics of the dusty air flow dispersed phase in a rotating cyclone

The grain dust is characterized by a wide interval of particle dispersion. Such dispersed particles can flow around in transitional and turbulent regimes; however, the number of such particles is insignificant.

The influence of turbulent pulsations, affecting the movement of finely dispersed particles is taken into account based on equation [30-32]:

$$\frac{1}{\tau}\frac{dr}{dt} - \Omega_0^2 r + \frac{C(t)}{m_s} = 0\,, \qquad (1)$$

where C*(t)* is the coefficient of random influence, which is the delta of the correlation function of time with a zero-mean value; Ω_0 - angular velocity of swirler rotation, [rad/s]; m_S - mass of dispersed particle; [g].

Turbulent pulsations influence only the movement of finely dispersed particles d_s < 5 μm [32-33], for the separation of which it is necessary to use an additional device - a pre-cleaner. Dispersed particles of a size of d_s = 200 μm are significantly deflected and some of them fall on the blinds of the main channel and further into the sedimentation chamber.

Finely dispersed particles practically do not have time to deviate to the walls of the main channel. Simultaneously, the trajectories of larger dispersed particles are significantly deviated, and some of them fall through the blinds of the channel to the sedimentation chamber, where their sedimentation takes place. Simultaneously, the highly dispersed particles are not able to accelerate. Then, the turbulent nature of the flow becomes significant. That is, up to the pre-cleaner zone, calculations can be carried out using the Stokes formula for almost any grain dust particles of any size.

During this process, some dispersed particles obviously will reach the walls of the main channel before entering the pre-cleaner zone. For this, it is necessary that their entrance radius meets the condition:

$$r_0 > \frac{\frac{D_0}{\Omega_0}\sqrt{\frac{U_0}{8 l_0 \tau}}}{\left(1+\frac{1}{\beta}\right)e^{(\beta-1)\frac{L_0}{2\tau U_0}} + \left(1-\frac{1}{\beta}\right)e^{-(\beta-1)\frac{L_0}{2\tau U_0}}}\,, \qquad (2)$$

where U_0 is the speed of the air flow at the entrance to the cyclone, [m/s]; l_0 - width of pre-cleaner, [m]; L_0 - length of the main working zone of the developed rotary cyclone, [m]; τ - relaxation time of a dispersed particle in the air flow, [s]; D_0 - the diameter of the rotary cyclone inlet nozzle, [m].

In addition, we assume a uniform distribution of dispersed particles at the entrance to the rotary cyclone across the cross section of the flow.

Then, the efficiency of separating the dispersed particles from the dusty air flow in the main working area of the developed rotary cyclone is defined by the expression:

$$\eta_1 = 1 - \\ - \frac{2\frac{1}{\Omega_0^2}\frac{U_0}{l_0\tau}}{\left[\left(1+\frac{1}{\beta}\right)e^{(\beta-1)\frac{L_0}{2\tau U_0}} + \left(1-\frac{1}{\beta}\right)e^{-(\beta-1)\frac{L_0}{2\tau U_0}}\right]^2}\,. \qquad (3)$$

The efficiency of the dispersed particles separation of a size of 50 μm to 120 μm, in the main channel of the

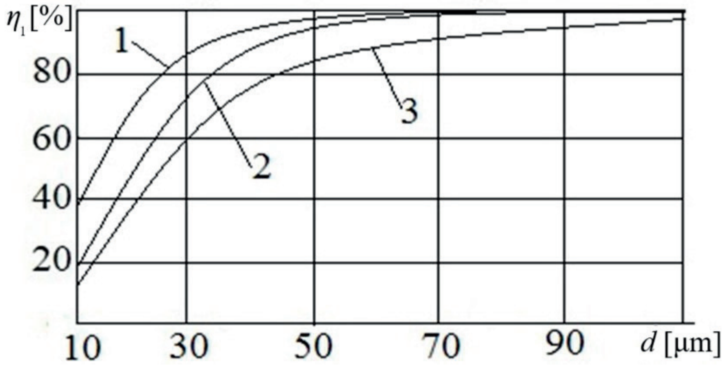

Figure 1 *Dependencies of the dusty air flow cleaning efficiency in the main channel of the developed rotary cyclone on the speed of the air flow: 1 - U_0 = 5 m/s; 2 - U_0 =10 m/s; 3 - U_0 =15 m/s (Ω = 105 rad/s; D_0 = 0.1 m; l_0 = 0.3 m)*

developed rotary cyclone (Figure 1), is in the range of 85 to 100 %. Insufficient efficiency of finely dispersed particles separation up to 50 µm in size is explained by the limitation of the main channel dimensions of the rotary cyclone and the insignificant weight of the particles themselves. This requires the use of an additional dust separator. Reducing the speed of the air flow, in the range under investigation, helps to increase the cleaning coefficient of the main channel of the developed rotary cyclone by 35 to 45 %.

The efficiency of dispersed particles separation of a size of 50 to 120 µm, in the main channel of the developed rotary cyclone (Figure 1), is in the range of 85 to 100 %. Insufficient efficiency of separation of finely dispersed particles up to 50 µm in size, is explained by the limitation of the main channel dimensions of the rotary cyclone and the insignificant weight of the particles themselves. This requires the use of an additional dust separator. Reducing the speed of the air flow, in the range under investigation, helps to increase the cleaning coefficient of the main channel of the developed rotary cyclone by 35 to 45 %.

After the dispersed particles reach the pre-cleaner zone, the force of the air flow, directed radially towards the axis, begins to act on them. In addition, the centrifugal force, directed radially from the axis, continues to act.

Down the equation for the radial component of ta dispersed particle velocity [33-35]:

$$\frac{dW_r}{dt} = -\xi\frac{3}{8}\frac{\rho}{\rho_s r_s}(W_r - U_r)^2 + \frac{W_\phi^2}{r}, \tag{4}$$

where U_r - speed of the air flow in the cyclone working area [m/s] and it is expressed as:

$$U_r = \frac{(D_0^2 - D_d^2)U_0}{8rl_0}, \tag{5}$$

further l_0 - width of the pre-cleaner [m]; D_d - diameter of the pre-cleaner discs' the central hole [m]; W_r - a component of the dispersed particle velocity in a radial direction [rad/s].

The equation for the acceleration in a radial direction of a dispersed particle has the following form:

$$\frac{d^2r}{dt^2} = -\xi\frac{3}{8}\frac{\rho}{\rho_s r_s}\left(\frac{dr}{dt} - Ur\right)^2 + r\cdot\Omega_0^2. \tag{6}$$

For the fine dispersed particles flowing in the laminar mode, Equation (5) can be written as:

$$\frac{dr}{dt} = \tau\cdot\Omega_1^2\cdot r - \frac{(D_0^2 - D_d^2)U_0}{8rl_0}, \tag{7}$$

where Ω_1 - rotation frequency of the pre-cleaner [rpm]. It is considered $\Omega_1 = \Omega_0$.

It turns out that, if the dispersed particle entered the zone of the pre-cleaner at a radius that satisfies the inequalities:

$$r > \frac{\sqrt{D_0^2 - D_d^2}}{\Omega_1}\sqrt{\frac{U_0}{8l_0\tau}}, \tag{8}$$

then, due to centrifugal forces, it will be thrown to the walls of the main channel and enter the chamber.

The dispersed particles, that will be closer to the channel axis, can be drawn into the pre-cleaner. Their further dynamics will be determined by the after-cleaner parameters. Simultaneously, a dispersed particle larger in size, which flows around in a turbulent mode, when inequality in Equation (8) is fulfilled, will also be thrown to the walls of the channel due to centrifugal forces and will enter the chamber.

Then, only the dispersed particles, the entrance radius of which when entering the pre-cleaner zone is:

$$r_1 > \frac{2\frac{\sqrt{D_0^2 - D_d^2}}{\Omega_0}\sqrt{\frac{U_0}{8l_0\tau}}}{\left(1+\frac{1}{\beta}\right)e^{(\beta-1)\frac{L_0-l_0}{2\tau U_0}} + \left(1-\frac{1}{\beta}\right)e^{-(\beta+1)\frac{L_0-l_0}{2\tau U_0}}}, \tag{9}$$

will reach a radius satisfying condition in Equation (8).

On the other hand, it is obvious that dispersed particles, whose entrance radius is the following:

$$r_2 > \frac{D_d}{\left(1+\frac{1}{\beta}\right)e^{(\beta-1)\frac{L_0-l_0}{2\tau U_0}} + \left(1-\frac{1}{\beta}\right)e^{-(\beta+1)\frac{L_0-l_0}{2\tau U_0}}}, \tag{10}$$

will not fall into the central hole of the pre-cleaner discs.

If it is assumed that the dispersed particles are uniformly distributed at the inlet along the cross section of the flow, then the separation efficiency of dispersed particles (without considering the particles that are separated before they reach the pre-cleaner zone) is equal to:

$$\eta_2 = 1 - \frac{\max\left(2\frac{1-(D_d/D_0)^2}{\Omega_0^2}\frac{U_0}{l_0\tau}, 4\left(\frac{D_d}{D_0}\right)^2\right)}{\left[\left(1+\frac{1}{\beta}\right)e^{(\beta-1)\frac{L_0-l_0}{2\tau U_0}} + \left(1-\frac{1}{\beta}\right)e^{-(\beta+1)\frac{L_0-l_0}{2\tau U_0}}\right]^2} \tag{11}$$

The dispersed particles, the diameters of which are close to the grain dust particles (considered in micrometers), are partially separated during their movement to the pre-cleaner (Figure 2). Then, the dispersed particles are directed between the plates of the shutter separator 3 to the settling chamber 6 (Figure 3).

Particles of a diameter of 20 to 100 µm are also partially separated during their movement to the pre-cleaner. Then, the remaining particles are separated during their rotation in the pre-cleaner zone.

Figure 3 shows the scheme of the developed rotary cyclone design elements, where Figure 3a depicts the entire model. Then, the device without the louver separator plates is shown in Figure 3b and Figure 3c depicts the detail of the multi-disc cleaner.

The research analysis on the dispersed composition of the grain dust [36-38] established the fractional composition:

- particles of sizes up to 1 µm comprise 8.3 %;
- particles of sizes from 1 to 5 µm comprise 16.6 %;

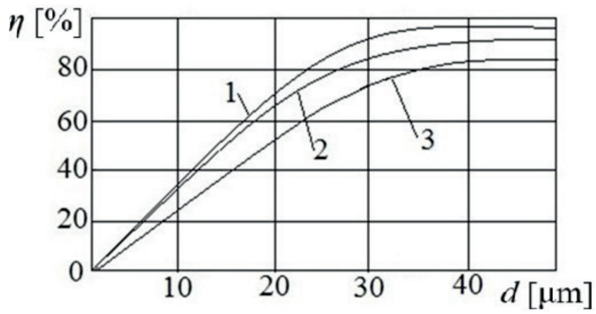

Figure 2 *Dependencies of the dusty air flow cleaning coefficient on the number of discs of the developed rotary cyclone post-cleaner: 1 - n = 9 units, l_0 = 0.0315 m; 2 - n = 6 units, l_0 = 0.021 m; 3 - n = 3 units, l_0 = 0.0105 m (U_0 = 10 m/s; D_0 = 0.1 m; D_d = 0.01 m)*

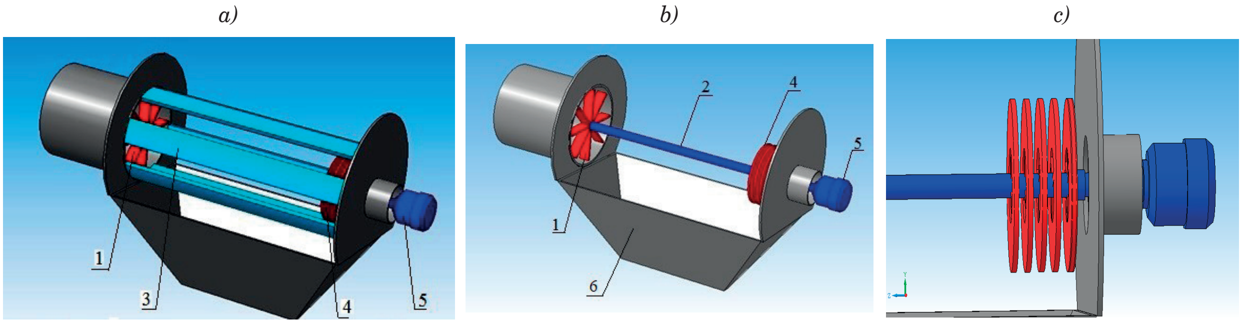

Figure 3 *The scheme of the developed rotary cyclone design elements: 1 - impeller; 2 - shaft; 3 - louver separator plates; 4 - multi-disc pre-cleaner; 5 - electric motor; 6 - deposition chamber*

Table 1 *Research results of the purification coefficients of the developed rotary cyclone dependence on the air flow velocity from the rotor speed*

Air flow velocity U_0 [m/s]	Cleaning coefficient η [%]		
	W = 105 [rad/s]	W = 210 [rad/s]	Cyclone design parameters
6	93.1	91.1	n = 6 pcs.; h = 1 mm; α = 20°; b = 20 mm
7	93.2	91.2	
8	93.3	91.4	
9	93.4	91.5	
10	93.5	91.8	
11	93.6	92.1	
12	93.7	92.5	
13	93.8	92.8	

- particles of sizes from 5 to 10 μm comprise 24.8 %;
- particles larger than 10 μm - 50.3 %.

Numerical calculation of the optimal mathematical expressions established that the fine-dispersed fraction up to 1 μm is almost not separated. The efficiency of removing large-dispersed particles (over 1 μm) reaches 67.9 to 79.2 %.

5 Research results of the dispersed phase dynamics of the dusty air flow in a rotating cyclone

Studies of the developed rotary cyclone efficiency involved determining the coefficient of dusty air flow purification with varying values of the following important factors: air flow velocity U_0, the distance between the disks h, angle of inclination of the swirler blades α, the width of the louver opening b, motor rotor speed Ω; the number of discs of purifier n.

The research proved the dependencies of the developed rotary cyclone cleaning coefficients on its design and technological parameters (Figure 4).

Analysis of research (Table 1) shows that the maximum efficiency of the air flow cleaning process is η = 93.1 to 93.8 %, at air flow velocity U_0 = 6 m/s to 13 m/s and at shaft speed Ω = 105 rad/s.

Thus, within the range of the studied air flow rate (Table 2) U_0 =6 to 13 m/s, maximum cleaning coefficient is 91.1 to 92.8 %, which is 2.3 to 2.5 % more than at α = 30°.

***Table 2** Research results of the purification coefficients of the developed rotary cyclone dependence on the air flow velocity from the tilt angle of the impeller blades*

Air flow velocity U_0 [m/s]	Cleaning coefficient η [%]			
	α = 10°	α = 20°	α = 30°	Cyclone design parameters
6	90.2	91.1	89.0	n = 6 pcs; b = 20 mm; h = 1 mm; W =105 rad/s
7	90.5	91.3	89.1	
8	90.7	91.5	89.2	
9	90.8	91.7	89.4	
10	91.0	92.0	89.5	
11	91.2	92.1	89.9	
12	91.8	92.5	90.1	
13	92.0	92.8	90.5	

***Table 3** Research results of the purification coefficients of the developed rotary cyclone dependence on the distance between the disks of the purifier*

Air flow velocity U_0 [m/s]	Cleaning coefficient η [%]			
	U_0 = 6 m/s	U_0 = 10 m/s	U_0 = 13 m/s	Cyclone design parameters
0.5	90.0	89.2	89.0	n = 6 pcs.; α = 20°; b =15 mm; Ω =105 rad/s
0.75	91.9	91.2	90.8	
1.0	92.4	91.5	91.1	
1.25	91.1	90.2	90.1	
1.5	88.3	87.7	87.9	

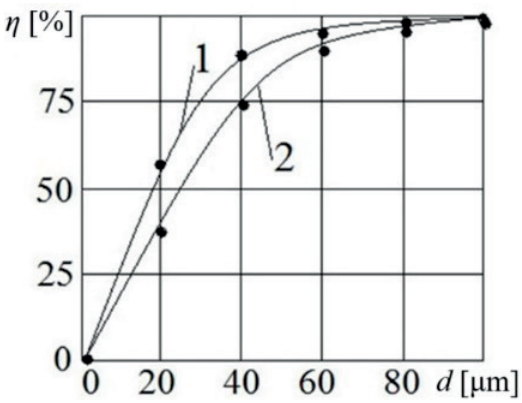

***Figure 4** Dependencies of the developed rotary cyclone cleaning coefficient on the size of dispersed particles: 1 - U_0 = 10 m/s; 2 - U_0 = 15 m/s (Ω = 1000 rpm; n = 6 units; b = 15 m; h = 1 mm)*

***Table 4** Comparative analysis of the experimental and theoretical research results of the developed rotary cyclone*

Cleaning stages	30-50 μm	100-150 μm	Total [%]	Experimental [%]	Theoretical new values [%]	Impeller rotations [rpm]	Flow velocity [m/s]	Error [%]
Before cleaning	50	50	100	-	-	-	-	-
After cleaning	13.1	2.6	15.7	85.3	85	1000	10	0.4
	18.2	3.0	21.2	78.8	78.2	500	10	0.8
	4.8	2.0	6.8	93.2	92	1000	6	1.3
	9.5	2.8	12.3	87.7	87.2	500	6	0.6

Analysis of the dependencies (Table 3) shows that the distance between the disks of the purifier, that provides maximum efficiency of the developed rotary cyclone η = 90.1 to 92.4 %, is h = 0.75 mm to 1.25 mm.

Experimental studies analysis proved that increasing the velocity of air flow, in the ranges under study, increases the cleaning coefficient of the developed rotary cyclone from 4 to 4.8 to 89 to 93.8 %. The obtained parameters of the rotary cyclone are: the angle of the blades α = 20°, the rotor speed Ω = 105 rad/s, the distance between the disks of the purifier h = 1 mm.

To obtain a complete picture, for increasing the efficiency of cleaning the dusty flow, the determination of the fractional cleaning coefficient (Figure 4) was carried out for the fractions of dispersed particles that were researched.

The analysis of dependencies (Figure 4) established that at the speed of the air flow in the developed rotary cyclone U_0 = 10 m/s to 15 m/s, the cleaning coefficient is η = 5 to 98 % for dispersed particles up to 90 μm in size. It should be noted that the developed rotary cyclone captures dispersed particles d_s = 1 μm to 40 μm with an efficiency of η = 5 to 87 %, which significantly affects the of the air flow cleaning process intensification in mobile grain separators.

The obtained experimental dependencies of the overall cleaning coefficient of the developed rotary cyclone from dispersed particles at the air flow rate typical for aspiration systems of mobile grain separators are shown in Table 4.

The discrepancy between the results of the experiments and the data of theoretical studies, concerning the efficiency determination of the dusty air flow cleaning process, does not exceed 3.8 to 4.3 %, confirming the adequacy of the developed mathematical modelling.

Determining the discrepancy between the results of researching the efficiency of the dusty air flow cleaning process was carried out with the variation of significant parameters: the frequency of the rotor rotation and the speed of the air flow at the inlet. Varying the parameters of the rotary cyclone, within the established ranges, results in a discrepancy of 0.4 to 1.3 % in the results of researching the efficiency of the dusty air flow cleaning process. This also confirms the adequacy of the developed mathematical modelling the dusty air flow cleaning process.

As a result of conducting experimental studies, the dependencies of the radial component change rate of the dispersed particles velocity and the dispersed particle radial coordinate in the main channel of the rotary cyclone were obtained.

6 Conclusion

It was established that the velocity components of the multiphase medium depend by 15 to 35 % on the design and technological parameters of the developed rotary cyclone, which confirms the possibility of dispersed particles redistribution and the dusty air flow cleaning process intensification. The ranges of component of the carrier and dispersed phases velocities were determined by solving the obtained mathematical models. It was established that the efficiency of the dusty air flow cleaning process on the developed rotary cyclone is 85 to 92 %.

The dependencies of the cleaning coefficient on the air flow velocity were experimentally proved. Increasing the velocity of the air flow in the range under study, increases the cleaning coefficient of the developed rotary cyclone by 4.0 to 4.8 to η= 91.0 to 93.8 %. The ranges of variation of the obtained parameters of the rotary cyclone were: the angle of the blades inclination α = 20°, rotor speed Ω = 105 rad/s, the distances between the disks of purifier h = 1 mm.

Acknowledgment

Funding by the EU Next Generation EU through the Recovery and Resilience Plan for Slovakia under the project No. 09I03-03-V01-00129.

Conflicts of interest

The authors declare that they have no known competing financial interests or personal relationships that could have appeared to influence the work reported in this paper.

References

[1] ISO 14644-4:2022. Cleanrooms and associated controlled environments.
[2] EN 481:1993. Workplace atmospheres - size fraction definitions for measurement of airborne particles.
[3] ISO 7708:1995. Air quality, Particle size fraction definitions for health-related sampling
[4] WANG, Y., ZHU, Q., HUANG, T., HAN, X., LIN, M. Modelling and simulation of nonlinear dynamic flow field and temperature field of depyrogenation tunnel. *Facta Universitatis, Series: Mechanical Engineering* [online]. 2024, **22**(1), p. 45-62. ISSN 0354-2025, eISSN 2335-0164. Available from: https://doi.org/10.22190/FUME221221011W

[5] CZAKO, R., VALKO, D., GASPAROVIC, P., ANDOGA, R., ADAM, N., FOZO, L. Inlet air flow sensing for the iSTC-21v small jet engine. *Acta Polytechnica Hungarica* [online]. 2024, **21**(10), p. 243-262. ISSN 1785-8860. Available from: https://doi.org/10.12700/APH.21.10.2024.10.16

[6] SAID, M., BOUDA, N. N., HARMAND, S. 3D numerical investigation of heat transfer performance in liquid-liquid taylor flow. *Journal of Applied and Computational Mechanics* [online]. 2024, **10**(1), p. 183-204. eISSN 2383-4536. Available from: https://doi.org/10.22055/jacm.2023.44421.4211

[7] CABAN, J., NIEOCZYM, A., MISZTAL, W., BARTA, D. Study of operating parameters of a plate conveyor used in the food industry. *IOP Conference Series: Materials Science and Engineering* [online]. 2019, **710**, 012020. ISSN 1757-899X. Available from: https://doi.org/10.1088/1757-899X/710/1/012020

[8] KLIMENDA, F., STERBA, J., CERNOHLAVEK, V., PONIKELSKY, J., MARAN, P. Draft of robotic workstation for laser engraving. *Manufacturing Technology* [online]. 2021, **21**(3), p. 357-363. ISSN 1213-2489, eISSN 2787-9402. Available from: https://doi.org/10.21062/mft.2021.049

[9] KLIMENDA, F., SOUKUP, J., STERBA, J. Noise and vibration analysis of conveyor belt. *Manufacturing Technology* [online]. 2021, **19**(4), p. 604-608. ISSN 1213-2489, eISSN 2787-9402. Available from: https://doi.org/10.21062/ujep/341.2019/a/1213-2489/MT/19/4/604

[10] CIESLAR, K., PLONKA, S. Modeling of rough rotary milling of crankshaft pins. *Scientific Journal of Silesian University of Technology. Series Transport* [online]. 2023, **121**, p. 45-61. ISSN 0209-3324, eISSN 2450-1549. Available from: https://doi.org/10.20858/sjsutst.2023.121.4

[11] MARCZUK, A., CABAN, J., ALESHKIN, A. V., SAVINYKH, P. A., ISUPOV, A. Y., IVANOV, I. I. Modeling and simulation of particle motion in the operation area of a centrifugal rotary chopper machine. *Sustainability* [online]. 2019, **11**(181), 4873. eISSN 2071-1050. Available from: https://doi.org/10.3390/su11184873

[12] NESTERENKO, O. V., LESHCHENKO, S. M., VASYLKOVSKYI, O. M., PETRENKO, D. I. Analytical assessment of the pneumatic separation quality in the process of grain multilayer feeding. *INMATEH - Agricultural Engineering*. 2017, **53**(3), p. 65-70. ISSN 2068-4215, eISSN 2068-2239.

[13] BISWAS, A., PAL B. B. Application of fuzzy goal programming technique to land use planning in agricultural system. *Omega* [online]. 2005, **33**(5) p. 391-398. ISSN 0305-0483, eISSN 1873-5274. Available from: https://doi.org/10.1016/j.omega.2004.07.003

[14] Cimbria DELTA combi cleaner 157 [online] [accessed 2023-06-27]. Available from: https://www.nexeed.ca/wp-content/uploads/2016/09/157_Combi_cleaner_157.pdf

[15] DORMAN, R. G. *Dust control and air cleaning: monographs in heating* [online]. Elsevier, 1974. ISBN 978-0-08-016750-3. Available from: https://doi.org/10.1016/C2013-0-05612-5

[16] YUAN, Z., KHAKZAD, N., KHAN, F., AMYOTTE, P. Dust explosions: a threat to the process industries. *Process Safety and Environmental Protection* [online]. 2015, **98**, p. 57-71. ISSN 0957-5820, eISSN 1744-3598. Available from: https://doi.org/10.1016/j.psep.2015.06.008

[17] HUTTER, K., RAJAGOPAL, K. R. On flows of granular materials. *Continuum Mechanics and Thermodynamics* [online]. 1994, **6**, p. 81-139. ISSN 0935-1175, eISSN 1432-0959. Available from: https://doi.org/10.1007/BF01140894

[18] JONES, C. Preventing grain dust explosions [online] [accessed 2023-12-26]. Oklahoma Cooperative Extension Service, 2017. Available from: https://extension.okstate.edu/fact-sheets/preventing-grain-dust-explosions-2.html

[19] KISELEV, A. P., KUZMINSKY, V. A., SBOEV, D. S. The laminar-turbulent transition zone in 2D and 3D boundary layers with emphasis on effect of free stream turbulence. In: 29th ICAS Congress: proceedings [online]. 2014. Available from: https://www.icas.org/ICAS_ARCHIVE/ICAS2014/data/papers/2014_0374_paper.pdf

[20] VATULIA, G., LOVSKA, A., PAVLIUCHENKOV, M., NERUBATSKYI, V., OKOROKOV, A., HORDIIENKO, D., VERNIGORA, R., ZHURAVEL, I. Determining patterns of vertical load on the prototype of a removable module for long-size cargoes. *Eastern-European Journal of Enterprise Technologies* [online]. 2022, **6**(7-120), p. 21-29. ISSN 1729-3774, eISSN 1729-4061. Available from: https://doi.org/10.15587/1729-4061.2022.266855

[21] PANCHENKO, S., GERLICI, J., VATULIA, G., LOVSKA, A., RAVLYUK, V., HARUSINEC, J. Studying the load of composite brake pads under high-temperature impact from the rolling surface of wheels. *EUREKA, Physics and Engineering* [online]. 2023, **2023**(4), p. 155-167. ISSN 2461-4254A, eISSN 2461-4262, Available from: https://doi.org/10.21303/2461-4262.2023.002994

[22] VATULIA, G., LOVSKA, A., MYAMLIN, S., STANOVSKA, I., HOLOFIEIEVA, M., HOROBETS, V., NERUBATSKYI, V., KRASNOKUTSKYI, Y. Revealing the effect of structural components made of sandwich panels on loading the container transported by railroad. *Eastern-European Journal of Enterprise Technologies* [online]. 2023, **1**(7-121), p. 48-56. ISSN 1729-3774, eISSN 1729-4061. Available from: https://doi.org/10.15587/1729-4061.2023.272316

[23] LOVSKA, A., STANOVSKA, I., NERUBATSKYI, V., HORDIIENKO, D., ZINCHENKO, O., KARPENKO, N., SEMENENKO, Y. Determining features of the stressed state of a passenger car frame with an energy-absorbing

material in the girder beam. *Eastern-European Journal of Enterprise Technologies* [online]. 2022, **5**(7-119), p. 44-53. ISSN 1729-3774, eISSN 1729-4061. Available from: https://doi.org/10.15587/1729-4061.2022.265043

[24] GUO, L., CHENG, H., YAO, Z., RONG, Ch., WANG, Z., WANG, X. CFD-DEM method is used to study the multi-phase coupling slag discharge flow field of gas-lift reverse circulation in drilling shaft sinking. *Scientific Reports* [online]. 2024, **14**(1). eISSN 2045-2322. Available from: https://doi.org/10.1038/s41598-024-64519-1

[25] ALI, M., GHERISSI, A., ALTAHARWAH, Y. Experimental and simulation study on a rooftop vertical-axis wind turbine. *Open Engineering* [online]. 2023, **13**(11), 13853. ISSN 2391-5439. Available from: https://doi.org/10.1515/eng-2022-0465

[26] NIE, W., CHENG, CH., LIU, Q., HUA, Y., JIANG, CH., ZHANG, H., BAI, P., ZHU, Z., LIU, CH. Evolutionary analysis of dust pollution in the comprehensive excavation face based on linear regression method. *Powder Technology* [online]. 2024, **436**, 119476. ISSN 0032-5910, eISSN 1873-328X. Available from: https://doi.org/10.1016/j.powtec.2024.119476

[27] AZAROV, V. N., BOROVKOV, D. P., REDHWAN, A. M. Application of swirling flows in aspiration systems. *International Review of Mechanical Engineering (IREME)*. 2014, **8**(4), p. 750-753. ISSN 1970-8734, eISSN 2532-5655.

[28] TER LINDEN, A. J. Investigations into cyclone dust collectors. *Proceedings of the Institution of Mechanical Engineers* [online]. 1949, **160**(1), p. 233-251. ISSN 0020-3483, eISSN 2058-1203. Available from: https://doi.org/10.1243/pime_proc_1949_160_025_02

[29] JIAO, J., ZHENG, Y., WANG, J., SUN, G. Experimental and numerical investigations of a dynamic cyclone with a rotary impeller. *Chemical Engineering and Processing: Process Intensification* [online]. 2008, **47**(9-10), p. 1861-1866. ISSN 0255-2701, eISSN 1873-3204. Available from: https://doi.org/10.1016/j.cep.2007.10.015

[30] KOTOV, B., SPIRIN, A., KALINICHENKO, R., BANDURA, V., POLIEVODA, Y., TVERDOKHLIB, I. Determination the parameters and modes of new heliocollectors constructions work for drying grain and vegetable raw material by active ventilation. *Research in Agricultural Engineering* [online]. 2019, **65**(1), p. 20-24. ISSN 1212-9151, eISSN 1805-9376. Available from: https://doi.org/10.17221/73/2017-RAE

[31] LUKAC, B. J., ORSBORN, J. H., HOREJSI, M. J., CRABB, R. J., PIKESH, D. W. Rotary air screen for a work machine [online]. U.S. Patent No. 6,514,303. 4 Feb. 2003. Available from: https://www.freepatentsonline.com/y2002/0088208.html

[32] MISIULIA D. ANDERSSON, A. G., LUNDSTROM, T. S. Effects of the inlet angle on the flow pattern and pressure drop of a cyclone with helical-roof inlet. *Chemical Engineering Research and Design* [online]. 2015, **102**, p. 307-321. ISSN 0263-8762, eISSN 1744-3563. Available from: https://doi.org/10.1016/j.cherd.2015.06.036

[33] MISIULIA, D., ELSAYED, K., ANDERSSON, A. G. Geometry optimization of a deswirler for cyclone separator in terms of pressure drop using CFD and artificial neural network. *Separation and Purification Technology* [online]. 2017, **185**, p. 10-23. ISSN 1383-5866, eISSN 1873-3794. Available from: https://doi.org/10.1016/j.seppur.2017.05.025

[34] MAJOCCO, V. G. Experimental investigations of various material systems to characterize the separation behavior of a non-conventional air classifier for grain cleaning (in German) [online]. Dissertation for the academic degree Bachelor of Science (B.Sc.). Anhalt: Anhalt University of Applied Sciences, 2015. Available from: http://dx.doi.org/10.25673/5655

[35] MIKHAILOV, Y., ZADOSNAIA, N., RUBTSOV, N., KANGALOV, P. Methodology for determining the parameters of the air flow in a pneumatic separator with a closed air system [online]. Melitopol, Ukraine: 2017. Available from: http://elar.tsatu.edu.ua/bitstream/123456789/4608/1/Journal-of-agriculture-and-environment-36-41.pdf

[36] MISIULIA, D., ANDERSSON, A. G., LUNDSTROM, T. S. Computational investigation of an industrial cyclone separator with helical-roof inlet. *Chemical Engineering and Technology* [online]. 2015, **38**(8), p. 1425-1434. ISSN 0930-7516, eISSN 1521-4125. Available from: https://doi.org/10.1002/ceat.201500181

[37] BETTGE, A., RUBENTHALER, G. L., POMERANZ. Y. Air-aspirated wheat cleaning in grading and in separation by functional properties. *Cereal Chemistry* [online]. 1989, **66**(1), p. 15-18. ISSN 0009-0352, eISSN 1943-3638 Available from: https://www.cerealsgrains.org/publications/cc/backissues/1989/Documents/66_15.pdf

[38] KOSHKAREV, S., AZAROV, V., AZAROV, D. The decreasing dust emissions of aspiration schemes appliing a fluidized granular particulate material bed separator at the building construction factories. *Procedia Engineering* [online]. 2016, **165**, p. 1070-1079. ISSN 1877-7058. Available from: https://doi.org/10.1016/j.proeng.2016.11.821

COMPARATIVE ESTIMATION OF MANEUVERABILITY OF THE MULTI-TRACK ROAD TRAINS OF DIFFERENT LAYOUT SCHEMES

Volodymyr Sakhno[1], Igor Murovanyi[2], Oleksandr Razboinikov[1], Olekcii Palamarchyk[1], Valerii Dembitskyi[2,*]

[1]National Transport University, Kyiv, Ukraine
[2]Lutsk National Technical University, Lutsk, Ukraine

*E-mail of corresponding author: dvm2@meta.ua

Valerii Dembitskyi 0000-0002-1006-9218,
Igor Murovanyi 0000-0002-9749-980X,
Olekcii Palamarchyk 0009-0003-9782-1015
Volodymyr Sakhno 0000-0002-5144-7131,
Oleksandr Razboinikov 0000-0003-3024-0999

Resume

Today, in the constructions of multi-link road trains, two main layout schemes are used, as a rule - trailer (car + n trailers) and semi-trailer (tractor car + n semi-trailers).

Previously conducted studies established that the maneuverability indicators of the road trains can be determined on wheels rigid in the lateral direction, that is, according to kinematic models, which are based on the angles of assembly of the road train links. These angles are defined for both a three-link trailer and a semi-trailer vehicle train, for different locations of the extended link.

For the semi-trailer road trains, the requirements for maneuverability are not met, and therefore the trailer links must be equipped with more or less complex control systems. With a direct control drive on the front axles of the second and third semi-trailers, when turning at 90º and 180º, only the first layout scheme satisfies the requirements for maneuverability.

Available online: https://doi.org/10.26552/com.C.2025.005

Article info

Received 20 June 2024
Accepted 30 September 2024
Online 6 November 2024

Keywords:

maneuverability
road train
three-link trailer
semi-trailer
folding angles
turning angles

ISSN 1335-4205 (print version)
ISSN 2585-7878 (online version)

1 Issue

Ensuring sustainable and stable development of the state's economy necessitates putting into operation the intermodal transport systems. One of the most promising and widespread among them is container transportation. To maintain the competitiveness of container transportation, it is important to put into operation the modern designs of containers, designed for the transportation of a wide range of goods. That can be achieved by putting into operation the multi-modal vehicles [1-4]. A container is the most perspective and widespread multi-modal vehicle. A container delivery is ordered, not only by big trade companies, but by the enterprises of middle and little range that make import and export of goods, as well, [5]. Most customers choose exactly the container transportation due to the clear advantages, namely a goods preservation; a reduction of terms for cargo-handling works due to what the goods delivery time is reduced; a possibility of transporting of any goods, including dangerous, perishable, bulked, heavy-weight and off-clearance loads; a universality as a container can be transported by a car, train and sea transport that allows to reduce the expenses of time and money for a load delivery into the final destination; a possibility of the prefabricated loads delivery; a computerization of the delivery process operation [6]. The choice depends on the load peculiarities and a distance where this load should be delivered. A load transportation price depends on this, as well. Container freight transportation by the two-track, and in recent years, three-track road trains are the most popular. This is due to a number of advantages of three-track road trains compared to two-track trains [7-8] - less specific weight, that is a weight that is equal to a unity of carrying capacity; a lower cost price of the industrial mass production of the trailers and semi-trailers then the vehicles that correspond to them by the carrying capacity; a bigger specific body area (approximately half as much again), that makes the significant operation advantages; the less investments into the building of storage areas as the trailers and semi-trailers do not need the covered

Figure 1 *Road train with two trailers [9]*

lodgings; a possibility to quickly plan the transportation with different structure of road train depending on the operating conditions; the less specific charges (per a single unit of carrying capacity) of labor force and materials for maintenance and repair works. It is not strange that in Europe there are 35-meter road trains with two trailers that can carry three containers [9]. It is explained by the fact that the Cargo transportation rules, as a traffic code, have a tendency to change from time to time. So recently in Denmark there was a thought about a necessity of using the long road trains of 34 meters on the general usage roads. Such an innovation is related to an intention to reduce the number of the exhaust gas emissions (Figure 1).

If the local politicians support this initiative, Denmark can become the second country in Europe where it would be allowed to drive the road trains more than 30 meters long, namely the wagons with double trailers (34.5 m), after such initiative on its roads was supported by Sweden, where such road trains have been operated for five last years already. An idea of using the long-dimension vehicles on its roads is also investigated in Poland. It is worth saying that in USA and Australia the length of road trains is not restricted, that is why one can meet there the real champions, for example, in Australia a general length of road train can become approximately 50 meters.

It is necessary to notice that the full masses, dimensions and permissible loads for the trucks in Europe are regulated by DIRECTIVE 2002/7/EC [10], where the maximum full mass of a two-track road train with a semi-trailer on a pneumatic support can not exceed 44 t. When using a three-track road trains, a general mass of a road train G_{an} is increasing up to 60 t, and of a multi-track ones - up to 100 t. Along with that for a two-track road train, it is possible to use a double-axle vehicle-tractor (at a load on a driving axle $G_2 = 0.25 \times G_{an} = 11.0$ t), for the three-track road train - a three-axle vehicle-tractor with a wheel formula 6x4 ($G_2 = 0.25 \times G_{an} = 15.0$ t), for a multi-track road train - a three-axle vehicle-tractor. A further increase of a mass of a multi-track road train up to 90to 100 t needs using of a multi-axle vehicle-tractor or a hybrid power drive of road train.

A base of multi-track road trains, together with vehicles-tractors, consists of trailers and semi-trailers. Along with that, at a great variety of layout schemes of multi-track road trains, a construction of the last-mentioned ones can be composed from a comparatively little number of constructively completed functional elements - modules [11]. This is a unique system “road train” can be represented as a composed of two or more sub-systems, articulated between them - “vehicle-tractor” and “trailer tracks (trailer, semitrailer)” depending on a layout scheme of a road train. Today, in the constructions of multi-track road trains, as a rule are used the two main layout schemes - trailer (vehicle + *n* trailers) and semi-trailer (vehicle-tractor + *n* semitrailers). That is why it is reasonable to compare two these layout schemes at a transportation of three containers.

2 Literature sources analysis

Modern development of public and truck transport leads to increasing f the vehicles demand for passenger and cargo carrying. This tendency proves the arguments of power economy and decreasing of environmental pollution level that is caused but a restricted number of the vehicles and drivers necessary to carry a great number of loads and passengers. As a consequence, the trucks and city buses manufacturers today design the constructions of high capacity in the form of joint and multi-track vehicles. [12-15]. The swing joints make the long vehicles to be unique in use and admit a quick maneuverability even in dense urban conditions. However, the maneuverability of the long-articulated vehicles can be dangerous even for experienced drivers. So, the researcher Altafini [16] showed that the tracks with a great number of trailers (MTAHV) demonstrate the unstable operation modes at high speeds, including an assembly of tracks, a swinging of trailer and turning over. These unstable, unfavorable operation modes, can lead to the traffic accidents. On the other side, these vehicles have bad maneuverability at low speeds.

To increase a safety of the multi-track road trains operating, the numerous investigations were conducted, for example, Latif, Chalhoub and Pilipchuk [17] was examined a using of a slide mode controller, as well as a controller with feedback with an integral state at different driving situations and the pavement conditions.

In a research work [18] was shown that the interconnections between the axles and the tracks of the vehicles with some trailers can create a specific oscillating behavior of the trailers during the vehicle's maneuvers. These oscillations are a direct consequence of a vehicle kinematic feature, related with a construction of a traction and towed device. At an example of one pair of tracks of the vehicles there are accepted the regularities of its turning that are expanded in future on a road train with a free number of trailers. Numerous results obtained for a kinematic of three trailers approve the theoretical thoughts that give some cardinal view on a problem.

That is why the typical kinematic models of the multi-track road trains will be useful while solving such problems as: a formal analysis of the kinematic features, a quick planning of the nominal maneuvers, a prediction of the operation modes etc., [19-21].

For a kinematic vehicle model with n trailers was offered an adaptive control scheme based on a neural network of a radial-basis function (RBFNN), [22].

As a conducted analysis has shown, a lot of research works are dedicated to the problem of improving of the operating indices of the multi-track vehicles [23-27].

The development of compact and easy to use mathematic models of the articulated vehicles for planning, controlling and localization of driving, becomes increasingly important in a time of intellectual transport systems, especially when there is a need for effective predictions of driving for the multi-track vehicles of different kinematic structures [28-33]. In a reference [34] a module algorithm approach to the kinematic modeling of non-holonomic (multiple-unit) articulated buses was offered, including the trucks with n-trailers (as a separate case), that consists of traction vehicle passively joined to a free number of guided and unguided trailers and with different placement of controlled axles in a kinematic chain. Kinematic models are valid at a condition of absolute rolling of all wheels of a vehicle (without sliding/sliding) that is practically approved for the conditions of maneuverability at low speed. In a research work [21] it is presented a conception and an analysis of stability of a feedback control system to track a trajectory of a road train with free number of articulated trailers. Thanks to the use of a cascade management structure, the proposed solution is modular and easily scalable depending on the number of trailers. A formal analysis of the closed system assures the sufficient conditions for an asymptotic tracking of a totality of the so-called sample trajectories with trajectory curvature both invariable and variable in time. The cascade law of trajectory control, investigated in the article, solves a problem of tracking the kinematics of a multi-track road train.

At the same time, considerably less attention in the literature is given to the issues of kinematic modeling and analysis of semi-trailer road trains (such as B-double and B-triple), which differ in design from more common trailer road trains, as well as to the study of their maneuverability. In a scientific article [35] was shown that for the road trains of semi-trailer scheme a kinematic model is more complicated than in a standard case of a road train with some trailers concerning its controllability. Along with that, the more complicated equations can be interpreted as the virtual steering control of the wheels situated on the semi-trailers, whose turning angles are found by the non-linear feedback from an output state of a system configuration.

A curvilinear motion of a road train is characterized by such mode parameters as running speed, turning radius and turning angles of controlled wheels, that during the road train operation do not stay constant. That is why to estimate the maneuverability of the vehicles, both kinematic and dynamic indices are used.

The dynamic indices are assured by a system "engine-transmission" of a traction vehicle or vehicle-tractor.

The kinematic indices should assure:

- an overall traffic lane (OTL), that is equal to a difference of external and internal overall turning radii. Taking into consideration that the overall turning radii are fixed (R_{eo}=12.5 m, R_{io}=5.3 m), an overall traffic lane would be also fixed (B_0 = 7.2 m);
- a possibility of backward running.

The least studied until today is a question of possibility of a road train backward running that was not almost theoretically considered for the multi-track road trains. However, for the multi-track road trains that run as a rule between terminals situated at the city entrance, a problem of backward running is not actual.

The authors examine a maneuverability of the three-track road trains of different layout schemes [36], as though if a train has more than three tracks, the difficulties concern the fact that an investigation of running of such a multi-track vehicle is rather complicated because of the necessity to take into consideration an influence of many factors on the running character.

As is known, the characteristics of maneuverability and running stability of a vehicle are determined by a combination of operating, mass-geometric and construction parameters of its modules and their control systems. In general case, the desirable combinations of named parameters from the point of view of maneuverability and stability in a range of operating loadings and running speeds, even for the same vehicle can be different. As a consequence, on the early phases of vehicle creation, it is difficult to get the precise construction parameters and quantity indices by the criterion of maneuverability and its running stability. The success in solving such problems depends on the

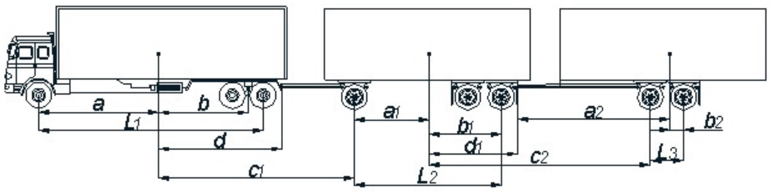

Figure 2 *Layout scheme of a trailer road train*

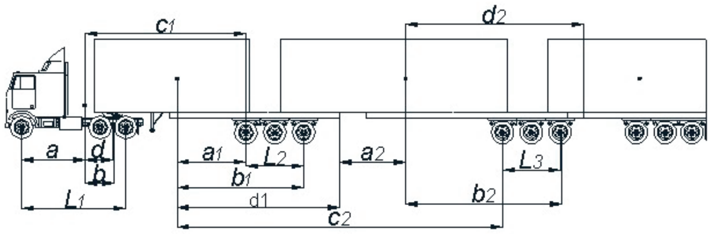

Figure 3 *Layout scheme of a semi-trailer road train*

fact how successfully a mathematical model and its substantial parameters, which describe a behavior of a dynamic system in different running modes, are chosen. For maneuverability it is an equation in a plane-parallel movement, for stability - in spatial one. So, in a research work [36] the differential equations were derived of plane-parallel movement to find the parameters of maneuverability and running stability of the two-track semi-trailer and three-track trailer road trains, however, the using of these equations to comparatively estimate the multi-track road trains - container carriers can lead to a substantial fault. Because of this, the aim of a given research work is a comparative estimation of multi-track road trains - container carriers of different layout schemes by the maneuverability parameters.

3 Research requirements

The overall lane of curvilinear movement of a multi-track road train, in contrast to a rectilinear movement lane, has a difficult form, restricted by the projections of trajectories on a horizontal plane of external wing, concerning a turning center of a vehicle-tractor and rear end of trailer or semi-trailer. The overall traffic lane (OTL) of a road train at turning is determined by a main trajectory of a vehicle-tractor and a displacement of trajectory of trailer or semi-trailer from the main trajectory to the turning center. The overall traffic lane and the overall passage (a part of space taken by a road train at turning) get their maximum at the stable curvilinear, that is circular, trajectory. That is especially valid on that trajectory that the overall traffic lane of a multi-track road train should be determined. In a research work [36] was shown that the indices of the road trains maneuverability (at a movement with the speeds that do not exceed 10 m/s) it is possible to determine on the rigid in lateral direction wheels, that is by the kinematic models.

The next layout schemes of the multi-track road trains are examined - container carriers with the uncontrollable trailer tracks:

- a road train-container carrier composed of three trailers, Figure 2;
- a road train-container carrier composed of three semi-trailers (road train of type B-triple), Figure 3.

Each of these layout schemes was examined in two variants that were characterized by a location of a 40-foot container - inside or at the end of a road train.

All the indices of maneuverability are determined by the parameters of a curvilinear movement of a road train, the main of them are the assembly angles of a road train. So, for a trailer road train these would be two assembly angles: the first one between a tractor

$$
\begin{aligned}
&\frac{d\varphi_1}{dt}+\frac{\nu_A}{L_1\dfrac{\sin(\pi/2-\varphi_2-\alpha_1)}{\sin(\varphi_1+\varphi_2+\alpha_1)}}-\frac{\nu_{C1}tg\theta}{a+b-d}=0\\
&\frac{d\varphi_2}{dt}-\frac{\nu_{C1}\sin(\pi/2-\varphi_1)}{\dfrac{a_1+b_1}{tg\varphi_1}\sin(\pi/2\varphi_2-\alpha_1)\times\sqrt{1+\left(\dfrac{d_1-c_1}{a_1+b_1}tg\varphi_2\right)^2}}-\frac{\nu_A\sin(\varphi_1+\varphi_2+\alpha_1)}{L_2\sin(\pi/2-\varphi_1-\alpha_1)}=0,\\
&\frac{d\varphi_3}{dt}-\frac{\nu_{C1}\sin(\varphi_1+\varphi_2+\alpha_1)\times L_1^2\sin(\gamma_1+\varphi_3+\alpha_2)}{L_2L_3\sin\varphi_2\sin(\pi/2-\varphi_3-\alpha_2)}\times\\
&\times\frac{\sin(2/\pi-\varphi_2-\alpha_1)ctg\gamma_1}{\dfrac{a_2+b_2}{tg\varphi_2}\times\sqrt{1+\left(\dfrac{d_2-c_2}{a_2+b_2}tg\varphi_2\right)^2}+L_2\dfrac{\cos\varphi_1}{\sin(\varphi_1+\varphi_2+\alpha_1)}-L_3\sin(\pi/2-\varphi_2-\alpha_1)ctg\gamma_1}-\\
&-\frac{\nu_{C1}L_1\sin(\varphi_1+\varphi_2+\alpha_2)}{L_2L_3\sin(\pi/2-\varphi_2-\alpha_2)}=0.
\end{aligned}
\tag{1}
$$

$$
\begin{aligned}
\alpha_1 &= \operatorname{arctg}\left(\frac{d_1 - c_1}{a_1 + b_1}\operatorname{tg}\varphi_1\right),\\
\alpha_2 &= \operatorname{arctg}\left(\frac{d_2 - c_2}{a_2 + b_2}\operatorname{tg}\varphi_2\right),\\
\gamma_1 &= \operatorname{arctg}\left(\frac{l_1 \sin(\varphi + \varphi_1 + \alpha_1)}{L_1 \sin(\pi/2\varphi_2 - \alpha_1)} \times \frac{1}{\sqrt{1 - \left\{\dfrac{\left[\dfrac{\sin(\pi/2 - \varphi_2 - \alpha_1)}{\sin(\varphi_2 + \varphi_1 + \alpha_1)}\right]^2 + 1 - \left[\dfrac{\sin(\pi/2 - \varphi_1)}{\sin(\varphi_2 + \varphi_1 + \alpha_1)}\right]^2}{2 \times \dfrac{\sin(\pi/2 - \varphi_2 - \alpha_1)}{\sin(\varphi_2 + \varphi_1 + \alpha_1)}}\right\}^2}}\right),\\
\gamma_2 &= \operatorname{arctg}\left(\frac{L_2 \sin(\varphi_3 + \alpha_2)}{L_3 \sin(\pi/2 - \alpha_2)} + \frac{1}{\sqrt{1 - \left\{\dfrac{\left[\dfrac{\sin(\pi/2 - \alpha_2)}{\sin(\varphi_3 + \alpha_1)}\right]^2 + 1 - \left[\dfrac{\sin(\pi/2 - \varphi_3)}{\sin(\varphi_3 + \alpha_2)}\right]^2}{2 \times \dfrac{\sin(\pi/2 - \alpha_1)}{\sin(\varphi_3 + \alpha_1)}}\right\}}}\right).
\end{aligned}
\tag{2}
$$

In Equations (1), (2) the following notations are adopted:
L_1, L_2, L_3 - a base of tracks of a road train, m;
v_A - a road train running speed, m/s;
v_C - a vehicle-tractor mass center speed, m/s;
θ - a turning angle of the controlled wheels of a vehicle-tractor, rad;
a - a distance from a mass center of a vehicle-tractor to a front axle;
b - a distance from a mass center of a vehicle-tractor to an axle of balance beam of rear axles;
d - a distance from a mass center of a vehicle-tractor to a point of joining of first trailer track;
φ_1 - an assembly angle between the vehicle-tractor and a first trailer track;
φ_2 - an assembly angle between the first and second trailer track;
φ_3 - an assembly angle between the second and third trailer track;
a_1, a_2 - a distance from a mass center of the first (second) trailer track to a front axle of trailer and a point of joining with a previous track (of semi-trailer);
b_1, b_2 - a distance from a mass center of the first (second) trailer track to a rear axle of trailer (semi-trailer);
c_1 - a distance from a mass center of vehicle-tractor to a front axle of the first trailer track;
d_1 - a distance from a mass center of the first trailer track to a point of joining with the second trailer track;
c_2 - a distance from a mass center of the first trailer track to a front axle of the second trailer track;
d_2 - a distance from a mass center of the second trailer track to a point of joining with the third trailer track.

and the first trailer track, and the second one - between the second and third trailer track, and for a road train of type B-triple - these would be three assembly angles: the first one between the vehicle-tractor and the first semi-trailer, the second one - it is an angle between the first and second semi-trailers, and the third one is between the second and third semi-trailer. Since the most common case is a road train of type B-triple, the assembly angles were determined for it, as it is shown in [36].

In given system of equations (2), the additional angles are determined by the dependences.

For a trailer road train, it is necessary to adopt $\varphi_1 = 0$.

Since the road train comes through different phases of turning, these are namely - an entry in turning, a movement in a circle, an exit of turning, a linear movement of a road train, so the assembly angles should be determined exactly for these phases.

Figure 4 shows an example of the assembly angles of the road trains tracks of a semi-trailer scheme. For the road trains of trailer scheme the assembly angles are for 17 and 21 % smaller than the second and third assembly angles of the semi-trailer road train for different turning phases.

By the found assembly angles of the road train tracks, the overall turning radii of a road train and a presumptive maneuverability index - an overall traffic lane - are determined.

In Tables 1 and 2 are given the layout schemes of typical road trains that are constructed thanks to a software of Scania company, and t an overall lane of these road trains is determined, using the Equations (1) - (6), at circular movement and entry in turning.

As it follows from the data of Table 1, none of the layout schemes of three-track road train satisfies the requirements of DIRECTIVE 2002/7/EC concerning maneuverability. Taking into account a character of such road trains operation (running between terminals at the city entrance), more important are the parameters of maneuverability of a road train at the turning of 90° and 180°.

In Table 2 there are given the values of overall radii and of overall traffic lane of the road trains that are investigated, at the named turnings.

As it follows from Table 2, almost all the trailer road trains, in contrast to the semi-trailer ones, at turning of 90° and 180°, satisfy the requirements of DIRECTIVE

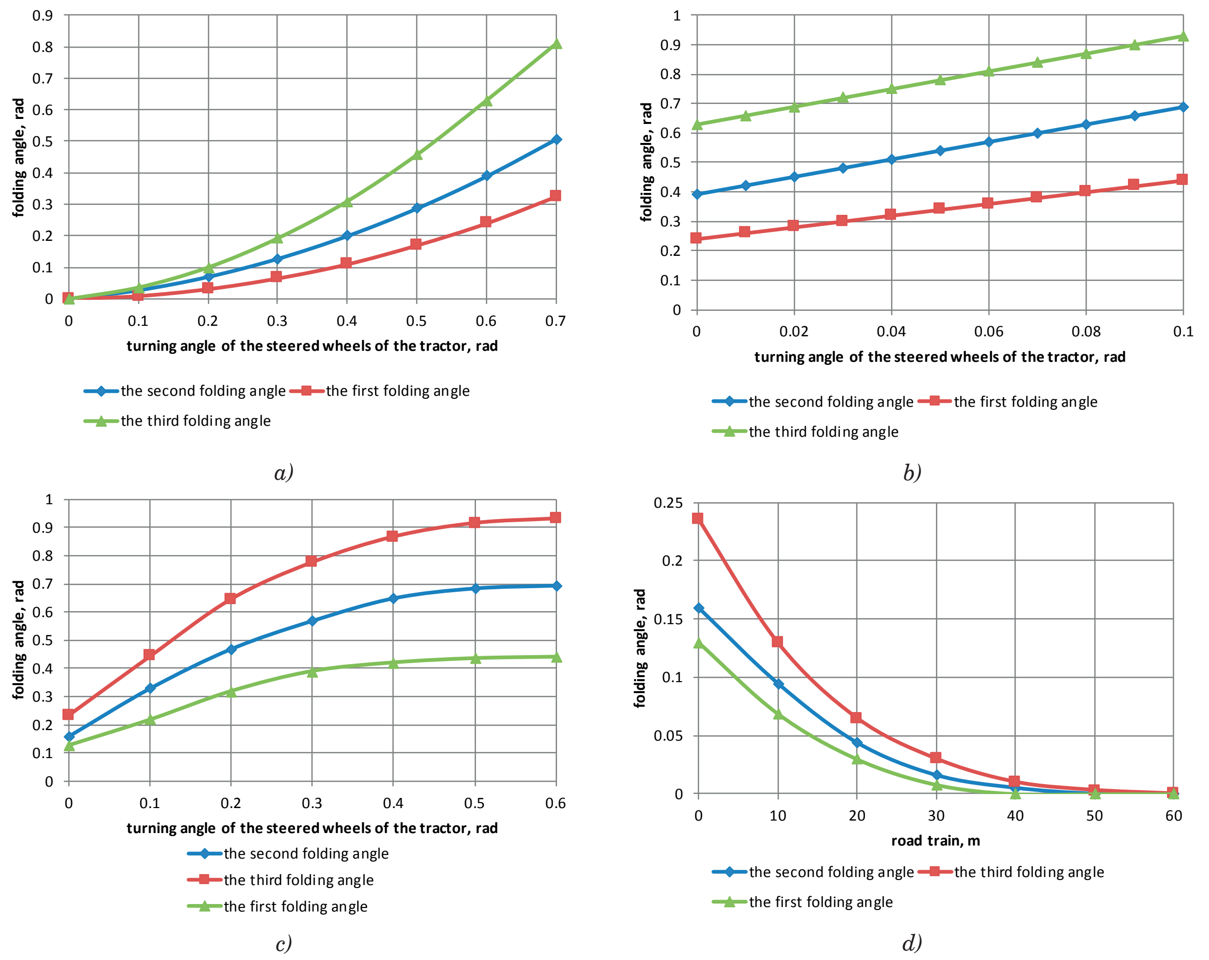

***Figure 4** Change of assembly angles of the road train for different turning phases:a) entry in turning; b) movement in a circle; c) exit of turning; d) tractor movement on a linear trajectory*

2002/7/EC concerning maneuverability. Because of that, the semi-trailer road trains should be equipped with the control systems.

In a research work [36] is shown that for the trailer and semi-trailer road trains, the most distributed are the systems of direct control when a turning angle of the controlled wheels (axle) of trailer track is determined as a function of assembly angle. Since the second and third trailer tracks should be, first of all, equipped with the control systems, so exactly these tracks should have the controlled wheels (axles) whose turning is made correspondingly to an assembly angle.

While having the controlled trailer tracks, the assembly angles for different turning phases are written like [36]:

- at entry in turning:

$$\frac{d\varphi_2}{d\theta} = \frac{tg(\theta)}{K_n \cdot L_2} \times \times \left(1 - \frac{L_2}{tg(0)} \times \times \frac{\left(\sin\left(\frac{\varphi_2}{i_0}\right) - \frac{C \cdot tg(\theta)}{L_2} \cdot \cos\left(\frac{\varphi_2}{i_0}\right) \right)}{L_2 \cdot \left(\frac{\varphi_2}{i_0} - \varphi_2\right)} \right), \tag{3}$$

$$\frac{d\varphi_3}{d\theta} = \frac{\left(\sin\left(\frac{\varphi_2}{i_0}\right) - \frac{C \cdot tg(\theta)}{L_2} \cdot \cos\left(\frac{\varphi_2}{i_0}\right) \right)}{K_n \cdot L_2 \cdot \cos\left(\frac{\varphi_2}{i_0} - \varphi_2\right)} - - \frac{\left(\cos(\varphi_2) + \frac{C \cdot tg(\theta)}{L_1} \cdot \sin(\varphi_2) \right)}{K_n \cdot \cos\left(\frac{\varphi_3}{i_1} - \varphi_3\right)} \times \times \frac{\sin\left(-\frac{\varphi_2}{i_0} + \varphi_2 + \frac{\varphi_3}{i_1} - \alpha_1 \right)}{L_3 \cdot \cos\left(\frac{\varphi_2}{i_0} - \varphi_2 + \alpha_1\right)}, \tag{4}$$

where K_n - a mode turning coefficient;
θ - a turning angle of the controlled wheels of a vehicle-tractor, rad;

- at movement in a circle:

$$\frac{d\varphi_2}{d\varphi_K} = \left(1 - R_{0MIN} \times \times \frac{\left(\sin\left(\frac{\varphi_2}{i_0}\right) - \frac{C}{R_{0MIN}} \cdot \cos\left(\frac{\varphi_2}{i_0}\right) \right)}{L_2 \cdot \cos\left(\frac{\varphi_2}{i_0} - \varphi_2\right)} \right), \tag{5}$$

Table 1 *Turning parameters of three-link road trains*

Road train type		Turning parameters, m		
		R_{eo}	R_{io}	B_o
1	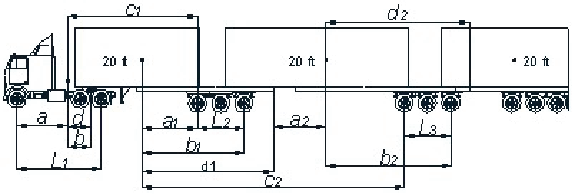	5.3	13.925	8.625
2	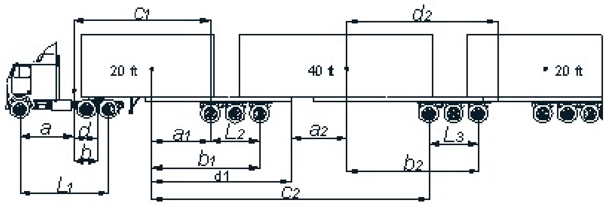	5.3	14.401	9.101
3	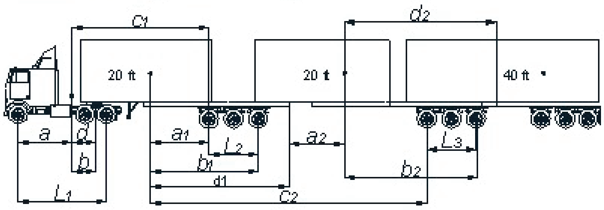	5.3	14.625	9.325
4	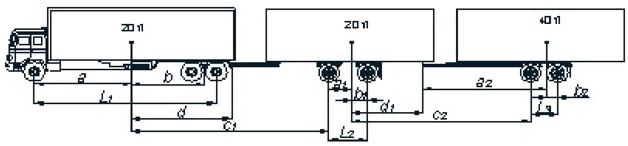	5.3	12.433	7.133
5	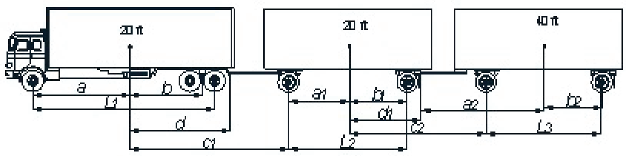	5.3	12.053	6.753
6	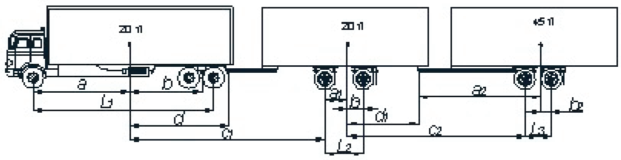	5.3	14.723	9.101

Table 2 *Overall radii and overall traffic lane of the road trains*

Road train type	Turning parameters, m					
	180º			90º		
	R_{eo}	R_{io}	B_0	R_{eo}	R_{io}	B_0
1	13.925	5.731	8.194	13.925	6.143	7.782
2	14.401	5.750	8.651	14.401	6.183	8.218
3	14.625	5.766	8.859	14.625	6.209	8.416
4	12.433	5.353	7.080	12.433	5.707	6.726
5*	12.053	5.638	6.415	12.053	5.959	6.094
6	14.723	7.058	7.665	14.723	7.521	7.202

*Note: trailers with the separated axles with controlled front axles

$$\frac{d\varphi_3}{d\varphi_K}=\frac{\left(\sin\left(\frac{\varphi_2}{i_0}\right)-\frac{C}{R_{0MIN}}\cdot\cos\left(\frac{\varphi_2}{i_0}\right)\right)}{L_2\cdot\cos\left(\frac{\varphi_2}{i_0}-\varphi_2\right)}-$$
$$-\frac{\left(\cos(\varphi_2)+\frac{C}{R_{0MIN}}\cdot\sin(\varphi_2)\right)}{L_3\cdot\cos\left(\frac{\varphi_3}{i_0}-\varphi_3\right)}\times \tag{6}$$
$$\times\frac{\sin\left(-\frac{\varphi_2}{i_0}+\varphi_2+\frac{\varphi_3}{i_1}-\alpha_1\right)}{\cos\left(\frac{\varphi_2}{i_0}-\varphi_2+\alpha_1\right)},$$

where φ_K - an angle of inclination of the road train, rad;

- at exit of turning are used the same Equations (3) and (4), but a mode coefficient of turning K_n should be taken with negative sign;
- at a linear movement of tractor-vehicle (at this phase the assembly angles do not depend anymore on a position of driving wheels but only on a distance that is passed by a vehicle-tractor, then $d\theta=K_n\cdot dS_0$, where S_0 - the initial value of the path, at $\theta = 0$ one will get:

$$\frac{d\varphi_2}{dS_0}=-\frac{\sin\left(\frac{\varphi_2}{i_0}\right)}{L_2\cdot\cos\left(\frac{\varphi_2}{i_0}-\varphi_2\right)}, \tag{7}$$

$$\frac{d\varphi_3}{dS_0}=\frac{\sin\left(\frac{\varphi_2}{i_0}\right)}{L_2\cdot\cos\left(\frac{\varphi_2}{i_0}-\varphi_2\right)}-$$
$$-\frac{\cos(\varphi_2)}{\cos\left(\frac{\varphi_2}{i_0}-\varphi_2+\alpha_1\right)}\times \tag{8}$$
$$\times\frac{\sin\left(-\frac{\varphi_1}{i_0}+\varphi_1+\frac{\varphi_2}{i_1}-\alpha_1\right)}{L_3\cdot\cos\left(\frac{\varphi_3}{i_1}-\varphi_3\right)},$$

where C - a distance from a rear axle of a first semi-trailer to a point of joining with the second semi-trailer;
α_1 - an angle between a perpendicular to a rear axle of tractor and a ray that joins a point of joining of the first semi-trailer with the second one and an immediate turning center of a road train;
K_n - a mode turning coefficient;
i_o, i_1 - correspondingly the speed ratio of the front wheels control linkage of the second and third semi-trailers (according to the data from [15] we take as equal i_o = 0.5 and i_2=0.6).

Introduction of the trailers tracks control leads to a reducing of first and second assembly angles, correspondingly for 18 to 20% and 27 to 32%. It leads to a decreasing of an overall track lane of a road train, while making different turning by it, Table 3.

Analysis of the data of Table 3 shows that the three-track semi-trailer road trains even with the controlled second and third semi-trailers, while carrying one 40- or 45-feet container and two 20-feet containers, do not satisfy the requirements concerning a maneuverability and at turning of both 90° and 180°, taking into account their significant length (about 36 m). Issuing from a presented analysis, one can make a conclusion that for the multi-track road trains there is actual a choice of type of the wheels (axles) control linkage of the semi-trailer tracks and their location in the road train compound.

4 Results discussion

While carrying three containers - two 20-feet and one 40 or 45-feet, there is important not only a choice of layout scheme of road train (trailer, semi-trailer one), but a location of the elongated track (for carrying 40- and 45-feet containers) in a road train compound, as well. This choice is possible to do based on the analysis of maneuverability indices of trailer and semi-trailer road trains.

Previously conducted studies established that the maneuverability indices of the road trains (when moving at speeds not exceeding 10 m/s) can be determined on wheels rigid in the lateral direction, that is, according to kinematic models, which are based on the assembly angles of the road train tracks. These angles are defined for both a three-track trailer and a semi-trailer road train for different locations of the extended track.

Based on the found assembly angles of the tracks, the overall turning radii of the road train and the overall maneuverability index - the overall traffic lane - are determined. At the same time, it is shown that none of the layout schemes of the three-link road train, except for the road train with separated and controlled axles of the trailer tracks (scheme 5), does not satisfy the requirements of DIRECTIVE 2002/7/EC concerning maneuverability. Taking into account the kind of the

Table 3 *Overall radii and overall traffic lane of road trains with guided trailers*

Road train type	Turning parameters, m								
	Movement in a circle			Turning 180º			Turning 90º		
	R_{eo}	R_{io}	B_o	R_{eo}	R_{io}	B_o	R_{eo}	R_{io}	B_o
1	5.3	13.063	7.763	12.925	6.405	6.520	12.925	6.731	6.194
2	5.3	13.491	8.191	14.401	6.615	7.786	14.401	7.005	7.396
3	5.3	13.693	8.393	14.625	6.832	7.793	14.625	6.209	8.416

operation of such road trains (running between terminals at the entrance to the city), the maneuverability parameters of the road train at typical turns 90° and 180° are more important. For such turns, the trailer road trains are more promising, for which the requirements of the DIRECTIVE concerning maneuverability are met at turnings of 90° and are almost fulfilled when turning at 180°. For semi-trailer road trains, the requirements for maneuverability are not met, and therefore the trailer tracks must be equipped with more or less complex control systems. With a direct control drive on the front axles of the second and third semi-trailers, when turning at 90° and 180°, only the first layout scheme satisfies the requirements for maneuverability. Therefore, for the semi-trailer scheme, it is necessary to develop a more advanced control system in comparison to the direct control drive.

5 Conclusions

1. The maneuverability indices of the three-track road trains on wheels rigid in the lateral direction were determined, that is, according to kinematic models, which are based on the assembly angles of the road train tracks. These angles are defined for both a three-track trailer and a semi-trailer road train for different locations of the extended track. Thus, while entering a turning the first and second assembly angles of a trailer road train are for 12 and 15 % smaller than the second and third assembly angles of a semi-trailer road train. This correlation is valid with a little deviation (5-7 %) for other turning phases, as well.
2. It was shown that none of the layout schemes of the three-track road train, except for the road train with separated and controlled axles of the trailer tracks (scheme 5, Table 1), does not satisfy the requirements of DIRECTIVE 2002/7/EC concerning maneuverability. When turning at 90° and 180°, almost all the trailer road trains of all the layout schemes, in contrast to semi-trailer schemes, satisfy the requirements of DIRECTIVE 2002/7/EC.
3. There was found that at the controlled first axles of the second and third semi-trailers, an overall traffic lane of such road train, while comparing to an uncontrolled road train, at a movement in a circle is reducing for 10 to 12 %, but all the road trains do not satisfy the requirements concerning maneuverability.

Acknowledgment

The authors received no financial support for the research, authorship and/or publication of this article.

Conflicts of interest

The authors declare that they have no known competing financial interests or personal relationships that could have appeared to influence the work reported in this paper.

References

[1] LOVSKA, A, GERLICI, J., DIZO, J., KRAVCHENKO, O. Analysis of the strength of a hopper-typecontainer when transported by a semi-trailer. *Transport and Logistics: the International Journal*. 2023, **23**(55), p. 1-12. ISSN 2406-1069.

[2] WOODCOCK, A., TOVEY, M. (2020) Designing whole journey, multimodal transport provision. *The Design Journal* [online]. 2020, **23**(1), p. 91-112. eISSN 1756-3062. Available from: https://doi.org/10.1080/14606925.2019.1693210

[3] PORTAPAS, V., ZAIDI, Y., BAKUNOWICZ, J., PADDEU, D., VALERA-MEDINA, A., DIDEY, A. Targeting global environmental challenges by the means of novel multimodal transport: concept of operations. In: 2021 5th World Conference on Smart Trends in Systems Security and Sustainability WorldS4: proceedings [online]. IEEE. 2021. eISBN 978-1-6654-0096-1, p. 101-106. Available from: https://doi.org/10.1109/WorldS451998.2021.9514048

[4] CORNELL, A. Improving interconnectivity with multimodal transportation [online]. In: *Sustainable mega city communities*. WOODROW, W. C. (Ed.). Butterworth-Heinemann, 2021, ISBN 9780128187937, p. 191-202. Available from: https://doi.org/10.1016/B978-0-12-818793-7.00011-1

[5] PENCHEVA, V., ASENOV, A., SLADKOWSKI, A., IVANOV, B., GEORGIEV, I. Current issues of multimodal and intermodal cargo transportation [online]. In: *Modern trends and research in intermodal transportation. studies in systems, decision and control. Vol. 400.* SLADKOWSKI, A. (Ed.). Cham: Springer, 2022. ISBN 978-3-030-87119-2, eISBN 978-3-030-87120-8. Available from: https://doi.org/10.1007/978-3-030-87120-8_2

[6] FENG, X., SONG, R., YIN, W., YIN, X., ZHANG, R. Multimodal transportation network with cargo containerization technology: advantages and challenges. *Transport Policy* [online]. 2023, **132**, p. 128-143. ISSN 0967-070X. Available from: https://doi.org/10.1016/j.tranpol.2022.12.006

[7] TOPALIDS, V. A. Promising heavy-duty road trains for Eurasian transportation (in Russian) [online]. Available from: www.iru-cis.ru/iru-moscow/ 2007/02_sr/doc/21/ Topalidi_Uzbekistan_- Rus.pdf/

[8] TSCHOKE, M., BOYSEN, N. Container supply with multi-trailer trucks: parking strategies to speed up the gantry crane-based loading of freight trains in rail yards. *OR Spectrum* [online]. 2018, **40**, p. 319-339. ISSN 0171-6468, eISSN 1436-6304. Available from: https://doi.org/10.1007/s00291-017-0491-1

[9] 35-meter trucks with three trailers will appear in Europe [online]. Available from: inform@newsyou.info

[10] DIRECTIVE 2002/7/EC of European parliament and of the council of 18 February 2002 amending Council Directive 96/53/EC of 25 July 1996 laying down for certain road vehicles circulating within the Community the maximum authorized dimensions in national and international traffic and the maximum authorized weights in international traffic. Official Journal of the European Communities. 2002. No L67/47-49.

[11] SHKVARKO, K. V. Long-term three-link road trains - a new stage in the development of road transport in Ukraine on the way to Europe. *System Management Methods, Technology and Organization of Production, Repair and Operation of Cars: Scientific Journal*. 2003, **17**, p. 146-152. ISBN 978-966-632-215-2.

[12] LEDUC, G. *Longer and heavier vehicles. An overview of technical aspects* [online]. Technical Report EUR 23949 EN. Luxembourg: Joint Research Centre, Institute for Prospective Technological Studies, 2009. ISSN 1018-5593, ISBN 978-92-79-12983-4. Available from: https://doi.org/10.2790/12649

[13] ISLAM, M. Parallel design optimization of multi-trailer articulated heavy vehicles with active safety systems. Ontario, Canada: University of Ontario Institute of Technology Oshawa, 2013.

[14] HUANG, W., AHMADIAN, M., RAHIMI, A., STEIGINGA, L. Dynamics performance of long combination vehicles with active control systems. *Vehicle System Dynamics* [online]. 2023, **61**(7), p. 1831-1880. ISSN 0042-3114, eISSN 1744-5159. Available from: https://doi.org/10.1080/00423114.2023.2194545

[15] ZHU, S., HE, Y. A Coordinated control scheme for active safety systems of multi-trailer articulated heavy vehicles. In: The 28th IAVSD International Symposium on Dynamics of Vehicles on Roads and Tracks: proceedings. 2023.

[16] ALTAFINI, C. Some properties of the general n-trailer. *International Journal of Control* [online]. 2001, **74**(4), p. 409-424. eISSN 1366-5820. Available from: https://doi.org/10.1080/00207170010010579

[17] LATIF, A., CHALHOUB, N., PILIPCHUK, V. Control of the nonlinear dynamics of a truck and trailer combination. *Nonlinear Dynamics* [online]. 2020, **99**, p. 2505-2526. ISSN 0924-090X, eISSN 1573-269X. Available from: https://doi.org/10.1007/s11071-019-05452-1

[18] GOTTMANN, F., WIND, H., SAWODNY, O. On the influence of rear axle steering and modeling depth on a model based racing line generation for autonomous racing. In: 2018 IEEE Conference on Control Technology and Applications CCTA: proceedings [online]. 2018. eISBN 978-1-5386-7698-1, p. 846-852. Available from: https://doi.org/10.1109/CCTA.2018.8511508

[19] LJUNGQVIST, O., EVESTEDT, N., AXEHILL, D., CIRILLO, M., PETTERSSON, H. A path planning and path-following control framework for a general 2-trailer with a car-like tractor. *Journal of Field Robotics* [online]. 2019, **36**(8), p. 1345-1377. ISSN 1556-4959, eISSN 1556-4967. Available from: https://doi.org/10.1002/rob.21908

[20] GONZALEZ, D., PEREZ, J., MILANES, V., NASHASHIBI, F. A review of motion planning techniques for automated vehicles. *IEEE Transactions on Intelligent Transportation Systems* [online]. 2016, **17**(4), p. 1135-1145. ISSN 1524-9050, eISSN 1558-0016. Available from: https://doi.org/10.1109/TITS.2015.2498841

[21] TIAN, X., HE, R., SUN, X., CAI, Y., XU, Y. An ANFIS-based ECMS for energy optimization of parallel hybrid electric bus. *IEEE Transactions on Vehicular Technology* [online]. 2019, **69**(2), p. 1473-1483. ISSN 0018-9545, eISSN 1939-9359. Available from: https://doi.org/10.1109/TVT.2019.2960593

[22] CHENG, J., WANG, B., ZHANG, Y., WANG, Z. Backward orientation tracking control of mobile robot with N trailers. *International Journal of Control, Automation and Systems* [online]. 2017, **15**, p. 867-874. ISSN 1598-6446, eISSN 2005-4092. Available from: https://doi.org/10.1007/s12555-015-0382-7

[23] DULEBA, I. Kinematic models of doubly generalized N-trailer systems. *Journal of Intelligent and Robotic System* [online]. 2019, **94**, p. 135-142. ISSN 0921-0296, eISSN 1573-0409. Available from: https://doi.org/10.1007/s10846-018-0817-5

[24] GUEVARA, L., MICHALEK, M. M., CHEEIN, F. A. Collision risk reduction of N-trailer agricultural machinery by off-track minimization. *Computers and Electronics in Agriculture* [online]. 2020, **178**, 105757. ISSN 0168-1699. Available from: https://doi.org/10.1016/j.compag.2020.105757

[25] SHOJAEI, K., ABDOLMALEKI, M. Output feedback control of a tractor with N-trailer with a guaranteed performance. *Mechanical Systems and Signal Processing* [online]. 2020, **142**, 106746. ISSN 0888-3270. Available from: https://doi.org/10.1016/j.ymssp.2020.106746

[26] MICHALEK, M. M., PAZDERSKI, D. Forward tracking of complex trajectories with non-standard N-trailers of non-minimum-phase kinematics avoiding a jackknife effect. *International Journal of Control* [online]. 2019, **92**(11), p. 2547-2560. ISSN 0020-7179, eISSN 1366-5820. Available from: https://doi.org/10.1080/00207179.2018.1448117

[27] GAO, Y., CAO, D., SHEN, Y. Path-following control by dynamic virtual terrain field for articulated steer vehicles. *Vehicle System Dynamics* [online]. 2020, **58**(10), p. 1528-1552. ISSN 0042-3114, eISSN 1744-5159. Available from: https://doi.org/10.1080/00423114.2019.1648837

[28] KEYMASI, K. A., MOOSAVIAN, S. A. A. Dynamic modeling and tracking control of a car with trailers. *Multibody System Dynamics* [online]. 2016, **37**, p. 211-225. ISSN 1384-5640, eISSN 1573-272X. Available from: https://doi.org/10.1007/s11044-015-9472-9

[29] WONG, J. Y. *Theory of ground vehicles*. New York: Wiley, 2008. ISBN 9780470170380.

[30] JAZAR, R. *Truck dynamics: theory and applications*. New York: Springer, 2008. ISBN 978-0-387-74243-4, eISBN 978-0-387-74244-1.

[31] QUINGYUN, W., PENG, W., NING, C. Dynamics modeling and simulation of trailer with compliance steering system. *MATEC Web of Conferences* [online]. 2017, **139**, 00001. eISSN 2261-236X. Available from: https://doi.org/10.1051/matecconf/201713900001

[32] LJUNGQVIST, O., BERGMAN, K., AXEHILL, D. Optimization-based motion planning for multi-steered articulated vehicles. *IFAC-PapersOnLine* [online]. 2020, **53**(2), p. 15580-15587. ISSN 2405-8971, eISSN 2405-8963. Available from: https://doi.org/10.1016/j.ifacol.2020.12.2403

[33] SAKHNO, V. Maneuverability, movement stability of buses of the especially large size class. *Periodica Polytechnica Transportation Engineering* [online]. 2024, **52**(1), p. 104-112. ISSN 0303-7800, eISSN 0303-7800. Available from: https://doi.org/10.3311/PPtr.21856

[34] MICHALEK, M. M. Modular tracking controller for N-trailers with non-zero hitching offsets. In: 2015 American Control Conference: proceedings. 2015. p. 5371-5376.

[35] SAKHNO, V., POLIAKOV, V., LYASHUK, O., MUROVANYI, I., STELMASHCHUK, V., ONYSCHUK, V., TSON, O., ROZHKO, N. To the comparative evaluation of three-unit lorry convoys of the different component systems by maneuverability. *Scientific Journal of Silesian University of Technology. Series Transport / Zeszyty Naukowe Politechniki Slaskiej. Seria Transport* [online]. 2023, **121**, p. 189-201. ISSN 0209-3324, eISSN 2450-1549. Available from: https://doi.org/10.20858/sjsutst.2023.121.12

[36] POLYAKOV, V. M., SAKHNO, V. P. *Three-lane road trains. Maneuverability*. Luhansk: Knowledge, 2014. ISBN 978-617-579-918-5.

TECHNICAL CONDITION ASSESSMENT AND MODELLING OF REED VALVES IN VEHICLE ENGINE INTAKE SYSTEMS

Oleksandr Kravchenko[1,*], Alexander Khrulev[2], Juraj Gerlici[1], Oleksii Saraiev[3],Serhii Danets[4]

[1]University of Zilina, Zilina, Slovakia
[2]International Motor, Nemishaeve, Kyiv region, Ukraine
[3]Kharkiv National Automobile and Highway University, Kharkiv, Ukraine
[4]Kharkiv State Research and Forensic Science Center of the Ministry of Internal Affairs of Ukraine, Kharkiv, Ukraine

*E-mail of corresponding author: avtoap@ukr.net

Oleksandr Kravchenko 0000-0003-4677-2535,
Alexander Khrulev 0000-0002-6841-9225,
Juraj Gerlici 0000-0003-3928-0567,
Oleksii Saraiev 0000-0001-6582-560X,
Serhii Danets 0000-0003-4155-1856

Resume

The purpose of the study was to evaluate the effectiveness of using a simple reed valve model of an engine with periodic workflow. To achieve this purpose, models of the reed valve have been developed and determined that the quasi-stationary model allows one to find the air flow through the reed valve with an accuracy of 5-6%. The limits of permissible values, at which the model has a minimal error, correspond to Strouhal number of 0.2-0.3. This data confirmed that with proper consideration of the existing limitations, the quasi-stationary model gives results close to those provided by the complex dynamic models.

Article info

Received 17 July 2024
Accepted 30 September 2024
Online 13 November 2024

Keywords:

engine with periodic workflow
pulse jet engine
intake reed valve
modelling
quasi-stationary model
dynamic model

ISSN 1335-4205 (print version)
ISSN 2585-7878 (online version)

Available online: https://doi.org/10.26552/com.C.2025.006

1 Introduction.

A reed-type check valve is a fairly common design element that is used in the intake systems of some types of engines. The operating principle of a reed valve is quite simple. The petal is affected by the pressure drop between the inlet channel and the control volume (chamber). The vacuum in the chamber causes the petal to bend (lift) and open the inlet to allow air or the air/fuel mixture to pass through. When the pressure in the chamber subsequently increases, the valve closes, which stops the air supply and also prevents its reverse flow (ejection) from the chamber.

Despite its simple principle, the reed valve operates under dynamic loads that affect its performance. In addition, reed valves are known to be damaged by such loads. This raises the problem of mathematical modelling of the valve operation, including when creating mathematical models of engines.

Modelling a reed valve has its own characteristics, which is especially important when pairing (integrating) its model with the entire engine model. This requires solving the problem of correct selection and construction of a valve model. There is also the question of the dimensionality of the valve model if it is to be included in the overall engine cycle model, especially at the initial stage of its development.

2 Literature review and problem statement

Currently, the reed valve (Figure 1) is found as an element for controling the flow of working fluid in various machines and units. Thus, in 2-stroke spark-ignition gasoline engines, the reed valve controls the intake directly into the crank chamber [1], and numerous experimental [2] and theoretical studies [3] are dedicated to this process. Besides that, the reed valve provides the flow control in air compressors [4-6] and hydraulic units [7].

Valved pulse jet engines, which became widespread in the past [8], also incorporate similar types of reed

a b

c

***Figure 1** Reed valves: a - of a 2-stroke internal combustion engine (similar valves were used on full-size valved pulse jet engines), b - of a small-sized valved pulse jet engine, c - of an air compressor*

valves [9]. Unlike the compressors and 2-stroke engines, there are not too many studies on the reed valves for the pulse jet engines [10]. Known sources are often limited to technical data of valve mechanisms of various pulse jet engine models and experimental data [11]. However, research on reed valves has been carried out for a number of years in relation to pulse detonation engines [12].

The reed valve is a common modelling object, and a significant number of works are devoted to this topic [13-14]. When creating new engines and units, it is necessary to determine the parameters of elements and assemblies, including the reed valve, which determines the practical need for a detailed study of its operation. In this case, the greatest difficulties usually arise in ensuring the specified durability of the structure due to significant impact loads when the petal is seated on the support plate, as a result of which its fatigue cracking is observed (Figure 2a, b, c). At the same time, the most severe operating conditions arise when the reed valve is exposed to a high temperature of the working environment, which significantly accelerates destructive processes (Figure 2d).

It is obvious that these problems can be solved in general by simulating the valve operation under various conditions. In this case, it is advisable to use the valve model, not only to test the valve itself, but to study the cause of its destruction, as well. In addition, the development of a valve model is also of practical interest from the point of view of creating the engine model as a whole, in which the valve model is included as an integral part.

The simplest one is the so-called quasi-stationary or quasi-static model [7], in which the valve petal is assumed to be statically loaded, and dynamic processes are not taken into account. In such a model, obviously, the lift of the valve petal depends only on the instantaneous pressure drop across the valve.

As the frequency of forced oscillations increases, dynamic phenomena begin to influence the petal motion. This is, first of all, the rebound of the petal from the limiter and the valve plate [7]. In addition, the elastic line of the petal can bend [15], which can also affect the area opened by the reed valve and the air flow for a given drop. For these reasons, the vast majority of studies solve the dynamic problems of reed valve motion.

When studying a reed valve, it is customary to imagine it in the form of a beam (Figure 3a) with a fixed seal [5] and a distributed mass [4]. This model is used both in quasi-stationary [12] and dynamic formulations [7]. The hybrid models are also used, when the valve lift is calculated using one model, and the elastic line of the petal is determined using another [15]. At the same time, the simpler models also became widespread, for

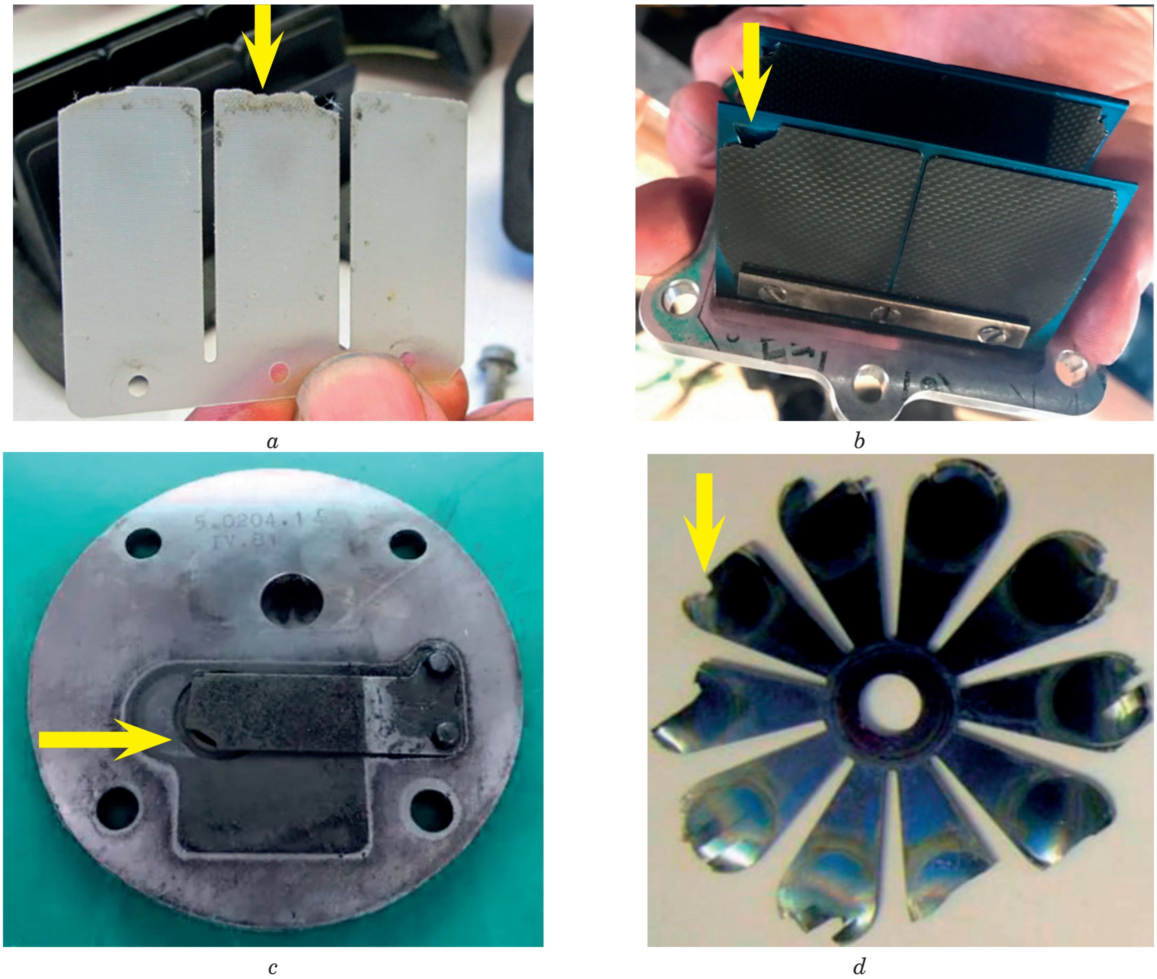

Figure 2 *The most common damage to petal valves in operation: fatigue cracking of petals in two-stroke gasoline engines with crank-chamber purging of cylinders (a - metal petals, b - plastic petals), in air compressors (c) and in pulse-jet engines (d - result of thermo-mechanical impact)*

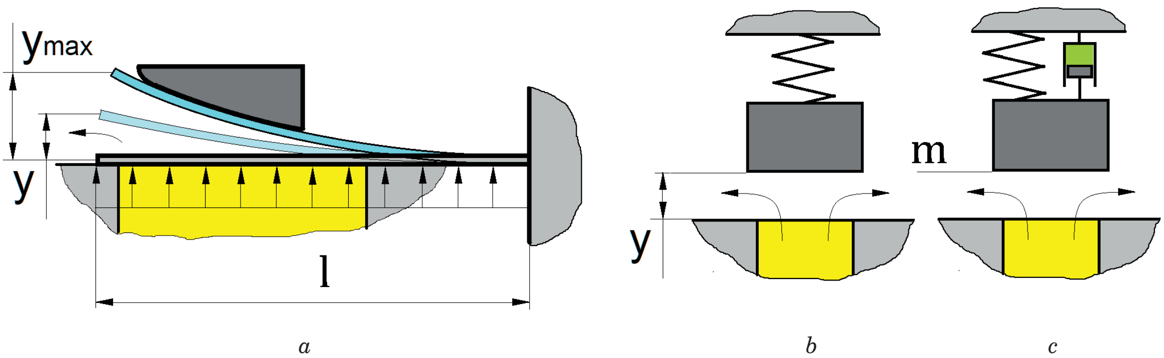

Figure 3 *Possible simplified representations of a reed valve as a beam with a fixed embedment (a) and as a spring-loaded mass (b), including damping (c)*

example, in the form of a spring-loaded mass (Figure 3b, c), including those with damping [7]. In this case, the reed valve can be shown either as a simple mass on an elastic spring [6, 13], or as the same mass on an elastic beam [16-17]. In the latter case, the movement of the petal can be described by equations not of the first or second [12], but of the fourth order, as well [15].

A special place in the reed valve research is occupied by modelling of gas-dynamic processes. It is necessary to calculate the air flow through the valve, since the air flow is then included in the general object model for calculating the parameters of the control volume (cylinder, combustion chamber). For this purpose, the 3D flow modelling has become widespread as the most accurate method [16]. At the same time, a 3-dimensional model of the reed valve itself is often created [14, 18].

However, despite the advances in the reed valve modelling, the complex representation of the reed valve in various models does not always correspond to the overall modelling task. For example, if a detailed study of the operating process of the reed valve itself is being carried out, a 3D model is indeed justified. However, often we are talking about a complete model of the object, which in many cases is thermodynamic, that is, 0-dimensional, and the channels adjacent to the control volume are modeled using 1-dimensional gas-dynamic models [19-20]. For such conditions, the use of complex 3-dimensional models is completely inconvenient, and in some cases, when it comes to developing and debugging the new object models and calculation programs, it is generally unacceptable.

At the same time, some simpler reed valve models have been made, including quasi-stationary ones, and those based on the representation of the petal in the form of a beam fixed at one end or a spring-loaded mass (Figure 3). However, that work was not always completed. In many cases, it is not entirely clear what the reliability of certain models is and where their acceptable areas of application are. It is also not completely clear which of the known reed valve models can be integrated into the overall object model, and how model error can affect the modelling results of the entire object.

3 The aim and objectives of the study

The purpose of this study was to justify the choice of a reed valve model to effectively describe its motion - both as a part of a general model of an engine with periodic workflow, and as a separate model to determine the causes of reed valve damage.

To achieve this goal, it seems appropriate to solve the following problems:

- analyze the operating cycle of an engine with periodic workflow, determine the pattern of the reed valve influence on it,
- select the parameter most suitable for subsequent comparative analysis of different reed valve models,
- consider in detail the quasi-static and dynamic models of the reed valve, create a calculation algorithm,
- perform modelling of the reed valve motion in different operating modes of the engine type under consideration and
- conduct a comparative analysis of the models' reliability and accuracy, determine the conditions for their most effective use when modelling processes in the engines with periodic workflow.

4 The study materials and methods

The object of the study was a reed valve of an engine with periodic workflow. An engine of this type has a control volume in the form of a cylinder or combustion chamber [20], with channels (pipes) of air intake and gas exhaust systems. The reed valve is a control element of the engine intake system (Figure 4). With a positive pressure drop between the volume and the environment, the valve takes a closed position. However, with a negative pressure drop, when pressure in the control volume falls down below the ambient pressure, the petal lifts and passes air from the environment into the control volume.

Determination of the air flow parameters in a reed valve, when modelling engines with periodic workflow, is possible by analytical solution and/or numerical integration of differential equations that describe this process. In a specific task, a numerical-analytical method was chosen, when, using simplifying assumptions, an analytical determination of the petal lift as a function of the pressure drop was first carried out, and then a numerical solution was performed for the differential equation of the petal motion over the process time. In this case, the numerical simulation method was used as a test method to evaluate the results obtained by the analytical method.

The initial data were approximate geometric dimensions, their relationships and characteristics of elements of engines with periodic workflow [8, 11, 20].

The main hypothesis in the analytical solution was the assumption that under certain conditions, determined by the frequency of the process, the petal motion and air flow on the valve can be considered as a quasi-stationary process [7]. To implement the numerical method, a number of additional simplifying assumptions were made. The derivation of the petal motion equations was carried out within the framework

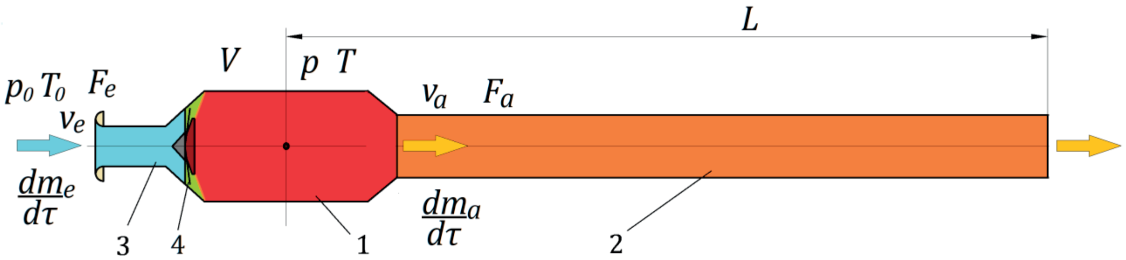

Figure 4 A simplified diagram of an engine with periodic workflow: 1 - control volume, 2 - resonant exhaust pipe, 3 - inlet pipe, 4 - check reed valve

of the analogy of the petal movement as a concentrated and spring-loaded mass. The concept also took into account the possible elastic dynamic rebound of the petal in extreme positions.

All the calculations and modelling were carried out in an Excel environment with the XLfit extension [20]. The software choice was due to the limited volume of calculations (no more than 400 time points per cycle), their test nature, and the lack of ready-made standard programs for solving the problem under consideration.

5 The results of studying the reed valve working process in the engine with periodic workflow

5.1 The reed valve effect on the operating cycle of an engine with periodic workflow

When solving the problem, it is important that the air flow through the inlet reed valve is associated with a thermodynamic model that describes the state of the gas in the control volume into which the air flows through the valve. The control volume V within the framework of a 0-dimensional theory [21-22] can always be described by a system of 2 differential equations of the 1st order for gas temperatureand pressure, which can be obtained from the equation of the first law of thermodynamics (energy) and the equation of state of an ideal gas in the form [23-24]:

$$\begin{cases} \dfrac{d\bar{T}}{d\bar{t}} = f_1\left(\bar{T}, \bar{p}, \dfrac{d\bar{m}}{d\bar{t}}, \dfrac{d\bar{Q}}{d\bar{t}}, V...\right) \\ \dfrac{d\bar{p}}{d\bar{t}} = f_2\left(\bar{T}, \bar{p}, \dfrac{d\bar{m}}{d\bar{t}}, \dfrac{d\bar{Q}}{d\bar{t}}, V...\right) \end{cases}, \tag{1}$$

where V is the volume, $\bar{T}$ is the temperature, $d\bar{m}/d\bar{t}$ is the mass flow of gas from or into the control volume (through the corresponding pipes), $d\bar{Q}/d\bar{t}$ is the rate of heat release in the volume.

The system of equations in Equation (1) includes the air flow rate into the volume under consideration or out of it. It directly depends on the pressure drop and the nature of the flow of air and gas at the inlet and outlet of the volume [20], including the characteristics of the reed valve. Therefore, the reed valve model must be a part of a 0-dimensional thermodynamic model of an engine with periodic workflow. Accordingly, not only the accuracy of engine modelling, but the ability to simulate self-oscillations and the stability of its operating cycle, as well, depend on the reed valve model.

It is obvious that the air flow rate is also the resulting (integral) parameter of the entire process of the air flow through the reed valve. In this case, both the instantaneous and the total air flow rate per cycle are equally important for the same given air parameters in front of the valve and valve geometry itself.

5.2 Determination of air flow rate through the reed valve

In general, the flow rate can be determined by the air parameters in the channel in front of the reed valve as:

$$\frac{d\bar{m}_e}{d\bar{t}} = \mu \bar{\rho}_e \bar{\upsilon}_e F_e \,, \tag{2}$$

where ρ_e is the air density and velocity in front of the valve; F_e is the cross-sectional area of the input channel; $\mu = 1/\sqrt{1+\xi_\Sigma}$ is a flow coefficient [25], which depends on the hydraulic resistance of the channel and reed valve (valve system) ξ_Σ [26].

When developing the models, equations written in dimensionless form were used. To do this, one should move on to dimensionless variables: pressure $p = \bar{p}/\bar{p}_o$, temperature $T = \bar{T}/\bar{T}_o$, velocity $\upsilon = \bar{\upsilon}/\bar{\upsilon}_o$, time $t = \bar{t}\bar{\alpha}_o/L$, coordinate $x = \bar{x}/L$, where $\bar{p}_o, \bar{T}_o$ are the ambient pressure and temperature, respectively; $\bar{\alpha}_o = \sqrt{\gamma_o \bar{R}_o \bar{T}_o}$ is the speed of sound in the environment; $\bar{R}$ is a gas constant; $\gamma_o = 1.4$ is the heat capacity ratio; L is the characteristic size of the engine (hereinafter, the overbar indicates dimensional values).

If one takes the length of the exhaust pipe L as the characteristic size of the engine, which determines the cyclic operation, then the cross-sectional area of the exhaust pipe F_a can be chosen as the characteristic area. In addition, if one does not take into account the dynamic pressure [27] at the inlet (in some types of engines with periodic workflow it is not present), then Equation (2) can be approximately written as follows:

$$\frac{dm_e}{dt} = \frac{1}{\sqrt{1+\xi_\Sigma}} \Phi p^{\frac{1}{k_o}} \sqrt{\frac{2}{\gamma_o - 1}\left(1 - p^{\frac{\gamma_o}{\gamma_o - 1}}\right)}, \tag{3}$$

where the dimensionless parameter is:

$$\Phi = \frac{F_e}{F_a} = \left(\frac{D_e}{D_a}\right)^2, \tag{4}$$

and D_e, D_a are the diameters of the input channel and the resonance pipe of an engine with a periodic workflow, respectively.

Obviously, to determine the flow rate, it is necessary to find the hydraulic resistance of the reed valve. In the absence of more accurate data, one can use the known dependencies for the hydraulic resistance coefficient on the valve lift value. Thus, for a poppet valve, there is an approximate formula [25]:

$$\xi_\Sigma = 0.55 + 4\left(\frac{b}{d} - 0.1\right) + \frac{0.155}{(\bar{y}/d)^2}, \tag{5}$$

where $\bar{y}$ is the lift of the valve petal, d is the characteristic diameter of the hole opened by the petal, b is the amount of overlap of the hole by the petal when completely closed (Figure 5).

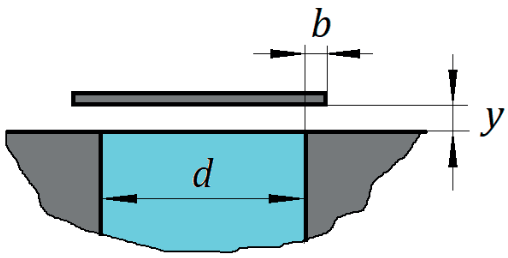

Figure 5 *The diagram of a poppet valve analogy, accepted for determining the hydraulic resistance coefficient of the reed valve*

5.3 Reed valve models of an engine with periodic workflow

The quasi-stationary reed valve model is obviously the simplest and assumes that the frequency of natural oscillations of the valve petal is many times greater than the frequency of forced oscillations corresponding to the engine process frequency. In this case, the inertia of the valve petal motion and, first of all, its delay when the pressure drop changes, can be neglected and the problem can be considered quasi-stationary.

Within the framework of the quasi-stationary model, the petal lifting height does not depend on its speed and acceleration, but is determined only by stationary parameters. These are the pressure drop Δp and the petal toughness. It means, that the petal can be considered as a beam with one-sided embedding and a load distributed along the length (Figure 2a). For such conditions, the petal lifting from the distributed load [28] can be written as:

$$\bar{y} = \frac{\bar{q}l^4}{8\bar{E}I_x}, \tag{6}$$

where $\bar{E}$ is the elastic modulus of the valve petal material; I_x is the moment of inertia of the section along the axis; l is the length of the valve petal.

Considering that $I_x = \delta^3 b/12$, where δ and b are the thickness and width of the valve petal, respectively, and $\bar{q} = \Delta\bar{p}l$, after substituting into Equation (6) and transformations, the formula was obtained:

$$y = \frac{\bar{y}}{l} = 1.5\frac{\Delta p}{S}, \tag{7}$$

where $\Delta p = \Delta\bar{p}/\bar{p}_o$ is the dimensionless pressure drop across the reed valve; $\bar{p}_o$ is the ambient pressure, and the dimensionless parameter Sactually determines the valve petal stiffness:

$$S = \frac{\bar{E}}{\bar{p}_o}\left(\frac{\delta}{l}\right)^3, \tag{8}$$

where $\bar{E}$ is the modulus of elasticity, δ is the thickness, l is the length.

Equation (7) establishes the desired dependence of the valve petal lift on the pressure drop.

To assess the applicability of the quasi-stationary model, it is necessary to know the natural frequency of the valve petal and, at a minimum, compare it with the forced frequency (the cycle frequency of an engine with periodic workflow).

The petal natural vibration frequency f, when it is fixed on one side, can be easily found using the formula given in [29]. Further, taking into account the environment speed of sound and the fact that the pressure $\bar{p}_o$ and temperature $\bar{T}_o$ are related by the equation of state of an ideal gas $\bar{p}_o = \bar{\rho}_o\bar{R}_o\bar{T}_o$, the valve petal natural frequency was obtained in the following final form:

$$\bar{f} = \frac{1}{\bar{\tau}} = 0.1615\frac{\bar{\alpha}_o}{\sqrt{l\delta}}\sqrt{\frac{S}{\gamma_o\rho_m}}, \tag{9}$$

where $\rho_m = \bar{\rho}_m/\bar{\rho}_o$ dimensionless density of the material.

A preliminary analysis of Equation (9), taking into account stiffness in Equation (8), shows that the frequency of natural vibrations is proportional to the stiffness and inversely proportional to the density of the valve petal material. As an example, one can consider a steel valve petal with the following parameters: thickness 0.25 mm, length 25 mm, from which, with an elastic modulus of $2 \cdot 10^{11}$ Pa, from Equations (8) and (9), one can obtain a frequency $\bar{f} = 327$ Hz.

Within the framework of the dimensionless time $t = \bar{t}\alpha_o/L$, adopted above, the dimensionless frequency (equal to the Strouhal number of the process under study [30]) is the inverse of time and amounts to $f = \bar{f}L/\bar{\alpha}_o$. Based on this, it is possible to roughly determine the limitation on the use of a quasi-stationary model depending on the size factor. For example, with a process frequency of 150 Hz and a characteristic length L = 0.8 m, the Strouhal number will be approximately 0.30-0.35. At the same time, the dimensionless natural vibration frequency of the valve petal is two or more times higher.

To determine the scope of application of a quasi-stationary model of a specific reed valve as a part of a general engine model, it is necessary to understand what processes such a model does not take into account, and how this affects to the air flow rate through the valve. To do this, it is necessary to compare the simulation result to what is given by more realistic models that take into account the dynamics of the valve petal motion.

In general, the valve petal can be represented as a beam with one side fixed. The motion of such a beam can be described by a fourth order partial differential equation [4, 13]:

$$\frac{\partial^2}{\partial \bar{x}^2}\left(\bar{E}I_x \frac{\partial^2 \bar{y}}{\partial \bar{t}^2}\right) + m_x \frac{\partial^2 \bar{y}}{\partial \bar{t}^2} = q(\bar{x}, \bar{t}), \tag{10}$$

where m_x, $q(x, t)$ are the distributed mass of the element and the load on the beam, -is the longitudinal coordinate, is the vertical coordinate (lift), $\bar{t}$ is the time.

Equation (10) in the general case allows one to calculate the instantaneous shape of the beam elastic line. However, within the framework of the above-adopted shown of the valve in the form of a spring-loaded and concentrated mass (Figure 3), the equation of Newton's second law is usually used, which determines the acceleration of the valve petal as the second derivative of its lift with respect to time [6, 17, 31]

$$m\frac{d^2\bar{y}}{d\bar{t}^2} = \Sigma \bar{F}_i, \tag{11}$$

where m is the mass of the valve petal; $\bar{F}$ is force acting on the valve petal; $\bar{y}$ is the vertical coordinate (lift); $\bar{t}$ is the time.

Let the Equation (11) be written in the dimensionless form, simultaneously reducing its order. To do this, it is possible to replace the 2nd derivative of the petal lift with the 1st derivative of its velocity (acceleration). Then, this equation with the equation for the petal velocity, as the 1st derivative of its lift, with consideration of rebound [32], forms a system of 1st order differential equations for the petal lift and velocity:

$$\begin{cases} \theta \dfrac{du}{dt} = -\dfrac{2}{3}Sy + \Delta p \\ \lambda \dfrac{dy}{dt} = u \end{cases}, \tag{12}$$

where $\theta = \gamma_o \rho_M \lambda\left(\frac{\delta}{l}\right)$ is a dynamic coefficient; $\rho_M = \bar{\rho}_M/\bar{\rho}_o$ is a dimensionless density of the valve blade material; $\lambda = l/L$ is a relative length of the valve petal.

To solve the problem, some engines with a periodic workflow were analyzed [33] and the necessary geometric characteristics were selected, including the length and diameter of the resonance exhaust pipe L = 0.80 m, D_a = 0.04 m, the diameter of the inlet pipe D_a = 0.035 m, as well as the dimensions of the petal valve $\delta = 0.00025$ m, l = 0.025 m, b = 0.012 m, y_{max} = 0.2 (a block of 10 valves located around a circle was considered).The operation of an engine was modeled by specifying the law of gas pressure change in the control volume. For this, the shape of the pressure oscillations (sinusoid), their amplitude $(\Delta p = 0.3)$ and frequency $(f = Sh = 0.1 - 0.7)$ were specified.

6 Results and discussion

6.1 Results of mathematical modelling of valve the petal motion

The calculation results show that the petal motion within the dynamic model (Figure 6a) differs significantly from what is given by the quasi-stationary model (Figure 6b). The main difference is the petal rebound from the stop plate and from the valve plate, when the petal position is determined by its inertia, and not just by the pressure drop, as in the quasi-steady model.

However, comparison of models in terms of the air flow rate under these conditions (Figure 7b) did not give a significant difference. Even with the reverse air flow presence, the difference was only 6 % (the dynamic model corrects the air flow rate downward compared to the quasi-stationary one). Such results indicated the need to study the valve petal when operating at other possible frequencies.

The first thing that was revealed, with an increase in the frequency of the engine's operating process, was an increasing dynamic lag in the petal motion when it opens and closes (Figure 8). The influence of the frequency of natural oscillations of the petal in Equation (9) is clearly visible - with an increase in the frequency

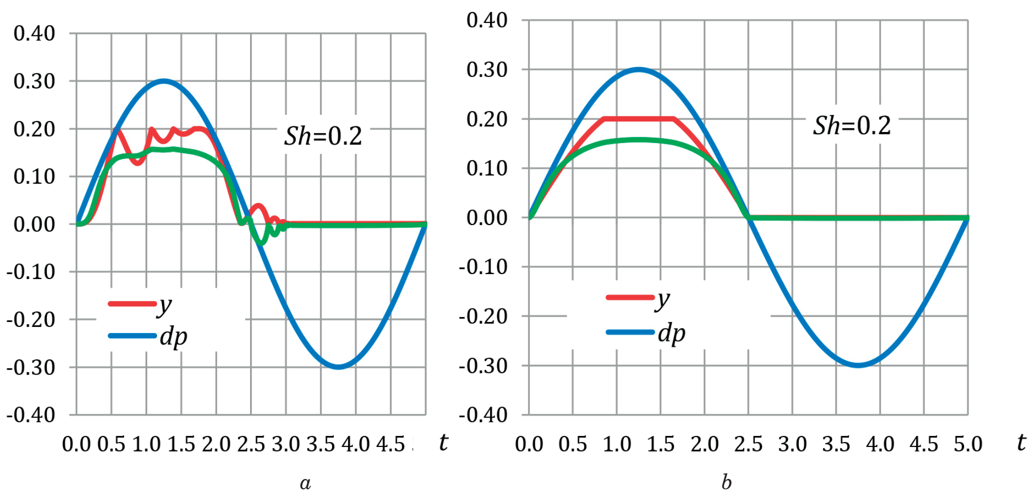

Figure 6 *Difference in petal motion calculated by: a - dynamic model; b-quasi-stationary model*

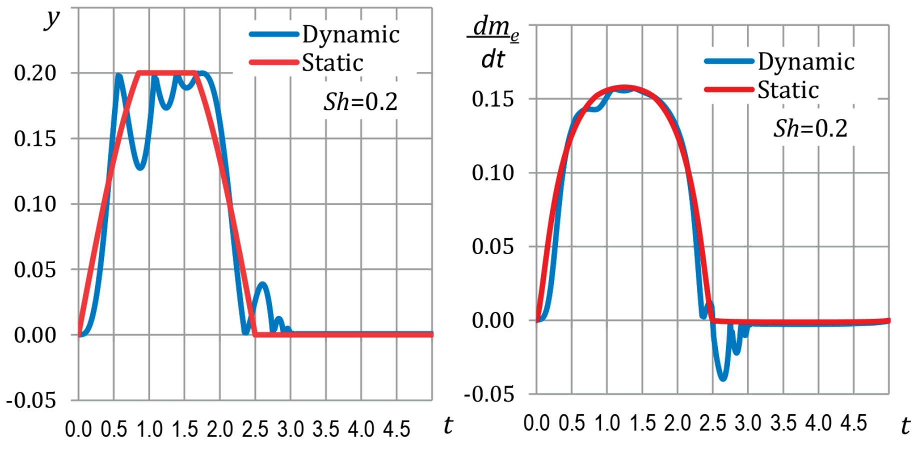

a *b*

Figure 7 *Comparison of instantaneous parameters calculated using the quasi-stationary and dynamic models: a - valve petal lift; b - air flow rate through the reed valve*

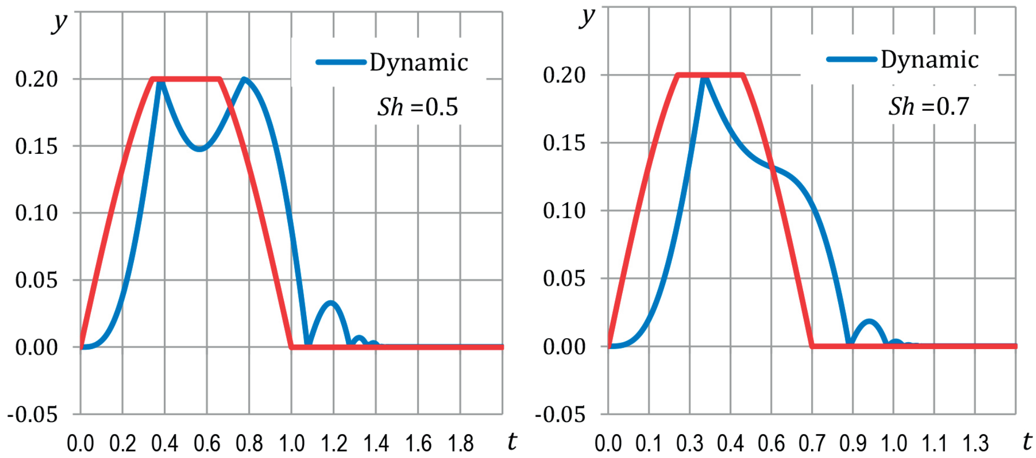

a *b*

Figure 8 *Valve petal lift profile at high frequencies: a - Sh =0.5; b - Sh =0.7*

of forced oscillations, the number of complete oscillations of the valve petal near the extreme positions decreases.

At the same time, a significant change in the valve petal velocity profile occurs (Figure 9a). Moreover, a noticeable increase in the petal motion velocity, when rebounding from the valve and stop plates (Figure 10a), causes intense petal vibrations.

Obviously, this can lead to a decrease in the durability of the valve petal due to the fatigue cracking mentioned above (Figure 2). It is not yet possible to draw unambiguous conclusions based on the valve petal speed alone and, moreover, to obtain any specific figures for its durability without additional research. This is due, among other things, to the influence of the number of impacts during the petal rebound, which may be greater at lower frequencies. However, in any case, the impact speed will be the parameter that determines the durability of the reed valve.

The process of the valve petal lag with increasing frequency of forced oscillations has also a significant effect on the air flow rate (Figure 9b). At a low frequency of the process the flow rate curve over the cycle is close to quasi-stationary, and the difference is made only by the oscillations of the valve petal at the extreme points. At a high frequency the picture is fundamentally different.

Indeed, with increasing frequency of forced oscillations, the difference grows rapidly (Figure 10b). In addition, with increasing frequency, the phase shift of the valve petal lift and air flow rate curves to the late side increases. At small values of the Strouhal number, rather intense oscillations of the valve petal are excited not only during the rebound, but during lifting (Figure 9a), as well, which also causes an increase in the difference in air flow rate (Figure 10b). However, at low frequencies, the result may be affected by the instability of the calculation, as well as the need to clarify the coefficient of recovery for specific structures.

6.2 Comparative analysis of the accuracy and reliability of the models

The modelling results indicate that the Strouhal number can be used to evaluate the range of

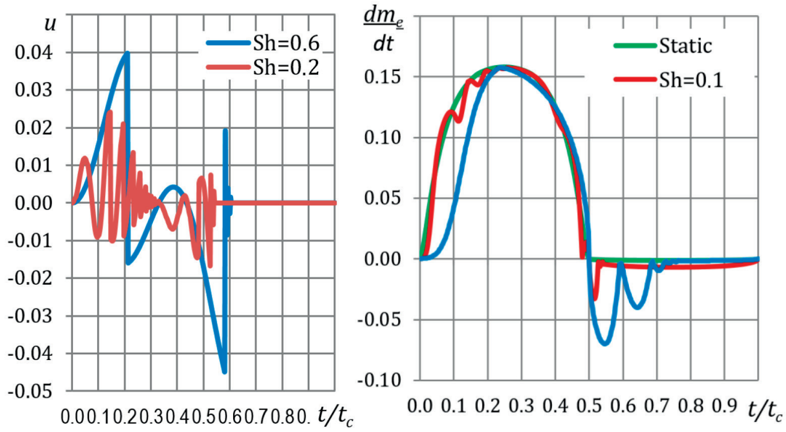

a b

Figure 9 *Changes in parameters over the cycle with increasing frequency of the process: a - valve petal speed profile; b - air flow rate profile*

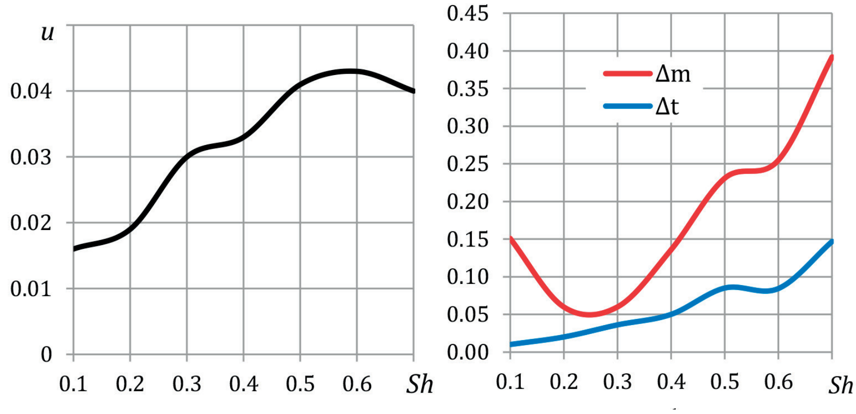

a b

Figure 10 *The resulting curves of parameters depending on the frequency of the process (Strouhal number): a - the speed of the valve petal at the moment of impact on the valve block; b - error of the quasi-stationary model in terms of air flow rate and oscillation phase*

Table 1 *Basic parameters of known pulse jet engines [34, 35]*

Engine model	Argus As 014[34]	Solar PJ32[35]	Tiger-jet M1[33]	Dyna-jet [33]
Resonant tube length, m*	2.60	1.50	0.406	0.430
Operating frequency, Hz	45	85	250	220
Strouhal number	0.33	0.32	0.30	0.28

*the length of the pipe includes the length of the transition part between the control volumeanda pipe.

applicability of a particular reed valve model. This is especially noticeable when comparing the models under consideration. For example, when the Sh value is above 0.40-0.50 (high frequency of the process), there is a significant discrepancy between the models in air flow rate, which reaches 25% or more with the same law of change in pressure drop and other parameters. The situation is not much better when the Sh value is below 0.10-0.15 (low process frequency), when the discrepancy in flow rate reaches 15%. Overall, this data indicates excessively high errors in the quasi-static model, which significantly overestimates air flow rate compared to the more realistic dynamic model.

However, in the range of Strouhal numbers Sh = 0.20-0.30 (average frequency), on the contrary, there is a satisfactory agreement between the models for air flow rate, with an accuracy of no worse than 5-6%. If one compares this result with the operating frequencies of known types of engines with a periodic workflow, one can note that for valved pulse-jet engines of different sizes (Table 1), the Strouhal number corresponding to the operating frequency falls within the specified range, grouping near the value Sh = 0.30.

For other types of engines, evaluation of methods using the Strouhal number is applicable, as well.

Thus, in known designs of 2-stroke gasoline internal combustion engines with crank-chamber purging of the cylinders [1, 3], the Strouhal number for the reed valve is close to those indicated in Table 1 at maximum mode. Accordingly, as the crankshaft rotation speed decreases, the operating point on the curve (Figure 10b) will shift towards decreasing the error of the quasy-stationary method, with the exception, possibly, of only the lowest rotation frequencies. A similar picture is observed in piston compressors, where the operating point, corresponding to the operating speed, is usually located in the same part of the diagram (Figure 10b).

7 Conclusion

A simple quasi-stationary model of the intake reed valve of an engine with periodic workflow, designed to close 0-dimensional thermodynamic models of the full cycle, and an alternative dynamic model for mathematical modelling of the valve reed motion, are considered.

Based on the data obtained, a comparative analysis of the accuracy and reliability of the quasi-stationary and dynamic models of the reed valve was carried out. It has been established that the quasi-stationary model makes it possible to find the air flow rate through the reed valve with an accuracy of 5-6% for a pressure drop varying according to a sinusoidal law, if the frequency and/or the Strouhal number do not exceed the range of permissible values. The permissible limits for changes in the frequency of forced oscillations, corresponding to the Strouhal number of 0.20-0.30, in which the quasi-stationary model has a minimal error compared to the dynamic model, are found.

The data obtained confirms that, with proper consideration of the existing limitations, the quasi-stationary model gives results close to those provided by more complex dynamic models, including those with a higher dimension. This indicates the possibility of using a quasi-stationary model for elements such as reed valves as an approximate alternative to more complex dynamic models, which is especially important when creating and preliminary debugging of 0-dimensional thermodynamic models of engines with periodic workflow.

Acknowledgements

The authors like to express their gratitude to the AB-Engineering Mechanical Processing Center, Odesa, and the International Motor Bureau, Nemishaeve, Kyiv oblast, Ukraine, for technical support, including for providing materials and technical data of different engines, as well as for help in the research.

Funded by the EU NextGenerationEU through the Recovery and Resilience Plan for Slovakia under the project No. 09I03-03-V01-00129.

Conflicts of interest

The authors declare that they have no known competing financial interests or personal relationships that could have appeared to influence the work reported in this paper.

References

[1] BLAIR, G.P. *The basic design of two-stroke engines*. Warrendale: Society of Automotive Engineers, Inc., 1993. ISBN 1-56091-008-9.

[2] HAMASAKI, K., TANAKA, Y. Effect of reed valve configuration on the charging characteristics of a crankcase-compressed two-stroke engine. Kagoshima University Repository Content. 1991, 33, p. 13-22.

[3] WESTOFF, P., SERVIAS, J., ROWINSKI, D. Evinrude two-stroke reed FSI modelling and validation. Presentation [online] [accessed 2023-10-19]. Available from: https://convergecfd.com/resources/reedFSIv3_distCVG.pdf

[4] KNUTSON, A.L. Modelling and experimental validation of disc and reed style check valves for hydraulic applications [online]. Thesis. University of Minnesota, 2016. Available from: https://hdl.handle.net/11299/185082

[5] FORNITZ, K. H. Numerical modelling of a suction reed valve from a reciprocating compressor using fluid structure interaction. Master's thesis. PECT10-2-F18. Esbjerg: Aalborg University, 2018.

[6] HOPFGARTNER, J., ALMBAUER, R., EGGER, A., ZUBER, B., LANG, M. Investigation of force-assisted suction reed valves in hermetic reciprocating compressors. *Proceedings of the Institution of Mechanical Engineers, Part E: Journal of Process Mechanical Engineering*[online]. 2022, **236**(1), p. 26-35. ISSN 0954-4089, eISSN 2041-3009. Available from: https://doi.org/10.1177/0954408918818739

[7] CHAUDHURI, A. Static and dynamic deformations of a reed valve immersed in hydraulic fluid. In: 2014 COMSOL Conference: proceedings. 2014.

[8] TORDA, P., VILLALBA, I. P., BRICK, J. H. Project SQUID. Technical report NO. 9. New York: Polytechnic Institute of Brooklyn, 1948.

[9] TORDA, P. Compressible flow through reed valves for pulse jet engines. ProQuest dissertations and theses. New York: Polytechnic Institute of Brooklyn, 1949.

[10] TAO, G., PAXSON, D.E., ZHENG, F., KUZNETSOV, A.V., ROBERTS, W. L. Comparison between numerically simulated and experimentally pulsejet. In: 44th Joint Propulsion Conference and Exhibit cosponsored by AIAA, ASME, SAE, and ASEE: proceedings. 2008.
[11] SIMPSON, B. The enthusiast's guide to pulsejet engines [online]. 2. revision. 2004. Available from: https://www.academia.edu/28974608/Pjbookrev2a
[12] FUKUNARI, M., YAMAGUCHI, T., KOMURASAKI, K., ODA, Y., IKEDA, R., KAJIWARA, K., TAKAHASHI, K., SAKAMOTO, K. Air-breathing system using reed valve for pulse detonation microwave rocket. *Transactions of the Japan Society for Aeronautical and Space Sciences, Aerospace Technology Japan*[online]. 2016,**14**, p. 1-7. eISSN 1884-0485. Available from: https://doi.org/10.2322/tastj.14.1
[13] LEMOINE, B., LE MARREC, L., HIRSCHBERG, A. Modelling pressure cycle and interaction with reed valves in a reciprocating compressor. In: VI International Conference on Computational Methods for Coupled Problems in Science and Engineering: proceedings. 2015.
[14] WANG, Y., WANG, J., HE, Z., SUN, J., WANG, T., LIU, CH. Investigation on dynamic characteristics of the reed valve in compressors based on fluid-structure interaction method. *Applied Sciences* [online]. 2021, **11**, 3946. eISSN 2076-3417. Available from: https://doi.org/10.3390/app11093946
[15] OOI, K. T., CHAI, G. B., KWEK, E. C. A Simple valve model to study the performance of a small compressor. In: International Compressor Engineering Conference: proceedings [online]. 1992. Paper 803. p. 147-155. Available from: https://docs.lib.purdue.edu/icec
[16] GONZALEZ, I., NASERI, A., RIGOLA, J., PEREZ-SEGARRA, C.D., OLIVA, A. A fluid-structure interaction solver for the fluid flow through reed type valves. *IOP Conference Series: Materials Science and Engineering* [online].2017, **232**, 012032. ISSN 1757-899X. Available from: https://doi.org/10.1088/1757-899X/232/1/012032
[17] SARAF, A.H., KULKARNI, R. K., SHAH, J., UTSAV, V. Mathematical modelling of reed valve lift with crank angle in piston compressors. *Journal of Emerging Technologies and Innovative Research (JETIR)*. 2020, **7**(8). p. 2253-2257. ISSN 2349-5162.
[18] CUNNINGHAM, G., KEE, R. J., KENNY, R. G. Reed valve modelling in a computational fluid dynamics simulation of the two-stroke engine. *Proceedings of the Institution of Mechanical Engineers, Part D Journal of Automobile Engineering*[online]. 1999,**213**(1), p. 37-45. ISSN 0954-4070, eISSN 2041-2991. Available from: https://doi.org/10.1243/09544079915266
[19] KHRULEV, A., SARAIEVA, I., VOROBIOV, O., SOKHIN, A. Evaluation of the possibility of using mathematical models for expert research of car engine damage. *Vehicle and Electronics. Innovative Technologies* [online]. 2022, **21**, p. 79-86. eISSN 2226-9266. Available from: https://doi.org/10.30977/VEIT.2022.21.0.06
[20] KHRULEV, A. Determination of gas parameters in resonant pipes and channels of engines with a periodic workflow using the piston analogy method. *Eastern-European Journal of Enterprise Technologies*[online]. 2023,**5/7**(125), p. 50-59. ISSN 1729-3774, eISSN 1729-4061. Available from: https://doi.org/10.15587/1729-4061.2023.288520
[21] KALIKATZARAKISA, M., CORADDUA, A., THEOTOKATOSA, G., ONETO, L. Development of a zero-dimensional model and application on a medium-speed marine four-stoke diesel engine. In: 3rd International Conference on Modelling and Optimisation of Ship Energy Systems MOSES2019: proceedings. 2021.
[22] KHRULEV, A., DMITRIEV, S. Study of the conrod deformation during piston interaction with liquid in the internal combustion engine cylinder. *Journal of Mechanical Engineering and Sciences* [online]. 2019,**14**(2), p. 6557-6569. ISSN 2289-4659, eISSN 2231-8330. Available from: https://doi.org/10.15282/jmes.14.2.2020.03.0515
[23] KHRULEV, A. Analysis of pneumatic catapult launch system parameters, taking into account engine and UAV characteristics. *Advanced UAV* [online]. 2023,**3**(1), p. 10-24. eISSN 2822-6976. Available from: https://publish.mersin.edu.tr/index.php/uav/article/view/1045
[24] KHRULEV, A., SARAEV, O. Building a mathematical model of the destruction of a connecting rod-piston group in the car engine at hydraulic lock. *Eastern-European Journal of Enterprise Technologies*[online]. 2022, **3/7**(117), p. 40-49. ISSN 1729-3774, eISSN 1729-4061. Available from: https://doi.org/10.15587/1729-4061.2022.259454
[25] IDELCHIK, I. E. *Handbook of hydraulic resistance. Coefficients of local resistance and of friction*. New York: Israel Program for Scientific Translations Ltd., 1966.
[26] ZHANG. Z. *Hydraulic transients and computations*. 1. ed. Berlin: Springer, 2020. ISBN 978-3030402327.
[27] ZUCHER, R.D., BIBLARZ, O. *Fundamentals of gas dynamics*. 3. ed. John Wiley and Sons, 2020. ISBN 978-1-119-48170-6.
[28] JINDAL, U.C. *Strength of materials*. Delhi: Umesh Publications, 1989. ISBN 9789332501232.
[29] TIMOSHENKO, S. *Vibration problems in engineering*. Van Nostrand Company Inc., 2008.
[30] MOUSSOU, P., TESTUD, P., AUREGAN, Y., HIRSCHBERG, A. An acoustic criterion for the whistling of orifices in pipes. Draft PVP2007-726157. In: ASME 2007 Pressure Vessels and Piping Conference: proceedings [online]. Vol. 4. 2007. ISBN 0-7918-4282-7, p. 345-353. Available from: https://doi.org/10.1115/PVP2007-26157

[31] MU, G., WANG, F., MI, X. Modelling of the reed valves in reciprocating compressors and investigation of their dynamics characteristics. *Journal of Engineering Research*[online].2019,**7**(4), p. 343-357. ISSN 2307-1877, eISSN 2307-1885. Available from: https://kuwaitjournals.org/jer/index.php/JER/article/view/3119
[32] HASHEMNIA, K. Experimental study of the effect of temperature on the coefficient of restitution of steel balls impact to some industrial metal sheets at elevated temperatures. *Powder Technology*[online].2020, **368**, p. 170-177. ISSN 0032-5910, eISSN 1873-328X. Available from: https://doi.org/10.1016/j.powtec.2020.04.053
[33] AHMADIAN, S. Computational approach in sizing of pulsejet engine[online]. 2014. Available from: https://www.researchgate.net/publication/284511823_Computational_Approach_in_Sizing_of_Pulsejet_Engine
[34] ANAND, V., JODELE, J., ZAHN, A., GELLER, A., PRISELL, E., LYRSELL, O., GUTMARK, E. Revisiting the Argus pulsejet engine of V-1 buzz bombs: an experimental investigation of the first mass-produced pressure gain combustion device. *Experimental Thermal and Fluid Science*[online]. 2019, **109**, 109910. ISSN 0894-1777, eISSN 1879-2286. Available from: https://doi.org/10.1016/j.expthermflusci.2019.109910
[35] LITKE, P.J., SCHAUER, F. R., PAXSON, D.E., BRADLEY, R.P., HOKE, J. L. Assessment of the performance of a pulsejet and comparison with a pulsed-detonation engine. In: 43rd AIAA Aerospace Sciences Meeting and Exhibit: proceedings[online]. 2005. Available from: https://doi.org/10.2514/6.2005-228

Appendix

Table A *Nomenclature*

Symbol	Definition
L	length, m
F	area, m^2
V	volume, m^3
l	length, m
b	width, m
δ	thickness, m
$\bar{E}$	modulus of elasticity, Pa (N/m^2)
I_x	moment of inertia, m^4
$\bar{v}$	air velocity, m/s
M	Mach number
γ	heat capacity ratio
R	gas constant, J/kg.K
$\bar{p}$	pressure, Pa
$\bar{T}$	temperature, K
$\bar{\rho}$	density of gas (air), kg/m^3
$\bar{t}$	time, s
$\Delta \bar{t}$	step in time, s
$\bar{x}$	longitudinal coordinate, m
$\bar{y}$	vertical coordinate (lift), m
$\bar{u}$	speed of movement of the valve petal, m/s
$\bar{a}$	speed of sound, m/s
ξ	coefficient of hydraulic resistance
μ	flow coefficient
f	process frequency, s^{-1}
Sh	Strouhal number
$\bar{m}$	mass, kg
$\bar{Q}$	amount of heat, W

The overbar over gas parameters indicates the dimensional values.

EFFECTS OF MOVEMENT DIRECTION THROUGH A SWITCH ON ACCELERATIONS AND NATURAL FREQUENCIES OF A PNEUMATIC SUSPENSION OF HIGH-SPEED ROLLING STOCK

Andrii Kuzyshyn[1,*], **Vitalii Kovalchuk**[1], **Yuriy Royko**[2]

[1]Department of Railway Transport, Lviv Polytechnic National University, Lviv, Ukraine
[2]Department of Transport Technologies, Lviv Polytechnic National University, Lviv, Ukraine

*E-mail of corresponding author: andrii.y.kuzyshyn@lpnu.ua

Andrii Kuzyshyn 0000-0002-3012-5395, Vitalii Kovalchuk 0000-0003-4350-1756,
Yuriy Royko 0000-0003-0055-9413

Resume

The research object is a pneumatic spring of the second stage of spring suspension of the high-speed railway rolling stock in movement conditions by a switch. Full-scale dynamic tests of a pneumatic spring for the high-speed railroad rolling stock were carried out. It was found that the average values of vertical accelerations in the trailing and facing directions in the wind turbines moving by the switch are 1.307 m·s^{-2} and 1.279 m·s^{-2}, respectively. The ratio of the average values of longitudinal accelerations in the trailing and facing directions within the wind turbines is 1.01, and at the wind turbine bases is 2.15. It is found that the average value of the first natural frequency of oscillations of the pneumatic spring is 3.53 Hz, while the logarithmic decrement of the oscillation attenuation is 0.321.

Available online: https://doi.org/10.26552/com.C.2025.007

Article info
Received 22 July 2024
Accepted 14 October 2024
Online 6 November 2024

Keywords:
rolling stock
pneumatic spring
switch
acceleration
frequency
logarithmic decrement

ISSN 1335-4205 (print version)
ISSN 2585-7878 (online version)

1 Introduction

One of the reasons for the increase in the level of vibrations of the structural elements components of rolling stock, the force of the wheelset‘s interaction with the rail track, is the movement of the rolling stock by the switch (Figure 1) [1]. It should be emphasized that the influence of the switch on dynamic indicators and rolling stock safety indicators is usually more sensitive at increased traffic speeds [2-3].

The design feature of the mechanical part of the diesel trains DPKr-2 and DPKr-3 and the electric train EKr-1 “Tarpan” is the use of a pneumatic spring suspension system in the second stage of the spring suspension. The specified spring suspension system consists of a pneumatic spring, an additional tank, a connecting pipeline and other structural elements [5].

The design of the pneumatic spring (Figure 2) allows the use of a rubber cord shell to improve the vibration protection properties of the rolling stock and the comfort of passenger transportation.

One of the conditions for the high-quality rolling stock operation is assessing its vibration-proof properties. These include, first of all, the frequency characteristics of individual components of the mechanical part of the rolling stock, in particular, the pneumatic spring (Figure 2).

A significant disturbing factor in the interaction of the rolling stock with the railroad track is a switch. Therefore, it is important and relevant to establish the frequency characteristics of the pneumatic spring of the high-speed rolling stock in the movement conditions by the switch. From a practical point of view, this would make it possible to control the dynamic characteristics of the rubber cord shell of the pneumatic spring and detect their deviations during the rolling stock operation.

2 Analysis of literature data and problem statement

Both theoretical and experimental methods are used to study the dynamic operation of a high-speed rolling stock pneumatic spring. Theoretical methods are

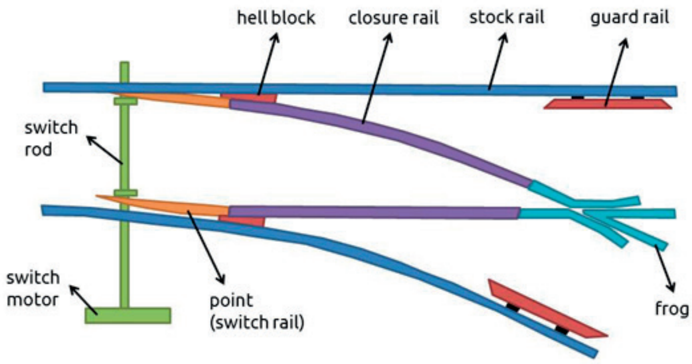

Figure 1 *Structural elements of the switch [4]*

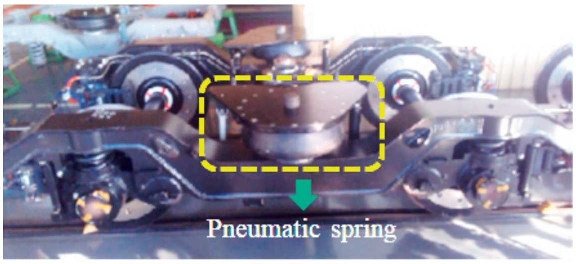

Figure 2 *Structural installation of a pneumatic spring for the high-speed railway rolling stock*

mainly based on mathematical models and specialized software. The main mathematical models describing the dynamic behaviour of a pneumatic spring are mechanical, thermodynamic, and finite element models.

Authors of [6] presented a nonlinear thermodynamic model of an air spring, which is a combination of two different models: the Berg model [7] and the Haupt and Sedlan model [8], which allows taking into account the elastic and viscoelastic parameters of the rubber cord shell of an air spring. To verify the adequacy of the proposed model, the authors conducted tests, where it was found that the maximum body vibrations at a speed of 80 km·h^{-1} occur in the frequency range of 1.5-3 Hz. Subsequently, by selecting the appropriate parameters of the structural elements of the pneumatic spring suspension system, the Sperling ride comfort index was investigated [9]. However, the authors did not take into account the effect of the switching gear on the dynamic behavior of the pneumatic spring.

In [10], the authors considered the classical and dynamic models of a pneumatic spring based on the MATLAB/Simulink software package. It was established that the pneumatic springs, in the second stage of the spring suspension, in the equation with elastic-damping elements, reduce the acceleration and displacement of the body by 27 % and 10 %, respectively.

Paper [11] presents a study of driving comfort by assessing accelerations in the body, which shows the difficulties in choosing the optimal damping coefficient of the secondary suspension. Using a valve with a variable orifice in the connection between the pneumatic spring and the additional reservoir is proposed.

In [12], the authors experimented in the laboratory to determine the quasi-static and dynamic behaviour of a pneumatic spring suspension system.

The effect of the volume of the additional reservoir, and the length and diameter of the connecting pipeline on the characteristics of the pneumatic spring suspension system was investigated in [13].

A series of experiments was conducted in [14] to determine the vertical stiffness of a pneumatic spring.

In [15], a nonlinear model of the air suspension system was developed to take into account the influence of nonlinear flow characteristics of altitude control valves and the pressure drop. Experimental studies have shown the importance of such consideration when assessing the safety of the rolling stock at low speeds in a curved section of a small-radius railway track. In addition, the influence of the lever angle of the pneumatic spring height adjustment valve on the wheel load imbalance during the passage of curved sections of a small-radius track is studied in [16].

In [17], based on experimental studies, the authors developed an analytical model of the operation of a pneumatic spring suspension system. It is established that the dimensions of the connecting pipeline, additional tank and pneumatic spring are the most important design parameters to determine the behaviour of the pneumatic spring suspension system. In the tests, the authors determined the vertical stiffness, reaction of the spring-loaded mass, and damping of the pneumatic system.

In [18], the authors conducted two groups of experiments: quasi-static and dynamic. That made it possible to study the force-displacement hysteresis loop and the damping effect of the rubber cord shell of a pneumatic spring.

In [19], the stiffness of a pneumatic spring in the vertical and horizontal directions was experimentally studied. In the modelling process, the movement of rolling stock in a straight and curved section of a railway track was considered.

In [20], the authors performed dynamic tests of the transverse stiffness of a pneumatic spring. It is established that the lateral stiffness of the pneumatic spring increases with increasing internal pressure and decreases with increasing disturbance amplitude.

It should be noted that the interaction of the rolling stock wheelset with the rail track, when moving by a switch, compared to moving on a straight and curved section of the railroad track, is special, which causes additional dynamic loads on the rolling stock. Namely, studies [21-22] found that the magnitude of dynamic impact loads depends on the speed and geometry of the switch, as well as the stiffness of the track [23-24]. To study the effect of the switch stiffness on the force interaction of the "rolling stock-switch" system, numerical calculation models were developed in [25-26].

To determine the vertical and horizontal transverse forces of interaction, the authors in [27] conducted complex experimental studies using a strain gauge wheelset. In [28-29], it was found that an increase in the speed of movement leads to an increase in the horizontal transverse force in both trailing and facing directions of the switch. The direction of movement of the switch has no significant effect on the vertical force.

In addition, as a result of the force interaction, significant vibrations of the rolling stock-switch system occur. The study of the rolling stock dynamic behaviour, and establishment of the resonance phenomenon in the movement conditions by a switch of rolling stock, are given in [30].

Taking into account the influence of changes in the rail profile and its local flexibility on the force interaction of the switch with rolling stock is given in [31]. In [32], the nature of changes in the equivalent taper of the wheel and rail in the switch zone, depending on the change in the wheel profile, was studied. In addition, the influence of the wheel profile and the coefficient of friction on the magnitude of contact forces and stresses is studied in [33]. The study of three-dimensional contact geometry, which takes into account the combined influence of different rail profiles and the angle of deviation in the direction of the rolling stock movement, is presented in [34].

The influence of the technical condition of the switch elements and undercarriage of the rolling stock on the power interaction „rolling stock - track" was studied in [35-36]. In addition, in [37], it was found that the dynamic interaction of the rolling stock and the switch leads to the accumulation of stresses on the rolling surface of the crosspiece. This further affects the formation of defects that cause additional dynamic of forces.

In works [38-40] the influence of the railway track ballast disorder on the increase of dynamic load on the rolling stock is studied. In addition, in works [41-43] the authors investigated the issues of wear of the cores of switches. It was found that the amount of core wear affects the level of dynamic interaction between the rolling stock and the crossing.

The analysis of research works shows that the main attention is paid to determining the forces of interaction, on the value of which the dynamic performance of the rolling stock and traffic safety indicators depend. However, increasing the speed of the rolling stock suggests the need to study its vibration-proof properties, based on determining the vertical and horizontal accelerations of structural elements. Considering that the pneumatic spring suspension system is the main structural component of the rolling stock mechanical part, determination and study of vertical accelerations of its structural elements when passing through the switch is an urgent task and requires further research.

The analysis of [6-20] shows the importance of studying the dynamic characteristics of a pneumatic spring of high-speed rolling stock. However, most studies are conducted in laboratory conditions (a sinusoidal bump is taken as a disturbance), which does not take into account the real conditions of interaction between the rolling stock and a track.

This study aims to determine the accelerations of the rubber cord shell of the pneumatic spring of high-speed rolling stock when interacting with the switch wind turbines in the trailing and facing movement. This would make it possible to set the natural frequencies and logarithmic decrements of the vibration attenuation of the air spring rubber cord shell.

To achieve this goal, the following tasks were set:

- develop a methodology for the full-scale testing of a high-speed rolling stock pneumatic spring when interacting with switch points;
- determine the vertical, transverse and longitudinal accelerations of the rubber-cord shell of the pneumatic spring;
- determine the natural frequencies and logarithmic decrees of attenuation of vibrations of the rubber-cord shell of a pneumatic spring.

3 Methodology of the full-scale tests of a pneumatic spring in movement conditions by a switch

Dynamic tests of the pneumatic spring of the high-speed rolling stock were carried out within the arrow of the switch. The view of the test unit on the switch is shown in Figure 3.

Mobile installation for testing the pneumatic spring of the high-speed rolling stock within switch *1*, consists of a pneumatic spring *4*, which is rigidly fixed to the supporting structure of the stand *5*. The spring is loaded

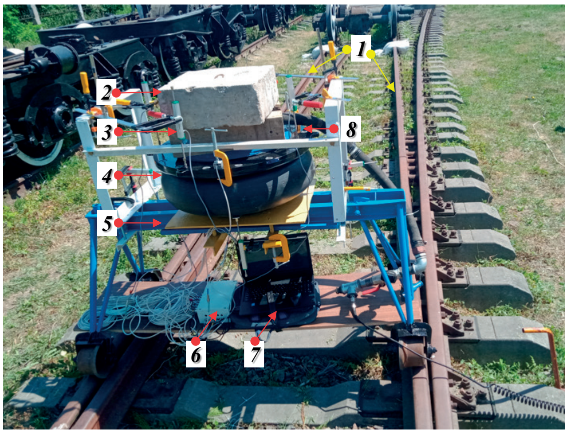

Figure 3 *Movable installation on the switch to test the pneumatic spring: 1 - switch; 2 - concrete block; 3 - high-frequency potentiometric linear displacement sensor; 4 - pneumatic spring; 5 - supporting structure of stand; 6 - analogue-to-digital converter; 7 - laptop; 8 - analogue acceleration sensor*

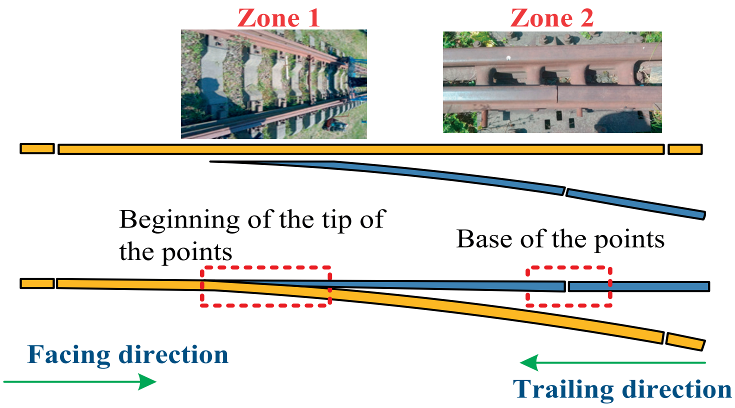

Figure 4 *Characteristic sections of the switch when the test unit is moving*

with a reinforced concrete block *2*.

When the unit moves by the switch, the spring oscillates, which is associated with the design features of the switch: the presence of joints, a transition curve, etc. [36-37]. Spring vibrations are recorded by an analogue acceleration sensor *8*. The signal is read by an analogue-to-digital converter *6* and it is transmitted to the laptop *7* and stored in its memory.

In this study, the experimental program provided for recording acceleration vibrations when the unit moves in the facing (from the tip of the points towards the crosspiece) and trailing (from the crosspiece to the tip of the points) directions. Spring accelerations were recorded seven times in different directions of the moving unit motion.

Special attention is paid to two sections when the unit moves by the switch (Figure 4): the beginning of the tip of the points and the base of the points.

When moving along Zone 1 (the beginning of the tip of the points) and Zone 2 (the base of the points), in addition to vertical action, there is a significant horizontal action on the test unit, as well. This causes lateral vibrations of the pneumatic spring of the high-speed rolling stock.

Based on the results of seven passes in the facing and trailing directions of the switch, graphs of acceleration records were obtained. Later, accelerations were analyzed and dynamic parameters of the pneumatic spring were determined using the frequency analysis methods, such as natural oscillation frequencies and logarithmic decrees of oscillation attenuation.

4 Results of experimental studies of vibration-proof properties of a pneumatic spring

4.1 Determination of accelerations of the rubber-cord shell of a pneumatic spring of the high-speed rolling stock when interacting with the points of the switch

During the full-scale tests, records of vertical, transverse and longitudinal accelerations of the rubber-cord shell of a high-speed rolling stock pneumatic spring were obtained when the test unit interacted with the points and base of the wind turbines of the switch in the trailing and facing directions, Figures 5-7.

According to the obtained records, the two zones of a sharp increase in accelerations of the rubber-cord shell of a pneumatic spring in the vertical, transverse and longitudinal directions, are distinguished, namely Zone 1 - this is the beginning of the tip of the points and

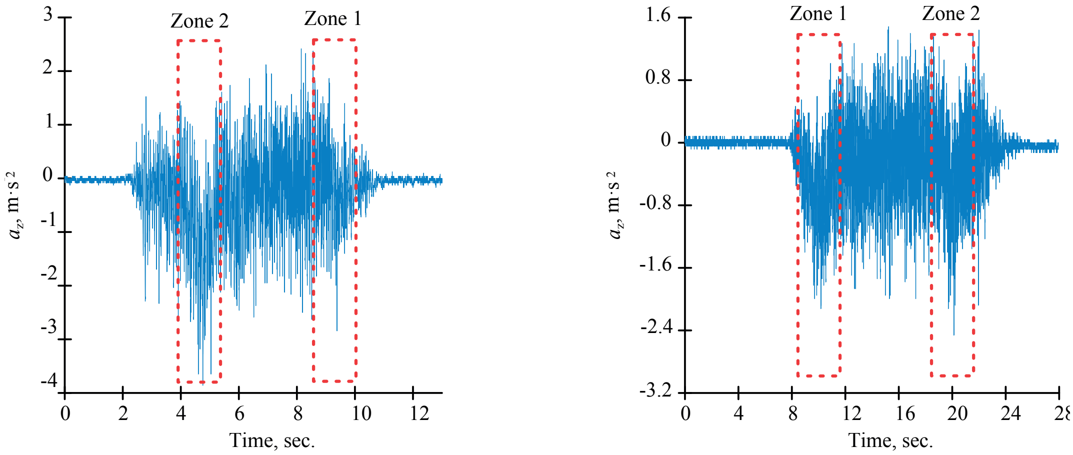

a) b)

Figure 5 *Record of vertical accelerations of the rubber-cord shell of a pneumatic spring in the trailing (a) and facing (b) directions*

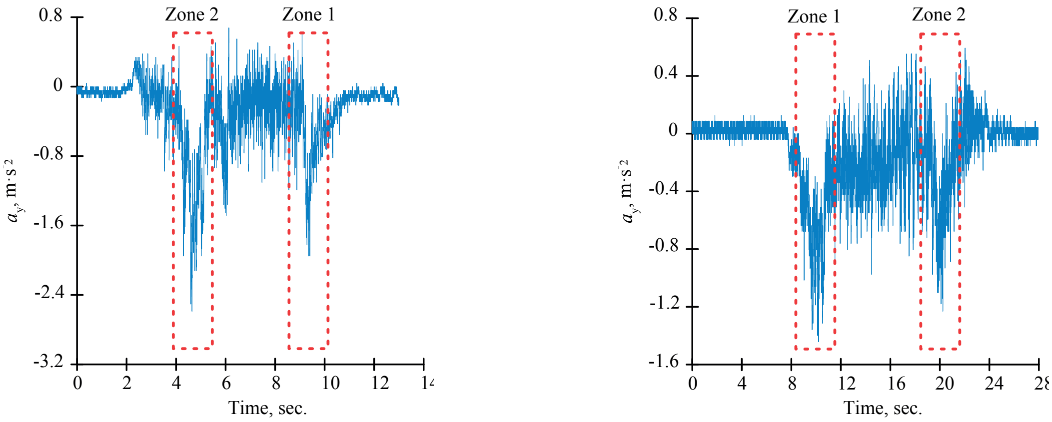

a) b)

Figure 6 *Record of transverse accelerations of the rubber-cord shell of a pneumatic spring in the trailing (a) and facing (b) directions*

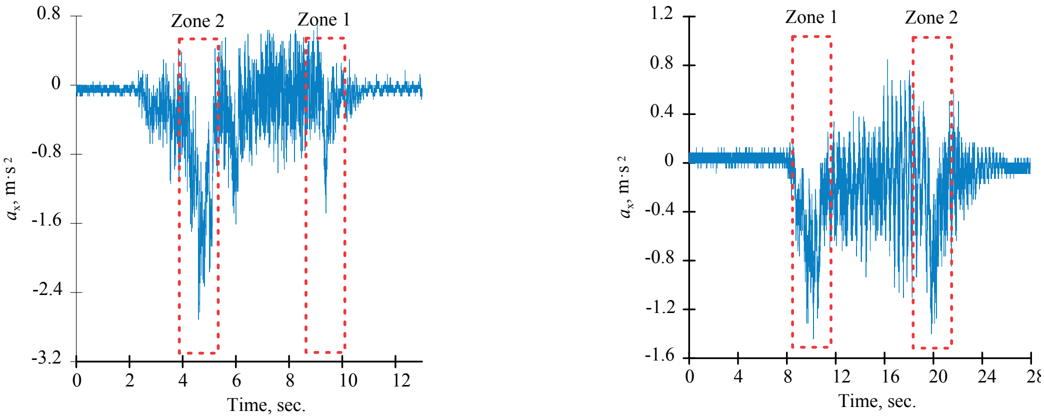

a) b)

Figure 7 *Recording of longitudinal accelerations of the rubber-cord shell of a pneumatic spring in the trailing (a) and facing (b) directions*

Zone 2 - the base of wind turbines. The sharp increase in accelerations in these zones is due to their geometric features, which leads to an increased force interaction of the wheelset with the rail track.

Using the selected zones, for each experiment performed, the maximum values of accelerations are found in all the considered planes, when the test unit moves in the trailing and facing directions (Figure 8-9).

As shown in Figure 8, it was established that the maximum values of vertical accelerations of the rubber cord shell of the pneumatic spring, during the gravity and anti-gravity movement of the test installation in Zone 1 of the switch, vary within 1.017-1.593 m·s^{-2} and 0.893-1.677 m·s^{-2}, respectively. When the test unit moves in Zone 2, the maximum values of vertical accelerations are within 1.091-2.859 m·s^{-2} and 1.075-1.691 m·s^{-2}, Figure 9.

Comparing the average values of vertical accelerations in the trailing and facing directions, when moving wind turbines of the switch, it was found that their values are 1.307 m·s^{-2} and 1.279 m·s^{-2}, respectively. However, when moving through the root of the windmills of the switch, the vertical accelerations of the rubber-cord shell of the pneumatic spring in the trailing and facing directions have discrepancies, the value of which in percentage terms is 29.04 %.

It should be noted that determination of the value of transverse accelerations of elements of the high-speed rolling stock mechanical part is the main factor in the study of the driving comfort criterion. As shown in Figure 8, it was found that when the windmill zone moves in the trailing direction, the maximum values of transverse accelerations are in the range of 0.936-1.816 m·s^{-2}, and in the facing direction within 0.932-1.571 m·s^{-2}. At the same time, the average acceleration values are 1.594 m·s^{-2} and 1.343 m·s^{-2}, respectively. This percentage is 15.74 %. When moving in Zone 2 (wind turbine base) in the trailing direction, the maximum values are within 1.344 -2.404 m·s^{-2}, and in the facing one within 0.586-1.372 m·s^{-2}. This difference in transverse accelerations of the pneumatic spring rubber-cord shell of the high-speed rolling stock in the trailing and facing directions is

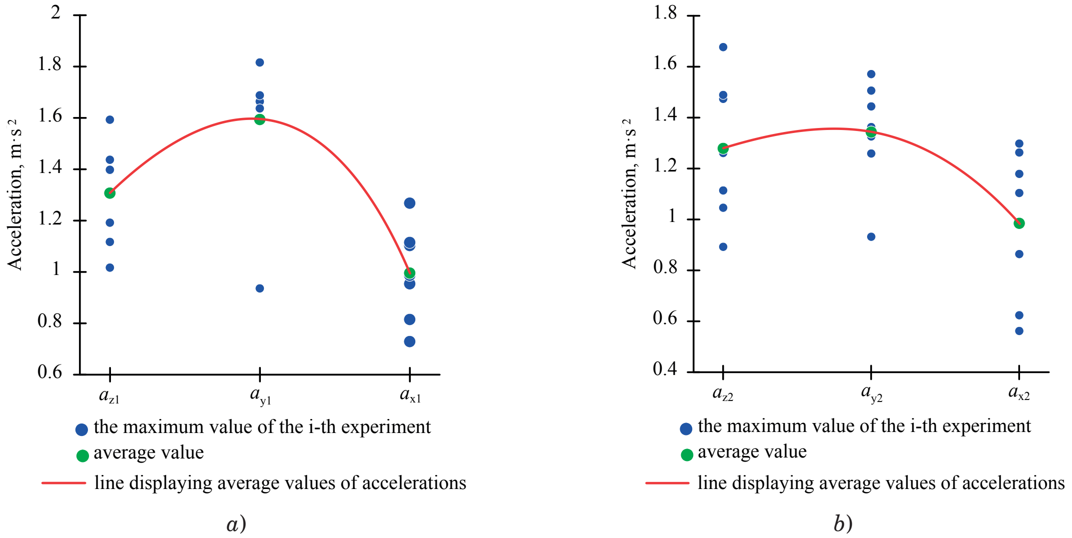

Figure 8 *Average of vertical (a_{z1}, a_{z2}), lateral (a_{y1}, a_{y2}) and longitudinal (a_{x1}, a_{x2}) acceleration values of the rubber-cord shell of a pneumatic spring in the trailing (a) and facing (b) directions when passing Zone 1 of the switch*

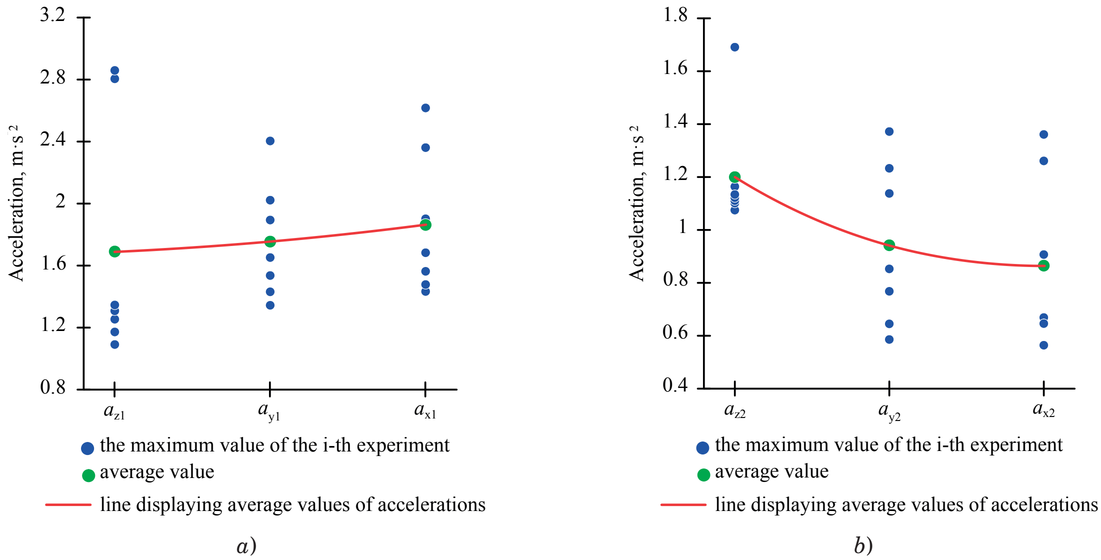

Figure 9 *Average of vertical (a_{z1}, a_{z2}), lateral (a_{y1}, a_{y2}) and longitudinal (a_{x1}, a_{x2}) acceleration values of the rubber-cord shell of a pneumatic spring in the trailing (a) and facing (b) directions when passing Zone 2 of the switch*

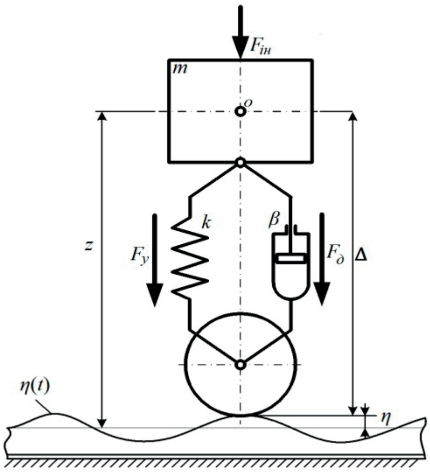

Figure 10 *Flat model with one degree of freedom under kinematic perturbation: k - stiffness of the rubber-cord shell of the pneumatic spring; β - damping coefficient; N is the amplitude of the unevenness; m is the mass that falls on the pneumatic spring; z is the absolute displacement; δ is the relative displacement (deflection)*

explained by the peculiarities of rolling the wheels of the rolling stock from the frame rails to the points and from the points to the frame rails of the switch, which causes lateral vibrations.

A comparison of the longitudinal accelerations average values of the pneumatic spring rubber-cord shell, during the movement with the points of the switch, showed a slight difference in trailing and facing movement, which cannot be said about the zone of the root of wind turbines. The ratio of the average values of accelerations during the trailing movement to accelerations that occur in the facing direction in the zone of wind turbines is 1.01, and in the zone of the base of the points is 2.15. This is caused by the passage of the wheel ridge between the frame rail and the point of the switch, which causes an additional longitudinal effect on the pneumatic spring.

The maximum values of longitudinal accelerations in the trailing direction in the wind turbine zone are 0.729-1.268 $m \cdot s^{-2}$, and in the facing direction - 0.562-1.298 $m \cdot s^{-2}$. In the wind turbine base zone, the maximum acceleration values are 1.433-2.617 $m \cdot s^{-2}$ and 0.564-1.361 $m \cdot s^{-2}$, respectively.

Next, using the obtained records of vertical, transverse and longitudinal accelerations of the pneumatic spring rubber-cord shell, the natural frequency of vibrations of the rubber-cord shell of a pneumatic spring of high-speed rolling stock and the logarithmic decrement of vibration attenuation are determined.

4.2 Determination of the natural frequency and attenuation decrement of vibrations of the rubber-cord shell of a pneumatic spring

Natural vibrations occur when an elastic mechanical system is thrown out of equilibrium. This can be done by quickly removing the static load or by instantly applying and removing external force. Displacements with variable acceleration appear as a result.

The frequency of natural vibrations can be found using the calculation scheme of a dynamic model with one degree of freedom (Figure 10).

During the system movement, kinematic perturbation causes vertical fluctuations in the super-spring structure characterized by a generalized coordinate z. The system has the following forces:

- inertial force:

$$F_{iH} = -m\ddot{z}\,, \tag{1}$$

- elastic force:

$$F_y = -k\Delta = -k(z-\eta)\,, \tag{2}$$

- dissipative force:

$$F_\partial = -\beta\dot{\Delta} = -\beta(\dot{z}-\dot{\eta})\,. \tag{3}$$

Using the D'alembert principle, the oscillation equation of the model under consideration is:

$$F_{iH} + F_y + F_\partial = 0\,. \tag{4}$$

Taking into account Equations (1)-(3), the oscillation equation can be written as:

$$m\ddot{z} + \beta\dot{z} + kz = \beta\dot{\eta} + k\eta\,. \tag{5}$$

The obtained Equation (5) is the equation of vertical vibrations of the model, the left-hand side of which is eigenvalues, and the right-hand side is forced. Solving the oscillation equation will allow to get the value of vertical displacements z, speeds $\dot{z}$ and accelerations $\ddot{z}$ masses m and evaluate the dynamic properties of the model.

To determine the first natural frequency of vibrations of the pneumatic spring rubber-cord shell of the high-speed rolling stock, when passing through the switch,

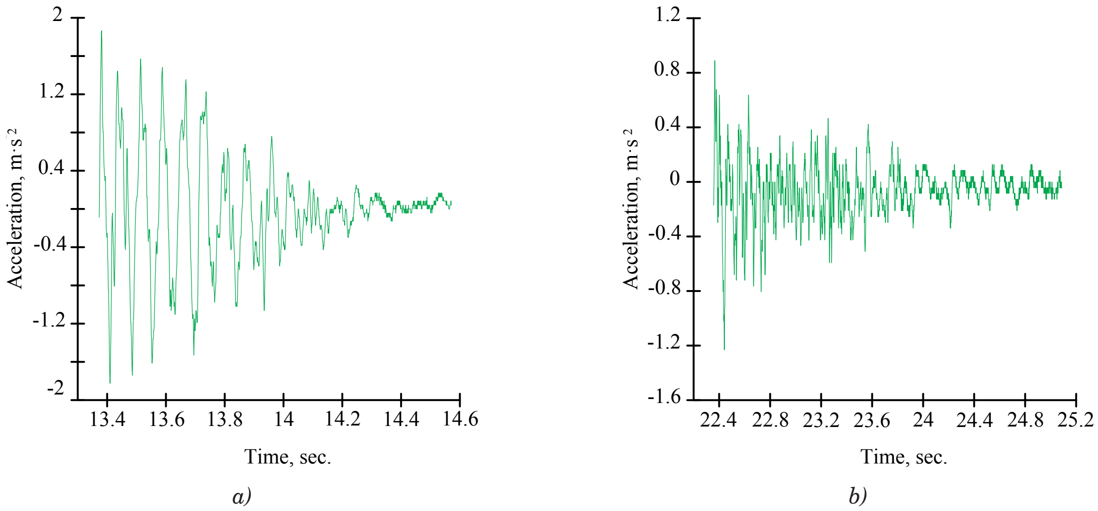

***Figure 11** Record of vertical accelerations during the free vibrations of the rubber-cord shell of a pneumatic spring: a) trailing direction; b) facing direction*

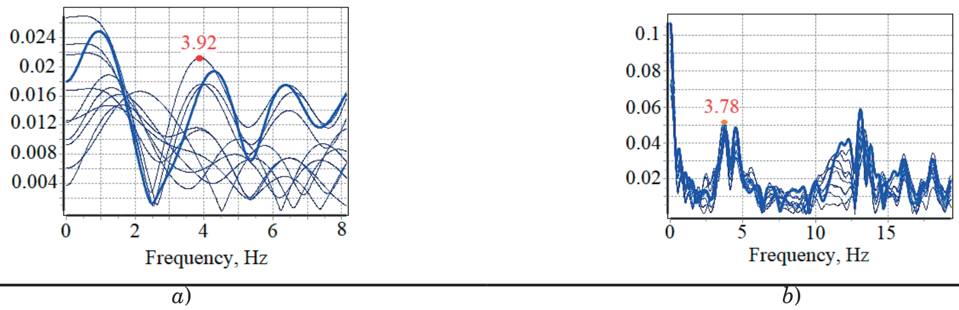

***Figure 12** Graphs of the amplitude spectrum of free vertical vibrations of the rubber-cord shell of a pneumatic spring in conditions of movement by the switch: a) in the trailing direction; b) in the facing direction*

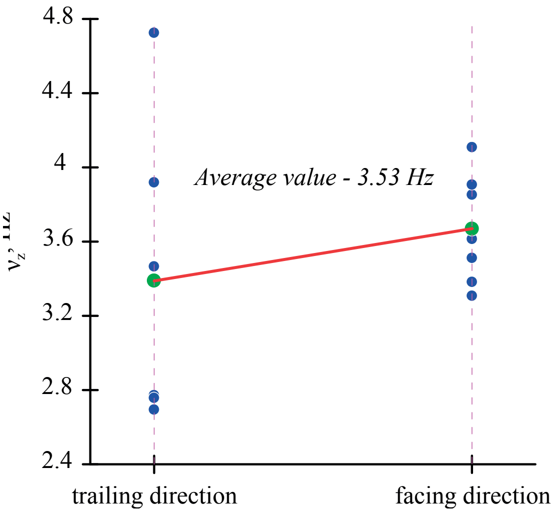

***Figure 13** Natural frequencies of vertical vibrations of the rubber-cord shell of a high-speed rolling stock pneumatic spring*

zones of free vibrations of the system in the trailing and facing directions of movement by the switch are highlighted (Figure 11) and the method used [44].

The result of frequency analysis is to obtain graphs of the amplitude spectrum of vibrations shown in Figure 12, which determine the first natural frequency of vibrations of the rolling stock pneumatic spring rubber-cord shell.

Based on the results of experimental driveways of the test unit in Zone 1 and Zone 2 of the switch, in the trailing and facing directions, the average values of the frequency of vertical natural vibrations of the pneumatic spring were obtained (Figure 13).

Analysis of the amplitude spectrum graphs showed that the natural frequencies of the pneumatic spring of the high-speed rolling stock vary between 3.31 and 4.11

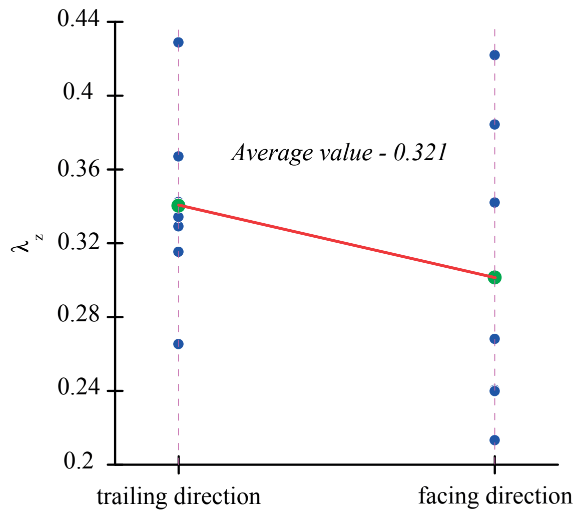

Figure 14 *Logarithmic decrement of attenuation of vibrations of the rubber-cord shell of a pneumatic spring of high-speed rolling stock*

Hz in the direction of movement of the switch and 2.76 to 4.72 Hz in the conditions of the trailing direction and facing the direction of movement. It is established that the average value of the natural oscillation frequency of a pneumatic spring is 3.53 Hz, which can later be used in establishing resonant zones and impact zones of a mechanical system of the high-speed rolling stock.

Next, the logarithmic attenuation decrement is used to quantify the attenuation of vibrations.

The logarithmic decrement of oscillation attenuation, which is the logarithm of the ratio of two amplitudes, separated by a time interval of one period, is found by:

$$\lambda = \ln\frac{A(t)}{A(t+T)} = \ln\frac{A_0 e^{-\beta t}}{A_0 e^{-\beta(t+T)}} = \frac{2\pi\beta}{\omega}, \qquad (6)$$

where ω is the cyclic frequency of attenuated vibrations.

Therefore, by analyzing the records of vertical deformations of the rubber-cord shell of a pneumatic spring, in the zones of its free vibrations, the average values of the logarithmic decrement of oscillation attenuation are obtained (Figure 14).

The logarithm value of the rate of decrease in the amplitude of vibrations is in the range of 0.265-0.43 for the trailing direction by a switch, and for the facing direction - 0.213-0.422. It is established that the average value of the logarithmic decrement of attenuation of pneumatic spring vibrations is 0.321.

These values can later be used to determine the damping properties of the pneumatic spring of high-speed railway rolling stock.

5 Discussion of results of the dynamic behaviour of a pneumatic spring by a switch

To determine the dynamic properties of a pneumatic spring of high-speed railway rolling stock, a comprehensive methodology for the full-scale testing of a pneumatic spring using a mobile test unit has been developed, Figure 3. This made it possible to obtain accelerograms of vertical, transverse and longitudinal accelerations of the pneumatic spring when the test unit moves in the trailing and facing directions of the switch, Figures 5-6. As a result, special areas of acceleration changes of the rubber-cord shell of the pneumatic spring are established: the beginning of the tip of the points and the base of the points.

Comparison of the average values of vertical accelerations in the trailing and facing directions, during the movement of the test unit by wind turbines of the switch, showed their practical coincidence, which cannot be said about the number of accelerations in the zone of the root of windmills, where the percentage difference is 29.04 %. In the transverse direction, the difference in the average acceleration values in the trailing and facing directions for the zone of the tip of the points does not exceed 15.75 %, and for the zone of the wind turbine base is 46.31 %. In the longitudinal direction, the difference is 1.11 % for the tip zone of the points and 53.55 % for the zone of the wind turbine base.

Frequency analysis of oscillation records showed that the average value of the first natural oscillation frequency of the pneumatic spring is 3.53 Hz, and the logarithmic decrement of oscillation attenuation is 0.321.

One of the limitations of the conducted research is that the natural oscillation frequencies of the pneumatic spring of high-speed rolling stock are obtained without taking into account the manometric air pressure in it. The next stage of research and development will be to conduct field tests of the pneumatic spring at a certain initial gauge pressure. This would make it possible to study its influence on the dynamic characteristics of the pneumatic spring suspension system in the movement conditions by a switch.

6 Conclusions

1. A comprehensive methodology for the full-scale testing of a pneumatic spring of high-speed rolling stock, while moving along a switch, has been developed. A mobile test unit has been developed to determine the vibration-proof properties of a pneumatic spring. It consists of a load-bearing structure, a pneumatic spring of high-speed railway rolling stock and measuring equipment. This made it possible to conduct experimental tests of the pneumatic spring when the installation moves in the facing and trailing directions.
2. When the test unit moves along the switch elements, records of vertical, transverse and longitudinal accelerations of the rubber-cord shell of the pneumatic spring are obtained. It was found that in the vertical direction, the maximum difference between the average acceleration values in the trailing and facing directions is 29.04 %, in the transverse direction - 46.31% and in the longitudinal direction-53.55 %.
3. Based on the obtained graphs of the amplitude spectrum, it is established that the average value of the first natural frequency of vibrations of a pneumatic spring is 3.53 Hz, and the logarithmic decrement of attenuation of vibrations is 0.321.

Acknowledgements

The authors express their gratitude to the management and staff of the design bureau of the Kryukiv Carriage Works for providing pneumatic springs and consultations on research into the features of their operation.

Conflicts of interest

The authors declare that they have no known competing financial interests or personal relationships that could have appeared to influence the work reported in this paper.

References

[1] KUZYSHYN, A., KOSTRITSA, S., URSULYAK, L., BATIG, A., SOBOLEVSKA, J., VOZNYAK, O. Research of the impact of geometric unevenness of the railway track on the dynamic parameters of the railway rolling stock with two-stage spring suspension. *IOP Conference Series: Materials Science and Engineering* [online]. 2019, **664**, 012024. ISSN 1757-899X. Available from: https://doi.org/10.1088/1757-899X/664/1/012024

[2] KUZYSHYN, A., BATIG, A., KOSTRITSA, S., SOBOLEVSKA, J., DOVHANIUK, S., DZHUS, V. Study of the dynamic behavior of rolling stock using a computer experiment. *IOP Conference Series: Materials Science and Engineering* [online]. 2020, **985**, 012002. ISSN 1757-899X. Available from: https://doi.org/10.1088/1757-899X/985/1/012002

[3] KUZYSHYN, A., BATIG, A., KOSTRITSA, S., SOBOLEVSKA, J., KOVALCHUK, V., DOVHANYUK, S., VOZNYAK, O. Research of safety indicators of diesel train movement with two-stage spring suspension. *MATEC Web of Conferences* [online]. 2018, **234**, 05003. eISSN 2261-236X. Available from: https://doi.org/10.1051/matecconf/201823405003

[4] How many types of railway turnouts there are? - AGICO Group [online]. Available from: http://www.railroadfastenings.com/blog/railway-turnout-types.html

[5] KUZYSHYN, A., KOVALCHUK, V., STANKEVYCH, V., HILEVYCH, V. Determining patterns in the influence of the geometrical parameters of the connecting pipeline on the dynamic parameters of the pneumatic spring of railroad rolling stock. *Eastern-European Journal of Enterprise Technologies* [online]. 2023, **7**(121), p. 57-65. ISSN 1729-3774, eISSN 1729-4061. Available from: https://doi.org/10.15587/1729-4061.2023.274180

[6] SAYYAADI, H., SHOKOUHI, N. Improvement of passengers ride comfort in rail vehicles equipped with air springs. *World Academy of Science, Engineering and Technology* [online]. 2009, **53**, p. 827-833. Available from: https://doi.org/10.5281/zenodo.1071388

[7] BERG, M. A three-dimensional airspring model with friction and orifice damping. *Vehicle System Dynamics* [online]. 1999, **33**(1), p. 528-539. ISSN 0042-3114, eISSN 1744-5159. Available from: https://doi.org/10.1080/00423114.1999.12063109

[8] HAUPT, P., SEDLAN, K. Viscoplasticity of elastomeric materials: experimental facts and constitutive modelling. *Archive of Applied Mechanics* [online]. 2001, **71**, p. 89-109. ISSN 0939-1533, eISSN 1432-0681. Available from: https://doi.org/10.1007/s004190000102

[9] DUKKIPATI, R. V., HARG, V. K. *Dynamics of railway vehicle systems*. Academic press, Harcourt Brace Jovanovich, Publishers, 1984. ISBN 9780124313071.

[10] MOHEYELDEIN, M. M., ABD-EL-TAWWAB, A. M., ABD EL-GWWAD, K. A., SALEM, M. M. An analytical study of the performance indices of air spring suspensions over the passive suspension. *Beni-Suef University*

Journal of Basic and Applied Sciences [online]. 2018, **7**(4), p. 525-534. ISSN 2314-8535. Available from: https://doi.org/10.1016/j.bjbas.2018.06.004

[11] ALONSO, A., GIMENEZ, J. G., NIETO, J., VINOLAS, J. Air suspension characterisation and effectiveness of a variable area orifice. *Vehicle System Dynamics* [online]. 2010, **48**(1), p. 271-286. ISSN 0042-3114, eISSN 1744-5159. Available from: https://doi.org/10.1080/00423111003731258

[12] FACCHINETTI, A., MAZZOLA, L., ALFI, S., BRUNI, S. Mathematical modelling of the secondary airspring suspension in railway vehicles and its effect on safety and ride comfort. *Vehicle System Dynamics* [online]. 2010, **48**(1), p. 429-449. ISSN 0042-3114, eISSN 1744-5159. Available from: https://doi.org/10.1080/00423114.2010.486036

[13] SAYYAADI, H., SHOKOUHI, N. Effects of air reservoir volume and connecting pipes length and diameter on the air spring behavior in rail vehicles. *Iranian Journal of Science and Technology Transaction B: Engineering*. 2010, **34**, p. 499-508. ISSN 1028-6284.

[14] XU, L. Mathematical modeling and characteristic analysis of the vertical stiffness for railway vehicle air spring system. *Mathematical Problems in Engineering* [online]. 2020, **220**, p. 1-12. ISSN 1024-123X, eISSN 1563-5147. Available from: https://doi.org/10.1155/2020/2036563

[15] NAKAJIMA, T., SHIMOKAWA, Y., MIZUNO, M., SUGIYAMA, H. Air suspension system model coupled with leveling and differential pressure valves for railroad vehicle dynamics simulation. *Journal of Computational and Nonlinear Dynamics* [online]. 2014, **9**(3), p. 1-9. ISSN 1555-1415, eISSN 1555-1423. Available from: https://doi.org/10.1115/1.4026275

[16] TANAKA, T., SUGIYAMA, H. Prediction of railway wheel load unbalance induced by air suspension leveling valves using quasi-steady curve negotiation analysis procedure. *Proceedings of the Institution of Mechanical Engineers, Part K: Journal of Multi-body Dynamics* [online]. 2019, **234**(1), p. 19-37. ISSN 1464-4193, eISSN 2041-3068. Available from: https://doi.org/10.1177/1464419319867179

[17] NIETO, A., MORALES, A., GONZALEZ, A., CHICHARRO, J. M., PINTADO, P. An analytical model of pneumatic suspensions based on an experimental characterization. *Journal of Sound and Vibration* [online]. 2008, **313**(1-2), p. 290-307. ISSN 0022-460X, eISSN 1095-8568. Available from: https://doi.org/10.1016/j.jsv.2007.11.027

[18] ZHU, H., YANG, J., ZHANG, Y., FENG, X. A novel air spring dynamic model with pneumatic thermodynamics, effective friction and viscoelastic damping. *Journal of Sound and Vibration* [online]. 2017, **408**, p. 87-104. ISSN 0022-460X, eISSN 1095-8568. Available from: https://doi.org/10.1016/j.jsv.2017.07.015

[19] QI, Z., LI, F., YU, D. A three-dimensional coupled dynamics model of the air spring of a high-speed electric multiple unit train. *Proceedings of the Institution of Mechanical Engineers, Part F: Journal of Rail and Rapid Transit* [online]. 2017, **231**(1), p. 3-18. ISSN 0954-4097, eISSN 2041-3017. Available from: https://doi.org/10.1177/0954409715620534

[20] XU, L. Research on nonlinear modeling and dynamic characteristics of lateral stiffness of vehicle air spring system. *Advances in Mechanical Engineering* [online]. 2020, **12**(6), p. 1-15. ISSN 1687-8132, eISSN 1687-8140. Available from: https://doi.org/10.1177/1687814020930457

[21] ANDERSSON, C., DAHLBERG, T. Wheel/rail impacts at a railway turnout crossing. *Proceedings of the Institution of Mechanical Engineers, Part F: Journal of Rail and Rapid Transit* [online]. 1998, **212**(2), p. 123-134. ISSN 0954-4097, eISSN 2041-3017. Available from: https://doi.org/10.1243/0954409981530733

[22] ANDERSSON, C., DAHLBERG, T. Load impacts at railway turnout crossing. *Vehicle System Dynamics* [online]. 1999, **33**(1), p. 131-142. ISSN 0042-3114, eISSN 1744-5159. Available from: https://doi.org/10.1080/00423114.1999.12063076

[23] ALFI, S., BRUNI, S. Mathematical modelling of train-turnout interaction. *Vehicle System Dynamics* [online]. 2009, **47**(5), p. 551-574. ISSN 0042-3114, eISSN 1744-5159. Available from: https://doi.org/10.1080/00423110802245015

[24] BRUNI, S., ANASTASOPOULOS, I., ALFI, S., VAN LEUVEN A., GAZETAS, G. Effects of train impacts on urban turnouts: Modelling and validation through measurements. *Journal of Sound and Vibration* [online]. 2009, **324**, p. 666-689. ISSN 0022-460X, eISSN 1095-8568. Available from: https://doi.org/10.1016/j.jsv.2009.02.016

[25] JOHANSSON, A., NIELSEN, J., BOLMSVIK, R., KARLSTROM, A., LUNDEN, R. Under sleeper pads-influence on dynamic train-track interaction. *Wear* [online], 2008, **265**(9-10), p. 1479-1487. ISSN 0043-1648, eISSN 1873-2577. Available from: https://doi.org/10.1016/j.wear.2008.02.032

[26] MARKINE, V., STEENBERGEN, M., SHEVTSOV, I. Combatting RCF on switch points by tuning elastic track properties. *Wear* [online]. 2011, **271**(1), p. 158-167. ISSN 0043-1648, eISSN 1873-2577. Available from: https://doi.org/10.1016/j.wear.2010.10.031

[27] KASSA, E., NIELSEN, J. Dynamic interaction between train and railway turnout: full-scale field test and validation of simulation models. *Vehicle System Dynamics* [online]. 2008, **46**(1), p. 521-534. ISSN 0042-3114, eISSN 1744-5159. Available from: https://doi.org/10.1080/00423110801993144

[28] KASSA, E., ANDERSSON, C., NIELSEN, J. Simulation of dynamic interaction between train and railway turnout. *Vehicle System Dynamics* [online]. 2006, **44**(3), p. 247-258. ISSN 0042-3114, eISSN 1744-5159. Available from: https://doi.org/10.1080/00423110500233487

[29] KASSA, E., NIELSEN, J. Stochastic analysis of dynamic interaction between train and railway turnout. *Vehicle System Dynamics* [online]. 2008, **46**(5), p. 429-449. ISSN 0042-3114, eISSN 1744-5159. Available from: https://doi.org/10.1080/00423110701452829

[30] CHEN, J., WANG, P., XU, J., CHEN, R. Simulation of vehicle-turnout coupled dynamics considering the flexibility of wheelsets and turnouts. *Vehicle System Dynamics* [online]. 2021, **61**(3), p. 739-764. ISSN 0042-3114, eISSN 1744-5159. Available from: https://doi.org/10.1080/00423114.2021.2014898

[31] ALFI, S., BRUNI, S. Mathematical modelling of train-turnout interaction. *Vehicle System Dynamics* [online], 2009, **47**(5), p. 551-574. ISSN 0042-3114, eISSN 1744-5159. Available from: https://doi.org/10.1080/00423110802245015

[32] HAO, C., XU, J., QIAN, Y., AN, B., WANG, P., YI, Q., WANG, S. Impact of wheel profile evolution on the lateral motion characteristics of a high-speed vehicle navigating through turnout. *Vehicle System Dynamics* [online], 2023, **62**(8), p. 2079-2097. ISSN 0042-3114, eISSN 1744-5159. Available from: https://doi.org/10.1080/00423114.2023.2274468

[33] PALSSON, B., NIELSEN, J. Damage in switches and crossings considering stochastic spread in railway traffic parameters. In: 10th International Conference on Recent Advances in Structural Dynamics RASD 2010: proceedings. 2010.

[34] CHEN, Y., WANG, J., CHEN, J., WANG, P., XU, J., AN, B. A novel three-dimensional wheel-rail contact geometry method in the switch panel considering variable cross-sections and yaw angle, *Vehicle System Dynamics* [online]. 2021, **60**(9), p. 3174-3197. ISSN 0042-3114, eISSN 1744-5159. Available from: https://doi.org/10.1080/00423114.2021.1941140

[35] KOVALCHUK, V., SYSYN, M., SOBOLEVSKA, J., NABOCHENKO, O., PARNETA, B., PENTSAK, A. Theoretical study into efficiency of the improved longitudinal profile of frogs at railroad switches. *Eastern-European Journal of Enterprise Technologies* [online]. 2018, **4/1**(94), p. 27-36. ISSN 1729-3774, eISSN 1729-4061. Available from: https://doi.org/10.15587/1729-4061.2018.139502

[36] KOVALCHUK, V., BOLZHELARSKYI, Y., PARNETA, B., PENTSAK, A., PETRENKO, O., MUDRYY, I. Evaluation of the stressed-strained state of crossings of the 1/11 type turnouts by the finite element method. *Eastern-European Journal of Enterprise Technologies* [2017]. 2017, **4/7**(88), p. 10-16. ISSN 1729-3774, eISSN 1729-4061. Available from: https://doi.org/10.15587/1729-4061.2017.107024

[37] KOVALCHUK, V., SYSYN, M., HNATIV, Y., BAL, O., PARNETA, B., PENTSAK, A. Development of a promising system for diagnosing the frogs of railroad switches using the transverse profile measurement method. *Eastern-European Journal of Enterprise Technologies* [online]. 2018, **2/1**(92), p. 33-42. ISSN 1729-3774, eISSN 1729-4061. Available from: https://doi.org/10.15587/1729-4061.2018.125699

[38] IZVOLT, L., DOBES, P., PAPANOVA, Z., MECAR, M. Experimental monitoring of dynamic parameters of the sub-ballast layers as a prerequisite for a high-quality and sustainable railway line. *Sustainability* [online]. 2024, **16**, 2229. eISSN 2071-105. Available from: https://doi.org/10.3390/su16062229

[39] IZVOLT, L., KARDOS, J., DOBES, P., NAVIKAS, D. Comprehensive assessment of the effectiveness of the application of foam and extruded polystyrene in the railway substructure. *Buildings* [online]. 2024, **14**, 31. eISSN 2075-5309. Available from: https://doi.org/10.3390/buildings14010031

[40] IZVOLT, L., DOBES, P., PAPAN, D., MECAR, M. Static modulus of deformation of uncemented layers of the railway substructure-comparison of values and determination of correlation dependence according to the test procedure of the Slovak Railways and Deutsche Bahn A.G. *Buildings* [online]. 2023, **13**, 2016. eISSN 2075-5309. Available from: https://doi.org/10.3390/buildings13082016

[41] SYSYN, M., GERBER, U., NABOCHENKO, O., KOVALCHUK, V. Common crossing fault prediction with track based inertial measurements: statistical vs mechanical approach. *Pollack Periodica* [online]. 2019, **14**(2), p. 15-26. ISSN 1788-1994, eISSN 1788-3911. Available from: https://doi.org/10.1556/606.2019.14.2.2

[42] SYSYN, M., IZVOLT, L., NABOCHENKO, O., KOVALCHUK, V., SESTAKOVA, J. PENTSAK, A. Multifractal analysis of the common crossing track-side measurements. *Civil and Environmental Engineering* [online]. 2019, **15**(2), p. 101-114. eISSN 2199-6512. Available from: https://doi.org/10.2478/cee-2019-0014

[43] SYSYN, M., NABOCHENKO, O., GERBER, U., KOVALCHUK, V., PETRENKO, O. Common crossing condition monitoring with on-board inertial measurements. *Acta Polytechnica. Journal of Advanced Engineering* [online]. 2019, **59**(4), p. 423-434. ISSN 1210-2709, eISSN 1805-2363. Available from: https://doi.org/10.14311/AP.2019.59.0423

[44] REDCHENKO, V. P., KRYUCHKOV, Y. V., REDCHENKO, T. V. Study of the problem of detecting bridge defects using vibration diagnostics. *Bulletin of the Dnipropetrovsk National University of Railway Transport* (in Ukrainian). 2018, **39**, p. 168-172. ISSN 2307-3489, eISSN 2307-6666.

OPTIMIZATION OF GEAR PAIRS IN THE TWO STAGE PLANETARY GEARBOX USING AHP AND TOPSIS METHOD

Jelena Jovanović[1], Sandra Gajević[1], Slavica Miladinović[1], Lozica Ivanović[1], Jasmina Blagojević[2], Milan Bukvić[1], Blaža Stojanović[1,*]

[1]University of Kragujevac, Faculty of Engineering, Kragujevac, Serbia
[2]Metalac a.d., Metalac Inko d.o.o., Gornji Milanovac, Serbia

*E-mail of corresponding author: blaza@kg.ac.rs

Sandra Gajević 0000-0002-7169-8907,
Lozica Ivanović 0000-0002-9503-593X,
Milan Bukvić 0000-0003-2892-0389,
Slavica Miladinović 0000-0002-4408-0634,
Jasmina Blagojević 0000-0002-5302-786X,
Blaža Stojanović 0000-0003-4790-2856

Resume

The optimization of gear pairs in a two-stage planetary gearbox was performed using the Analytic Hierarchy Process (AHP) and the Technique for Order of Preference by Similarity to Ideal Solution (TOPSIS). A total of 18 combinations of input parameters were analyzed, varying: gear width (20, 22, 24 mm), module (2.25, 2.5, 2.75 mm) and material (16MnCr5, 34CrNiMo6). Safety factor from pitting (Sh) and safety factor from tooth fracture (Sf) were numerically obtained and those two parameters were chosen as criteria for optimization. TOPSIS identified alternative 1 (20 mm width, 2.25 mm module, 16MnCr5 material) as the optimal solution, demonstrating the highest safety factor values. Additionally, the optimization achieved satisfactory results regarding the mass of gear pairs. After optimization, the mass of gear pairs decreased by 20% compared to the pre-optimization version.

Article info

Received 16 August 2024
Accepted 27 November 2024
Online 17 December 2024

Keywords:

spur gears
planetary gearbox
AHP
TOPSIS
optimization

Available online: https://doi.org/10.26552/com.C.2025.014

ISSN 1335-4205 (print version)
ISSN 2585-7878 (online version)

1 Introduction

Mechanical transmissions, as the name suggests, mechanically transmit power and motion from the driving machine to the driven machine. The development of mechanical transmissions dates back to ancient civilizations, where people crafted various mechanisms from objects found in their environment to facilitate their work. As society progressed, these transmissions evolved [1-2].

In a modern history of mechanical transmissions, with the development of industry and capitalism, efforts have been made to reduce the production and maintenance costs, while emphasizing increased efficiency and reliability. Mechanical transmissions have paralleled the development of industry and science, advancing in terms of load capacity calculations, material selection and geometry. With the advance of automation, monitoring and control of their operation has been greatly facilitated, while robotics development has enabled the implementation of these transmissions in devices performing specific tasks.

In modern engineering practice, the optimization of the design of mechanical transmissions becomes crucial to achieve high efficiency, reliability and cost reduction. With ever-increasing demands for energy-efficient and long-lasting systems, engineers face the challenge of optimizing the transmission characteristics, while minimizing production and maintenance costs, which sets new standards in the field of design and application of these systems.

Continuous investment in development of advanced software allows engineers to model and test transmissions in a virtual environment before the physical production, minimizing the possibility of errors during their manufacture. One such mechanical transmission that has evolved from a basic to a complex geometric element is the gear pair, which consists of two meshing gears. Gear pairs have undergone numerous modifications in terms of geometry and material selection to align their characteristics with their intended applications.

The need to optimize the space and energy utilization, as well as the demand for high transmission ratios, have led to the emergence and development of planetary gear transmissions. Planetary gear transmissions are gear transmissions consisting of the two central gears and satellites. This type of transmission represents a challenging endeavor in terms of design, production, and assembly.

Over the past decades, manufacturing technologies have advanced significantly, with one direction being the development and application of new materials for gear transmissions, including the use of polymers, ceramics, and composites. The use of polymer gears has experienced a significant increase primarily due to numerous advantages compared to steel gears. Mass production is cheaper when manufactured by injection molding, they can operate without additional lubrication, absorb noise and vibrations better and are resistant to corrosion and other chemical reactions. Zorko et al. [3] presented the possibility of replacing the fossil-based polymers with bio-based polymers, such as polyoxymethylene (POM) and polyamide 66 (PA 66). The potential of bio-based polymers was studied based on gear lifetime testing. The results show that gears made of bio-based polyamide have a lifespan three and a half times longer than POM gears and ten times longer than PA66 gears. Ceramic materials, due to their higher pressure resistance compared to tensile strength, are not a good choice for gear manufacturing. However, due to several advantages such as low weight, wear resistance, high-temperature resistance and chemical resistance, considerable attention is being given to them and possible solutions for their application in gears are being developed. Vasileiou et al. [4] explored the application of ceramic gears and structural solutions in their work. They also compared the performance of ceramic gears against steel gears.

The use of composite materials for gear manufacturing is becoming challenging in modern engineering due to numerous advantages. Gears made of composite materials are lighter compared to steel gears, have better corrosion resistance, fatigue resistance, etc. Hybrid steel-composite gears, composite-bodied gears with a steel gear rim, represent a technology that is rapidly developing. The concept of such gears was introduced in 2012 by the NASA Research and Development Center, replacing conventional steel gears in aviation. This prototype successfully operated for three hundred million cycles and was 20% lighter than a steel gear [5]. Under the normal operating conditions, these gears performed well, but under unlubricated conditions, they exhibited shortcomings. Hybrid steel-composite gears were tested in unlubricated conditions in 2017 and the results showed that the composite softened at high temperatures (above 232 °C), necessitating the discovery of composites capable of withstanding operation at such high temperatures. Waller et al. [5] addressed this issue in their work, studying and researching composite materials specifically for the manufacture of hybrid steel-composite gears for aviation. The research was based on experimentation involving different types of matrices and fiber orientations. Various samples were first examined under a microscope and then tested for pressure resistance using a testing device. Subsequently, they created 3D models tested in Abaqus CAE software. They concluded that Carbon/BMI composite provides greater pressure resistance than carbon-epoxy at temperatures above 204 °C, and the thermal resistance of multidirectional laminate layers is identical to steel, reaching a balance between the resistance and thermal conductivity.

The application of new materials for gear transmissions is a key aspect of modern engineering focused on improving system performance and efficiency. Efforts are directed towards finding materials that can meet and satisfy all the requirements of modern technical systems, while providing better performance compared to conventional materials. By employing modern analysis and testing methods, new materials are being developed that can meet expectations regarding reliability and longer lifespan, while reducing production costs and thereby reducing costs. Additionally, the use of these materials can have a positive environmental impact compared to steel, reducing electricity consumption during production, enabling recycling and reuse, reducing emissions of harmful gases, biodegradability, etc.

There is extensive research on the complex dynamic characteristics of planetary gear transmissions, employing various methodologies to optimize system performance in terms of vibration efficiency [6-7], power transmission efficiency [6, 8-9], geometric characteristics [10]. Furthermore, another group of researchers has studied the gear tooth wear and its impact on system dynamics Li et al. [11], Tian et al. [12]. Li et al. [11], modeled the planetary gear system with helical gears in a wind turbine gearbox with tooth surface damage, concluding that the tooth damage leads to abnormal vibrations and lateral stripes in frequency signals. Tian et al. [12] investigated the impact of angular misalignment on the prediction of wear in planetary gear sets with rotating carriers, finding that the combined effect of angular misalignment and rotating carrier results in a greater wear at the ends of the tooth face width. Another group of researchers, Huangfu et al. [13], predicted the gear wear in planetary gear transmissions using a developed dynamic model employing geometrically adaptively loaded tooth contact analysis (GA-LTCA) method. They validated their developed model through the finite element analysis and failure testing, demonstrating accurate predictions of wear profiles and wear characteristics throughout the gear's life cycle.

Although there are numerous studies of the dynamic characteristics of planetary gears and methods for improvement of their efficiency, the challenge of optimization of the safety factor against pitting (Sh) and the safety factor against tooth breakage (Sf) in planetary gear pairs remains significant. Optimization of these safety factors is important for ensuring the long-term reliability and safe operation of planetary gears, especially under the high loads and demanding operational conditions. The aim of this study was to optimize the safety factor from pitting (Sh) and safety factor from tooth breakage (Sf) of planetary gear pairs. Optimization is performed by combining the Analytic Hierarchy Process (AHP) and Technique for Order Preference by Similarity to Ideal Solution (TOPSIS) methods to determine the optimal parameter values based on predefined criteria weights.

2 Planetary transmissions

Mechanical transmissions find their widest application in engineering. Mechanical transmissions transfer mechanical energy from the driving to the driven machine, often altering speed, torque and sometimes direction of movement. Planetary gear transmissions belong to a special group of mechanical power transmissions. Initially, their application was focused on solving problems for transport and military vehicles. As they developed, their range of applications expanded continuously. Effective use of space within the planetary gear housing is achieved by the ability to fill the space between the central gears with a larger number of satellites, contributing to reduced loads and selection of smaller gear modules. Due to their compact design, they are two to three times lighter than the conventional transmissions of the same power and gear ratio [1-2]. Some of the main advantages of planetary transmissions include: the high gear ratio with small dimensions, compact construction, high degree of coupling enabling more uniform distribution of loads, capability of transmitting higher torque, ability to achieve various gear ratios, and high efficiency. However, they also exhibit certain drawbacks such as: occurrence of centrifugal forces, sensitivity to changes in center distances, and complex and costly manufacturing processes [1].

Throughout the time, engineers have strived to bring planetary transmissions to perfection, which they have done, because today these transmissions appear in all branches of industry and represent a key segment in most modern technical systems.

3 Methodology

The kinematics and dynamics calculation of the $B_{ha}{}^{b}$ concept planetary gearbox was performed for the following input parameters: driving machine is EM with 7 kW power and speed of 1200 rpm, the gear ratio of the planetary gearbox is 4 and the transmission efficiency is 0.97. This design of the planetary gearbox has two stages with three satellites each. The calculations of planetary gearbox were conducted based on literature [1], while the calculation of gear pairs was performed using the Inventor software package based on initial data. During the calculation of gear pairs, the safety factor from pitting (Sh) and safety factor from the tooth breakage (Sf) of planetary gear pairs were recorded based on varied factors, along with numerical results used for the optimization of gear pairs in the mentioned planetary gearbox.

The next step in this research was the application of the AHP and TOPSIS methods to achieve optimal values of safety factors for the tooth flanks and tooth bottoms of the gear pairs.

3.1 Analytic hierarchy process

The AHP is a multi-criteria decision-making method used for systematic analysis and decision-making in complex problems, involving multiple alternatives and criteria [14]. It breaks down complex problems into simpler and more understandable elements through the hierarchical decomposition. Developed in the 1980s, the method owes its advancement to the research and scientific work of American scientist Thomas Saaty. It is widely applied in various fields such as engineering, management, economics, medicine and others [15]. A pivotal component of the AHP method is Saaty's scale, also known as the comparison scale, which determines the relative importance between criteria. Saaty's scale (Table 1) consists of 9 levels, each level comprising a numerical value and corresponding description [14-18].

Based on existing research and applications of the AHP method, the following steps are provided [16, 18-19]:

Step 1: Creating a pair-wise comparison matrix using the Saaty's scale. Comparison is made for each criterion relative to another, using a value from the Saaty's scale. A criterion compared to itself always has a value of 1.

Table 1 *Saaty's scale*

Importance	
1	Two criteria are equally important.
3	One criterion is moderately more important than the other.
5	One criterion is significantly more important than the other.
7	One criterion is much more important than the other.
9	One criterion is extremely more important than the other.
2,4,6,8	Intermediate values.

After the pair-wise comparisons, matrix A is formed where a_{ij} represents the relative preference of criterion A_i over criterion A_j.

$$A = [a_{ij}] = \begin{bmatrix} 1 & a_{12} & \cdots & a_{1n} \\ \frac{1}{a_{12}} & 1 & \cdots & a_{2n} \\ \cdots & \cdots & \cdots & \cdots \\ \frac{1}{a_{1n}} & \frac{1}{a_{2n}} & \cdots & 1 \end{bmatrix}, \tag{1}$$

Step 2: Calculating the normalized weight w_j using Equations (2) and (3):

$$w_j = \frac{GM_i}{\sum_{i=1}^{n} GM_i}. \tag{2}$$

where, the value GM_i is calculated as follows:

$$GM_i = \left(\prod_{i=1}^{n} a_{ij}\right)^{\frac{1}{n}} \tag{3}$$

Step 3: Determining the maximum eigenvalue of the comparison matrix $\lambda_{\max}$ and calculating the consistency index CI:

$$CI = \frac{\lambda_{\max} - n}{(n-1)}. \tag{4}$$

Step 4: Calculating the random consistency index RI (Table 2) for the criteria used in the decision-making process. Criteria represent different factors or characteristics used in the decision-making. Each criterion has its importance relative to the others. Criteria are included as input parameters, when used to determine or rank alternatives, while they are assigned output values when used to generate results based on input data.

Step 5: Calculate the consistency ratio CR using Equation (5):

$$CR = \frac{CI}{RI} \tag{5}$$

If the CR value is 0.1 or lower, accept the obtained criteria weights. However, if the calculated CR exceeds 0.1, it indicates unsatisfactory consistency, and it is necessary to repeat the comparison, i.e., recreate the comparison matrix as shown in Step 1.

3.2 TOPSIS method

The TOPSIS is a multi-criteria decision-making method used for ranking and selecting the best alternative, considering multiple criteria. It was developed in 1981 by Hwang and Yoon. The best alternative is the one with the shortest Euclidean distance from the positive ideal solution (PIS) and the greatest Euclidean distance from the negative ideal solution (NIS). This method is highly efficient compared to other metaheuristic methods, due to its numerous characteristics, such as reliability, ease of reaching solutions, procedural transparency, compatibility with other methods, and more. It finds extensive applications across various industries, including the project management, financial analysis, industrial engineering, and marketing for analyzing and selecting marketing strategies and products. The steps used in its implementation are detailed below based on research [14-23].

Step 1: Formation of a decision matrix from all the alternatives and criteria. Assuming that the alternatives are denoted by M and criteria by N, the decision matrix *D* takes the following form:

$$D = \begin{bmatrix} x_{11} & x_{12} & \cdots & x_{1N} \\ x_{21} & x_{22} & \cdots & x_{2N} \\ \cdot & \cdot & \cdots & \cdot \\ x_{M1} & x_{M2} & \cdots & x_{MN} \end{bmatrix}. \tag{6}$$

Step 2: Formation of the normalized decision matrix. The normalized value r_{ij} can be calculated using:

$$r_{ij} = \frac{x_{ij}}{\sqrt{\sum_{i=1}^{m} x_{ij}^2}}, \tag{7}$$

where: x_{ij} - performance score of alternative i with respect to criterion j.

Step 3: Definition of criterion weights and formation of the weighted normalized decision matrix. The weighted normalized value v_{ij} can be calculated using:

$$v_{ij} = w \cdot r_{ij}, \tag{8}$$

where: r_{ij} - normalized value,
w_j - criterion weight.

Step 4: Definition of the PIS and NIS. When defining the positive ideal in Equation (9) and negative ideal solution in Equation (10), it is crucial to adhere to the recommendation regarding whether the criteria are considered from a benefit or cost perspective.

$$v_{ij}^{+} = \{(\textstyle\sum_i^{\max} v_{ij}/j \in J);(\textstyle\sum_i^{\min} v_{ij}/j \in J')/ \; i = 1,2\ldots. n), \tag{9}$$

$$v_{ij}^{-} = \{(\textstyle\sum_i^{\min} v_{ij}/j \in J);(\textstyle\sum_i^{\max} v_{ij}/j \in J')/ \; i = 1,2\ldots. n), \tag{10}$$

Here, $J = (j = 1, 2, ..., n)/j$ refers to criteria considered from a benefit perspective, while $J' = (j = 1, 2, ..., n)/j$ refers to criteria considered from a cost perspective.

Step 5: Calculation of the distance of each alternative from the PIS D^+ (11) and NIS D^- (12) using the Euclidean distance:

Table 2 *Values of random consistency index depending on the number of criteria*

Number of criteria	1	2	3	4	5	6	7	8	9
Random consistency index RI	0.00	0.00	0.58	0.90	1.12	1.24	1.32	1.41	1.45

$$D_i^+ = \sqrt{\sum_{j=1}^{n} (v_{ij} - v_j^+)}\,, \tag{11}$$

$$D_i^- = \sqrt{\sum_{j=1}^{n} (v_{ij} - v_j^-)}\,. \tag{12}$$

Step 6: Calculation of the relative closeness to the ideal solution using:

$$C_i^+ = \frac{D_i^-}{(D_i^+ + D_i^-)}\,, \tag{13}$$

where C_i^+ is within the range $0 \leq C_i^+ \leq 1$.

Step 7: Ranking of alternatives. Based on the values of C_i^+, alternatives are ranked in descending order. The alternative with C_i^+ closest to 1 will be ranked as the 1st.

In this study, the AHP method was selected due to its capability to rank alternative criteria through a hierarchical structure, enabling clear definition and quantification of the weights of various safety factors in the optimization of gear pairs. In contrast, the TOPSIS method is well-suited for selecting the optimal solution through comparison to the ideal solution, thereby ensuring precise ranking of alternatives. This combination provides a systematic and efficient approach to optimization in line with the objectives of this study.

4 Optimization of gear pairs in planetary gear transmission

Before conducting the optimization of gear pairs in the planetary gear transmission, it is necessary to perform the kinematic and dynamic calculations of the planetary gear transmission (Figure 1). The concept of $B_{ha}{}^{b}$ shown in the Figure 1 consists of a central gear designated as “a”, located on the input shaft “I” of the planetary gear transmission, engaged with satellite gear “g”. Satellites “g” and “f” are mounted on shaft “II”, with satellite “f” engaged with an internally toothed central gear identified as “b”. The carrier of a satellite “h” is connected to the output shaft “III”.

After the calculation, the number of teeth for the gears of the planetary gear transmission was determined ($z_a = 21, z_g = 29, z_f = 40, z_b = 90$), satisfying all checks, and the number of satellites N = 3 was adopted. To optimize the gear pairs, 18 different alternatives were created using 3 input parameters (tooth width, module and material). Table 3 provides the values of the input parameters.

The aim of optimization is to obtain optimal values for the safety factor from pitting (Sh) and safety factor from the tooth breakage (Sf) for both gear pair. Since optimization is performed for both gear pairs, the criteria considered are Sh_1, Sf_1, Sh_2 and Sf_2. These criteria values are obtained based on the input parameters in the Auto-desk Inventor software package. Table 4 presents various variations of input and output parameters with criterion values.

4.1 Application of AHP and TOPSIS methods

The procedure for implementing these methods is described in the previous section, so here are presented only the results obtained from these methods. Based on the first step of the TOPSIS method, a decision matrix A was formed, followed immediately by the calculation of the normalized decision matrix, as shown in Table 4.

During the optimization, it is very important to correctly determine the criterion weights, considering

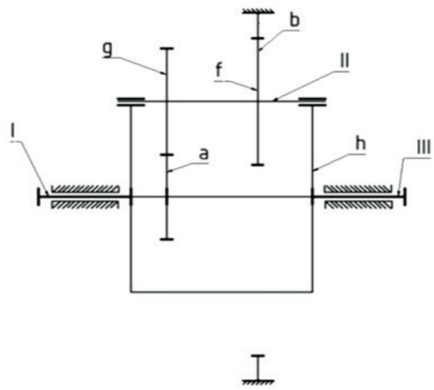

Figure 1 *Concept $B_{ha}{}^{b}$ of the planetary gear transmission*

Table 3 *Input parameters*

Parameter	Mark	Unit	Level I	Level II	Level III
Width of gear pair	b	mm	20	22	24
Module of gear pair	m	mm	2.25	2.5	2.75
Material of gear pair	M	/	1 (16MnCr5)	2 (34CrNiMo6)	/

that they have a key role in ranking the alternatives. Following this, the determination of criterion weights, using the AHP method, and formation of the weight-normalized decision matrix, were performed according to the steps described in the previous section. Criteria are assigned to output parameters. Criteria weights have been determined, with Sh_1 and Sh_2 each accounting for 33.3%, and Sf_1 and Sf_2 each accounting for 16.7%. Based on the calculated consistency ratio CR, which is 0, it can be concluded that the obtained criteria weights

Table 4 *Combinations of input parameters with the decision matrix*

Alter.	Parameters			Decision matrix				Normalized decision matrix			
	b	m	M	Sh_1	Sf_1	Sh_2	Sf_2	Sh_1	Sf_1	Sh_2	Sf_2
1	20	2.25	1	1.117	4.229	2.673	3.969	0.217	0.180	0.220	0.186
2	22	2.25	1	1.150	4.529	2.741	4.212	0.223	0.193	0.382	0.198
3	24	2.25	1	1.178	4.798	2.802	4.443	0.229	0.205	0.391	0.209
4	20	2.5	1	1.226	5.034	2.898	4.596	0.238	0.215	0.404	0.216
5	22	2.5	1	1.258	5.349	2.970	4.875	0.244	0.228	0.414	0.229
6	24	2.5	1	1.290	5.668	3.036	5.140	0.250	0.242	0.423	0.241
7	20	2.75	1	1.349	5.824	3.116	5.244	0.262	0.248	0.435	0.246
8	22	2.75	1	1.363	6.210	3.192	5.559	0.264	0.265	0.445	0.261
9	24	2.75	1	1.397	6.578	3.262	5.858	0.271	0.281	0.455	0.275
10	20	2.25	2	1.034	4.410	2.475	4.139	0.201	0.188	0.345	0.194
11	22	2.25	2	1.065	4.723	2.538	4.393	0.207	0.201	0.354	0.206
12	24	2.25	2	1.091	5.004	2.595	4.633	0.212	0.213	0.362	0.218
13	20	2.5	2	1.134	5.250	2.684	4.793	0.220	0.224	0.374	0.225
14	22	2.5	2	1.165	5.578	2.751	5.084	0.226	0.238	0.384	0.239
15	24	2.5	2	1.194	5.911	2.812	5.360	0.232	0.252	0.392	0.252
16	20	2.75	2	1.227	6.073	2.886	5.469	0.238	0.259	0.403	0.257
17	22	2.75	2	1.262	6.476	2.957	5.797	0.245	0.276	0.412	0.272
18	24	2.75	2	1.294	6.860	3.022	6.109	0.251	0.293	0.421	0.287

Table 5 *Determination of PIS, NIS, their distances, relative closeness and rank*

Alter.	Sh_1	Sf_1	Sh_2	Sf_2	D^+	D^-	C_i	Rank
1	0.372	0.706	0.073	0.031	0.028	0.456	0.943	1
2	0.383	0.756	0.127	0.033	0.083	0.399	0.827	3
3	0.392	0.801	0.130	0.035	0.121	0.353	0.745	5
4	0.408	0.841	0.135	0.036	0.161	0.311	0.659	7
5	0.419	0.893	0.138	0.038	0.212	0.257	0.549	9
6	0.430	0.947	0.141	0.040	0.264	0.203	0.434	11
7	0.449	0.973	0.145	0.041	0.295	0.174	0.371	13
8	0.454	1.037	0.148	0.044	0.357	0.109	0.235	15
9	0.465	1.099	0.151	0.046	0.418	0.047	0.101	17
10	0.344	0.736	0.115	0.032	0.052	0.429	0.893	2
11	0.354	0.789	0.118	0.034	0.094	0.375	0.799	4
12	0.363	0.836	0.121	0.036	0.139	0.328	0.702	6
13	0.378	0.877	0.125	0.038	0.181	0.284	0.611	8
14	0.388	0.931	0.128	0.040	0.236	0.229	0.493	10
15	0.398	0.987	0.131	0.042	0.292	0.174	0.373	12
16	0.409	1.014	0.134	0.043	0.321	0.144	0.310	14
17	0.420	1.081	0.137	0.045	0.388	0.080	0.170	16
18	0.431	1.146	0.140	0.048	0.453	0.036	0.074	18
PIS	0.344	0.706	0.073	0.031				
NIS	0.465	1.146	0.151	0.048				

***Table 6** Comparative overview of both gear pairs mass before and after the optimization*

	Before optimization		After optimization - alternative 1	
	gear pair *a-g*	gear pair *b-f*	gear pair *a-g*	gear pair *b-f*
Width of gear pair (mm)	25	25	20	20
Module of gear pair(mm)	2.5	2.5	2.25	2.25
Mass (kg)	1.065	3.641	0.794	2.359

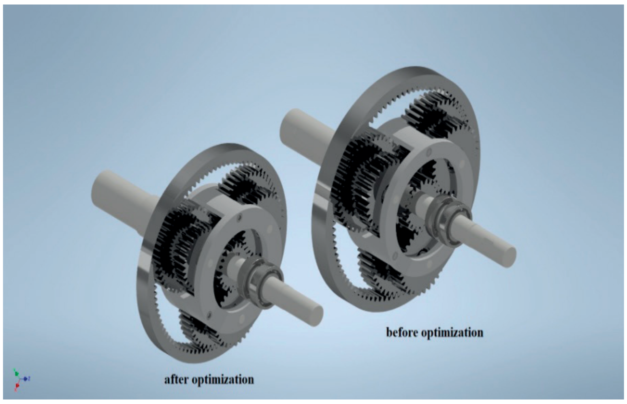

(a)

(b)

***Figure 2** Planetary gearbox: (**a**) gear pairs before and after optimization; (**b**) model*

are acceptable. Using the templates for forming the weight matrix of decision-making, the determination of the positive ideal solution (PIS) and negative ideal solution (NIS) is approached, with their values shown in Table 5. Table 5, also presents the distances of each alternative from the positive ideal solution D^+ and negative ideal solution D^- using the Euclidean distance, as well as the values of relative proximity to the ideal solution C_i. Finally, the last column displays the ranking of alternatives based on C_i.

As shown in Table 5, by ranking the values of C_i, it is concluded that the optimal parameter combination is alternative 1, where the parameter values are as follows: gear width 20 mm, module 2.25 mm, and material 1 (steel 16MnCr5). On the other hand, the least favorable parameter combination is alternative 18, where the parameter values are: width 24, module 2.75, and material 2 (34CrNiMo6). According to the chosen optimal version, the safety factor values Sh_1 and Sf_1 for the first gear pair are 1.117 and 4.229, respectively, while for the second gear pair Sh_2 and Sf_2 are 2.673 and 3.969, respectively.

Authors often justify or even accept the second-ranked alternative alongside the top-ranked alternative as the optimal solution in lot of scientific papers. This occurs in specific cases where the top-ranked alternative, due to various factors, cannot be selected as the most favorable solution. In this study, based on the results, it is observed that alternative 10 is ranked 2, and in the cases where alternative 1, for some reason cannot be accepted, alternative 10 would be considered as the optimal solution.

4.2 Analysis and discussion of results

The optimization of gear pairs achieved satisfactory results concerning the mass and overall dimensions, primarily of the gear pairs and subsequently of the entire planetary gearbox. Reducing the mass significantly impacts the inertia of the gearbox, which contributes to increased efficiency by reducing the energy required for the gearbox's operation and movement. Considering that planetary gearboxes are more expensive than other power transmissions, it is crucial to minimize production costs as much as possible. By reducing the mass and, consequently, the overall dimensions the consumption of materials and the time required for manufacturing are directly impacted, dictating the final costs of the planetary gearbox.

Besides the manufacturing costs and achieving greater efficiency, the power transmissions may encounter issues during handling and assembly. The reduction in mass positively affects easier handling, transport and assembly. Table 6 provides a comparative overview of data related to the width, module, mass and overall dimensions of gear pairs a-g and b-f before and after the optimization.

Given that the values of the width and module for both gear pairs are smaller after optimization, there has been a reduction in the mass and dimensions of the tip diameters. Consequently, during the design process, the housing, shafts, and the carrier of the satellites would have smaller dimensions and mass, which would further contribute to savings in materials and production resources. After applying the optimization methods to both gear pairs and obtaining the necessary results, modeling and assembly of the planetary gearbox elements into a single unit were performed. The dimensions of the carrier were adjusted according to the values obtained from the optimization, while the dimensions of the shafts remained the same. Figure 2a illustrates the difference in the gear pair a-g and b-f before and after optimization, while Figure 2b shows the model of a planetary gearbox.

The application of optimization methods on gear pairs is increasing, many researchers use optimization methods in their studies and scientific papers, striving to achieve the best possible results in this field. Singh et al. [22] optimized the surface temperature, wear rate and efficiency of polymer gears produced by injection molding using a combination of AHP-TOPSIS methods. For the optimization, 27 different combinations were created. The input parameters were material (ABS, HDPE and POM), rotational speed (600, 900 and 1200 min^{-1}) and torque (0.8, 1.2 and 1.6 Nm). The output values, or criteria, included the surface temperature, wear rate and efficiency. The results showed that the best performance of polymer gears is achieved with POM material, at 900 min^{-1} and 0.8 Nm. Nasr et al. [8], applied the Genetic Algorithm to optimize a planetary gearbox. The aim of the optimization was to reduce the weight and increase the gear ratio, while maintaining the safety factor within permissible limits. The input parameters included module, number of teeth, width, internal diameter of the central gear and satellite gears, and external diameter of the internally toothed gear. Various material types were studied, including the low alloy steel, stainless steel, aluminum and PET plastic. The results showed that the greatest weight savings in the planetary gearbox were achieved using the PET plastic gears. Miladinovic et al. [24] focused on the optimization of a Ravigneaux planetary gearbox. The goal was to reduce the weight, while considering the safety factor values. The input parameters considered were three different types of materials, three module values and three gear width values. The Taguchi and ANN methods were used for optimization and it was concluded that the module had the most significant impact on the safety factor, while the gear width had the least impact. Miladinovic et al. [25] applied the Taguchi method in their research to select optimal parameters for the driving gear in a planetary gearbox. For optimization, an L18 matrix was created with input parameters including module, material and gear width. The ANOVA analysis was used to determine the influence of parameters on the safety factor. The results showed that the module had the most significant influence on the safety factor against tooth flank failure at 80.953%, while the material had the least influence at 0.615%. The width had an influence of 18.392% on the safety factor. The Taguchi method yielded the optimal combination of parameters, where the module value was 2.25 mm, width 27 mm and material 16MnCr5. Gupta et al. [26] focused on selecting the optimal material for the production of gears in a planetary gearbox. The eight different materials were considered, with mechanical properties (tensile strength, yield strength, hardness) and costs being the criteria for optimization. In their study, next to the TOPSIS method, the COPRAS was, also applied. Comparing the results, they concluded that the optimal material for gear production is EN30A, with EN24 being the next best option.

Based on the previous research, it is planned to include the following elements in the future optimization process, when designing the planetary gear transmission, namely: housing, shafts, satellite carrier and the selection of suitable bearings. Special attention will be paid to the reduction of dimensions, which would result in additional weight reduction without compromising the reliability of the planetary gear transmission. This weight reduction contributes to savings in material and other resources required to manufacture the planetary gears. Therefore, it is recommended that the mentioned elements be included in the optimization process, which would enable a comprehensive analysis of the entire transmission with a special emphasis on dimensions. Such an approach can further improve the efficiency, reduce the production costs and contribute to development of modern, economical mechanical systems, thus ensuring the long-term sustainability and reliability of those transmissions.

5 Conclusions

Throughout the history, mechanical transmissions have played a significant role in various industrial and transportation systems. Their historical development reflects continuous improvements and the discovery of new, innovative solutions aimed at enhancing performance, efficiency and reliability. The application of planetary gear transmissions is diverse, encompassing a wide range of industries such as automotive, aerospace, mechanical and others.

Optimization methods play a crucial role in achieving the desired performance of planetary gear transmissions. Scientists continuously research and strive not only to discover new methods but to improve and refine existing ones to adapt them to specific problems, as well.

Based on the conducted optimization, the optimal variant of parameters was determined to achieve the optimal values of the safety factor from pitting (Sh) and the safety factor from tooth breakage (Sf) for both gear pairs. The key findings from this study indicate that the optimal parameters for the gear pairs are: the width of 20 mm, module of 2.25 mm and material 16MnCr5. The optimal combination of parameters is specified by alternative 1, where the parameter values are as follows: gear pair width of 20 mm, gear pair module of 2.25 mm, and gear pair material of

16MnCr5. The optimization of gear pairs results in approximately a 20% reduction in the weight of the planetary transmission, which subsequently reduces the transmission's inertia, contributing to increased efficiency in terms of reduced energy required for starting and operating the planetary transmission. Given that the planetary gear transmissions are significantly more expensive than other power transmissions, it is essential to contribute as much as possible to reducing the production costs. This optimization not only improves efficiency, but contributes to lowering the operating costs and extending the lifespan, as well. Therefore, during the design of other elements of the optimized transmission, such as the housing, shafts, satellite carrier, and the selection of appropriate bearings, the dimensions would be smaller, the weight reduced, leading to savings in material and other resources needed for production of the transmission. Reduction of the transmission weight directly contributes to the reduction of production costs, which is crucial in a competitive environment. More efficient, lighter and longer-lasting transmissions not only improve operational performance, but also enable companies to remain competitive on the market. This approach can significantly impact the reduction of wear, weight, inertia, vibrations, and noise, while also increasing the durability and robustness of these elements.

This also marks the direction for the future research, optimizing other elements of the transmission, where innovative materials, particularly hybrid composite materials, can be considered for the production of gear pairs. Additionally, the recommendation would be to use other optimization methods to verify the results obtained by this method. Further research should focus on investigating the effect of different materials and optimization methods on performance and reliability of the transmission. Research of efficiency, based on determination of the optimal types of materials, as well as the application of some new materials, can significantly change the dynamics of the transmission, which directly affects reliability. In addition to the types of materials, optimization can include various parameters related to the technology of manufacturing the transmission elements, with the aim of obtaining the highest quality parts, while reducing the costs and the production time.

Acknowledgment

The authors received no financial support for the research, authorship and/or publication of this article.

Conflicts of interest

The authors declare that they have no known competing financial interests or personal relationships that could have appeared to influence the work reported in this paper.

References

[1] TANASIJEVIC, S., VULIC, A. Mechanical transmissions: planetary transmissions, variators (in Serbian). Kragujevac: Faculty of Mechanical Engineering in Kragujevac, 2006.

[2] STANOJEVIC, M., TOMOVIC, R., IVANOVIC, L., STOJANOVIC, B. Critical analysis of design of Ravigneaux planetary gear trains. *Applied Engineering Letters* [online]. 2022, **7**(1), p. 32-44. ISSN 2466-4677, eISSN2466-4847. Available from: https://doi.org/10.18485/aeletters.2022.7.1.5

[3] ZORKO, D., DEMSAR I., TAVCAR, J. An investigation on the potential of bio-based polymers for use in polymer gear transmissions. *Polymer Testing* [online]. 2021, **93**, 106994. ISSN 0142-9418, eISSN1873-2348. Available from: https://doi.org/10.1016/j.polymertesting.2020.106994

[4] VASILEIOU, G., ROGKAS, N., MARKOPOULOS, A., SPITAS, V. Fully ceramic versus steel gears: potential, feasibility and challenges. *Proceedings of the Institution of Mechanical Engineers, Part C: Journal of Mechanical Engineering Science* [online]. 2024, **238**(3), p. 775-784. ISSN 0954-4062, eISSN2041-2983. Available from: https://doi.org/10.1177/09544062231198633

[5] WALLER, M., MCINTYRE, S., KOUDELA, K. Composite materials for hybrid aerospace gears. *Journal of the American Helicopter Society* [online]. 2020, **65**(4), p. 1-11. Available from: https://doi.org/10.4050/JAHS.65.042010

[6] YOUNES, E., CHANGENET, C., BRUYERE, J., RIGAUD E., PERRET-LIAUDET, J. Multi-objective optimization of gear unit design to improve efficiency and transmission error. *Mechanism and Machine Theory* [online]. 2022, **167**, 104499. ISSN 0094-114X, eISSN1873-3999. Available from: https://doi.org/10.1016/j.mechmachtheory.2021.104499

[7] SHAHABI, A., KAZEMIAN, A. H. Dynamic and vibration analysis for geometrical structures of planetary gears. *Journal of Solid Mechanics* [online]. 2021, **13**(4), p. 384-398. ISSN 2008-3505, eISSN 2008-7683. Available from: https://doi.org/10.22034/jsm.2020.1898690.1585

[8] NASR, M., MAALAWI, K., YIHIA, K. multi-objective optimization of planetary gear train using genetic algorithm. *Journal of International Society for Science and Engineering* [online]. 2022, **4**(3), p. 74-80. ISSN 2636-4425, eISSN2682-3438. Available from: https://doi.org/10.21608/jisse.2022.144284.1059

[9] XU, X., CHEN, J., LIN, Z., QIAO, Y., CHEN, X., ZHANG, Y., XU, Y., LI, Y. Optimization design for the planetary gear train of an electric vehicle under uncertainties. *Actuators* [online]. 2022, **11**(2), 49. eISSN 2076-0825. Available from: https://doi.org/10.3390/act11020049

[10] KORTA, J., MUNDO, D. Multi-objective micro-geometry optimization of gear tooth supported by response surface methodology. *Mechanism and Machine Theory* [online]. 2017, **109**, p. 278-295. ISSN 0094-114X, eISSN1873-3999. Available from: https://doi.org/10.1016/j.mechmachtheory.2016.11.015

[11] LI, M., LUO, Y., QU, L., XIE, L., ZHAO, B. Influence of ring gear flexibility on the fatigue reliability of planetary gear systems in heavy helicopters. *Mechanism and Machine Theory* [online]. 2024, **191**, 105520. ISSN 0094-114X, eISSN1873-3999. Available from: https://doi.org/10.1016/j.mechmachtheory.2023.105520

[12] TIAN, H., HAN, H., ZHAO, Z., HAN, C., MA, H. Wear prediction and meshing characteristics for the planetary gear set considering angular misalignment and rotating carrier. *Engineering Failure Analysis* [online]. 2022, **140**, 106583. ISSN 1350-6307, eISSN1873-1961. Available from: https://doi.org/10.1016/j.engfailanal.2022.106583

[13] HUANGFU, Y., DONG, X., CAO, Y., LI, Z., PENG, Z., SUN, Y. A life-cycle dynamic wear degradation model of planetary gear systems. *Wear* [online]. 2024, **542-543**, 205281. ISSN 0043-1648, eISSN1873-2577. Available from: https://doi.org/10.1016/j.wear.2024.205281

[14] SIMIC, S., MILOSEVIC, M., KOSEC, B., BOZIC, D., LUKIC, D. Application of the multicriteria decision-making for selecting optimal maintenance strategy. *Advanced Engineering Letters*[online].2024, **2**(4), p. 151-160. eISSN 2812-9709. Available from: https://doi.org/10.46793/adeletters.2023.2.4.3

[15] CHAKLADAR, N. D., CHAKROBORTY, S. A combined TOPSIS-AHP method based approach for non-traditional machining process selection. *Proceedings of the Institution of Mechanical Engineers Part B Journal of Engineering Manufacture* [online]. 2008, **222**, p. 1613-1623. ISSN 0954-4054, eISSN2041-2975. Available from: https://doi.org/10.1243/09544054JEM1238

[16] ISWARI, V., ARINI, F., MUSLIM, M. Decision support system for the selection of outstanding students using the AHP-TOPSIS combination method. *Lontar Komputer: Scientific Journal of Information Technology* [online]. 2019, **10**(1), p. 40-48. ISSN 2088-1541, eISSN 2541-5832. Available from: https://doi.org/10.24843/LKJITI.2019.v10.i01.p05

[17] SAATY, T., VARGAS, L., ST, C. *The analytic hierarchy process*. Springer, 2022. ISBN 978-1-4614-3597-6.

[18] EMOVON, I., OGHENENYEROVWHO, O. Application of MCDM method in material selection for optimal design: a review. *Results in Materials* [online]. 2020, **7**, 100115. eISSN 2590-048X. Available from: https://doi.org/10.1016/j.rinma.2020.100115

[19] MOUSAVI-NASAB, S. H., SOTOUDEH-ANVARI, A. A comprehensive MCDM-based approach using TOPSIS, COPRAS and DEA as an auxiliary tool for material selection problems. *Materials and Design* [online]. 2017, **121**, p. 237-253. ISSN 0264-1275, eISSN1873-4197. Available from: https://doi.org/10.1016/j.matdes.2017.02.041

[20] TIWARI, S. K, PANDE, S. Selection of gear manufacturing process using MCDM-TOPSIS approach. *International Journal of Production Engineering*[online]. 2017, **3**, p. 7-13. eISSN2340-4876. Available from: https://doi.org/10.37628/ijpe.v3i2.373

[21] TERAN, C. V., MARTINEZ-GOMEZ, J., MILLA., J. C. L. Material selection through of multi-criteria decisions methods applied to a helical gearbox. *International Journal of Mathematics in Operational Research*[online]. 2020, **17**(1), p. 90-109. ISSN 1757-5850, eISSN1757-5869. Available from: https://doi.org/10.1504/IJMOR.2020.109035

[22] SINGH, P. K., SINGH, A. K., SIDDHARTHA, SARKAR, P. Optimizing the performance parameters of injection-molded polymer spur gears. *Proceedings of the Institution of Mechanical Engineers, Part L: Journal of Materials: Design and Applications* [online]. 2021, **235**(4), p. 717-727. ISSN 1464-4207, eISSN2041-3076. Available from: https://doi.org/10.1177/1464420720977561

[23] GAJEVIC, S., MARKOVIC, A., MILOJEVIC, S., ASONJA, A., IVANOVIC, L., STOJANOVIC, B. Multi-objective optimization of tribological characteristics for aluminum composite using Taguchi Grey and TOPSIS approaches. *Lubricants* [online]. 2024, **12**(5), 171. eISSN 2075-4442. Available from: https://doi.org/10.3390/lubricants12050171

[24] MILADINOVIC, S., GAJEVIC, S., STOJANOVIC, B., MILOJEVIC, S. Optimization of Ravigneaux planetary gear set. *IETI Transactions on Engineering Research and Practice*[online]. 2018, **12**, p. 34-41. eISSN2616-1699. Available from: https://doi.org/10.6723/TERP.201812_2(2).0005

[25] MILADINOVIC, S., GAJEVIC, S., NOVAKOVIC, M. Application of Taguchi method for the selection of optimal parameters of planetary driving gear. *Applied Engineering Letters*. 2016, **1**, p. 98-104. ISSN 2466-4677, eISSN2466-4847.

[26] GUPTA, D., PHADATARE, K., SHAIKH, A., PAWALE, M. Material optimization of gear and pinion for planetary gearbox. Project report. Mumbai: University of Mumbai, 2014.

JUSTIFICATION OF THE METHOD OF VEHICLE ENGINE RADIATOR ULTRASONIC CLEANING

Baurzhan Moldabaev[1], Kirill Sinelnikov[2], Aliya Kukesheva[2,*]

[1]NJSC E. A. Buketov Karaganda University, Karaganda, Republic of Kazakhstan
[2]NPJSC Abylkas Saginov Karaganda Technical University, Karaganda, Republic of Kazakhstan

*E-mail of corresponding author: aliya.kukesheva@bk.ru

Baurzhan Moldabaev 0000-0002-2102-1834, Kirill Sinelnikov 0000-0001-5073-5716, Aliya Kukesheva 0000-0002-3063-5870

Resume

The article presents theoretical and experimental results on ultrasonic cleaning of a vehicle radiator. Criterion relationships between ultrasound energy, kinetic energy of the liquid, and shock wave energy were established, enabling the evaluation of cavitation energy efficiency and cleaning effectiveness. Experimental confirmation was obtained using a developed full-size bench. Using the developed full-size bench, the numerical values of parameters were obtained that made it possible to calculate the values of energies involved in the cavitation process, the ratio of which allows evaluating the effectiveness of washing the radiator from scale. The cavitation coefficient of erosion efficiency was established, proving the effectiveness of ultrasonic cleaning. Results confirm the applicability of this method for cleaning the vehicle radiators.

Article info

Received 4 August 2024
Accepted 26 November 2024
Online 13 December 2024

Keywords:

cooling system
ultrasound energy
kinetic energy of liquid
shock wave energy
similarity theory and dimensional analysis
cavitation coefficient
erosion efficiency

Available online: https://doi.org/10.26552/com.C.2025.015

ISSN 1335-4205 (print version)
ISSN 2585-7878 (online version)

1 Introduction

The internal combustion engine (ICE) is the main part of a vehicle that combines a lot of integrated systems and ensures their proper operation, however, the operation of the internal combustion engine results in air pollution due to exhaust gases. The failure of almost any system involved in the engine operation leads to increased formation of harmful and toxic substances in the processed gases, which, in turn, has an impact on the environment, harms human health and contributes to the development of serious diseases [1-3]. One of the main components of the internal combustion engine is the cooling system that removes excess heat from the engine elements and maintains the optimal operating temperature.

If the operating temperature in the cooling system is disrupted, this leads to the overheating of the engine that subsequently causes irreversible consequences in violating its technical condition, performance and failure of the other systems involved in the operation of the internal combustion engine [4].

This in turn leads to increased air pollution and the risk of various diseases.

In general, the cooling system malfunctions account for about 25-30% of all the internal combustion engine failures. One of the main malfunctions of the cooling system is its overheating. Overheating can be caused for various reasons. The most common cause of this malfunction is the formation of scale on the system elements. The appearance of scale depends on various factors, such as: untimely vehicle maintenance, oil getting into the antifreeze, radiator tightness, quality of detergents, rust formation on the internal surfaces of the system and the effect of decomposition products of antifreeze components. The combination of these factors leads to the scale depositing on the elements of the cooling system, in particular on the walls of the cooling jacket, which contributes to decreasing the heat transfer between the system parts and subsequent clogging of thin channels and tubes of vehicle radiators [5].

The radiator, being one of the main elements of the internal combustion engine cooling system, consists of thin-walled tubes through which the coolant flows. This component ensures the required operating temperature of the engine coolant, while giving off the excess heat to the flow of oncoming air.

Radiators are descaled using mechanical and chemical methods. The mechanical cleaning method is characterized by high labor intensity and the accompanying large expenditure of time and money on the cleaning process. During the mechanical cleaning, radiator tubes are often damaged and become unusable [6].

The chemical method for descaling radiators involves flushing with distilled water and adding various chemical agents. Radiators made from different metals, such as aluminum, brass, copper, or galvanized steel, are subject to different risks when using such methods.

Aluminum radiators are particularly vulnerable to corrosion caused by acidic or alkaline cleaning agents. Incorrect chemical selection can lead to damage to aluminum surfaces, formation of holes, and leaks.

While the copper and brass radiators are more resistant to corrosion, they can also suffer from aggressive chemicals, which may cause copper leaching and solder degradation. Acids can destroy the zinc coating on galvanized steel, leading to corrosion of the steel base.

Copper, with its excellent thermal conductivity, is an effective material for radiators as it helps to dissipate engine heat more quickly. However, aluminum radiators are lighter and less costly to manufacture, making them the preferred choice for modern vehicles.

As a result, it can be concluded that chemical methods for cleaning radiators have significant disadvantages, including high physical and time costs for the cleaning process and a destructive impact on the radiator's functional condition.

In this regard, we propose the use of an ultrasonic cleaning method for descaling the radiator tubes. Under the influence of ultrasound, the speed and level of liquid movement inside the radiator are significantly increased, facilitating its penetration into the internal surface of the scale buildup [7].

In industry and mechanical engineering, there are widely used methods to achieve various purposes using ultrasonic impact, for example, cleaning, welding, flaw detection, machining and cutting. In recent years, a number of successful studies have been carried out to reduce the harm of exhaust gases and to analyze their impact [8-11]. New methods of cleaning the exhaust gases and vehicle radiators by cavitation and coagulation using ultrasonic impact are being considered [12-13].

The cleaning process is characterized by the joint manifestation of various nonlinear effects that arise in the liquid when they are affected by ultrasonic vibrations. In particular, when cleaning radiator tubes with ultrasound, the cavitation effect is observed that arises from the energy of the ultrasonic wave and depends on changing the parameters of the intensity and pressure of the shock waves. Under the effect of cavitation, in the liquid cavitation bubbles form that collapse near the contaminants and destroy the scale layer and the other deposits [14].

In general, the ultrasonic method does not require significant use of manual labor and the other mechanical effects from the outside, thereby greatly simplifying the cleaning process.

In connection with the above, the proposed method of cleaning the vehicle radiator from the scale is relevant.

The research hypothesis is the probability of cleaning the radiator using the ultrasonic impact.

The purpose of the study is to establish the dependences that determine the mode and efficiency of the ultrasonic cleaning process for radiators of internal combustion engines.

To achieve the goal of the study, the following tasks were solved: the physical essence of the cavitation process was considered; criterion energy dependences were obtained that allowed evaluating the energy efficiency of the cavitation process when cleaning the radiator with ultrasound; an experimental bench for radiator cleaning was developed and the results were analyzed; the cavitation coefficient of erosion activity was obtained, the numerical value of which confirmed the effectiveness of radiator cleaning by ultrasound.

The scientific novelty lies in obtaining dependences that allow designing the technology of cleaning radiators with ultrasound.

The practical significance lies in obtaining calculated dependences and the algorithm of the cleaning process.

2 Materials and methods

The physical essence of the process of cleaning radiator tubes by cavitation is as follows. Cavitation refers to the formation of pulsating bubbles filled with gas in a liquid. In an ultrasonic wave, during the half-periods of rarefaction, cavitation bubbles appear that collapse sharply after moving to the region of increased pressure generating strong hydrodynamic disturbances in the liquid and intense radiation of acoustic waves. At the same time, destruction of the surfaces of solid bodies adjacent to the cavitating liquid occurs in the liquid.

The general picture of the process of cavitation formation in the liquid is presented in the following form. The liquid is exposed to low-intensity ultrasonic vibrations. It is known that an ultrasonic wave passing through the liquid forms compression zones and rarefaction zones changing places in each half-cycle of the wave and characterized by the appearance of alternating pressure. As the intensity of ultrasound increases, the violation of the liquid homogeneity is observed. In the rarefaction phase (low pressure), emission of dissolved gases begins in the weakest places with formation of one long-lived bubble. In this case, the resulting bubble oscillates linearly with the ultrasound frequency relative to its equilibrium radius R. It is obvious that the maximum amplitude A will be observed in bubbles resonant for a given frequency f, therefore, in the compression phase, under the effect of increased pressure and surface tension forces, the bubble collapses. Further increasing of the intensity leads to violation of the linearity of the bubble walls vibrations. The stage of stable cavitation begins, in which the bubble itself becomes a source of ultrasonic vibrations. In this regard, waves, microcurrents and electrical discharges appear on its surface. When the intensity value reaches more than I >2.5 W/cm^2, the stage of unstable cavitation occurs that is characterized by the formation of rapidly growing gas bubbles that, in the compression phase, instantly contract in volume and collapse [15].

At the moment of collapse, the pressure and temperature of the gas reach significant values (according to some sources, up to 100 MPa and 10,000 ^{0}C). After the bubbles collapse, a spherical shock wave propagates in the surrounding liquid and quickly decays in space. The collapse means the following phenomenon: decreasing the radius R of the bubble to the minimum value R_{min} or decreasing the radius of the cavity, that is, its deformation and disintegration into several bubbles [16].

A review of publications and patents on the research topic demonstrates that ultrasonic cleaning, due to the phenomenon of cavitation, is an effective and environmentally friendly method for cleaning vehicle radiators from rust and other contaminants. Authors of [17] discussed approaches to optimizing ultrasonic cleaning for different types of contaminants, including rust, and the importance of ultrasonic wave frequency in enhancing the cleaning process's efficiency.

Kamar et al. described the process of cleaning the heat exchangers in [18]. They explained in detail how ultrasonic cavitation helps remove deposits and scale, while also increasing heat transfer efficiency. Patent US4705054A, titled "Ultrasonic Radiator Cleaning System," describes a cleaning system using ultrasound, specifically designed for heat exchangers and vehicle radiators. The patent covers the design of ultrasonic baths used for effectively removing contaminants [19].

Additionally, patent US20120291657A1, "Ultrasonic Cleaning Apparatus," describes an ultrasonic device for cleaning various surfaces, including vehicle parts. The system uses acoustic cavitation in liquids to clean rust and other contaminants [20].

Acoustic cavitation in liquids initiates various physical and chemical phenomena, such as sonoluminescence (glow of liquids); chemical effects (sound-chemical reactions); dispersion (grinding solid particles in the liquid), emulsification (mixing and homogenizing immiscible liquids) and mechanical erosion (destruction of surfaces) [21].

Mechanical erosion leads to destruction and cleaning of the interacting surface due to the formation of the cavitation region based on two characteristic manifestations of cavitation: shock waves and cumulative jets formed during the collapse of cavitation bubbles. Cumulative streams destroy the surface of a solid body due to the kinetic energy of the liquid. Small particles of a solid body, the dimensions of which are commensurate with the cross section of the cumulative jets, are carried away by them and make an additional contribution to the process of destruction of solid particles in the liquid [22].

Some of the energy of the primary sound field is spent for forming the cavitation region. At the stage of formation of the cavitation region, the field energy is spent for the appearance and growth of cavitation bubbles. The primary energy cannot be spent only for the formation of cavitation, since if the value of the primary energy of the sound field is lower than the energy spent for formation of cavitation $E<E_{cav}$, then the duration of the cavitation process will immediately stop. Consequently, part of this energy is given back when the bubbles collapse in various forms, primarily in the form of shock waves capable of producing mechanical erosion, which is effective in ultrasonic cleaning processes. Thus, the ratio of the energy spent for the formation of cavitation to the total energy of the primary sound field gives the parameter of the coefficient of cavitation utilization of acoustic energy, the value of which should not be greater than 1 $x<1$:

$$x = \frac{E_{cav}}{E}, \tag{1}$$

where E_{cav} is the energy spent for forming cavitation;
E is the total energy of the primary sound field.

If to denote the energy emitted in the form of shock waves by E_m and to relate it to the energy of the primary sound field, then their ratio will give the parameter that evaluates the measure of the erosive activity of cavitation or the cavitation coefficient of erosive efficiency:

$$\varepsilon = \frac{E_m}{E}, \tag{2}$$

where E_m is the energy given in the form of shock waves.

By definition, it is clear that the value of the parameter ε should not be greater than ε < 1. However, the closer the value of ε is to 1, the higher the erosive activity of the cavitation process.

It is known that for the appearance of mechanical erosion it is necessary that the values of the resulting mechanical stresses exceed their threshold values. Mechanical stresses are aimed at weakening the adhesion forces of the surfaces of the cleaned bodies interacting with the liquid, which lead to their subsequent separation and displacement from the surface during the cleaning process. Mechanical stresses are determined by the pressure of the shock wave. If the pressure of the shock wave exceeds the threshold stress values, then this can cause mechanical destruction (erosion), in which case the total volume of destruction will be proportional to the coefficient ε.

Currently, there is no satisfactory model of the cavitation region that adequately describes its behavior and the action of the individual cavitation bubble belonging to it. After all, the behavior of the cavitation region depends on many phenomena and factors that are completely impossible to take into account. In this case, the method of similarity theory and the dimensional analysis was used, since it is very effective in the analysis of complex processes, the mathematical description of which is difficult to form. In addition, this method allows establishing the characteristic and convenient parameters that determine the main effects and modes of the processes. At the same time, the combination of this method with thea general qualitative analysis of the mechanism of physical phenomena can be a fruitful theoretical method of research in a number of cases.

In accordance with the provisions of the method of similarity theory and dimensional analysis [23], the following fundamental variables were considered, taking into account the main factors of the cavitation region and allowing one to set parameters describing the process of ultrasonic radiator cleaning: the tube radius *(r)*, the tube length *(l)*, the section layer *(Δ)*, the fluid density *(ρ)*, the gravitational acceleration *(g)*, the ultrasonic exposure time *(t)*, the ultrasonic wave intensity *(I)*, and the shock wave pressure *(P)*. As a result, eight fundamental variables were obtained that depend on the shock wave pressure, the functional relationship of which can be written in the following form:

$$P = f(r, l, \Delta, \rho, g, t, I). \tag{3}$$

From here there follows such an equation:

$$\varphi\left(r, l, \Delta, \rho, g, I, \frac{P}{t}\right) = 0. \tag{4}$$

Then, the resulting variables are transformed by expressing their dimension in relation to three basic units of measurement: length L, mass M and time T (Table 1).

It is assumed that the number of basic dimensionless parameters through which all n variables can be expressed is equal to m. According to the resulting equation (Equation (4)), the number of variables is equal to n = 7, and the number of basic units of measurement is equal to k=3, in accordance with the ϖ-theorem, the number of basic dimensionless parameters will be equal to: $m = n - k = 7 - 3 = 4$. Therefore, the following equation is obtained:

$$\pi = \varphi(\pi_1, \pi_2, \pi_3, \pi_4). \tag{5}$$

From here there follows the equation:

$$\varphi(\pi_1, \pi_2, \pi_3, \pi_4) = 0, \tag{6}$$

where $\pi_1, \pi_2, \pi_3, \pi_4$ are dimensionless parameters that are determined as follows.

From n variables, three are selected, with independent dimensions, including three basic units (length L, mass M and time T); let this be the radius *(r)* of the radiator tube, the density of the liquid *(ρ)* and the acceleration of gravity *(g)*.

Then, the dimensionless parameters π_1, π_2, π_3 and π_4 were defined. The selected three variables (r, ρ, g) were included in each of the ϖ-terms, the remaining variables, namely: $\Delta, I, l, \frac{P}{t}$, were then, one at a time, included in the previously formed ϖ-terms with three main variables. The exponents of the three main variables that determine the dimensionless parameters are unknown, therefore they are denoted as x, y and z. The exponents of the remaining variables are accepted equal to -1. As a result, the relations for ϖ - terms will have the following form:

$$\pi_1 = r^{x1} \rho^{y1} g^{z1} \Delta^{-1}; \tag{7}$$

$$\pi_2 = r^{x2} \rho^{y2} g^{z2} I^{-1}; \tag{8}$$

$$\pi_3 = r^{x3} \rho^{y3} g^{z3} l^{-1}; \tag{9}$$

$$\pi_4 = r^{x4} \rho^{y4} g^{z4} \left(\frac{P}{t}\right)^{-1}. \tag{10}$$

The variables included in the ϖ-terms can be expressed in terms of basic dimensions. Since these terms are dimensionless, the exponents of each of the main dimensions must be equal to zero. As a result, for each of the ϖ-terms, three independent equations can be constructed (one for each dimension), which relate the exponents of the variables included in them. Solving the resulting system of equations makes it possible to

Table 1 *List of dimensional formulas for the basic variable values*

N	Variable	Designation	Unit	Dimensional formula
1	Tube radius	r	m	L
2	Tube length	l	M	L
3	Parcel layer	Δ	M	L
4	Liquid density	ρ	kg/m^3	ML^{-3}
5	Acceleration of gravity	g	m/s^2	LT^{-2}
6	Ultrasound exposure time	t	S	T
7	Ultrasonic wave intensity	I	W/m^2	M T^{-3}
8	Shock wave pressure	P	Pa	ML^{-1} T^{-2}

find the numerical values of the unknown exponents *x, y* and z. As a result, each of the ϖ-terms is defined in the form of a formula composed of specific quantities to the appropriate degree.

Then, the dimension equation for the first π -terms is composed:

$$\pi_1 = L^{x1}\left(\frac{M}{L^3}\right)^{y1}\left(\frac{L}{T^2}\right)^{z1}(L)^{-1}. \tag{11}$$

The exponents with the same bases are then added:

$$\pi_1 = L^{x1-3y1+z1-1}L^{y1}M^{-2z1}. \tag{12}$$

For the dimension π_1 to be equal to one, it is necessary to equate all the exponents to zero:

$$\begin{cases} x_1 - 3y_1 + z_1 - 1 = 0 \\ \quad - y_1 = 0 \\ \quad - 2z_1 = 0. \end{cases} \tag{13}$$

The system of algebraic equations contains three unknown quantities x_1, y_1, and z_1. By solving this system of equations it is found that $x_1 = 1$, $y_1 = 1$ and $z_1 = 1$.

Substituting these values of exponents into the first π_1 term, there is obtained the first dimensionless parameter:

$$\pi_1 = \frac{r}{\Delta}. \tag{14}$$

The similar calculation is then performed for the remaining ϖ-terms and the second, third and fourth dimensionless parameters are obtained:

$$\pi_2 = \frac{\rho rg\sqrt{rg}}{I}; \tag{15}$$

$$\pi_3 = \frac{r}{l}; \tag{16}$$

$$\pi_4 = \frac{\rho tg\sqrt{rg}}{P}. \tag{17}$$

Substituting the resulting ϖ-terms into Equation (4), the four dimensionless parameters are obtained:

$$\varphi\left(\frac{r}{\Delta}, \frac{\rho rg\sqrt{rg}}{I}, \frac{r}{l}, \frac{\rho rg\sqrt{rg}}{P}\right) = 0. \tag{18}$$

The equation for π_1 is then solved, where $\frac{r}{\Delta}$ to the left side of the equation $\frac{r}{\Delta}$ is derived. Then, the dimensionless parameters of the second, third and fourth ϖ-terms are reduced and a single criterion is obtained. Thus, one can write equation (18) in the following form:

$$\frac{r}{\Delta} = \varphi\left(\frac{Pl}{It}\right). \tag{19}$$

As mentioned earlier, mechanical stresses are determined by the the shock wave pressure. It should be understood as the force applied to the upper layer of liquid, causing displacement of the layers, namely the shear stress of the inner surface (scale) of the radiator tube relative to its cross-sectional area. Therefore, the pressure can be converted as the ratio of force to area:

$$P = F_p/S, \tag{20}$$

where F_p is the force conditioned by the shock wave pressure on the surface considered;
S is the cross-section area of the radiator tube.

Substituting this expression instead of P the following criterion is obtained as a result:

$$k_2 = \frac{F_p l}{SIt}. \tag{21}$$

It should also be noted that the intensity of ultrasonic vibrations is the amount of energy passing through the unit cross-sectional area of the radiator tube during the unit time of exposure to ultrasound. Therefore, it can be concluded that the product of area, ultrasound intensity and time gives the ultrasound energy parameter E_u. The product of the force, caused by the shock wave pressure, by the length of the radiator tube characterizes the work occurring inside the radiator's tube, which can be conditionally equated to the energy given off in the form of shock waves E_m. The energy of the shock wave contributes to formation of the mechanical stress on the scale area and leads to its subsequent separation from the inner surface of the tube. Then, the criterion obtained will have the following form:

$$k_2 = \frac{E_m}{E_u}. \tag{22}$$

The ultrasonic energy characterizes the total energy of the primary sound field that includes the energy spent for the formation of the cavitation process and the energy released in the form of shock waves.

Thus, the fundamental variables, which were selected, were reduced into dimensionless parameters and transformed into two similarity criteria:

$$k_1 = \frac{r}{\Delta}; \tag{23}$$

$$k_2 = \frac{E_m}{E_u}. \tag{24}$$

The first criterion k_1 characterizes the ratio of the geometric parameter of the radiator tube, namely the radius of the tube to the thickness of the scale. The second criterion k_2 characterizes the erosive efficiency of the cavitation process by the ratio of the energy released in the form of shock waves to the energy of the ultrasonic emitter.

Taking into account the law of conservation of momentum in a closed region, Borgnis derived an approximate theorem according to which it is believed that during the propagation of an acoustic wave, the energy of the sound field spent on the formation of cavitation E_{cav} is equal to the kinetic energy of the fluid flow E_{kin},:

$$E_{cav} = E_{kin} . \quad (25)$$

In addition, based on the approximate Borgnis theory, it is possible to determine the force due to the pressure of the ultrasonic wave through the force due to the energy of the sound field:

$$F = F_p + F_{kin} , \quad (26)$$

where F is the force caused by the energy of the sound field;
F_p is the force caused by the shock wave pressure on the surface considered;
F_{kin} is the force of the liquid flow kinetic energy.
It follows that

$$F_p = F - F_{kin} . \quad (27)$$

Having transformed equation (27) through the ultrasound energy and kinetic energy, one ultimately obtains the following equation, which allows to determine the force F_p caused by the the shock wave pressure:

$$F_p l = E_u - E_{kin} ; \quad (28)$$

$$F_p = \frac{E_u - E_{kin}}{l} , \quad (29)$$

where l is the radiator tube length.

From the obtained k_2 criterion is known that the product of the force caused by the shock wave pressure and the length of the radiator tube gives the energy released in the form of shock waves, $E_m = F_p l$.

The values of energy indicators, in particular the kinetic energy of the liquid in the radiator tube, were determined experimentally. For this purpose, the values of the parameters of mass and the liquid outflow from the radiator tube were set. To carry out the relevant experimental studies, a full-size test bench for ultrasonic cleaning of vehicle radiators was developed.

The bench is a setup (Figure 1) designed for cleaning radiators. It consists of the following elements: interior heater radiator 1, ultrasonic emitter 2; axial fan 3; circulation pump with heating element 4; filter 5; liquid reservoir 6; temperature control devices 7; rubber pipes 8.

The procedure of the experiment was as follows. At the preparatory stage, the setup for ultrasonic cleaning of radiators was assembled and connected. Then, the bench was filled with clean water and the parameters of this water were determined. At subsequent stages, water was heated to 50 °C. Next, ultrasound was applied to the radiator within various time intervals (600, 1200 and 1800 seconds), and then the liquid parameters (volume, mass, density and flow time) were determined. The final stage included saturation of water with air before exposure to ultrasound and analyzing the experimental results.

3 Results

According to the plan and procedure of the experiment, appropriate experimental studies were carried out, the results of which are presented in Table 2.

Based on the results of experimental studies (Table 2), calculations were carried out to determine the rate of fluid outflow, based on the parameters of the volume and time of fluid outflow. The following parameters were also determined by calculation: kinetic energy of the liquid, ultrasound energy and energy released in the form of shock waves. The calculation results are presented in Table 3.

Based on the calculation results, a graph of changing the parameters of mass and fluid flow rate was obtained,

1- interior heater radiator; 2 - ultrasonic emitter; 3 - axial fan; 4 - circulation pump with heating element; 5 - filter; 6 - liquid reservoir; 7 - temperature control devices; 8 - rubber pipes

***Figure 1** Mounting the emitter on the interior heater radiator*

***Table 2** Experimental study results*

Measured parameter	Unit	Exposure time, s.			
		0	600	1200	1800
Liquid volume (V)	ml	45	45	45	45
Liquid mass (m)	g	44.57	44.60	44.63	44.69
Liquid density (ρ)	g/cm^3	0.9904	0.9911	0.9917	0.9931
Effusion time (t)	s	9.93 s/l	9.73 s/l	9.22 s/l	9.20 s/l

***Table 3** Results of calculations*

Calculated parameter	Unit	Exposure time, s.			
		0	600	1200	1800
Effusion time, (ϑ)	Milliliter per second (ml/s)	100.7	102.7	108.45	108.69
Kinetic energy of the liquid flow, (E_{kin})	J	225.98 μJ	235.2 μJ	262.45 μJ	263.97 μJ
Ultrasound energy (E_u), (emitter power 50 W)	J	0	30 kJ	60 kJ	90 kJ
Energy given in the form of shock waves, (E_m)	J	-225.98 μJ	29 kJ	59kJ	89kJ

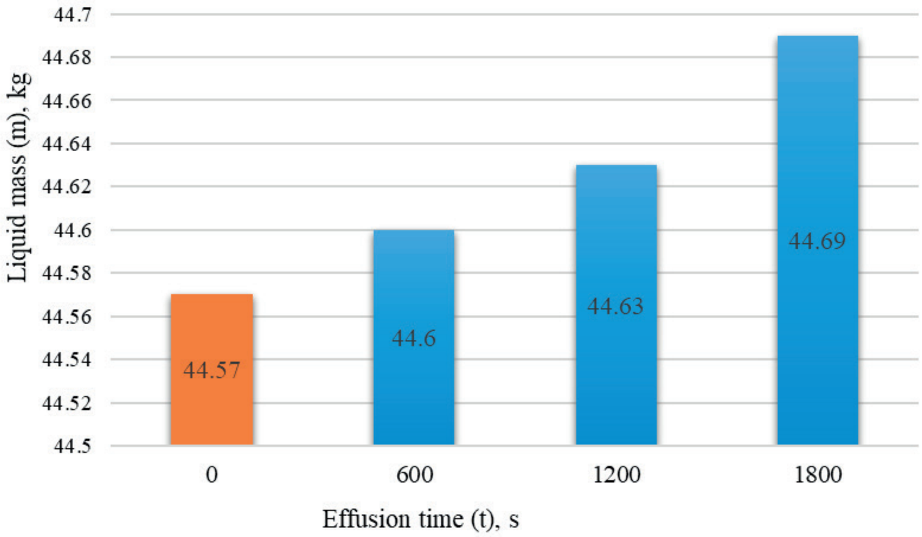

***Figure 2** Changing the liquid mass (m) depending on the time of exposure to ultrasound (t)*

as well as the graph of changing the energy versus the time of exposure to ultrasound, Figures 2 and 3, respectively.

From the dependences in Figures 2 and 3 it follows that with increasing the time of exposure to ultrasound, the mass and flow rate of liquid with scale increase compared to the mass and flow rate of the original liquid (not exposed to ultrasound). This is explained by the fact that a large amount of energy is formed in the liquid after exposure to ultrasound that is spent for formation of the cavitation process and leads to the washing of scale from the radiator tubes.

From Table 3 it follows that with increasing the time of exposure to ultrasound, the energy of the liquid increases. This increase in energy leads to the more efficient removal of contaminants from the radiator tubes and improved cleaning efficiency.

According to calculations, based on the obtained energy indicators, the numerical values of the coefficient of cavitation use of acoustic energy and the cavitation coefficient of erosion efficiency were calculated.

The coefficient of cavitation use of acoustic energy is determined as follows:

$$\begin{aligned} x &= \frac{E_{cav}}{E} = \frac{E_{kin}}{E_u}; \\ x_1 &= 0; \\ x_2 &= \frac{235.2 \cdot 10^{-6}}{30 \cdot 10^3} = 0.0078 \cdot 10^{-6}; \\ x_3 &= \frac{262.45 \cdot 10^{-6}}{60 \cdot 10^3} = 0.00437 \cdot 10^{-6}; \\ x_3 &= \frac{263.97 \cdot 10^{-6}}{390 \cdot 10^3} = 0.00293 \cdot 10^{-6}. \end{aligned} \tag{30}$$

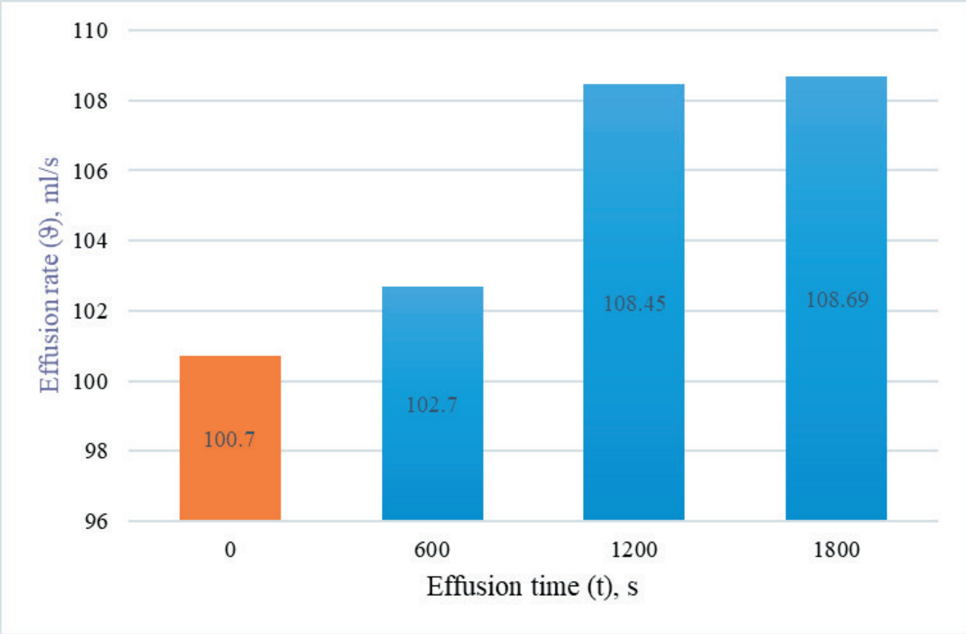

Figure 3 *Changing the effusion rate (ϑ) depending on the time of exposure to ultrasound (t)*

The cavitation coefficient of the erosion efficiency is determined as:

$$\begin{aligned} &\varepsilon = \frac{E_m}{E} = \frac{E_m}{E_u}; \\ &\varepsilon_1 = \frac{29}{30} = 0.96; \\ &\varepsilon_2 = \frac{59}{60} = 0.98; \\ &\varepsilon_2 = \frac{89}{90} = 0.99. \end{aligned} \tag{31}$$

Thus, the average cavitation coefficient of erosion efficiency is 0.98, thereby satisfying the condition $\varepsilon < 1$ and proving the effectiveness of ultrasonic radiator cleaning.

4 Conclusion

Based on the results of the study, the hypothesis about the possibility of determining dependences that allows assessing the effectiveness of radiator cleaning with ultrasound was confirmed.

Using the method of similarity theory and the dimensional analysis, criterion dependences were obtained that theoretically made it possible to consider the energy consumption for radiator cleaning and the erosive activity of the cavitation effect.

An experimental bench was developed, the purpose of which was to obtain numerical indicators of parameters that made it possible to calculate the energy consumed during the process of flushing the radiator from scale.

As a criterion proving the effectiveness of radiator cleaning with ultrasound, the cavitation coefficient of erosion efficiency was established, the numerical value of which confirmed the high effectiveness of ultrasonic cleaning.

The results obtained made it possible to prove scientific and practical significance of developing a methodology of calculating the parameters of the technological process of a radiator maintenance.

Acknowledgment

The authors received no financial support for the research, authorship and/or publication of this article.

Conflicts of interest

The authors declare that they have no known competing financial interests or personal relationships that could have appeared to influence the work reported in this paper.

References

[1] MAYER, A. *Particle filter retrofit for all diesel engines.* Renningen: Expert Verlag, 2008. ISBN 978-3-8169-2850-8.

[2] KADYROV, A., KRYUCHKOV, Y., SINELNIKOV, K., GANYUKOV, A., SAKHAPOV, R., KUKESHEVA, A. Studying the process of the internal combustion engine exhaust gas purification by an electric pulse.

Communications - Scientific Letters of the University of Zilina [online]. 2022, **24**(4), p. B275-B287 [accessed 2022-08-15]. ISSN 1335-4205, eISSN 2585-7878. Available from: https://doi.org/10.26552/com.C.2022.4.B275-B287

[3] KADYROV, A., KUKESHEVA, A., KRYUCHKOV, Y., PAK, I., KURMASHEVA, B., KABIKENOV, S. Development of calculation methodology for optimizing the operating mode of an electric pulse unit for cleaning exhaust gases. *Communications - Scientific Letters of the University of Zilina* [online]. 2024, **26**(1), p. B41-B53 [accessed 2023-11-02]. ISSN 1335-4205, eISSN 2585-7878. Available from: https://doi.org/10.26552/com.C.2024.011

[4] CASTIGLIONE, T., PIZZONIA, F., BOVA, S. A novel cooling system control strategy for internal combustion engines. *SAE International Journal of Materials and Manufacturing* [online]. 2016, **9**(2), p. 294-302 [accessed 2016-05-04]. ISSN 1946-3979, eISSN 1946-3987. Available from: https://doi.org/10.4271/2016-01-0226

[5] SVENSSON, M., BYTTNER, S., ROGNVALDSSON, T. Self-organizing maps for automatic fault detection in a vehicle cooling system. In: 4th International IEEE Conference Intelligent Systems: proceedings [online]. Vol. 3. IEEE, 2008. ISBN 978-1-4244-1739-1, p. 24-8-24-12. Available from: http://dx.doi.org/10.1109/IS.2008.4670481

[6] DEEPANKUMAR, S., SARAVANAN, B., SUDHIRKUMAR, V., BOOPALAN, N., SUNDARAMAHALINGAM, A., DHAYANEETHI, S. Design and analysis with optimization of car radiators using nanofluids [online]. In: *Advanced manufacturing systems and innovative product design*. DEEPAK, B. B.V. L., PARHI, D. R. K., BISWAL, B. B. (Eds.). Singapore: Springer, 2021. ISBN 978-981-15-9852-4 Available from: https://doi.org/10.1007/978-981-15-9853-1_4

[7] SHOUGANG, Q. Fault detection and maintenance of automobile engine cooling system. *Interdisciplinary Journal of Engineering and Environmental Sciences* [online]. 2023, **10**(2), p. 24-28 [accessed 2023-04-07]. ISSN 2994-2780. Available from: https://sadijournals.org/index.php/ijees/article/view/502

[8] SARSEMBEKOV, B. K., KADYROV, A. S., KUNAYEV, V. A., ISSABAYEV, M. S., KUKESHEVA, A. B. Method of cleaning internal combustion engine radiator tubes with ultrasound. *Material and Mechanical Engineering Technology* [online]. 2024, **6**(3), p. 44-53 [accessed 2024-08-15]. ISSN 2706-977X. Available from: https://doi.org/10.52209/2706-977X_2024_3_44

[9] KADYROV, A., SARSEMBEKOV, B., GANYUKOV, A., SUYUNBAEV, S., SINELNIKOV, K. Ultrasonic unit for reducing the toxicity of diesel vehicle exhaust gases. *Communications - Scientific Letters of the University of Zilina* [online]. 2022, **24**(3), p. B189-B198 [accessed 2022-02-07]. ISSN 1335-4205, eISSN 2585-7878. Available from: https://doi.org/10.26552/com.C.2022.3.B189-B198

[10] PAK, I., KADYROV, A., ASKAROV, B., SULEYEV, B., KARSAKOVA, A. Developing and studying the method of ultrasonic purification and utilization of internal combustion engine exhaust gases. *Communications - Scientific Letters of the University of Zilina* [online]. 2023, **25**(3), p. B245-B258. [accessed 2023-06-19]. ISSN 1335-4205, eISSN 2585-7878. Available from: https://doi.org/10.26552/com.C.2023.060

[11] KADYROV, A., BEMBENEK, M., SARSEMBEKOV, B., KUKESHEVA A., NURKUSHEVA, S. The influence of the frequency of ultrasound on the exhaust gas purification process in a diesel car muffler. *Applied Science* [online]. 2024, **14**(12), p. 1-19 [accessed 2024-06-24]. eISSN 2076-3417. Available from: https://doi.org/10.3390/app14125027

[12] KADYROV, A., SINELNIKOV, K., SAKHAPOV, R., GANYUKOV, A., KURMASHEVA, B., SUYUNBAEV, S. Studying the process of transport equipment cooling system ultrasonic cleaning. *Communications - Scientific Letters of the University of Zilina* [online]. 2022, **24**(4), p. B288-B300. [accessed 2022-07-28]. ISSN 1335-4205, eISSN 2585-7878. Available from: https://doi.org/10.26552/com.C.2022.4.B288-B300

[13] SAKHAPOV, R. L. Method of cleaning internal combustion engine radiator tubes with ultrasound. *Material and Mechanical Engineering Technology* [online]. 2024, **6**(2), p. 18-24 [accessed 2024-07-15]. ISSN 2706-977X. Available from: https://doi.org/10.52209/2706-977X_2024_2_18

[14] SUSLICK, C. P. Sonochemistry. *Science* [online]. 1990, **247**(4949), p. 1439-1445 [accessed 1990-03-23]. ISSN 0036-8075. Available from: https://doi.org/10.1126/science.247.4949.1439

[15] YAMASHITA, T., ANDO, K. Low-intensity ultrasound induced cavitation and streaming in oxygen-supersaturated water: role of cavitation bubbles as physical cleaning agents. *Ultrasonics Sonochemistry* [online]. 2019, **59**(3), p. 268-279 [accessed 2018-11-27]. ISSN 1350-4177, eISSN 1873-2828. Available from: https://doi.org/10.1016/j.ultsonch.2018.11.025

[16] JOOST ROOZE, J., REBROV, E. V., SCHOUTEN, J. C., KEURENTJES, J. T. F. Dissolved gas and ultrasonic cavitation - a review. *Ultrasonics Sonochemistry* [online]. 2013, **20**(1), p. 1-11 [accessed 2013-01-27]. ISSN 1350-4177, eISSN 1873-2828. Available from: https://doi.org/10.1016/j.ultsonch.2012.04.013

[17] YAMASHITA, T., YAMAUCHI, R., ANDO, K. Progress in ultrasonic cleaning research. *Japanese Journal of Multiphase Flow* [online]. 2018, **32**(2), p. 210-217 [accessed 2018-07-15]. ISSN 0914-2843, ISSN 1881-5790. Available from: https://doi.org/10.3811/jjmf.2018.T001

[18] KAMAR, N., MOSTEFA, M. L. P., MUHR, H., JOST, P. O. Influence of ultrasonic treatment on heat transfer in the heat exchanger. *Journal of Physics Communications* [online]. 2022, **6**(9), p. 1-17 [accessed 2022-09-16]. ISSN 1335-4205, eISSN 2585-7878. Available from: https://doi.org/10.1088/2399-6528/ac92c2

[19] FIELDS, J. T. Ultrasonic radiator cleaning system. US Patent. US4705054A. 10.11.1987.

[20] TEIICHIROU, Y. M., SHIN, I., TERUTAKA, Y., TSUMAKI, S. N., KITADA, Y. Ultrasonic cleaning apparatus US Patent. US20090025761A1. 29.01.2009.

[21] NAGARAJAN, R., DIWAN, M., AWASTHI, P., SHUKLA, A., SHARMA, P. Optimization of ultrasonic cleaning for erosion-sensitive microelectronic components. In: 17th Annual SEMI/IEEE Conference Advanced Semiconductor Manufacturing Conference: proceedings [online]. IEEE. 2006. ISBN 1-4244-0254-9, p. 233-237. Available from: https://doi.org/10.1109/ASMC.2006.1638750

[22] YUSOF, N. S. M., BABGI, B., ALGHAMDI, Y., AKSU, M., MADHAVAN, J., ASHOKKUMAR, M. Physical and chemical effects of acoustic cavitation in selected ultrasonic cleaning applications. *Ultrasonics Sonochemistry* [online]. 2016, **29**(1), p. 568-576 [accessed 2015-07-18]. ISSN 1350-4177, eISSN 1873-2828. Available from: https://doi.org/10.1016/j.ultsonch.2015.06.013

[23] KADYROV, A., KUKESHEVA, A., KRYUCHKOV, Y. (2024). Establishing the parameters of the operation mode of the electric pulse automobile muffler. *Journal of Applied Engineering Science* [online]. 2024, **22**(1), p. 89-99 [accessed 2024-03-17]. ISSN 1451-4117, eISSN 1821-3197. Available from: https://doi.org/10.5937/jaes0-45196

COMPUTER VISION TECHNOLOGIES IN CONTROLLING THE ELECTRIC DRIVE OF RAILWAY TRANSPORT

Yaroslav Kyrylenko*, Yurij Kutovoj, Tatiana Kunchenko, Oleksandr Nesterenko

Department of Automated Electromechanical System, NTU "KhPI", Kharkiv, Ukraine

*E-mail of corresponding author: yaroslav.kyrylenko1301@gmail.com

Yaroslav Kyrylenko 0000-0002-0331-617X

Resume

Analysis of statistical data on accidents on railways shows that most often an accident occurs due to the influence of the human factor, obstacles on the track, curvature of the track, the phenomenon of skidding and slipping in dynamic modes. The novelty of the proposed work consists in development of a mathematical model and a study of the automatic speed control, depending on the curvature of the track or in the presence of obstacles, and track defects, as well as measuring the linear speed of the railway transport as one of the main elements of the slip protection system and the system for implementing the maximum traction force. The solution of these problems is possible with the help of a multipurpose sensor, which is a video camera, to form the feedback signals to the control system.

Article info

Received 20 July 2024
Accepted 11 November 2024
Online 4 December 2024

Keywords:

electric drive
railway transport
neural regulator
computer vision
image processing
optical flow

Available online: https://doi.org/10.26552/com.C.2025.011

ISSN 1335-4205 (print version)
ISSN 2585-7878 (online version)

1 Introduction

Rail vehicles include electric locomotives, diesel locomotives, commuter trains and metro trains, trams, mine electric locomotives and other types of mechanisms for moving along a rail track. These modes of transport carry out the main transportation in most industrialized countries. One of the main elements of the railway transport, which determines its most important technical and economic indicators, is the traction electric drive.

A modern traction electric drive is often built based on the "frequency converter - asynchronous motor" system. Such an electric drive, using intelligent control systems and computer vision technologies, makes it possible to increase the level of automation and traffic safety in accordance with the international standard IEC-62267 and, in some cases, eliminate the human factor leading to emergency situations. Analysis of statistical data on accidents on railways shows that most often an accident occurs due to the influence of the human factor, obstacles on the track, curvature of the track, the phenomenon of skidding and slipping in dynamic modes [1].

This raises the problem of automatic speed control depending on the curvature of the track or in the presence of obstacles, track defects, as well as measuring the linear speed of the railway transport as one of the main elements of the skid protection system and the system for implementing the maximum traction force [2].

The solution of these problems is possible with help of a multi-purpose sensor, which is a video camera to form the feedback signals to control system.

2 Literature review

Over the past decade, several researchers have made significant advances in artificial intelligence applications in railway systems. A variety of review papers have been published [3] in the literature that explore the utilization of artificial intelligence in railway systems. However, all of these publications only focused on a specific aspect of the combination of AI and railway sub-domains [4].

Maintenance and inspection - The field of Maintenance and Inspection is predominantly influenced by Machine Learning, which is the most engaged AI technology. Traditional machine learning methods, such as Support Vector Machines (SVM), Decision Trees (DT),

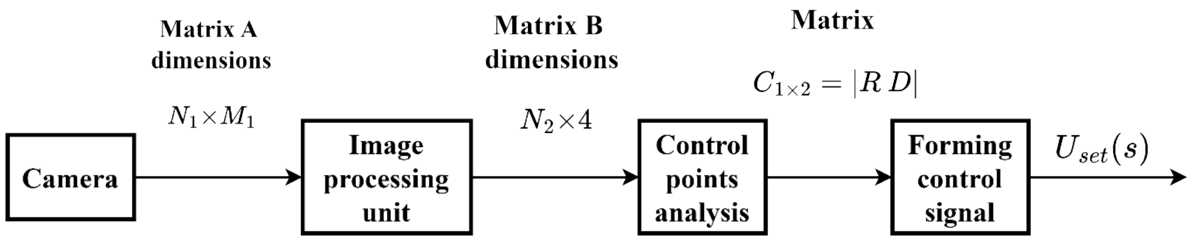

Figure 1 *Functional scheme of the image processing channel*

regression algorithms, and Artificial Neural Networks (ANN), have shown significant use in processing tabular datasets, particularly those that are labeled. In addition to the techniques previously mentioned, other approaches like the Big Data, Data Mining, and Pattern Recognition have been utilized in the realms of Fault Detection, Fault Diagnosis, and Failure Prediction. This integration has led to establishment of the decision support systems that enable the dynamic scheduling of maintenance and inspection tasks for railway tracks.

Safety and security - Hazardous events occur unpredictably, each possessing distinct spatial and temporal characteristics, which complicates the assessment of their potential consequences. The task of quantitatively identifying clusters of danger presents significant challenges for traditional machine learning algorithms, such as supervised learning models, as well as data mining techniques. This difficulty is exacerbated by the substantial disparity in sample sizes across various risk levels, where instances of low-risk events vastly outnumber those associated with severe hazards. Consequently, the less sophisticated models may fail to detect the latter. In the future, a synergistic approach that combines rule-based and case-based reasoning systems may enhance the decision-making capabilities regarding the allocation of safety resources. Furthermore, computer vision and image processing, characterized by their high degree of automation and robust detection accuracy in the real-world scenarios, have made considerable strides in the identification and analysis of environmental anomalies, as evidenced by the works of [5]. These methodologies typically leverage cloud-based information for comprehensive analysis.

Autonomous driving and control - The fusion of artificial intelligence with autonomous driving and control mechanisms has exhibited considerable potential, particularly in the realm of reinforcement learning [6]. Up to this point, researchers have largely demonstrated the effectiveness of vehicle control algorithms through theoretical simulations that combine real-world infrastructure with idealized characteristics of electrical traction motors. However, the actual conditions under which the trains operate are affected by numerous factors, including the deterioration of rail and wheel contacts, climatic variations, and unforeseen interruptions. Therefore, the existing theoretical simulations cannot be directly compared to practical real-world evaluations, which may lead to doubts about their applicability in genuine environments. An exception to this pattern is the paper [7] that utilizes Approximate Dynamic Programming, which introduces stochastic variations in both traction force and train resistance.

Traffic planning and management - The application of machine learning in optimization solutions may offer a hopeful trajectory for future advancements, combining the benefits of both exact and evolutionary methodologies. Conventional ML models (e.g., Regression Trees, RL algorithms), as an addition to the Bio-inspired algorithms. These algorithms have proven to be highly effective in addressing rescheduling challenges [8], the formulation of a schedule [9], and process of determining train paths [10-12].

These four above domains are the main ones for consideration in scope of this articles; beyond this focus there is a *revenue management, transport policy and passenger mobility*, as well.

3 Description of image processing algorithms

A universal sensor with wide technical capabilities is a video camera. The information coming from it is processed using special algorithms. Such a technology in obtaining and processing information is called computer vision (CV) technology [13].

In accordance with this technology, a video camera is installed on the driver's cab. The image from the camera is processed in the sequence, which is explained by the functional diagram shown in Figure 1.

In this diagram, the camera forms a video stream, which is fed to the image processing unit frame by frame. To represent the frame, a matrix is used, the dimensions of which correspond to the height and width of the frame. Values depend on the camera setting. At the output of the image processing unit, matrix B is formed, the size of the columns of which correspond to the coordinates of the left and right rails, respectively. The size of rows N_2 is equal to the number of control points; it depends on the range view at the railway road that is limitaed by the horizon. Values of coordinates change with step approximation 0.3 m. Four columns of matrix B contain values of coordinates of control points that represent the geometry of railway road: $X_{left\ rail}\ Y_{right\ rail}\ X_{right\ rail}\ Y_{right\ rail}$. Values of these coordinates are represented by the pixels coordinates. To convert the coordinates from pixels' coordinates to C_i systems, the calibration value was applied, which was calculated from geometry of the railway transport: height and width of the train and the railway road geometrical parameters. The block for analyzing the obtained control points forms a matrix C, which stores two values of R and D. The value R is the radius of curvature of the rail;

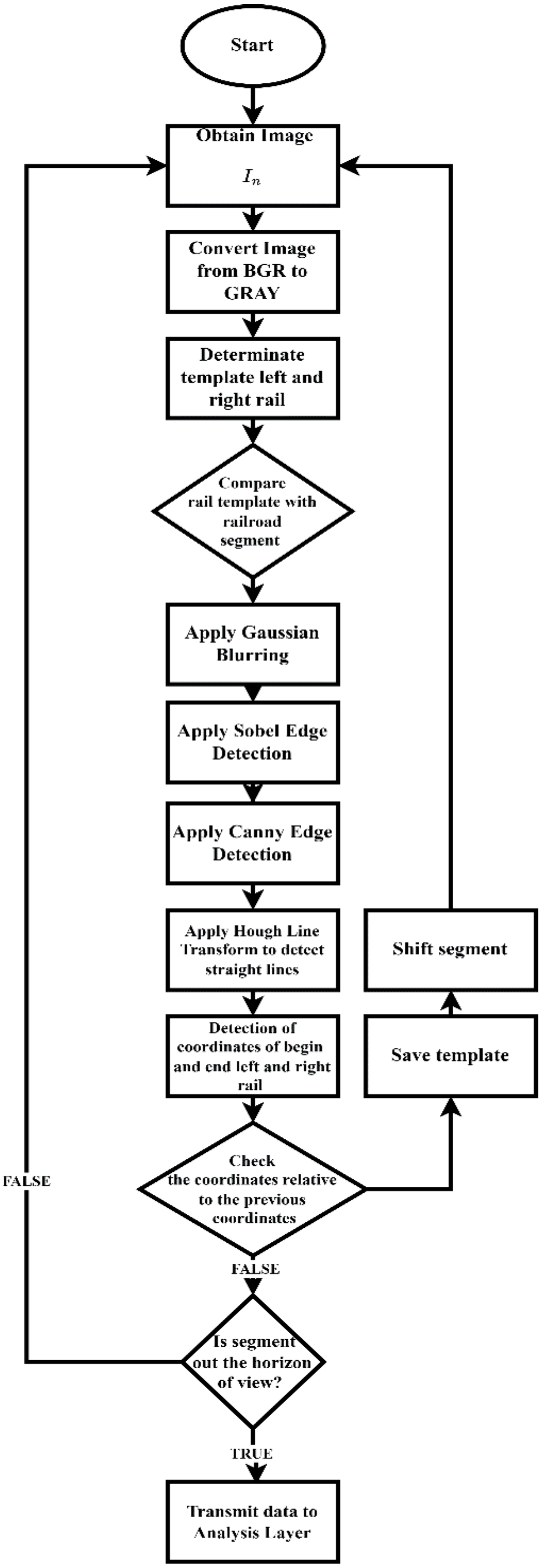

(a)

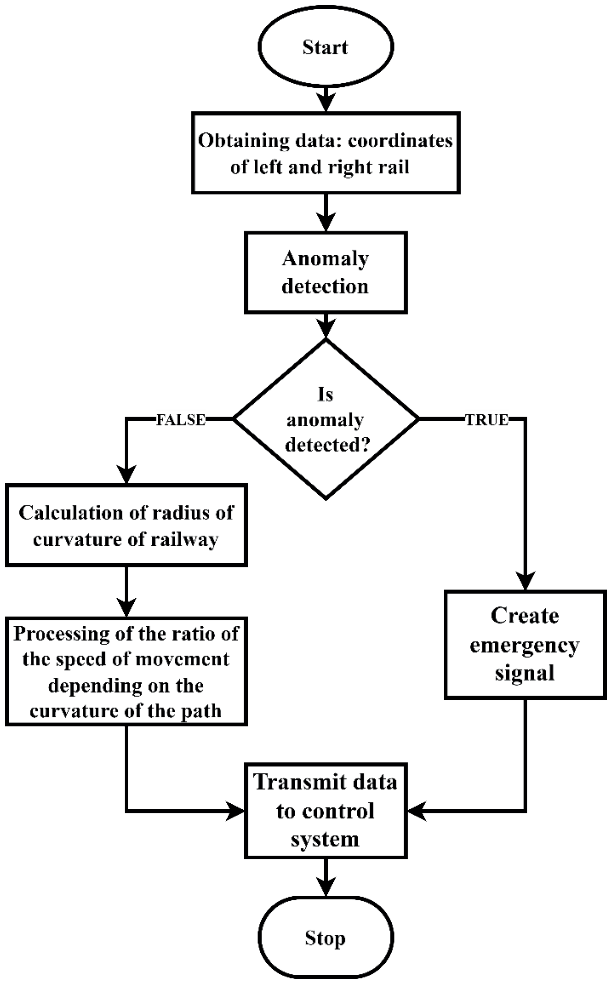

(b)

Figure 2 *The image processing algorithm (a); the algorithm for measuring the path curvature and identifying defects (b)*

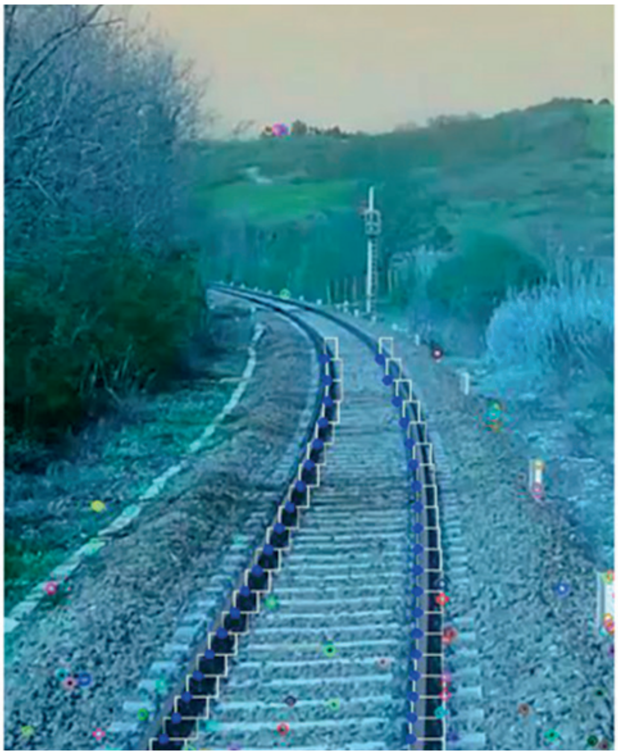

Figure 3 *Video frame showing control points*

D is equal to the defect code on the railway. The defect code is equal to 1 if a defect was detected, otherwise, the code is zero. The output device generates a speed set signal.

When processing the images, the open-source library of computer vision algorithms OpenCV is used [14]. The image processing algorithm is shown in Figure 2(a) and the algorithm for measuring the path curvature and identifying defects is shown in Figure 2(b).

The curve detection method, being the most traditional approach, involves pre-inputting the curve's position and curvature into a lookup table for subsequent use. For implementation of this method in vehicle control, it is imperative to accurately identify the curve's starting and ending points, as well as its position along the route. Whenever there is a change in the operating track, the curve data for the new track must be updated in the lookup table and employed accordingly. Any misjudgment in detecting the curve's position, while the vehicle is in motion, could potentially have adverse implications on both the safety and control of the vehicle. An internal measurement system, incorporating gyro sensors, acceleration sensors, and speed sensors, allows for the real-time measurements, while the vehicle is operational, enhancing accuracy and responsiveness. Nevertheless, this method is not without its drawbacks, as it is prone to offset errors stemming from the integration process within the curve extraction algorithm, and susceptible to variations in the vehicle's speed, which can impact its overall performance.

The performance of the algorithms was tested using mathematical modelling. For the numerical experiment, the ready-made video streams of the movement of rail vehicles in the presence of track curvature and track defects, are used. A frame of the finished video image with visualization of control points is shown in Figure 3. The blue dots positioned along the left and right rails serve as visual representations of control points, which are denoted by Matrix B in the diagram of the image processing channel. The white rectangles illustrate the segments of the rails, which are derived from the calculations of the control points.

4 Mathematical modelling of automatic speed control system depending on the path curvature

Mathematical model, in the form of a block diagram AC electric drive of the mainline electric locomotive DS3 [15], was compiled using generally accepted assumptions. In this case, the motor and converter are represented by aperiodic links, the clutch characteristic is approximated piecewise linearly. The model contains a neuroregulator that eliminates frictional self-oscillations that can occur in dynamic modes [16]. The block diagram has an additional speed control loop using an image channel from a video camera. Figure 4 shows the block diagram of the electric drive and the result of calculating the automatic speed reduction in the presence of path curvature.

Curves showing the railroad profile that are used for the simulation of the dynamics in the traction system are demonstrated in Figure 5. This test railroad profile

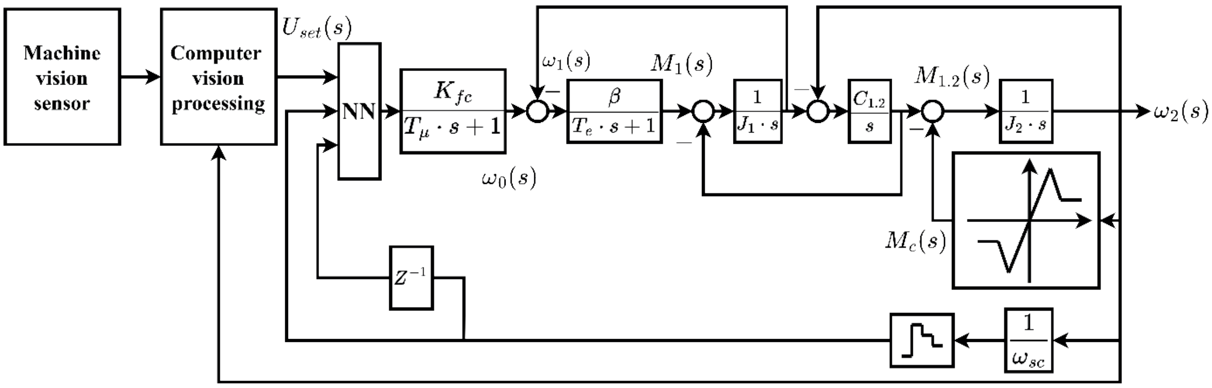

Figure 4 *Block diagram of traction AC electric drive DS3 locomotion*

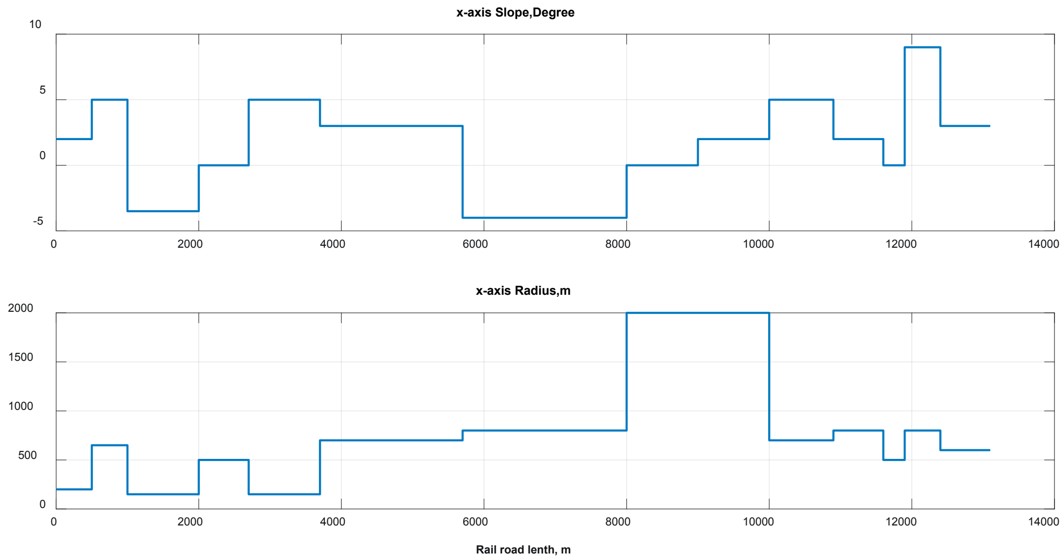

Figure 5 *Railroad profile for simulation load of traction system during moving*

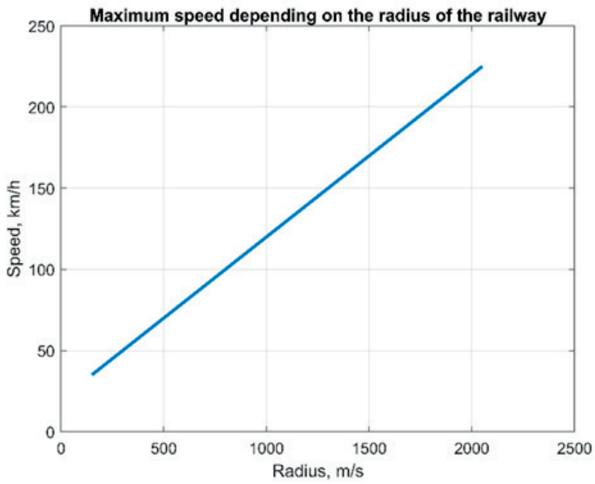

Figure 6 *Railroad profile for simulation load of traction system during moving*

contains combination of real world of railway parts and artificial parts that includes the emergency cases. Based on this profile the simulation model calculates resistance forces, that effect the traction system of the electrical locomotive DS3.

Integration of output signals from the image processing algorithms, in the chain of control railway traction system for simulation model is an issue of time of performance at this model and high load of processing data. To solve this issue, it was decided to get the time performance of image processing algorithms and substitute this block on a pure delay link. The

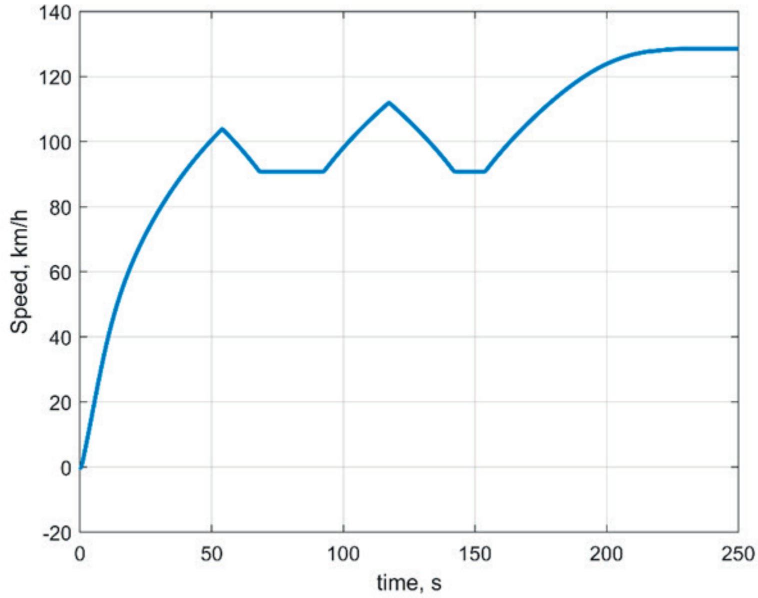

Figure 7 *Graph of automatic reduction of speed in the presence of path curvature*

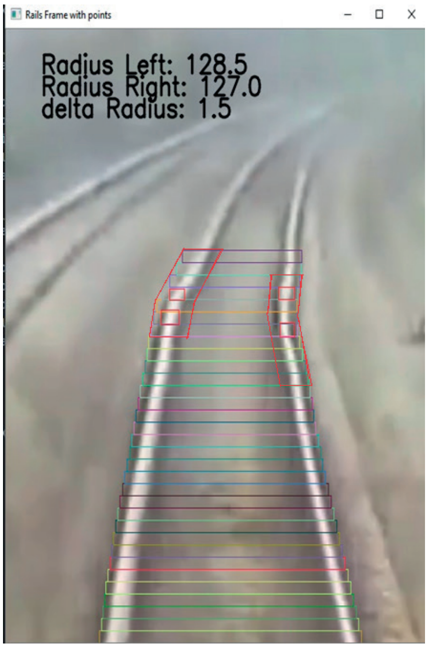

Figure 8 *Image of a rail track with a defect*

dependence of the speed on the radius of the railroad section is shown in Figure 6. These requirements were implemented in the simulation model as automation speed control depends on curvature.

Results of modelling the dynamical modes of traction electric drive with feedback from the video processing unit, are shown in Figure 7.

Similar calculations were performed for the AC electric drive of the T6B5 city tram. The tram moves along a path that has a defect due to thermal shift, as shown in Figure 8.

Passing such a defect at speed results in the tram derailing. The use of computer vision technologies allows to eliminate the human factor, slow down to a stop and thereby avoid an accident. The simulation of the electric drive of a city tram was performed using Simulink/ Matlab models [2], one of which is shown in Figure 9. The results of modelling and processing track defect detection system using computer vision are shown in Figure 10.

5 Algorithm for measuring the linear speed

For rail vehicles, measuring the linear speed makes it possible to solve the problem of protection against slipping and skidding, which, in turn, increases the traffic safety and reduces wasteful energy losses.

The use of radars, ultrasonic or inertial sensors significantly complicates the system and does not always

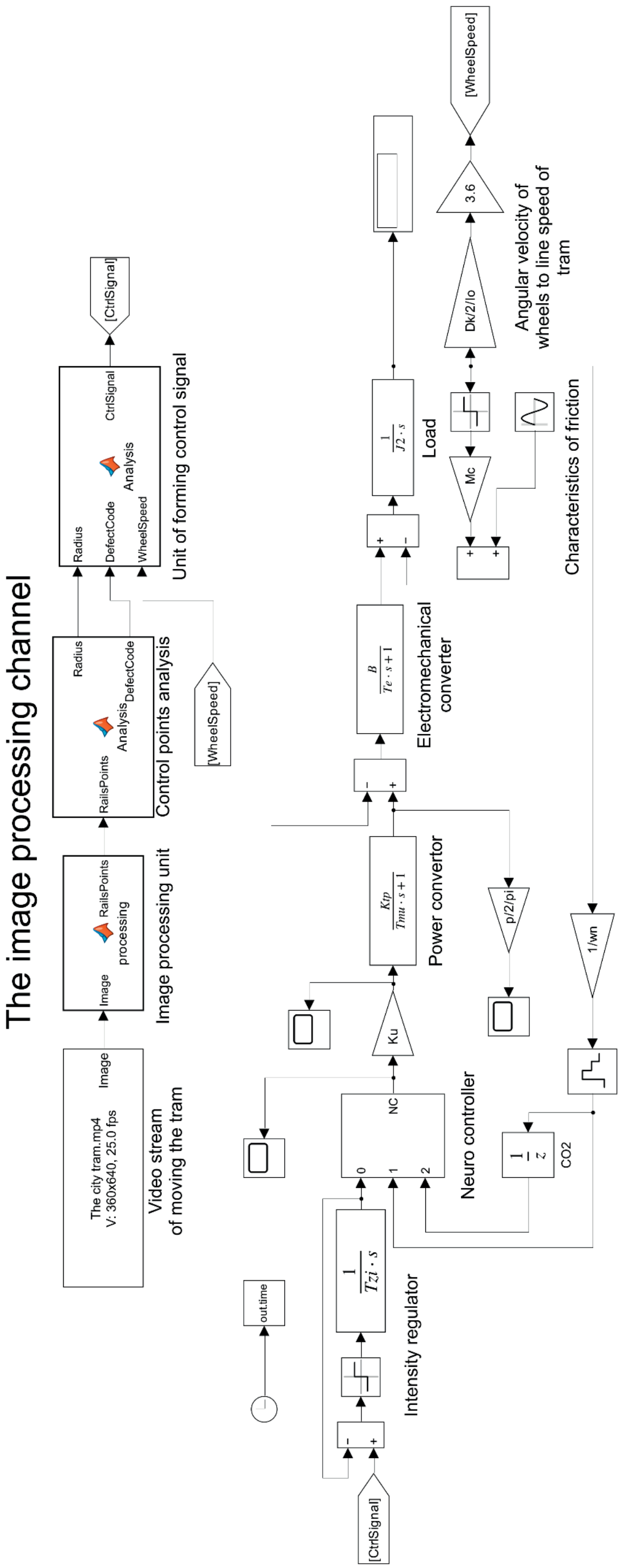

Figure 9 *Simulation model of AC electric drive of the T6B5 city tram with image processing channel*

provide the specified speed measurement accuracy, especially in the low-speed range.

Measuring the linear speed using a video camera is based on identifying the spatio-temporal differences in the sequence of images, identifying such functions that will differ when moving from one image to another. There is a number of analysis methods and algorithms for processing the optical flow from a video camera [17]. The Lucas-Canade algorithm is preferable because it works in real time, is insensitive to noise, and has sufficient accuracy [18].

The use of computer vision technologies makes it possible to measure the linear speed of rail vehicles. Determining the linear speed using the angular velocity

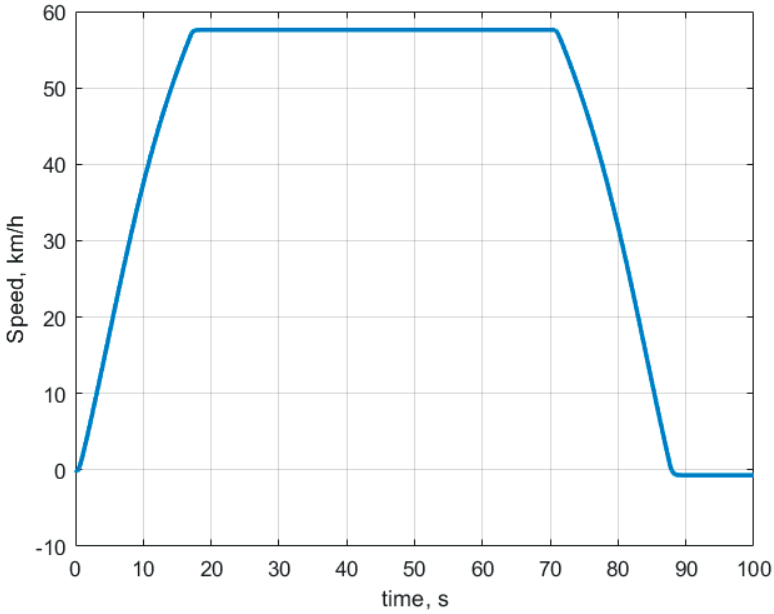

Figure 10 *Results of modelling a system with automatic speed control when a defect is detected*

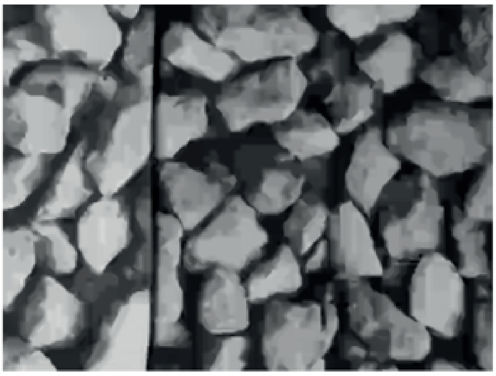

Figure 11 *Original images that simulate the surface over which the rail transport moves*

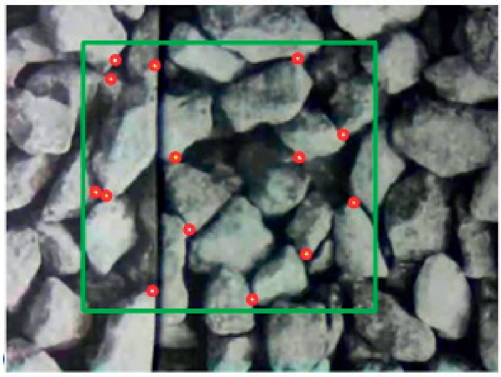

Figure 12 *Visualization of optical flow to obtain good features to be tracked*

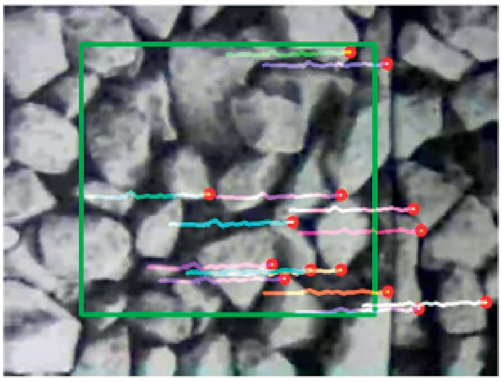

Figure 13 *Visualization of the movement of characteristic points in 50 frames*

sensors requires a wheel unit not connected to the traction motor, which is not possible in most practical cases. The use of radars, ultrasonic or inertial sensors significantly complicates the system and does not always provide the specified speed measurement accuracy, especially in the low-speed range.

Here $I_i(x, y, t)$ is a grayscale image at time t, with coordinates x, y, while $I_{i+1}(x+\Delta x, y+\Delta y, t+\Delta t)$ is the image at time, $t+\Delta t$, with coordinates $x+\Delta x, y+\Delta y$. Over time Δt the video camera has moved a distance d, which will lead to a shift in the characteristic points, as shown in Figures 11, 12, and 13.

The Kanade-Lucas optical flow algorithm is used because it is robust, accurate, insensitive to noise and non-uniform light intensity sources, and suitable for the real-time computation. In this method, let I_i be the greyscale image at time t_i and I_{i+1} be the greyscale image at time t_{i+1}. During this time interval, let the image be translated by distance = $(\Delta x, \Delta y)$, if A is a feature window in I_i and B be the same feature window in I_{i+1} as shown in Figure 14.

Then, the objective is to find d by minimizing the residual function $\in(d)$:

$$\in(d) = \iint_w (I_i(p) - I_{i+1}(p+d))^2 dxdy\,, \tag{1}$$

where: P_0 = the pixel coordinate of a generic image point. The upper left corner pixel coordinate is (0,0) and the lower right corner pixel coordinate base line skip is $n_x - 1, n_y - 1$ where n_x and n_y are the width and height of the image, respectively;
I_i and I_{i+1} are the greyscale values of the first image and the second image, respectively;
W is the feature window area, of size equal to $(w_x - 1, w_y - 1)$;
$d = (\Delta x, \Delta y)$ is the optical flow output or distance between features of two subsequent image frames.

In practice, the solution of minimizing can be achieved by using an iterative algorithm like the Newton-Raphson method.

6 Experimental measurements of the linear velocity at a test rig

The experimental setup consists of a moving carriage to which is attached a camera driven by a stepper motor. The motor drives a belt attached to the carriage and moves the camera at a controlled speed, as shown in Figure 15. The actual speed of the carriage is calculated from the known distance and time of movement of the carriage. The camera is an IMX219 module with an 8-megapixel sensor and has an extended field of view of 160 degrees, as shown in Figure 16. The camera can be set to different frame rates for certain frame sizes; at higher frame rates, the frame size that can be captured decreases, and vice versa. The maximum frame rate is 90 frames per second with an image size of 640 x 480 pixels.

The actual speed of the carriage is calculated from the known distance and time of movement of the carriage. Linear velocity calculations are based on the basic camera view, which is shown in Figure 17.

The obtained coordinates of characteristic points and their time changes, taking into account the camera model, allows to obtain equations for finding real coordinates, as:

$$X = Z_c \cdot \frac{x}{f}\,, \tag{2}$$

$$Y = Z_c \cdot \frac{y}{f}\,, \tag{3}$$

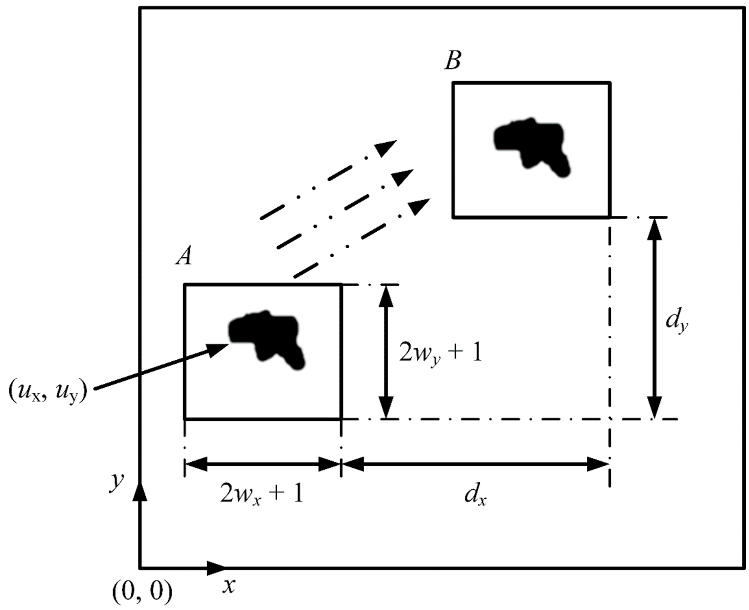

Figure 14 *Optical flow features and flow field*

where: Z_c is the real distance between the center of the camera sensor and the surface over which the camera is moving;
f is the focal length;
x, y is coordinates of characteristic points on the image;
X, Y is coordinates of the characteristic point in real space relative to the projection of the camera center onto the plane.

Calculation of the speed of movement of a characteristic point in pixels in the image is shown in the formula:

$$v_x = \Delta x \cdot \frac{1}{F}, \tag{4}$$

$$v_y = \Delta y \cdot \frac{1}{F}, \tag{5}$$

where $\Delta x, \Delta y$ - feature point displacement, calculated by the optical flow algorithm, F = frame rate per second (FPS), determines the time during which the characteristic point has shifted on the optical flow value.

The experimental setup allows to neglect the speed along the Z axis. Due to the rigid attachment of the camera to the carriage, and low movement speeds, which does not cause vertical vibrations, the surface was also assumed to be absolutely flat in the experiment. Based on the above listed assumptions and levels, the linear speed level was obtained.

Figure 18 shows the flow chart of algorithm to calculate the line speed based on optical flow.

The results of the experiment are shown in Table 1, where, V is the actual linear speed of the carriage obtained by calculation, V_{cv} is the linear speed of the carriage obtained using computer vision, Δ is the measurement error expressed as a percentage.

7 Conclusions

The camera is a multi-functional sensor that, together with the computer vision technology, allows to determine the movement parameters and makes it possible to respond to the environment in which the movement occurs.

Incorporating a video stream processing channel into the electric drive control system increases the

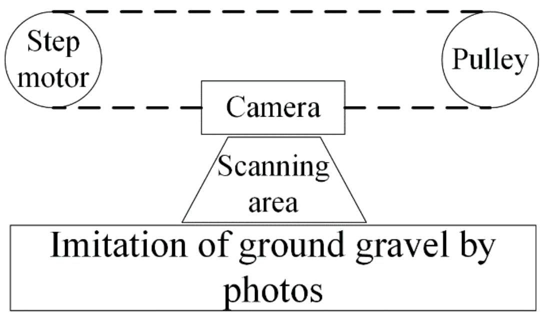

***Figure 15** Diagram of a test rig for measuring the linear speed*

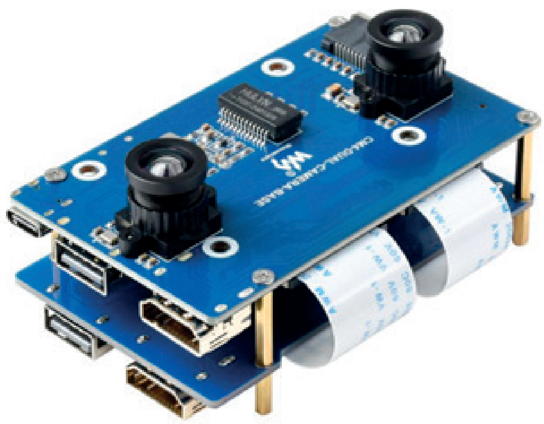

***Figure 16** Binocular camera board, designed for the Raspberry Pi 4 Compute Module*

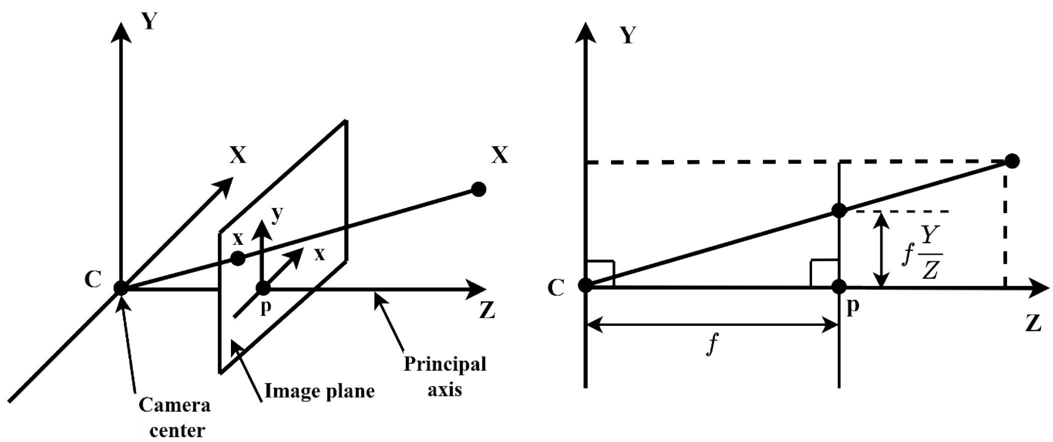

***Figure 17** Mathematical model of the camera*

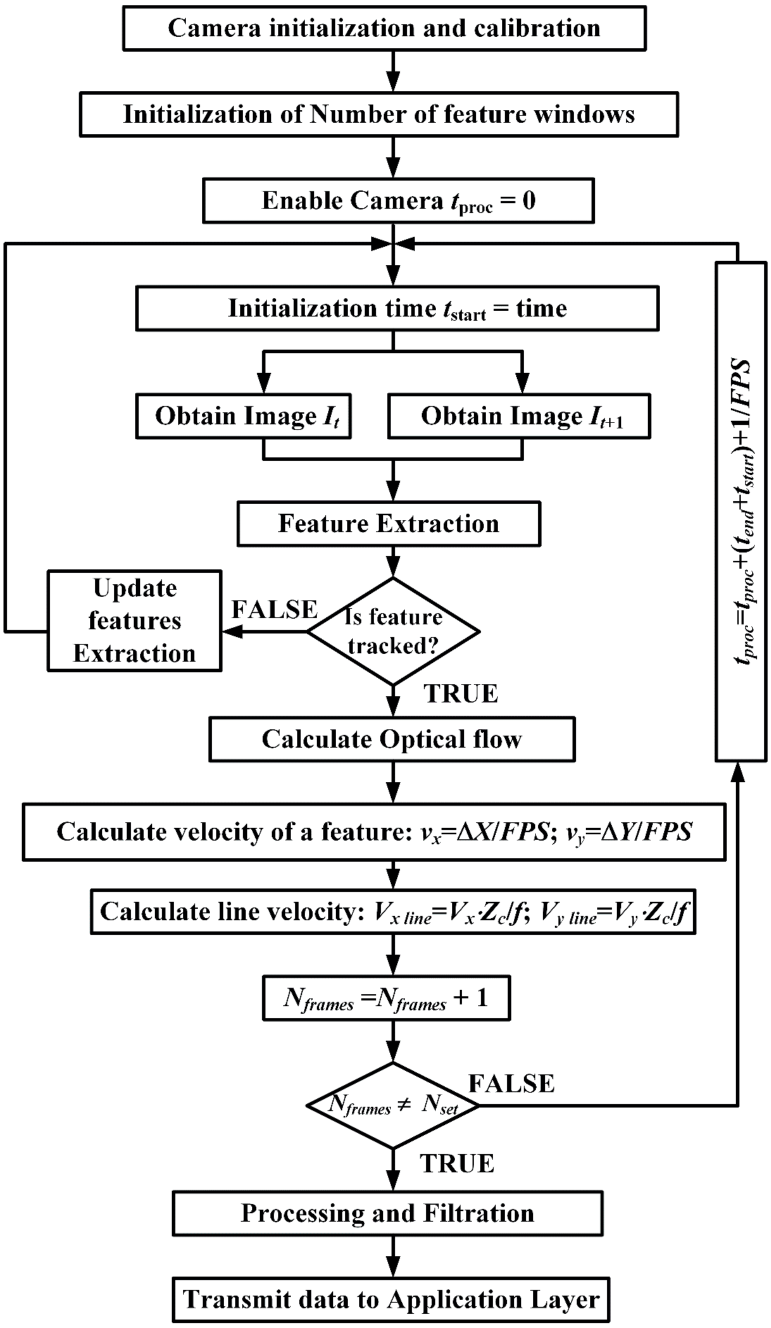

Figure 18 *Flowchart of optical flow-based speed calculation method*

Table 1 *Linear velocity values obtained by calculation and experiment*

No.	V, m/s	V_{cv}, m/s	Δ , %
1	0.15319	0.15097	1.449180756
2	0.19673	0.19399	1.392771819
3	0.24127	0.23854	1.131512413
4	0.28583	0.28163	1.469404891
5	0.32791	0.3238	1.253392699
6	0.37158	0.3664	1.394047042
7	0.41483	0.40811	1.619940699
8	0.45992	0.45188	1.74813011
9	0.50211	0.491	2.212662564

degree of automation and traffic safety of the rail vehicles.

Measuring the low linear speeds of rail vehicles, with an error not exceeding 2% makes it possible to determine the speed of excess sliding, and thereby develop a system for realizing the maximum traction force under adhesion conditions.

The current state of research is the fundamental base for integration to control system. During the conducted the experiments, the optimal hardware was chosen and the software was implemented. It combines a part the line speed measurements and the computer vision module of curvature estimation and defects detections.

In the future studies, the plan is to explore this platform using a stereo camera, which, in turn, will help improve the accuracy of measurements and expand the scope of application of this platform.

Acknowledgment

The authors received no financial support for the research, authorship and/or publication of this article.

Conflicts of interest

The authors declare that they have no known competing financial interests or personal relationships that could have appeared to influence the work reported in this paper.

References

[1] KUTOVOJ, Y. KYRYLENKO, Y., OBRUCH, I., KUNCHENKO, T. Application of intelligent control systems in electric drives of rail vehicles. In: 2021 IEEE 2nd KhPI Week on Advanced Technology (KhPIWeek): proceedings [online]. IEEE. 2021. eISBN 978-1-6654-1205-6, p. 709-713. Available from: https://doi.org/10.1109/KhPIWeek53812.2021.9570026

[2] KYRYLENKO, Y. KUTOVOJ, Y., OBRUCH, I., KUNCHENKO, T. Neural network control of a frequency-regulated electric drive of a main electric locomotive. In: 2020 IEEE Problems of Automated Electrodrive. Theory and Practice (PAEP): proceedings [online]. IEEE. 2020. eISBN 978-1-7281-9935-1, p. 1-4. Available from: https://doi.org/10.1109/PAEP49887.2020.9240880

[3] TANG, R., DE DONATO, L., BESINOVIC, N., FLAMMINI, F., GOVERDE, R M. P., LIN, Z., LIU, R., TANG, T., VITTORINI, V., WANG, Z. A literature review of Artificial Intelligence applications in railway systems. *Transportation Research Part C: Emerging Technologies* [online]. 2022, **140**, 103679. ISSN 0968-090X, eISSN 1879-2359. Available from: https://doi.org/10.1016/j.trc.2022.103679

[4] FLAMMMINI, F., TANG, T., LIU, R., LIN, Z., BESINOVIC, N., NARDONE, R., DE DONATO, L., MARRONE, S., PAPPATERRA, M., VITTORINI, V. RAILS Deliverable D 1.1: Definition of a reference taxonomy of AI in railways [online]. 2020. Available from: http://dx.doi.org/10.13140/RG.2.2.24887.75681

[5] ALAWAD, H., KAEWUNRUEN, S., AN, M. Learning from accidents: machine learning for safety at railway stations. *IEEE Access* [online]. 2020, **8**, p. 633-648. eISSN 2169-3536. Available from: http://doi.org/10.1109/ACCESS.2019.2962072

[6] YIN, J., CHEN, D., LI, L. Intelligent train operation algorithms for subway by expert system and reinforcement learning. *IEEE Transactions on Intelligent Transportation Systems* [online]. 2014, **15**(6), p. 2561-2571. ISSN 1524-9050, eISSN 1558-0016. Available from: http://dx.doi.org/10.1109/TITS.2014.2320757

[7] WANG, P., TRIVELLA, A., GOVERDE, R. M., CORMAN, F. Train trajectory optimization for improved on-time arrival under parametric uncertainty. *Transportation Research Part C: Emerging Technologies* [online]. 2020, **119**, 102680. ISSN 0968-090X, eISSN 1879-2359. Available from: http://doi.org/10.1016/j.trc.2020.102680

[8] PU, H., SONG, T., SCHONFELD, P., LI, W., ZHANG, H., HU, J., PENG, X., WANG, J., Mountain railway alignment optimization using stepwise and hybrid particle swarm optimization incorporating genetic operators. *Applied Soft Computing* [online]. 2019, **78**, p. 41-57. ISSN 1568-4946, eISSN 1872-9681. Available from: http://doi.org/10.1016/j.asoc.2019.01.051

[9] HICKISH, B., FLETCHER, D. I., HARRISON, R. F. Investigating Bayesian optimization for rail network optimization. *International Journal of Rail Transportation* [online]. 2020, **8**(4), p. 307-323. ISSN 2324-8378, eISSN 2324-8386. Available from: http://doi.org/10.1080/23248378.2019.1669500

[10] HO, T., TSANG, C.W., IP, K.H., KWAN, K. Train service timetabling in railway open markets by particle swarm optimisation. *Expert Systems with Applications* [online]. 2012, **39**(1), p. 861-868. ISSN 0957-4174, eISSN 1873-6793. Available from: http://doi.org/10.1016/j.eswa.2011.07.084

[11] HU, L.-Q., HE, C.-F., CAI, Z.-Q., WEN, L., REN, T. Track circuit fault prediction method based on grey theory and expert system. *Journal of Visual Communication and Image Representation* [online]. 2019, **58**, p. 37-45. ISSN 1047-3203, eISSN 1095-9076. Available from: http://doi.org/10.1016/j.jvcir.2018.10.024

[12] HU, C., LIU, X. Modeling track geometry degradation using support vector machine technique. In: In: ASME/IEEE Joint Rail Conference: proceedings [online]. 2016. Available from: http://doi.org/10.1115/JRC2016-5739

[13] KYRYLENKO, Y., K. YURIJ, K. TATIANA The robotic platform for measuring linear velocity using computer vision algorithms. In: 2022 IEEE 3rd KhPI Week on Advanced Technology (KhPIWeek): proceedings [online]. IEEE. 2022. eISBN 979-8-3503-9920-2, p. 1-4. Available from: http://doi.org/10.1109/KhPIWeek57572.2022.9916472

[14] SZELISKI, R. *Computer vision algorithms and applications* [online]. Cham: Springer, 2022. ISBN 978-3-030-34371-2, eISBN 978-3-030-34372-9. Available from: https://doi.org/10.1007/978-3-030-34372-9

[15] KLEPIKOV, V. *Dynamics of electromechanical systems with nonlinear friction*. Kharkiv: Publishing house NTU "KhPI", 2014, eISSN 978-617-687-029-6

[16] HORN, B. K. P., SCHUNCK, B. G. Determining optical flow. *Artificial Intelligence* [online]. 1981, **17**(1-3), p. 185-203. ISSN 0004-3702, eISSN 1872-7921. Available from: https://doi.org/10.1016/0004-3702(81)90024-2

[17] LIN, CH.-H., ZHU, R., LUCEY, S. The conditional Lucas and Kanade algorithm. *arXiv* [online]. 2016, 1603.08597. eISSN 2331-8422. Available from: http://arxiv.org/abs/1603.08597

[18] BIRCHFIELD, S. KLT: An implementation of the Kanade-Lucas-Tomasi feature tracker [online] [accessed 2024-11-15]. Available from: https://cecas.clemson.edu/~stb/klt/index.html

Dear colleagues,

Journal Communications - Scientific Letters of the University of Zilina are a well-established open-access scientific journal aimed primarily at the topics connected with the field of transport. The main transport-related areas covered include Civil engineering, Electrical engineering, Management and informatics, Mechanical engineering, Operation and economics, Safety and security, Travel and tourism studies. Research in the field of education also falls under these categories. The full list of main topics and subtopics is available at: *https://komunikacie.uniza.sk/artkey/inf-990000-0500_Topical-areas.php*

Journal Communications - Scientific Letters of the University of Zilina is currently indexed and accepted by CEEOL, Crossref (DOI), DOAJ, EBSCO Host, Electronic Journals Library (EZB), ERIH Plus, Google Scholar, Index Copernicus International Journals Master list, iThenticate, JournalGuide, Jouroscope, Norwegian Register for Scientific Journals Series and Publishers, ROAD, ScienceGate, SCImago Journal & Country Rank, SciRev, SCOPUS, Web of Science database, WorldCat (OCLC).

Journal Communications - Scientific Letters of the University of Zilina is preserved in CLOCKSS and Portico to guarantee long-term digital preservation and is archived in the national deposit digitalne pramene.

Authors can share their experiences with publishing in our journal on SciRev.

Journal Communications - Scientific Letters of the University of Zilina has been selected for inclusion in the Web of Science™. Articles published after 2022, beginning with 24(1), will be included in the product Emerging Sources Citation Index (ESCI).

I would like to invite authors to submit their papers for consideration. We have an open-access policy and there are **no publication, processing or other fees** charged for published papers. Our journal operates a standard single-anonymised review procedure, the successful completion of which is a prerequisite for paper publication.

The journal is issued four times a year (in January, in April, in July and in October).

I would also like to offer you the opportunity of using already published articles from past issues as source of information for your research and publication activities. All papers are available at our webpage: http://komunikacie.uniza.sk, where you can browse through the individual volumes. Our journal offers access to its contents in the open access system on the principles of the license **Creative Commons (CC BY 4.0)**.

For any questions regarding the journal Communications - Scientific Letters of the University of Zilina please contact us at: *komunikacie@uniza.sk*

We look forward to future cooperation.

Sincerely

Branislav Hadzima
editor-in-chief

SEISMIC LOADING AND REINFORCEMENT EFFECTS ON THE DYNAMIC BEHAVIOR OF SOIL SLOPES

Vishal S. Ghutke*, Anirban Mandal, Anjan Patel

Visvesvaraya National Institute of Technology, Ambazari, Nagpur, Maharashtra, India

*E-mail of corresponding author: vsghutke@gmail.com

Vishal S. Ghutke 0000-0002-2982-0438, Anirban Mandal 0000-0001-8146-6248, Anjan Patel 0000-0003-2645-613X

Resume

Despite the significant research on the seismic stability of earth structures, critical gaps remain in understanding the dynamic response of soil slopes with varying reinforcements. These gaps were addressed in this study by using a small shake table to investigate the dynamic behavior of soil slopes under different conditions. The research examines responses at various frequencies, the effect of reinforcement methods, and the impact of slope height. Results indicate that the higher frequencies and amplitudes lead to increased displacements, while reinforcement reduces crest displacement by 21 to 45%. Steeper slopes (35° and 40°) also show increased displacements by 9 to 65%, compared to a 30° slope. The importance of reinforcement in improving the seismic resilience of soil slopes is highlighted in this study, offering practical insights for engineering design.

Article info

Received 11 May 2024
Accepted 15 October 2024
Online 8 November 2024

Keywords:

seismic stability
soil slopes
reinforcements
shake table
dynamic loading,
unreinforced soil slopes

Available online: https://doi.org/10.26552/com.C.2025.008

ISSN 1335-4205 (print version)
ISSN 2585-7878 (online version)

1 Introduction

The slope stability analysis is a critical aspect of geotechnical engineering that is pivotal in ensuring the safety and longevity of civil engineering structures built on or adjacent to sloping terrain [1]. The stability of slopes is influenced by a myriad of factors, including geological and geotechnical conditions, external loads, and environmental factors. In this study, we delve into the intricate realm of slope stability analysis, focusing on comparing reinforced and unreinforced materials [2]. Slopes are ubiquitous in natural and engineered landscapes, presenting challenges that demand a comprehensive understanding of their behavior and the potential risks associated with instability [3]. Unstable slopes can lead to disastrous consequences, including landslides, erosion, and structural failures. Therefore, a thorough investigation into the slope stability is essential for designing resilient and safe structures in hilly and mountainous regions [4].

Reinforcement techniques have emerged as a proactive and innovative approach to enhance the slope stability [5]. Introducing various reinforcement materials, such as geosynthetics, geogrids, and soil nails, has opened new avenues for mitigating the slope instability and improving overall slope performance [6]. This study aim was contribute to the existing body of knowledge by evaluating and comparing the effectiveness of reinforced and unreinforced materials in slope stability analysis. The investigation involves a comprehensive review of relevant literature, case studies, and advanced analytical methods to assess the performance of slopes under different conditions. By considering both laboratory experiments and real-world applications, this study aim was to provide valuable insights into the mechanisms governing slope stability and the role of reinforcement in enhancing the overall resilience of slopes [7]. As societies continue to expand into diverse topographies, understanding the complexities of slope stability becomes increasingly crucial for sustainable and safe development [8]. The findings of this study are anticipated to contribute to the optimization of slope design practices, thereby fostering the development of robust infrastructure in areas prone to slope instability. The main objectives of this work are as follows:

- The dynamic response of soil slopes is investigated across different frequencies, aiming to understand how varying frequencies affect the slope stability under seismic conditions.

- The influence of reinforcement on soil slope behavior is analyzed, focusing on how various reinforcement techniques alter their dynamic performance.
- The effects of different amplitude levels on the dynamic response of soil slopes are examined, assessing the impact of amplitude changes on displacement and stability during seismic events.

2 Literature survey

Shinoda and Miyata [9] stated in geotechnical engineering, slope stability analysis is a challenging task because of the multimodal function optimization issue. Though its parameters for both unreinforced and reinforced soil slopes have not been fully explored, particle swarm optimization (PSO) is a highly effective technique for finding critical slip surfaces. The study computes safety factors by taking into account force and moment equilibriums, which include reinforcement tensile force. It was discovered that the PSO's computing efficiency increased the maximum number of slip surface nodes, and research was done on how sensitive PSO parameters were to safety factor variations.

Keskin and Kezer [10] examined slope stability in municipal solid waste (MSW) landfills using finite element and limit equilibrium methods. They discovered that employing geogrid materials can considerably improve the stability of landfill slopes. When the best geogrid settings are applied, the slope's safety factor can be raised by up to double. Geogrid- reinforced slopes can become steeper, allowing for additional solid waste storage. Given the high initial investment cost of MSW landfills, storing more solid waste with geogrids can result in large economic gains. The study offers optimal geogrid values for maximum reinforcing effects in MSW landfill slopes.

Jyothi and Krishna [11] focused on enhancing the slope stability of embankments built with locally accessible materials as a result of fast industrialization and urbanization. The authors proposed that geotechnical engineers can strengthen these embankments by using geogrid reinforcement with native soil or by replacing the soil with pond ash. The study looks at a road embankment with a crest width of 8 m, side slopes of 2H:1V, and a height of 5 m resting on 10 m thick c-/soil. The Mohr-Coulomb material and Morgenstern-Price approach are used to model the soils and compute the factor of safety (FoS) for a critical slip surface. The best arrangement of geogrids in the first and fourth layers in conjunction with the pond ash fill embankment results in a greater factor of safety of 2.928.

Arvin et al. [12] used the strength reduction technique (SRM) to study the three-dimensional stability of slopes reinforced with geocells. The research takes into account the surrounding soils, as well as the geocells and their filling. The slope stability parameters, such as geocell placement, multilayer reinforcement pattern, and geocell layer number, are assessed using ABAQUS to calculate FoS. Through the 3D-SRM slope stability analysis, the SRM procedure's dependability is confirmed.

Collin et al. [13] examined Yeager Airport's reinforced slope failure in 2015 at Charleston, West Virginia. Strength parameters, slope geometry, and soil reinforcement configuration are assessed using inverse limit-equilibrium and permanent deformation studies. Whereas finite-difference permanent deformation studies comprehend internal stresses and deformations of the reinforced soil slope, three-dimensional limit-equilibrium calculations concentrate on the direction of uniaxial geogrid reinforcement. The findings support field observations made after the breakdown and emphasize the value of carrying out several types of analysis in complex slope failures.

Patil et al, [14] examined the behaviour of model footings' bearing capacities on slopes of reinforced embankments constructed from pozzolanic waste materials, such as ground granulated blast furnace slag (GGBFS) and fly ash. It looks at how well rubber grid and geogrid, two forms of reinforcement, work to increase load carrying capability. That study took into account the position, embedment depth, and slope angle of reinforcement. The load carrying capacity is found to decrease with slope angle and edge distance, with a 1.2 embedment depth ratio being the ideal value. Rubber grid reinforcement outperforms geogrid reinforcement; the study highlights the efficient use of leftover Pozzolanic materials.

Amena [15] investigated the durability of clay soil filled embankments with plastic garbage. Utilizing PLAXIS 2D geotechnical software, the author examined stability in a range of scenarios, taking into account factors including embankment shape, material properties, and reinforcement strength. The findings indicate that the factor of safety falls with slope height and angle but rises with geogrid axial strength above 500 kN/m. The study conclusion is that embankment fill can be made from clay treated with plastic garbage.

Qiu et al. [16], looked into the failure modes and dynamic response patterns of concrete gravity dams exposed to powerful earthquakes. A reliable technique for investigating the failure modes and dynamic properties of these structures is dynamic shaking table testing. Using a gravity dam model on a shaking table, the research integrates different dynamic loads and looks at how damage develops. The findings offer guidance for gravity dam shaking table studies, the determination of structural dynamic characteristic parameters, and the validation of damage diagnosis techniques.

Wang et al. [17], investigated the impact of geohazards, such as earthquakes and heavy rains, on regional stability is examined in this study. It solves safety factors for slopes associated with rainfall and earthquakes using a three-dimensional slope dynamic model and a rigorous analysis technique. The findings indicate that saturation and permeability coefficient have a relatively minor influence on safety factors during rainfall, however, porosity has a larger effect. The authors found that when both horizontal and vertical seismic effects are taken into account, slope stability is reduced.

Beyene et al. [18], developed a construction with four walls joined by three slabs without coupling beams and showed strong coupling in a study on the interaction between slabs and reinforced concrete walls on a shaking table. Walls may collapse due to this unanticipated reaction mechanism, as demonstrated by previous earthquakes. The effective width (EW) of the slabs was shown to have a substantial impact on the response, raising the structure's overall stiffness and strength ratio. Longitudinal reinforcement buckling resulted from twofold maximum shear stresses and increased compression axial forces due to the increased BS and redistribution of demand among wall piers.

Hore et al. [19], used a shaking table to investigate the dynamic behavior of a wrap-around sand embankment. Sand beds with varying relative densities were prepared using a mobile, portable pluviator. In a Plexiglas container, a 408 mm-tall wrap-faced retaining wall model was built using a prototype to model a scale factor of N = 10. The percentages of Sylhet sand that were utilized were 48%, 64%, and 80%. Three distinct surcharge pressures and sinusoidal peak input motions were used in the tests. The amplification of acceleration was found to be proportional to the base acceleration and inversely related to the surcharge load. Face displacement rose with base acceleration and reduced with rising surcharge pressure.

The literature on slope stability analysis reveals a range of methods, such as particle swarm optimization (PSO) and finite element analysis, to identify the critical slip surfaces and optimize reinforcement configurations, essential for assessing slope behaviour under seismic conditions. While these studies demonstrate the effectiveness of geogrid and geocell reinforcements in improving stability, they often focus on static or simplified dynamic conditions, leaving gaps in understanding the full dynamic response of slopes during seismic events. Additionally, dynamic shaking table tests have provided insights into failure modes, yet they often lack comprehensive exploration of the interplay between seismic loading, slope reinforcement, and material properties. The problem lies in the limited experiment on the dynamic response of reinforced and unreinforced soil slopes under varied seismic conditions. This gap motivated our research, which aimed to use shaking table experiments to provide a deeper understanding of slope stability under seismic loading, focusing on the real-time dynamic behaviour of different slope configurations.

3 Research methodology

In this section, the process of creating a compact shake table for experimentation is delved into, with several crucial steps outlined. Initially, emphasis was placed on developing a model of a soil slope, wherein the specific soil type is carefully identified. This step is pivotal in ensuring the precision and applicability of the subsequent experiments. Following this, the focus shifts towards determining the optimal settings for acceleration and frequency on the shake table. These parameters are instrumental in replicating authentic seismic scenarios. Subsequently, attention turns to comprehending how the soil slope responds under diverse conditions. The approach involves subjecting the model to varying combinations of acceleration and frequency, accurately observing and recording the ensuing soil reactions. The data obtained from these experiments furnishes valuable insights into the dynamic behaviour of the soil slope, forming a solid foundation for subsequent analysis and interpretation. This systematic methodology establishes the framework for making meaningful contributions to understanding of soil behaviour in the face of seismic conditions.

3.1 Testing equipment and material

In this research, a scale factor of 1/10 $(\lambda = L_F/L_M = 10)$ was applied to create physical models, where L_F represents the full-scale prototype dimension, and L_M the model dimension. The geometric scale factor influences all dimensions, including length, height, and width, ensuring the physical model is a scaled-down representation of real-world soil slopes. Dynamic similarity was achieved using Froude scaling laws, which maintain similarity between the model and prototype by accounting for the effects of gravity [20]. This ensures that the dynamic response observed in the model correctly represents the behaviour at full scale. For instance, displacement scales with λ, velocities scale with $\lambda^{1/2}$, and accelerations remain the same across the model and prototype. As a result, the forces acting on the model, such as gravitational and inertial forces, were correctly scaled to maintain the accuracy of dynamic responses under the seismic loading.

To replicate the physical characteristics of full-scale soil and reinforcement materials, material properties were scaled by the geometric scale factor. The mass density of the model soil was adjusted to maintain similarity in inertial forces, with the stress-strain behavior of the materials scaled by λ. Specifically, the material density was scaled by λ^0 (constant), while the applied forces were scaled by λ^3 to account for the difference in model volume. These adjustments ensured that the mechanical behavior of both soil and reinforcement in the model mimicked that of the full-scale prototype, accounting for the significant contributions of both inertia and gravitational forces. By addressing these scaling principles, the physical model provides reliable insights into the dynamic behavior of soil slopes under the seismic conditions. The integration of geometric, dynamic, and material property scaling ensures that the results are transferable to the real-world applications, offering valuable implications for improving the seismic resilience of full-scale soil slopes.

3.1.1 Shake table

A shake table, sometimes referred to as a seismic simulator, is an advanced apparatus intended to mimic the intricate and frequently intense movements of the Earth's crust during an earthquake [20]. The shake table, which consists of a robust platform backed by a network of hydraulic or mechanical actuators, can imitate a variety of ground motions, enabling engineers and researchers to examine how buildings, bridges, and other infrastructure behave structurally during an earthquake [21]. The table's capacity to replicate various seismic activity levels and frequencies offers important insights into the structural resilience of buildings and aids in the creation of earthquake-resistant designs. By carefully adjusting the infrastructures table's movements, researchers may apply the dynamic stresses encountered during an earthquake to models or real structures [22]. The ability to test and improve seismic-resistant building materials and methods in a controlled setting advances earthquake engineering and improves our capacity to reduce the destructive effects of seismic occurrences on the built environment.

The experimental investigations were conducted using a state-of-the-art unidirectional shake table, as depicted in Figure 1. The shake table boasts a substantial-top surface area measuring 1.5 x 1.5 m, providing ample space for testing and analysis. With an impressive maximum load-carrying capacity of 2000 kg, the shake table is well-equipped to handle a diverse range of experimental setups.

This advanced apparatus offers remarkable control over testing parameters. The maximum theoretical frequency achievable on the shake table is 10 Hz, ensuring the simulation of a wide spectrum of dynamic conditions. Additionally, the shake table is capable of achieving a maximum displacement of ±50 mm, allowing for precise and controlled movements that replicate the real-world scenarios with a high degree of accuracy.

The robust specifications of the shake table make it an ideal platform for conducting experiments that require a combination of strength, precision, and versatility. This state-of-the- art equipment played a pivotal role in ensuring the reliability and comprehensiveness of the experimental data collected for the study.

3.1.2 Soil container

The experimental setup employed a rigid-type container with internal dimensions measuring 1.0 m x 1.0 m x 1.0 m. This container was securely affixed to a shake table to simulate dynamic movements. Crafted from sturdy Perspex glass with an 18 mm thickness, the container's structural integrity was further enhanced by incorporating flat and angle structural steel sections, as illustrated in Figure 1(a). To augment its shock-absorbing capabilities, Expanded Polyethylene (EPE) foam was strategically applied along the inner boundary of the container, oriented perpendicular to the anticipated direction of the shake table's movement [23]. This not only served to protect the contents, but added an extra layer of insulation against potential impact forces, as well.

Furthermore, the base of the container underwent a surface modification process to induce roughness. Industrial adhesives were employed to securely adhere sand particles to the base, creating a textured surface [24].

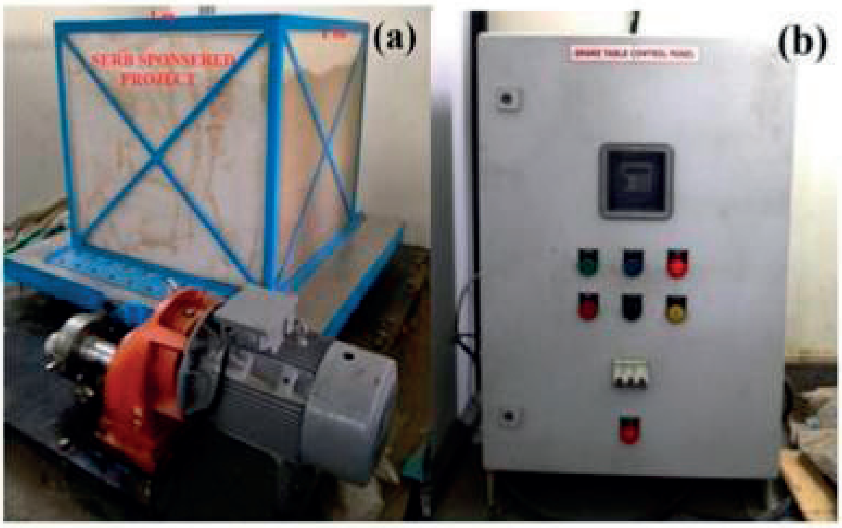

Figure 1 *(a) shake table and (b) control panel*

This deliberate roughness is instrumental in simulating real- world scenarios and introduces an additional layer of complexity to the experimental conditions. The construction and thoughtful enhancements of the container contribute to the precision and reliability of the experimental setup, ensuring accurate and meaningful results.

3.1.3 Absorbing boundary

The efficacy of a soil container's design in influencing the dynamic response of soil cannot be overstated, as improperly designed artificial boundaries can significantly impact the overall behaviour of the soil [25-26]. To mitigate undesirable effects, it is advisable to incorporate absorbing materials along the boundaries. In our current experimentation, commercially available EPE foam panels were chosen for utilization as absorbing boundaries.

In the experimental setup, these EPE foam panels were strategically positioned on both inner sides of the end walls, arranged perpendicular to the direction of shaking. This deliberate placement was aimed at minimizing any adverse boundary effects on the dynamic response of the soil. In this we maintained a foam thickness of 25 mm. This careful adherence to established principles ensured that our experimental conditions align with recognized standards, promoting reliable and meaningful results in the study of soil dynamics.

3.2 Material properties

Two distinct types of materials were employed as fill material in the project specifically, fine sand and coarse sand [27]. The reinforcement material chosen for this application is Geonet [28], characterized by an impressive axial strength of 50 kN/m, as illustrated in Figure 2. This strategic combination of fine and coarse sand, coupled with the robust axial strength of the Geonet, underscores a fine approach to optimizing the structural integrity of the project. To prepare the slope model fine sand and coarse sand are mixed in the proportion of 80:20; see Figure 2(a) of mixed soil. The shear strength [29] parameters (cohesion and friction) were determined by direct shear test. Table 1 illustrates the properties of mixed soil.

3.3 Preparation of reinforced slope

The preparation methodology for reinforced soil slopes closely mirrors that of their unreinforced counterparts. In both cases, careful attention is paid to key engineering principles. However, the integration of reinforcement introduces an additional layer of complexity and structural support. In the context of reinforced soil slopes, a pivotal element in the process involves the incorporation of a Geonet with a significant tensile strength of 50 kN/m. The Geonet, placed at 100 mm intervals, is utilized as a robust reinforcement mechanism, enhancing the slope's overall stability and strength. To prepare the slope surface the desired slope angle was marked on the soil container. The soil slope models were constructed in the container by the controlled volume method. The slope surface was initially supported by a wooden plank and then removed after preparation of the finished slope.

This study was also focused on replicating the relative spacing and interaction effects of reinforcement layers within the confines of our scaled model. The 100 mm interval was selected based on scaled-down dimensions that maintain similarity in dynamic experiments, adhering to geometric scaling laws and practical considerations in physical modeling. This

***Table 1** Properties of mixed soil*

Type of Soil	Mixed soil
Density of soil (kN/m3)	17 kN/m3
Cohesion (kN/m2)	0
The angle of internal friction (φ)	40°
Specific gravity (G)	2.7
Maximum void ratio	0.66
Minimum void ratio	0.54
Relative density	83.33%

(a) (b)

***Figure 2** Material used (a) mixed soil of fine sand and coarse sand, (b) Geonet* interval was deemed appropriate to capture significant interactions between the geogrid and soil in a controlled laboratory environment, facilitating the observation of dynamic responses under seismic loading conditions. Moreover, the research was aimed to provide insights into the dynamic behavior of reinforced soil slopes rather than precisely replicating every aspect of full- scale field conditions, which may involve variable terrain and construction practices. The chosen interval allowed to study the effectiveness of geogrid reinforcement in enhancing slope stability and strength under controlled seismic loading, contributing valuable data to the understanding and improvement of soil slope design practices.

By interspersing the Geonet at regular intervals, the slope gains a reinforced structure capable of withstanding greater loads and environmental pressures. This deliberate placement ensures a uniform distribution of reinforcement, minimizing the risk of localized weaknesses. The axial stiffness of 50 kN/m plays a crucial role in providing the necessary tensile strength to the soil, preventing excessive deformation and potential failure. This methodical approach to reinforced soil slope preparation not only aligns with established engineering practices for unreinforced slopes but introduces the strategic reinforcement element, as well. which significantly enhances the slope's overall resilience and longevity. The accurate placement of the Geonet reinforces the stability of the slope, offering a robust solution that stands up to the challenges posed by various environmental factors.

4 Result and discussion

In this research on the dynamic response of soil slopes under seismic loading conditions using scaled physical modelling, the comment regarding boundary conditions pertains to ensuring their accurate definition and assessment. Boundary conditions in this study encompassed several critical factors aimed at replicating real-world scenarios. These included setting the precise foundation conditions to replicate the soil bed characteristics encountered in the field, ensuring lateral constraints on the model slopes to simulate natural slope boundaries, and applying dynamic loading parameters that mirror seismic events of interest. The various frequencies were set on the control panel as shown in Figure 3. The vertical crest displacement was measured with a digital planimeter. The sinusoidal force was induced by changing the frequencies and amplitudes. The duration of each force was applied for 10 cycles of the shake table.

Furthermore, it is acknowledged that the precise calibration and validation of these boundary conditions were essential to ensure the reliability and relevance of our experimental outcomes. This calibration process involved rigorous testing and adjustment of model parameters to match the established benchmarks and theoretical predictions, thereby enhancing the accuracy and applicability of our findings. By addressing these aspects, this research was aimed to minimize biases and uncertainties associated with boundary conditions, thereby strengthening the scientific rigor and validity of our investigations into soil slope dynamics under seismic loading conditions. To ensure homogeneity in the built models for shake table tests under seismic loading, we controlled the material consistency, layering, compaction, model geometry, and boundary conditions. All the models were constructed using the same soil type, uniformly mixed, and compacted to consistent densities and moisture contents, ensuring identical mechanical properties. Sensor placements were standardized across models, and seismic loading was precisely replicated in each test. These measures were rigorously applied and monitored to eliminate variability, ensuring that any observed differences in the dynamic response were due to the seismic loading rather than inconsistencies in model construction. This approach was critical for the reliability and repeatability of the experimental results.

4.1 Shaking table setup

Shaking table tests on model slopes serve as a crucial method for examining how the slopes respond to dynamic loading conditions, specifically assessing their behaviour in relation to base shaking frequency and shake table amplitude. In this study, a slope angle of 30°, 35° and 40° has been adopted for all models to provide a consistent basis for observation and analysis. The slope fill comprises dry soil composed of both fine sand and coarse sand, carefully tamped to attain optimal compaction levels. The height of the slopes is consistently maintained at 300 mm across all tests, ensuring a standardized parameter for evaluating the dynamic response.

Figure 4 presents the completed slopes of the models, showing the physical manifestation of the constructed slopes. Meanwhile, Figure 5 presents a schematic diagram illustrating the intricate details of the soil slope model, offering a comprehensive visualization of the experimental setup. To explore the dynamic response further, the slope models undergo testing at

Figure 3 *Data acquisition method*

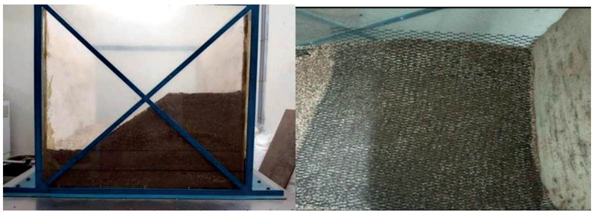

(a) (b)

Figure 4 *(a)Finished slope model (b) Placing of geonet*

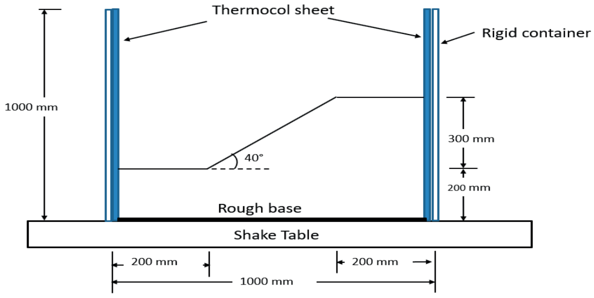

Figure 5 *Schematic diagram of soil the slope model*

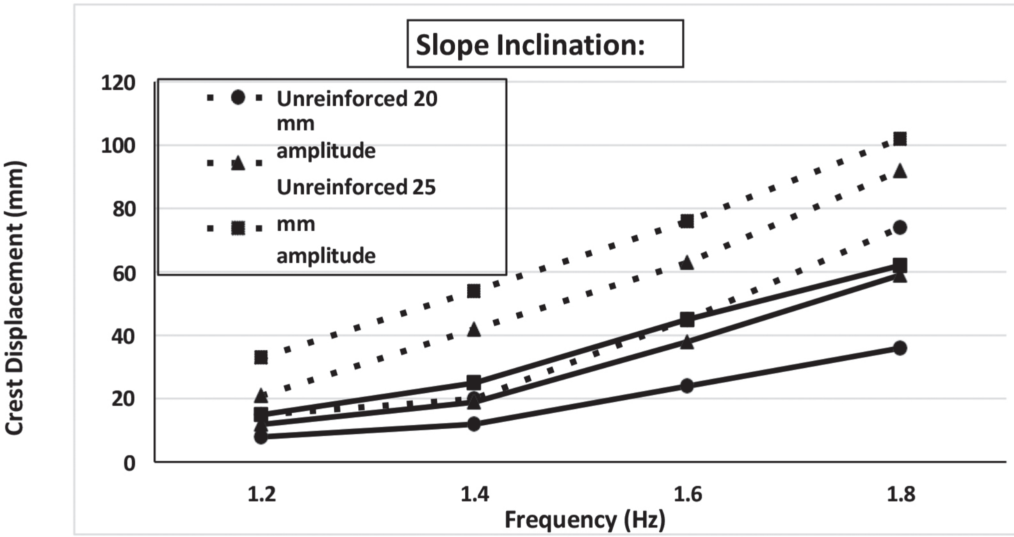

Figure 6 *Effect of frequency and amplitude on 30° unreinforced and reinforced soil slope model*

frequencies of 1.2,1.4, 1.6, and 1.8 hertz, encompassing a spectrum of loading conditions. Varied amplitudes of 20, 25, and 30 mm are applied during the tests, enabling a comprehensive examination of the slope behaviour under different dynamic parameters. This meticulous testing protocol allows for a nuanced understanding of how the slopes interact with varying frequencies and amplitudes, contributing valuable insights into the field of slope stability and earthquake engineering.

The shake table tests involved subjecting slope models to varying frequencies and amplitudes, with subsequent recording of crest settlements, as detailed in following Figures 6-11. Notably, the analysis reveals a consistent occurrence of bulging at the toe of each slope model, indicating a common pattern of deformation under the applied seismic conditions.

4.2 Experimental results of soil slope model without reinforcement

Figures 6-11 provided below present the empirical findings derived from a soil slope model with a height of 300 mm, encompassing diverse slope inclinations. These results offer a comprehensive overview of the performance and behaviour of the soil under varying slope conditions.

Figure 6, outlines the outcomes of an unreinforced and reinforced soil slope model subjected to varying frequencies, amplitudes, and corresponding measurements at a 30° slope inclination. Figure 6 shows that as frequency increases, the crest displacement rises. In addition, it indicates that with the increase of amplitudes from 20 mm to 30 mm, the crest displacement increases. This data serves as valuable information for understanding the dynamic behavior of the unreinforced soil slope under different loading conditions, offering crucial insights for geotechnical and structural analyses.

In the first trial at a frequency of 1.2 Hz, the crest displacement increases from 8 mm to 15 mm, as the amplitude rises from 20 to 30 mm for the reinforced soil slope model. This suggests that the higher amplitudes at this frequency result in an increased deformation of the reinforced soil slope. A similar trend is observed in subsequent trials at frequencies of 1.4, 1.6, and 1.8 Hz. Notably, as the frequency increases, there is a tendency for crest displacement to increase for the same amplitude. After a comparison of unreinforced and reinforced soil slope model, it is observed that there is a considerable reduction in the slope deformation. At a frequency of 1.2 Hz, the crest displacement is decreased from 15 mm to 8 mm, for an amplitude of 20 mm. A similar trend is observed for 25 mm and 30 mm amplitudes and for subsequent increase in frequency from 1.4 to 1.8 Hz.

While acknowledging that the higher magnitude seismic events may have higher frequency components, this study's focus on frequencies between 1.2 to 1.8 Hertz was aimed at capturing a realistic spectrum of seismic loading conditions relevant to the scaled physical model and providing insights into the dynamic response of soil slopes under controlled experimental settings. This information is valuable for understanding the stability and performance of the reinforced slope under different loading conditions, aiding in geotechnical engineering assessments and slope stability analyses. The reinforced nature of the slope suggests potential improvements in stability compared to unreinforced slopes, as indicated by the trends observed in the crest displacements.

Figure 7 summarizes the results obtained from testing an unreinforced and reinforced soil slope model inclined at 35° under different frequencies. In the first trial of an unreinforced slope model at a frequency of 1.2 Hz, as the amplitude increases from 20 to 30 mm, there is a corresponding rise in crest displacement from 18 to 36 mm. This suggests that the higher amplitudes

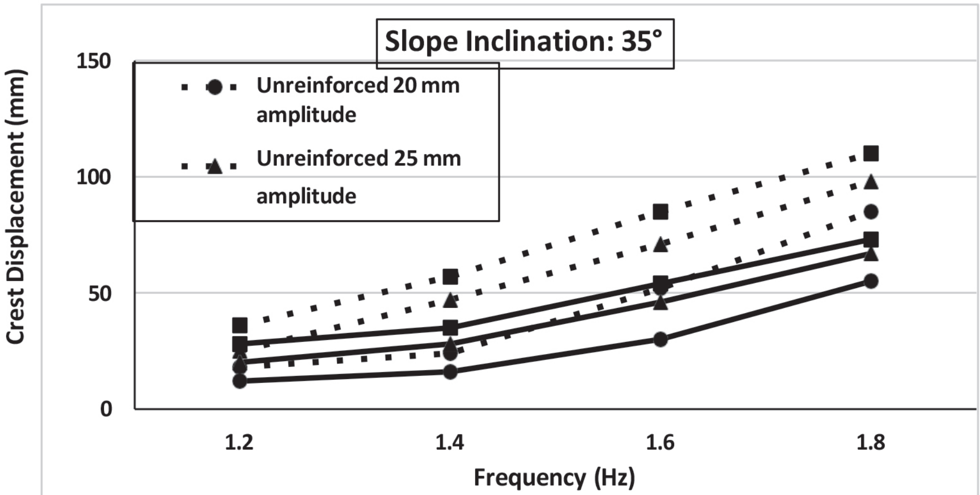

Figure 7 *Effect of frequency and amplitude on 35° unreinforced and reinforced soil slope model*

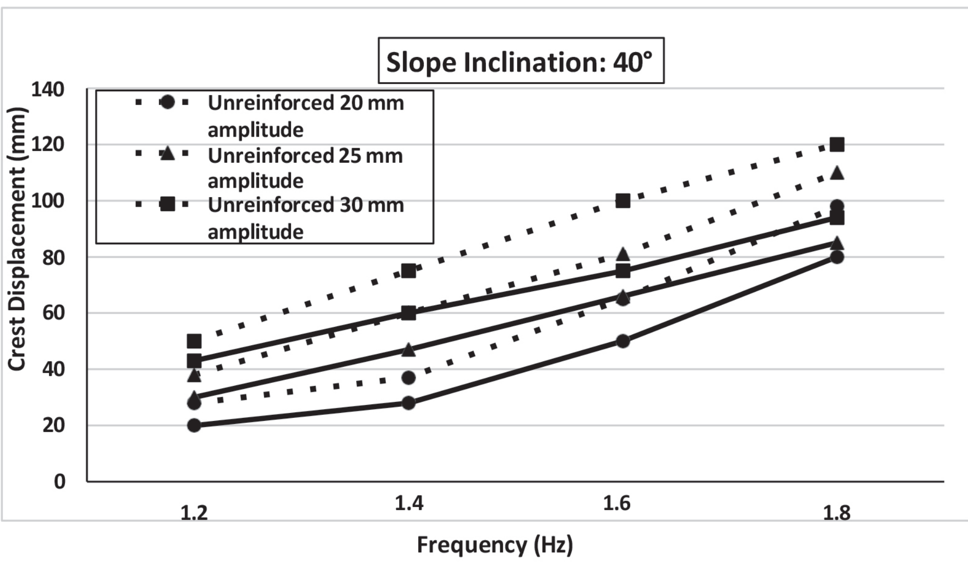

Figure 8 *Effect of frequency and amplitude on 40° unreinforced and reinforced soil slope model*

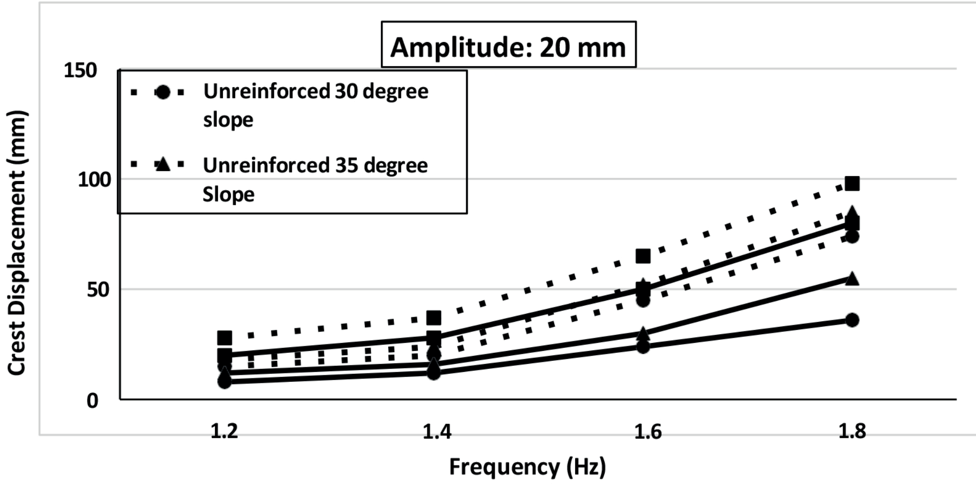

Figure 9 Effect of frequency and slope inclination on 20 mm amplitude on unreinforced and reinforced soil slope model

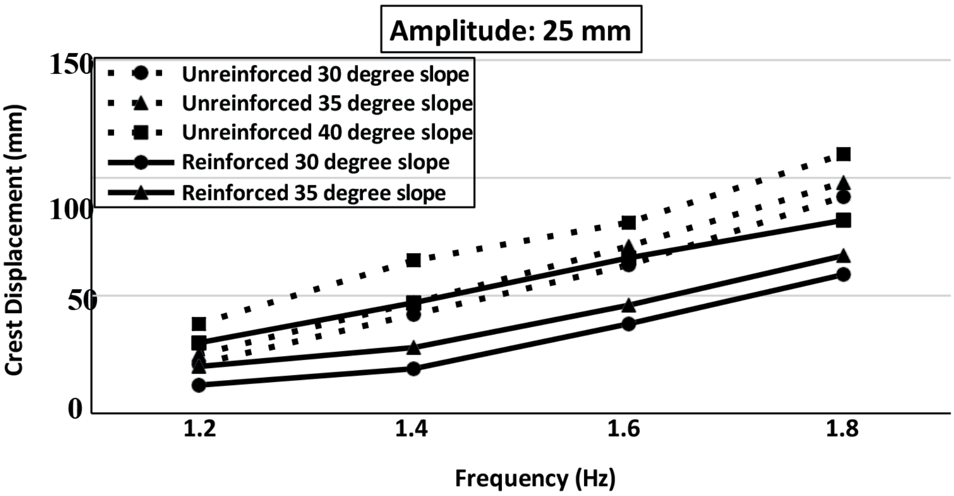

Figure 10 Effect of frequency and slope inclination on 25 mm amplitude on unreinforced and reinforced soil slope model

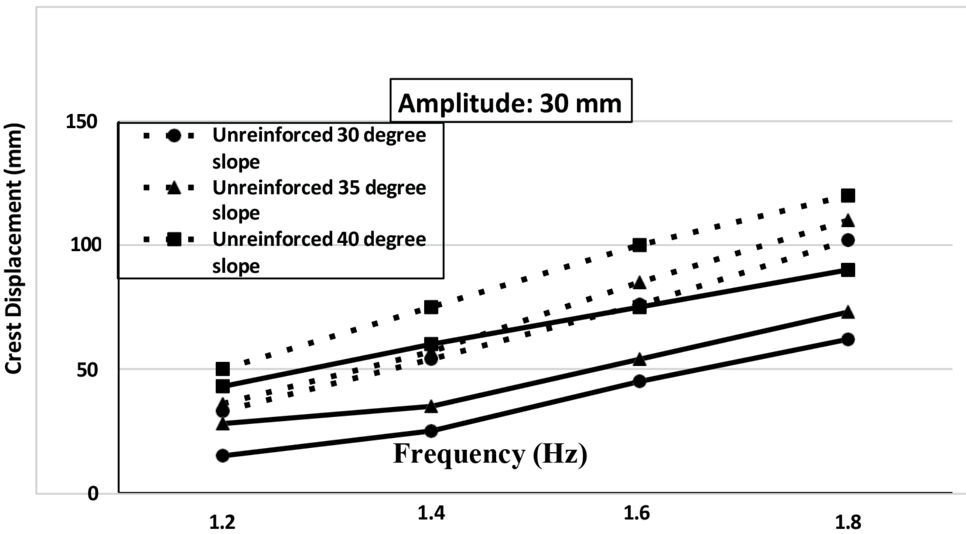

Figure 11 Effect of frequency and slope inclination on 30 mm amplitude on unreinforced and reinforced soil slope model

at this frequency lead to increased deformation of the soil slope. Similar trends are observed in subsequent trials at frequencies of 1.4, 1.6, and 1.8 Hz. It is found that by providing reinforcement, the crest displacement is decreased for amplitude of 20, 25 and 30 mm for the same frequency.

Figure 8, presents the results of tests conducted on an unreinforced and reinforced soil slope model inclined at 40° under varying frequencies. In the first trial at a frequency of 1.2 Hz, the crest displacement increases from 28 mm to 50 mm as the amplitude rises from 20 to 30 mm. This suggests that the higher amplitudes at this frequency result in increased deformation of the soil slope. A similar trend is observed in subsequent trials at frequencies of 1.4, 1.6, and 1.8 Hz.

Figure 11 provides valuable insights into the dynamic behavior of the unreinforced soil slope at a 40° inclination, highlighting the influence of varying frequencies and amplitudes on the slope's response. This information is essential for understanding the stability of the slope under different loading conditions, aiding in geotechnical engineering assessments and slope stability analyses. Overall, the data underscores the complex dynamic behavior of the reinforced soil slope, offering valuable insights for engineers and researchers engaged in geotechnical assessments and the design of resilient slope structures. Figures 9, to 11 represent the experimental results of the soil slope model for 300 mm height at 30°, 35° and 40° slope inclination with varying amplitude of 20 mm, 25 mm and 30 mm.

From the above Figures 9-11 it is observed that with the increase of slope inclination, the crest displacement increases. By providing reinforcement the crest displacement is decreased by 21 to 47%. When the tests were performed for the frequency 0.2 to 1 Hz there was not much crest displacement observed. At the frequency of 1.8 Hz, a considerable displacement was observed. Hence, the applied frequencies selected were 1.2 Hz to 1.8 Hz. Similarly at amplitudes of 5 to 15 mm a very small displacement was observed. Hence, for significant displacement applied amplitudes were selected as 20 mm, 25 mm and 30 mm.

The results of the research indicate a clear relationship between the displacement and factors such as frequency, amplitude, and slope angle. The significant reduction in crest displacement in reinforced soil slopes compared to unreinforced ones suggests that reinforcement effectively mitigates the destabilizing effects of seismic loading. This can be attributed to the increased shear strength and confinement provided by reinforcement, which enhances the slope's ability to resist deformation under dynamic conditions. The observed 21 to 45% reduction in displacement highlights the critical role of reinforcement in improving the slope stability, particularly in scenarios with high-frequency and high-amplitude seismic events.

The pronounced increase in displacement with steeper slope angles, particularly at 35° and 40°, can be explained by the increased gravitational forces acting on the slope, which exacerbate the tendency for soil to move downslope. As the slope angle increases, the driving forces surpass the resisting forces more easily, leading to greater deformation. The sharp rise in displacement at these steeper angles underscores the importance of considering slope geometry in stability assessments, as well as the need for effective reinforcement strategies to counteract the increased risk of failure in steep slopes under seismic loading.

5 Conclusion

In summary, the extensive examination of slope stability analysis, with a specific focus on both reinforced and unreinforced soil slopes, has yielded valuable insights into how the slopes behave under various conditions, such as frequency, amplitude, and slope angle. The findings suggest a noticeable correlation between the displacement and increases in frequency and amplitude, indicating that both reinforced and unreinforced soil slopes experience greater displacement as these factors intensify. A significant discovery from this research is the substantial reduction in crest displacement observed in reinforced soil slopes compared to unreinforced ones. The incorporation of reinforcement led to a remarkable 21 to 45% decrease in crest displacement, underscoring the efficacy of reinforcement techniques in improving slope stability.

Moreover, the research emphasizes the responsiveness of slope displacement to alterations in the angle of the slope. As the incline of the slope rises, there is a corresponding elevation in displacement, illustrating a direct correlation between the steepness of the slope and deformation. Specifically, at more pronounced angles such as 35° and 40°, the displacement demonstrates a significant increase, with respective increments of 9 to 18% and 35 to 65% compared to the 30° slope.

By carefully selecting a scale factor of 1/10 and validating it against theoretical predictions, we ensured the relevance of our findings to the real-world applications. Despite the criticisms that results could be predictable without experiments, our research demonstrates the necessity of empirical validation. By conducting the controlled experiments, this research provides tangible data that substantiates theoretical models and enhances their applicability in practice. This approach not only validates physical modeling methodologies but enriches the scientific understanding as well, by uncovering nuances and complexities that theoretical predictions alone may overlook. Thus, our study contributes robust insights that advance both theoretical frameworks and practical applications in geotechnical engineering, particularly in seismic hazard assessment and mitigation strategies.

Acknowledgment

The authors received no financial support for the research, authorship and/or publication of this article.

Conflicts of interest

The authors declare that they have no known competing financial interests or personal relationships that could have appeared to influence the work reported in this paper.

References

[1] BISCHETTI, G. B., DE CESARE, G., MICKOVSKI, S. B., RAUCH, H. P., SCHWARZ, M., STANGL, R. Design and temporal issues in soil bioengineering structures for the stabilisation of shallow soil movements. *Ecological Engineering* [online]. 2021, **169**, 106309. ISSN 0925-8574, eISSN 1872-6992. Available from: https://doi.org/10.1016/j.ecoleng.2021.106309

[2] UTEPOV, Y. B., MKILIMA, T., ALDUNGAROVA, A. K., SHAKHMOV, Z. A., AKHAZHANOV, S. B., SAKTAGANOVA, N. A., ABDIKEROVA, U. B., BUDIKOVA, A. M. Delving into earth dam dynamics: exploring the impact of inner impervious core and toe drain arrangement on seepage and factor of safety during rapid drawdown scenarios. *Infrastructures* [online]. 2023, **8**(10), 148. eISSN 2412-3811. Available from: https://doi.org/10.3390/infrastructures8100148

[3] CONGRESS, S. S. CH., PUPPALA, A. J. Geotechnical slope stability and rockfall debris related safety assessments of rock cuts adjacent to a rail track using aerial photogrammetry data analysis. *Transportation Geotechnics* [online]. 2021, **30**, 100595. eISSN 2214-3912. Available from: https://doi.org/10.1016/j.trgeo.2021.100595

[4] ZOU, Q., JIANG, H., CUI, P., ZHOU, B., JIANG, Y., QIN, M., LI, C. A new approach to assess landslide susceptibility based on slope failure mechanisms. *Catena* [online]. 2021, **204**, 105388. ISSN 0341-8162, eISSN 1872-6887. Available from: https://doi.org/10.1016/j.catena.2021.105388

[5] FIROOZI, A. A., FIROOZI, A. A. Application of machine learning in geotechnical engineering for risk assessment [online]. In: Machine learning and data mining - annual volume 2023. ACEVES-FERNANDEZ, M. A. (Ed.). IntechOpen, 2023. ISBN 978-0-85014-514-4, eISBN 978-0-85014-515-1, ISSN 2633-1403, p. 1-29. Available from: https://doi.org/10.5772/intechopen.113218

[6] YANG, K. H., THUO, J. N., CHEN, J. W., LIU, C. N. Failure investigation of a geosynthetic-reinforced soil slope subjected to rainfall. *Geosynthetics International* [online]. 2019, **26**(1), p. 42-65. ISSN 1072-6349, eISSN 1751-7613. Available from: https://doi.org/10.1680/jgein.18.00035

[7] SHARMA, S. Stability analysis of a hill slope in Uzan Bazaar Guwahati using FEM and LEM approach. Doctoral dissertation. 2023.

[8] PUENTE-SOTOMAYOR, F., EGAS, A., TELLER, J. Land policies for landslide risk reduction in Andean cities. *Habitat International* [online]. 2021, **107**, 102298. ISSN 0197-3975, eISSN 1873-5428. Available from: https://doi.org/10.1016/j.habitatint.2020.102298

[9] SHINODA, M., MIYATA, Y. PSO-based stability analysis of unreinforced and reinforced soil slopes using non-circular slip surface. *Acta Geotechnica* [online]. 2019, **14**, p. 907-919. ISSN 1861-1125, eISSN 1861-1133. Available from: https://doi.org/10.1007/s11440-018-0678-x

[10] KESKIN, M. S., KEZER, S. Stability of MSW landfill slopes reinforced with geogrids. *Applied Sciences* [online]. 2022, **12**(22), 11866. eISSN 2076-3417. Available from: https://doi.org/10.3390/app122211866

[11] JYOTHI, B. D., KRISHNA, V. R. Optimal arrangement of geogrids in road embankment using different fill materials. *Materials Today: Proceedings* [online]. 2021, **46**(17), p. 8507-8512. eISSN 2214-7853. Available from: https://doi.org/10.1016/j.matpr.2021.03.510

[12] ARVIN, M. R., ZAKERI, A., BAHMANI SHOORIJEH, M. Using finite element strength reduction method for stability analysis of geocell-reinforced slopes. *Geotechnical and Geological Engineering* [online]. 2019, **37**(2), p. 1453-1467. ISSN 0960-3182, eISSN 1573-1529. Available from: https://doi.org/10.1007/s10706-018-0699-0

[13] COLLIN, J. G., STARK, T. D., LUCARELLI, A., TAYLOR, T. P., BERG, R. R. Stability and stress-deformation analyses of reinforced slope failure at Yeager airport. *Journal of Geotechnical and Geoenvironmental Engineering* [online]. 2021, **147**(3), 04020179. ISSN 1090-0241, eISSN 1943-5606. Available from: https://doi.org/10.1061/(ASCE)GT.1943-5606.0002454

[14] PATIL, V. N., CHORE, H. S., SAWANT, V. A. Numerical analysis of reinforced embankment slopes made up of pozzolanic waste materials. *International Journal of Geo- Engineering* [online]. 2020, **11**(1), 19. eISSN 2198-2783. Available from: https://doi.org/10.1186/s40703-020-00126-z

[15] AMENA, S. Analysis of the stability of reinforced plastic waste treated clay as embankment fill on soft soils. *Advances in Civil Engineering* [online]. 2022, **2022**, 831970. ISSN 1687-8086, eISSN 1687-8094. Available from: https://doi.org/10.1155/2022/1831970

[16] QIU, J., HE, W., ZHENG, D., XU, Y., GUO, S., MA, T., LIU, Y. Dynamic failure experimental study of a gravity dam model on a shaking table and analysis of its structural dynamic characteristics. *Sensors* [online]. 2024, **24**(5), 1602. eISSN 1424-8220. Available from: https://doi.org/10.3390/s24051602

[17] WANG, J., WANG, Z., SUN, G., LUO, H. Analysis of three-dimensional slope stability combined with rainfall and earthquake. *Natural Hazards and Earth System Sciences* [online]. 2024, **24**(5), p. 1741-1756. eISSN 1684-9981. Available from: https://doi.org/10.5194/nhess-24-1741-2024

[18] BEYENE, A., TESEMA, N., FUFA, F., TSIGE, D. Geophysical and numerical stability analysis of landslide incident. *Heliyon* [online]. 2023, **9**(3), e13852. eISSN 2405-8440. Available from: https://doi.org/10.1016/j.heliyon.2023.e13852

[19] HORE, R., HOSSAIN, M. Z., ANSARY, M. A. Dynamic analysis of sand embankment by shaking table test. *International Journal of Civil Engineering* [online]. 2024, **22**(2), p. 209-224. ISSN 1735-0522, eISSN 2383-3874. Available from: https://doi.org/10.1007/s40999-023-00871-z

[20] CAO, Y., QU, Z., FU, H., JI, X., CHAKRABORTY, S. A substructural shake table testing method for full-scale nonstructural elements. *Mechanical Systems and Signal Processing* [online]. 2024, **218**, 111575. eISSN 1096-1216. Available from: https://doi.org/10.1016/j.ymssp.2024.111575

[21] SUN, L., BAI, Y., LAI, Z. Shaking table test on seismic performance of a large- span high-rise building. *Scientific Reports* [online]. 2024, **14**(1), 6580. eISSN 2045-2322. Available from: https://doi.org/10.1038/s41598-024-57068-0

[22] CAICEDO, D., KARIMZADEH, S., BERNARDO, V., LOURENÇO, P. B. Selection and scaling approaches of earthquake time-series for structural engineering applications: a state-of-the-art review. *Archives of Computational Methods in Engineering* [online]. 2024, **31**(3), p. 1475- 1505. ISSN 1134-3060, eISSN 1886-1784. Available from: https://doi.org/10.1007/s11831-023-10025-y

[23] GHUTKE, V., MODAK, S., SHANWARE, R., SHARMA, G., DONGARWAR, Y., SINGH, N. K., CHAKOLE, A. Dynamic behaviour of small-scale soil slope model. *Ijraset Journal for Research in Applied Science and Engineering Technology* [online]. 2023, **11**(IV), p. 4285-4297. ISSN 2321-9653. Available from: https://doi.org/10.22214/ijraset.2023.51279

[24] NEJMEH, K. Enhancing adhesion and water resistance in clayey adhesives mixtures: strategies for vertical and horizontal applications [online]. Doctoral dissertation. Champs-sur-Marne, France: Universite Gustave Eiffel, 2024. Available from: https://theses.hal.science/tel-04608994v1

[25] BAPIR, B., ABRAHAMCZYK, L., WICHTMANN, T., PRADA-SARMIENTO, L. F. Soil- structure interaction: a state-of-the-art review of modeling techniques and studies on seismic response of building structures. *Frontiers in Built Environment* [online]. 2023, **9**, 1120351. eISSN 2297-3362. Available from: https://doi.org/10.3389/fbuil.2023.1120351

[26] MALEKI, M., KHEZRI, A., NOSRATI, M., HOSSEINI, S. M. M. M. Seismic amplification factor and dynamic response of soil-nailed walls. *Modeling Earth Systems and Environment* [online]. 2023, **9**(1), p. 1181-1198. ISSN 2363-6203, eISSN 2363-6211. Available from: https://doi.org/10.1007/s40808-022-01543-y

[27] ALAINACHI, I. H. Shaking table testing of cyclic behaviour of fine-grained soils undergoing cementation: cemented paste backfill. Doctoral dissertation. Ottawa, Canada: University of Ottawa, 2020.

[28] HUTCHINSON, J., LEE, R., VAN HOUTTE, C., KAISER, A., WOTHERSPOON, L., BRADLEY, B. Development of an expanded earthquake and ground motion catalogue for New Zealand. 2021.

[29] STACHO, J., SULOVSKA, M., SLAVIK, I. Analysis of the shear strength of a soil-geosynthetic interface. *Civil and Environmental Engineering* [online]. 2023, **19**(1), p. 452-463. eISSN 2199-6512. Available from: https://doi.org/10.2478/cee-2023-0040

EXPLORING CONTRIBUTING FACTORS TO HOUSEHOLD VEHICLE OWNERSHIP IN DEVELOPING COUNTRIES: A CASE OF BANDA ACEH, INDONESIA

Ruslan Ruslan[1], Sofyan M. Saleh[2], Renni Anggraini[2], Sugiarto Sugiarto[2,3,*]

[1]Doctoral Program, School of Engineering, Post Graduate Program, Universitas Syiah Kuala, Banda Aceh, Indonesia
[2]Department of Civil Engineering, Universitas Syiah Kuala, Banda Aceh, Indonesia
[3]Center for Environmental and Natural Resources Research, Universitas Syiah Kuala, Banda Aceh, Indonesia

*E-mail of corresponding author: sugiarto@usk.ac.id

Ruslan Ruslan 0000-0001-9959-1936, Renni Anggraini 0000-0002-9956-8004, Sofyan M. Saleh 0009-0000-2911-814X, Sugiarto Sugiarto 0000-0001-8332-6142

Resume

Household car ownership has become a crucial issue in Indonesia due to rapid urbanization and economic growth, which have led to increased demand for personal vehicles. This surge in vehicles contributes to traffic congestion, pollution, and strains on urban infrastructure. This study aimed to investigate private vehicle ownership in relation to household characteristics and mobility attributes in developing country settings. The methodology used is the multinomial logit model (MNL) to analyze ownership patterns. The empirical results showed the significant impact of the income variable on vehicle ownership. Ownership of multiple private vehicles was more prevalent among individuals with a driver's license, males, and those who traveled longer distances. These outcomes could be invaluable for policymakers focused on reducing auto dependency and enhancing the efficiency of urban transportation systems.

Available online: https://doi.org/10.26552/com.C.2025.009

Article info

Received 26 May 2024
Accepted 2 October 2024
Online 8 November 2024

Keywords:

private vehicle
car ownership
household characteristics
mobility attributes
stated preference
multinomial logit

ISSN 1335-4205 (print version)
ISSN 2585-7878 (online version)

1 Introduction

Traffic congestion in Banda Aceh has become increasingly severe due to a thriving economy, population growth, and urbanization. This surge in private vehicle usage threatens the transportation system of the city. To maintain a smooth transportation system, it is crucial to reduce reliance on private vehicle and promote public transportation. However, the effectiveness of both existing and proposed public transportation remains uncertain. Banda Aceh, the capital of Aceh Province, is a burgeoning city and a hub for government administration, education, private offices, tourism, and numerous shopping centers. It attracts not only residents but also people from neighboring areas of Aceh Besar. In 2020, the city's population reached 259,913, with a density of 42 individuals per hectare, covering an area of 61.36 square kilometers and experiencing an annual population growth rate of approximately 2%. This growing population density has led to an increase in daily travel, resulting in new residential areas, shopping centers, and food hubs. Consequently, high levels of daily activities disrupt traffic flow and decrease road service quality.

The increasing reliance on private vehicle can primarily be attributed to the lack of improvement in the quality of public transportation services [1-2]. As a result, individuals with higher and middle incomes tend to opt for private vehicle [3]. This trend posed significant challenges for the transportation system, leading to congestion and environmental problems [4-5]. The consequences include the loss of time, difficulties in traffic flow, and an increased risk of traffic accidents. Therefore, a comprehensive understanding of the factors influencing private vehicle ownership is crucial for effective planning and management of urban transportation systems.

The current study aimed to exploring the factors affecting private car ownership intensity. In this study the term of exploring refers to a comprehensive investigation into the factors influencing vehicle ownership in households. This includes studying demographic, economic, and policy-related influences, and understanding how they shape vehicle ownership trends in a developing urban setting like Banda Aceh.. To achieve this, multinomial logit regression (MNL) was used as the analytical method. MNL regression model was developed to predict private vehicle ownership based on the number of vehicles owned. Following the estimation and validation of model under specific criteria, sensitivity analysis and policy scenario assessments were conducted. The study considered socioeconomic characteristics and built environment attributes as unique factors hypothesized to influence household vehicle ownership. Identifying the determinants of private vehicle ownership is crucial for developing consistent land-use and transportation policies that promote sustainable urban transportation systems. Therefore, by reducing household vehicle dependency, it is expected that auto traffic will decrease, flow will improve, and cleaner transportation will be facilitated.

The remaining sections of this paper are organized as follows: Section 2 presents a concise overview of the determinants of household vehicle ownership and the previously studied algorithms. Section 3 shows model's structure, data sources, and the mathematical foundation. The subsequent section addresses model's estimation, application outcomes, and policy implications. The concluding section provides closing thoughts and suggestions for future study.

2 Literature review

Studies on vehicle ownership often rely on aggregate and disaggregate models, or focused on motorcycles [6-9]. Aggregate model may be subject to aggregation bias and multicollinearity between explanatory variables [10]. In contrast, disaggregate modeling addresses these limitations by capturing individual choice behavior and explanatory variables at the individual level, leading to more reliable estimates. As a result, it has gained significant attention in recent studies on vehicle ownership. The dependent variable, the number of vehicles in household, is typically analyzed using ordered or unordered response choice models [11-12]. With household's decision to own vehicle, an individual's usage is measured in miles (or kilometers) per year, and the relationship between vehicle type and this variable can be examined simultaneously [13].

In-depth investigation has been conducted on the selection and usage of vehicle in developed countries, considering factors such as household characteristics and the number of vehicles owned [14-15]. However, studies in developing countries such as Indonesia, where the transportation system is significantly different, are less common. In many Asian countries, the focus tends to be on a single aspect of vehicle ownership [16] and [17-19], which limits the scope for policy-making. In recent years, studies of household vehicle ownership with panel data have increasingly adopted ordered-response model that account for state dependence and heterogeneity [20-22]. Panel data analysis of vehicle usage typically uses random and fixed effects specifications, allowing for unobserved heterogeneity [20, 23].

Studies on private car ownership and usage are relatively limited. For instance, [24] applied ordered probit and tobit/probit regression models with sample selection to investigate motorcycle usage in the metropolitan area of Jabotabek, Indonesia, identifying key explanatory variables such as residential location, land use, transportation system performance, and socioeconomic/demographic characteristics. A two-level Nested Logit (NL) model is widely used to examine household's decision to own motorcycles at the upper level and the choice of engine sizes at the lower level. Furthermore, a three-level NL model was proposed to analyze household joint choices regarding the number of cars, the number of motorcycles, and the mode of transportation for work [25]. An integrated model was also proposed to analyze choice behaviors associated with ownership, type, and usage of cars and motorcycles in Taiwan. Two related studies were recently conducted, namely [26], investigating the factors influencing private car ownership and vehicle usage measured in kilometers [27] and [28], examining the factors affecting motorcycle ownership and vehicle usage measured in kilometers. However, these studies are limited to developed countries and have not been conducted in Banda Aceh City, Indonesia. The current study aimed to investigate the factors influencing private car ownership and analyze their effects on private car ownership in Banda Aceh City. It was particularly beneficial for countries with poor public transportation systems and high automobile dependence, such as Indonesia.

3 Methodological framework

3.1 Car ownership model

Car possession model assessed the number of cars owned by households each year. Households may choose to alter or retain the number of cars in the following year. Traditional methods for this type of dependent variable usually use discrete choice, ordered logit or probit, and count data models [29]. However, the unordered discrete choice model is preferred because it provides a theoretical framework based on random utility theory commonly used to explain behavior propensity. In the framework of discrete choice analysis, a decision-maker (i.e., a household) was assumed to select the alternative (i.e., the number of cars owned) with the highest utility under the principle of utility maximization. Furthermore, the appeal (in terms of utility) of each alternative can be represented by the sum of the systematic (observable) and random (unobservable) error components. The total utility of alternative i for household n in year t is specified as:

$$U_{itn} = V_{itm} + \varepsilon_{itn}\,, \tag{1}$$

where $\boldsymbol{V_{itn}}$ is the observed component of utility; $\boldsymbol{S_{tn}}$ (household's characteristics) and Ltn (location characteristics and transportation system performance) are vectors of alternative specific variables that do not vary over alternatives; C_{itn} is a vector of generic variables including fixed and variable costs of the owned cars; these vary by alternatives and allow the same marginal effect on each alternative's utility; α_i (alternative specific constant), $\beta, \gamma, \delta,$ and λ and are the unknown parameters to be estimated; ε_{itn} is the random error term.

In Equation (1), lagged dummy variables are used to account for state dependence. For each alternative, when the number of cars owned by household n in year t is equal to the number of cars owned by household *n* in the previous year (t - 1), *then* D_{itn} = 1, and 0 otherwise. A statistically significant value of the state dependence parameter shows that car ownership in the current year is influenced by car ownership in the previous year. A discrete choice model can be formulated under specific distributional assumptions regarding the error term. MNL model is commonly used due to its straightforward probability formulation and efficient computational process. The probability expression for model is as follows:

$$P_{itn} = \frac{\exp(V_{itn})}{\sum \exp(V_{jtn})}. \tag{2}$$

The logsum parameter should be within the range of 0 to 1 to ensure consistency with utility maximization. MNL specification is more suitable when NL fails to surpass model. Likelihood ratio test can be used to evaluate MNL and different NL models, in order to ascertain whether the independence of irrelevant alternatives (IIA) assumption is valid [30].

The current study used MNL, a commonly used statistical method for analyzing discrete choices between multiple alternatives. The dependent variable in this model comprised three distinct categories representing varying levels of private car ownership, namely no private car ownership, one private car, and two private cars. MNL analysis facilitated investigating the influence of different factors on individuals' choices among these discrete categories of car ownership. By examining the coefficients associated with the various independent variables, the relative significance and effect of each factor on the probability of belonging to one of the specified categories of private car ownership can be determined. This method provided a robust foundation for exploring the intricate dynamics underlying individuals' decisions regarding car ownership. MNL delineates the relationships between the predictor variables and the probability of belonging to specific ownership categories, offering valuable insights into the factors influencing transportation choices and car ownership patterns.

3.2 Study area and data distributions

This study was conducted in Banda Aceh, the capital of Aceh Province, located in the westernmost part of Indonesia, as shown in Figure 1. It focused on households within the city, comprising nine districts, namely Baiturrahman, Banda Raya, Jaya Baru, Kuta Alam, Kuta Raja, Lueng Bata, Meuraxa, Syiah Kuala, and Ulee Kareng. Furthermore, residents living near Banda Aceh and Aceh Besar municipal areas were included as target respondents.

Revealed Preference (RP) survey method was used to obtain information about the socioeconomic characteristics, travel patterns, and mobility attributes of the targeted households. Furthermore, a paper-pencil direct interview was distributed to 400 respondents in 2020, resulting in 349 valid samples being analyzed. A summary of RP survey results is presented in Table 1.

Table 2 presents descriptive statistics in the form of frequency and percentage (%) of the total number of private car owners based on the aforementioned variables. A total of 349 participants took part in the study. Descriptive statistics was presented based on the collected data, including frequency, percentage, and cumulative percentage. The Table 2 provides a comprehensive overview of the socioeconomic and environmental characteristics of the study sample, presenting descriptive statistics on the frequency distribution and percentage of the various variables under study. Regarding socioeconomic characteristics, 193 respondents (55.30%) were male, while 156 (44.70%)

***Table 1** Summary of RP survey*

Description	Detail
The year of survey	2020
Target location	Banda Aceh city (nine districts and a surrounding area of Aceh Besar municipal)
Distribution sampling method	direct interviews and collected by the enumerators
Number of Sample	400 collected 349 valid/used for analysis
Distributions	Weekdays (80%) & Weekends (20%)

were female. In terms of age distribution, the majority fell within the 20-29 age group (76.22%). The highest level of education attained by the respondents was also reported, with the majority holding a bachelor's degree (53.87%). Furthermore, the Table 2 covers the distribution of occupation types and monthly income levels within specific categories. Being a student was the most prevalent occupation type (58.74%), and 98 respondents (28.08%) had a monthly income between 3-4.9 million IDR.

Table 3 provides information about mobility attributes and environmental characteristics of the respondents. Specifically, it details the travel time to the nearest bus stop, which refers to the duration of the respondents' journeys. The frequency of respondents in each travel time category was also presented, with 77 (22.06%) spending 2-4 minutes to reach the nearest bus stop. Also included was the travel purpose and origin-destination travel distance (in kilometers). The majority had a travel purpose related to school/college (52.72%), and 94 (26.93%) had travel distances of 4-6.9 kilometers.

Concerning the residential and destinations of trips, 112 respondents (32.09%) were from the Syiah Kuala district, and 162 (46.42%) traveled to the same district. Furthermore, the Table 3 presents characteristics of driving license ownership. The majority of the respondents had a type A driving license (60.46%). An overview of the number of private cars owned by the respondents was also provided. The majority did not own a private car (47.85%), while 142 (40.69%) owned one private car.

4 Empirical result and discussion

4.1 Private vehicle ownership model

A discrete choice multinomial logistic regression analysis was conducted to determine the factors influencing ownership of one or two private cars compared to not owning car. The dataset contained information from 349 respondents. The results of multinomial logistic regression estimation and the goodness of fit for the two models tested are presented in Table 4. In the first model, the initial log-likelihood value (LL_0) was -337.43, and after five iterations, convergence was reached at a log-likelihood value ($LL_{convergent}$) of -280.41. This model showed a significant influence of the variables, with an LR chi-square of 114.04 and a probability of less than 0.001. Furthermore, the pseudo R-squared value of 0.169 showed that model could explain approximately 16.90% of the variation in data.

The first model (car ownership in household) comprised several independent variables. The "Amount of income" variable, ranging from 5-6.9 million IDR (1 USD = 15.822 IDR), had a coefficient of 0.960 and

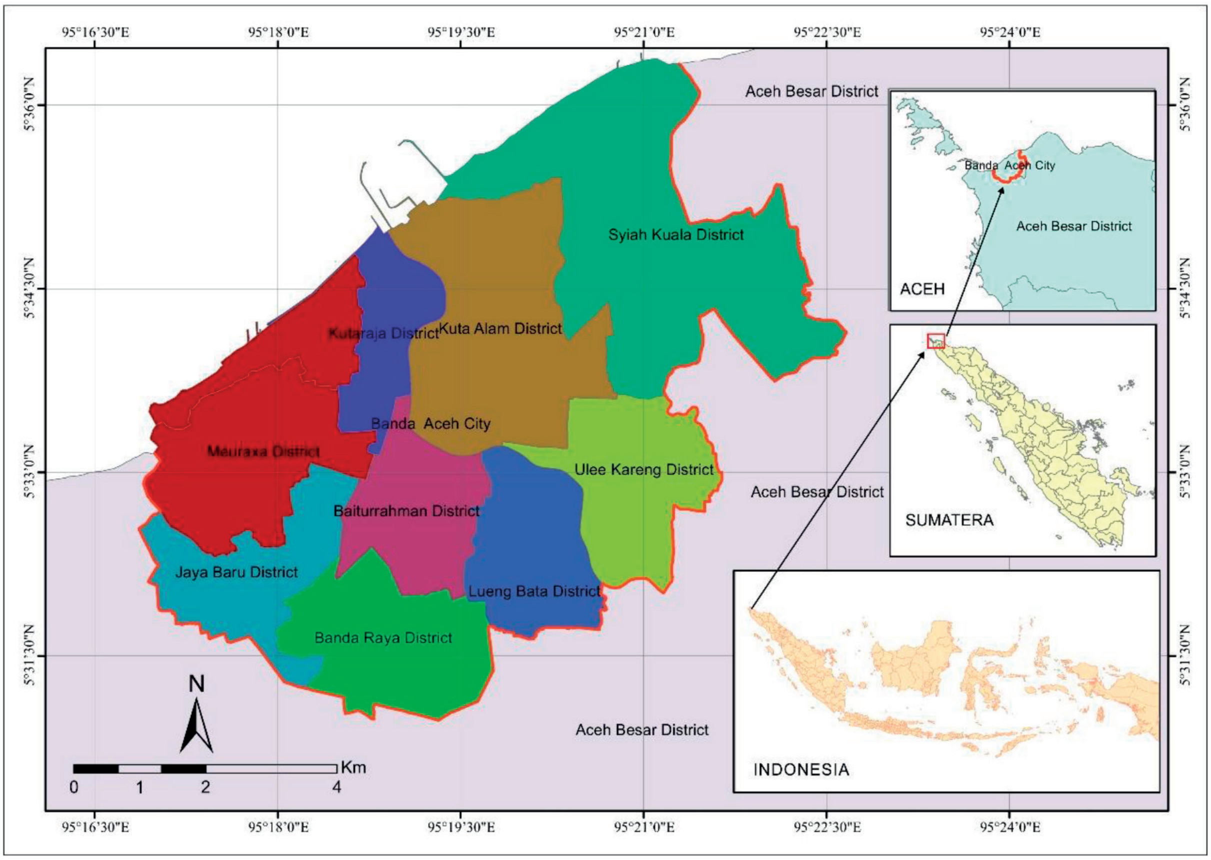

***Figure 1** Banda Aceh city (the area of study within the red area)*

***Table 2** Distribution of socioeconomic variables*

Variable	Freq.	Percent.	Cum.
Socioeconomic characteristics;			
Gender			
Male	193	55.30	55.30
female	156	44.70	100.00
Total	349	100.00	
Age group category			
17 -19 years	46	13.18	13.18
20 - 29 years	266	76.22	89.4
30 - 39 years	27	7.74	97.13
40 - 49 years	8	2.29	99.43
50 - 59 years	2	0.57	100
Total	349	100	
Educational level of household			
Primary education or equivalent	118	33.81	33.81
Diploma	23	6.59	40.4
graduate	188	53.87	94.27
postgraduate	20	5.73	100
Total	349	100	
Type of persons employed			
Government employees	38	10.89	10.89
Employee	34	9.74	20.63
Businessman or Self-employed	15	4.30	25.21
Housewife	56	15.19	100
College or school student	205	58.74	84.81
Total	349	100	
Monthly income in Indonesia Rupiah (IDR), 1 USD equal to 15,743 IDR			
< 1 million IDR	49	14.04	14.04
1 - 2.9 million IDR	68	19.48	33.52
3 - 4.9 million IDR	98	28.08	61.6
5 - 6.9 million IDR	66	18.91	80.52
7 - 9.9 million IDR	35	10.03	90.54
≥ 10 million IDR	33	9.46	100
Total	349	100	

a significance level of 0.040. Therefore, an increase in this category raised the probability of the event by 2.61 times. The “Ownership of Car License, SIM A; yes” variable had a coefficient of 2.356 and a significance level of 0.001, showing that owning a type A car license had a significant positive impact on the probability of the event. Meanwhile, the “Gender; male” variable had a coefficient of -0.529 and a significance level of 0.087, showing a weak negative influence on the event’s probability. The “Origin - Destination travel distance (Km); 10-12.9 Km” variable had a coefficient of 0.896 and a significance level of 0.020, showing that an increase in travel distance in this category could increase the probability of the event by 0.896 times. The constant variable had a coefficient of -0.954 and a significance level of 0.001, showing the basic value of the event’s probability of owning car in household.

The second model, comprising owning two cars in household, also converged after five iterations to achieve a log likelihood ($LL_{convergent}$) of -280.41. The LR chi-square value of 114.04 and a probability of less than 0.001 showed that the variables in this model had a significant influence. The Pseudo R-squared value of 0.169 showed that model could explain approximately 16.90% of the variation in data. The second model had the same independent variables as the first. The “Amount of income; 5-6.9 million Rupiah (dummy variable)” had a coefficient of 1.608 with a significance of 0.006. Therefore, an increase in this category could raise the probability of an event by approximately 4.993 times. The “Ownership of Car License, SIM A; yes” variable had a coefficient of 3.453 with a significance of 0.001,

__Table 3__ Distributions of mobility attributes (1/2)

Variable	Freq.	Percent.	Cum.
Built Environment characteristics			
Travel Time to Bus Stop			
< 2 minute	37	10.6	10.6
2-4 minute	77	22.06	32.66
5-6 minute	75	21.49	54.15
7-8 minute	55	15.76	69.91
9-10 minute	53	15.19	85.1
>10 minute	52	14.9	100
Total	349	100	
Type of Travel destination			
Work trip	67	19.2	19.2
Trip to school or campus	184	52.72	71.92
Shopping trip	41	11.75	83.67
travel for social activities	14	4.01	87.68
travel for recreational activities	23	6.59	94.27
Work trip	20	5.73	100
Total	349	100	
Travel distance			
<4 km	108	30.95	30.95
4-6.9 km	94	26.93	57.88
7-9.9 km	64	18.34	76.22
10-12.9 km	39	11.17	87.39
> 13	44	12.61	100
Total	349	100	
Location of residence (District)			
Baiturrahman	17	4.87	4.87
Banda Raya	12	3.44	8.31
Jaya Baru	6	1.72	10.03
Kuta Alam	38	10.89	20.92
Kuta Raja	3	0.86	21.78
Lueng Bata	29	8.31	30.09
Meuraxa	7	2.01	32.09
Syiah Kuala	112	32.09	64.18
Ulee Kareng	31	8.88	73.07
Aceh Besar	94	26.93	100
Total	349	100	
Travel destination location (District)			
Baiturrahman	51	14.61	14.61
Banda Raya	6	1.72	16.33
Jaya Baru	4	1.15	17.48
Kuta Alam	43	12.32	29.8
Kuta Raja	3	0.86	30.66
Lueng Bata	11	3.15	33.81
Meuraxa	4	1.15	34.96
Syiah Kuala	162	46.42	81.38
Ulee Kareng	14	4.01	85.39
Aceh Besar	51	14.61	100
Total	349	100	

***Table 3** Distributions of mobility attributes (2/2)*

Variable	Freq.	Percent.	Cum.
Mandatory trip duration (Minutes)			
< 10 minute	92	26.36	26.36
10 - 19 minute	142	40.69	67.05
20 - 29 minute	59	16.91	83.95
30 - 39 minute	31	8.88	92.84
40 - 49 minute	6	1.72	94.56
> 50 minute	19	5.44	100
Total	349	100	
Owning of driving license			
Owning a driving license, SIM A (motorcycle driving license)			
yes	211	60.46	60.46
not	138	39.54	100
Owning a driving license SIM C (private car driving license)			
yes	53	15.19	15.19
not	296	84.81	100
Total	349	100	
Car Ownership			
Number of owning a private car			
Zero vehicle; 0	167	47.85	47.85
One vehicle; 1	142	40.69	88.54
Two vehicles; 2	40	11.46	100
Total	349	100	

***Table 4** Empirical results of private vehicle ownership using MNL*

Variables	Coeff.	S.E	t-value
Model 1: Number of private vehicle ownership (private car=1)			
Monthly income (IDR);			
5 - 6.9 million (dummy variable)	0.960	0.469	2.05**
Owning a driving license (SIM A);			
Yes	2.356	0.329	7.17***
Gender;			
Male	-0.529	0.309	-1.71*
Travel distance Origin -Destination (Km);			
10-12.9 Km (dummy variable)	0.896	0.386	2.32**
Constant	-0.954	0.195	-4.90***
Model 2: Number of private vehicle ownership (private car =2)			
Monthly income (IDR);			
5 - 6.9 million (dummy variable)	1.608	0.587	2.74***
Owning a driving license (SIM A);			
yes	3.453	0.489	7.06***
Gender;			
Male	-2.157	0.492	-4.38***
Travel distance Origin -Destination (Km);			
10-12.9 Km (dummy variable)	0.922	0.572	1.61
Constant	-2.362	0.335	-7.06***
Summary of Statistics			
Pseudo r-squared	0.169		
Chi-square	114.05		
Akaike crit. (AIC)	580.82		
LL-Null	-337.43		

showing a significant positive influence on the chance of an event. The "Gender; male" variable had a coefficient of -2.157 with a significance of 0.001, showing a strong negative influence on the probability of occurrence. The "Origin - Destination travel distance (Km); 10-12.9 Km" variable had a coefficient of 0.922 with a significance of 0.107, showing a weak positive influence on the probability of an event. In addition, the constant had a coefficient of -2.362 with a significance of 0.001, showing the basic value of the probability of occurrence.

This analysis provided comprehensive insights into the impact of each factor on the probability of owning a private car in the multinomial regression model evaluated. Understanding these relationships could offer valuable guidance for creating sustainable and efficient transportation policies in Banda Aceh. To achieve this, transportation planning efforts can focus on developing mobility solutions that correspond with people's needs and preferences while considering the environmental and social consequences of owning a private vehicle.

The odds ratio value from the estimation of private vehicle ownership model could be interpreted using two models. One model comprised numerous independent variables. The "Amount of income; 5-6.9 million Rupiah (dummy variable)" had a coefficient of 0.960 with a significance level of 0.040, showing that an increase in this category could raise the probability of an event by 2.613 times (exp*0.960). The "Ownership of Car License, SIM A; yes" variable had an odds ratio of 10.55 with a significance of 0.001, showing that owning a type A car license significantly raised the chance of occurrence by 10.55 times. The "Gender; male" variable had an odds ratio value of -0.529 with a significance of 0.087, showing a modest negative impact on the probability of occurrence. Lastly, the "Origin - Destination travel distance (Km); 10-12.9 Km" variable had an odds ratio of 2.45 with a significance of 0.020, showing that an increase in travel distance in this category could raise the odds of an event by 2.45 times.

The second model had the same independent variables as the first model. The "Amount of income; 5-6.9 million Rupiah (dummy variable)" had an odds ratio of 4.99 with a significance of 0.006, showing that an increase in this category could result in an approximately 4.99 times greater chance of the event occurring. The "Ownership of Car License, SIM A; yes" variable had an odds ratio of 31,594 with a significance of 0.001, showing a significant positive influence on the event's chance of occurring, with an influence of 31,594 times. Furthermore, the "Gender; male" variable had an odds ratio of 0.12, with a significance of 0.001, showing a strong negative influence on the event's chance of occurring, reducing it by 0.12 times. Lastly, the "Origin - Destination travel distance (Km); 10-12.9 Km" variable had an odds ratio of 2.52 with a significance of 0.107, showing a weak positive influence on the event's chance of occurring.

Further insights regarding the interpretation of model could be obtained through marginal effect analysis. The estimation results provided a comprehensive understanding of the impact of each variable on the probability of private-car ownership in the multinational regression model evaluated. The utility function model equation for private car ownership, as derived from the parameter estimation results, is as follows: a) The utility function model for private car ownership for category 1, as presented in the parameter estimation results table, is:

$$U_{i,1} = -0.954 + (0.960^*X_2) + (2.356^*X_9) + + (-0.529^*X_1) + (0.896^*X_6) \tag{3}$$

and (b) The utility function model for private car ownership for category 2, based on the parameter estimation results table, is

$$U_{i,2} = -2.362 + (1.608^*X_2) + (3.453^*X_9) + + (-2.157^*X_1) + (0.922^*X_6). \tag{4}$$

In this context, the dependent variable is the "number of private car ownership," while the independent variables consist of four predictor variables, namely total income (variable X_2), ownership of SIM A (variable X_9), gender (variable X_1), and distance from origin to destination (variable X_6).

4.2 Model sensitivity

The sensitivity of model was assessed by calculating marginal effects, which measured the change in the outcome or response variable resulting from a small adjustment in a specific predictor variable while keeping other predictor variables constant. Marginal effects showed how a change in one independent variable influenced the dependent variable, solely considering the impact of that variable and disregarding the impact of others. In policy analysis and decision-making, marginal effects clarified how modifications in particular factors could lead to desired outcomes. The outcomes of the marginal effect analysis are presented in Table 4.

Table 5 presents the outcomes of the marginal effect estimation, offering insights into the variables influencing the probability of an individual owning a private car in the estimated model. These estimations showed the alterations in the probability of vehicle ownership when the predictor variables change. Furthermore, the relevant predictor variables were age group, education level, income level, travel duration from home to the nearest stop, travel destination, and distance between the origin and destination points. The average marginal effect estimate (dy/dx) for each variable measured the change in the probability of owning one private car when the variable changes.

Table 5 *Marginal Effect Calculation*

Variable	0 vehicle ownership	1 vehicle ownership	2 vehicle ownership
Income level; 5-6.9 m Rupiah (dummy variable)	-0.202	0.092	0.110
Vehicle License Ownership,SIM A; yes	-0.521	0.307	0.213
Gender; male	0.137	0.019	-0.157
Travel distance Origin-destination (Km); 10-12.9 Km (dummy variable)	-0.167	0.136	0.031

Note: dy/dx for factor levels is the discrete change from the base level.

Table 6 *Sensitivity analysis using monthly household income as driver*

Policy Scenario	Base Model (Calibrated Model)	Income Increase (+5%)	Income Increase (+10%)	Income Increase (+15%)
0 Private Car Ownership	0.4790	0.4780	0.4770	0.4760
1 Private Car Ownership	0.4070	0.4073	0.4079	0.4080
2 Private Car Ownership	0.1150	0.1154	0.1161	0.1161

The outcomes of the marginal effect estimation showed that an income level of 5-6.9 million IDR per month significantly increased the probability of owning a private car. The marginal effect estimate of 0.0916 (9.16%) showed the probability of owning a private car increased when the respondent fell within this income group. On the other hand, the “Ownership of Driving License, SIM A;” variable had a significant effect on the probability of owning a private car. Also, the average marginal effect estimate of 0.307 (30.7%) showed that changes in the SIM A ownership level significantly affected the probability of vehicle ownership. Regarding gender, males had a significant influence in reducing the probability of owning a private car. The average marginal effect estimate of 0.019 showed that males were associated with a decrease in the probability of vehicle ownership, with a 95% confidence interval ranging between -0.256 and -0.028. Furthermore, Travel Distance Origin - Destination (Km); 10-12.9 Km had a considerable impact in increasing the probability of owning a private car. The average marginal effect estimate of 0.136 showed that longer travel durations were correlated with an increase in the probability of vehicle ownership, with a 95% confidence interval ranging between 0.049 and 0.277.

The analysis of the marginal effect for the category of owning two private cars showed that individuals with an income level of 5-6.9 million IDR per month had a positive impact on the probability of owning two private cars, though not statistically significant. The marginal effect estimate of 0.110 showed that a change in this income group had a small influence on the probability of owning two private cars, with a 95% confidence interval. Owning a Driving License, SIM A, and a higher educational level had a significant positive influence on the probability of owning two private cars. The marginal effect estimate of 0.213 showed that a change in educational level had a significant impact on vehicle ownership, with a 95% confidence interval. However, being a male had a significant negative influence on the probability of owning two private cars. The marginal effect estimate of -0.156 showed that males were negatively correlated with the probability of vehicle ownership. Travel distance origin to destination (km); 10-12.9 km did not have a significant impact on the probability of owning two private cars, specifically 0.0312 (3.12%).

The analysis of marginal effect estimates provided a deeper comprehension of how individual predictor variables impacted the probability of owning one or more private cars. These results provided meaningful guidance for creating better and more sustainable transportation policies in urban areas. The results of the marginal effect estimates, obtained using delta method, provided insight into how discrete adjustments in specific variables affected the probability of car ownership within the context of the estimated model. These marginal effects showed the changes in the probability of vehicle ownership, considering standard errors and p-values.

4.3 Model applications for policy formulation

This study aimed to implement private vehicle ownership model in various scenarios focusing on household income levels ranging from 5-7 million Indonesian Rupiah per month. It also assessed the effect of the income levels on the number of vehicles owned. Specifically, various income level changes (5%, 10%, and 15% increases) were examined, as presented in Table 5.

Table 7 *Validation predicted model*

Classification				
Observed	Predicted			
	0	1	2	Percent Correct
Zero vehicle ownership (32)	22	10	0	68.75%
1 vehicle ownership (27)	8	18	1	66.66%
2 vehicle ownership (8)	2	6	0	0.00%
Overall Percentage	47.76%	50.74%	1.49%	59.7%

Note: Number of data testing: 67

Tables 5 and 6 present the effects of policy scenarios on household income levels and private car ownership, respectively. Table 6 compares actual conditions with different income change scenarios, while Table 5 explores how private car ownership might change due to income variations. In the base scenario (calibrated model), private car ownership percentages were 47.85%, 40.68%, and 11.46% for each ownership category. With a 5% income increase scenario, private car ownership rose to 40.70% and 11.50% for one and two private cars, respectively. A 10% income increase further raised private car ownership to 40.73% and 11.54% for one and two private cars, respectively. Lastly, in the most extreme scenario, a 15% income increase resulted in private car ownership percentages of 40.79% and 11.61% for one and two private cars, respectively. Sensitivity analysis in Table 5 provides crucial insights for policymakers and practitioners in transportation and public policy to understand the impact of various income change scenarios on private car ownership.

4.4 Model validation

The utility of the model requires rigorous verification to validate its accuracy. Table 7 illustrates the model's predictive capability, where 20% of the data was allocated to the testing subset and applied to the calibrated parameters. The model demonstrates an overall accuracy of 59.70%, suggesting a commendable level of generalizability. The decision to allocate 80% of the data for model calibration was instrumental in achieving an accuracy rate of 65.0%.

In terms of vehicle ownership prediction, the model exhibits reliable performance across different ownership categories. The highest accuracy was observed in the prediction of single-vehicle ownership, with a correct prediction rate of 66.66%. However, the model's highest mispredictions occurred in the zero-vehicle ownership and two-vehicle ownership categories. Despite these mispredictions, the model's performance concerning underfitting and overfitting remains within acceptable limits, with deviations from the testing data predictions staying below 10%. This indicates that the model's predictive reliability is within permissible bounds, ensuring its validity for further application.

5 Conclusions

In conclusion, this study explored discrete choices pertaining to the number of cars based on a survey of car ownership in Banda Aceh. To account for potential independence among alternatives and individual heterogeneity, MNL model was used. The study also assessed the impact of various management strategies on reducing the number of cars.

The initial results showed that a variable income range between 5 and 6.9 million IDR had a significant positive impact on the probability of car ownership. Owning car license (SIM A) significantly improved this probability. On the other hand, male gender had a negligible negative influence, while longer travel distances had a positive effect. In the second model, focusing on owning two cars, a variable income range of 5-6.9 million IDR and having car license (SIM A) significantly increased the probability of car ownership. Being male tended to significantly decrease this probability, and longer travel distances had a weak positive influence.

Sensitivity analysis showed that individual earning between 5-6.9 Million IDR per month had significant probability of owning a private car, contributing up to 9.2%. Owning a driving license also had a significant contribution of approximately 30.7% to car ownership. Conversely, being male had a negative impact on the probability of owning a private car by 1.9%. Longer travel distances tended to increase car ownership within households by 13.6%. Sensitivity analysis showed a similar trend for owning multiple cars within households, with owning a driving license and traveling longer distances contributing to 21.3% and 3.11% of car ownership, respectively.

The outcomes of model application showed that the probabilities of owning no, one, and two cars in household were 47.85%, 40.68%, and 11.46%, respectively. As household income increased by 5-7 million IDR, the proportions slightly moved to 40.70% and 11.48% for the one and two private car ownership categories, respectively. These proportions rose to 40.73% and 11.54%, respectively with a 10% income increase. In the most significant scenario, with a 15% income increase, the proportions further rose to 40.79% and 11.61% for the one and two private car ownership categories, respectively. These results showed the significant impact of the income variable on vehicle ownership, particularly in developing countries like Indonesia.

Vehicle ownership in Indonesia was significantly influenced by income and driving license ownership. The empirical results showed a positive and significant relationship between these variables, offering valuable insights for policymakers, particularly in reducing private mode dependence and improving the public transportation system. This study had certain limitations, including the focus on a typical medium-sized city in a developing country. Therefore, the results might not be applicable to other cities with distinct characteristics, affecting its usefulness for policymaking.

Acknowledgement

The authors gratefully acknowledge the financial support provided by Universitas Syiah Kuala under contract No. 308/UN11.2.1/PT.01.03/PNBP/2021 (H-Index Research) for this research.

Conflicts of interest

The authors declare that they have no known competing financial interests or personal relationships that could have appeared to influence the work reported in this paper.

References

[1] SALEH, S. M., SUGIARTO, S., SALMANNUR, A. Attitudinal dataset for mediating the effects of public acceptance on bus reform scheme in a developing country context. *Data in Brief* [online]. 2019, **25**, 104035. eISSN 2352-3409. Available from: https://doi.org/10.1016/j.dib.2019.104035

[2] SALEH , S. M., SUGIARTO, S. ANGGRAINI, R. Analysis on public' s response toward bus reform policy in Indonesia considering latent variables. *The Open Transportation Journal* [online]. 2019, **13**, p. 17-24. ISSN 2667-1212, eISSN 1874-4478. Available from: https://doi.org/10.2174/1874447801913010017

[3] IRZA, M., SUGIARTO, S., SALEH, S. M. Mode choice analysis among motorcycle and Trans Koetaradja urban bus and its contributing factors using revealed preference (RP) data. *IOP Conference Series: Materials Science and Engineering* [online]. 2021, **1087**(1), p. 12007. ISSN 1757-899X. Available from: https://doi.org/10.1088/1757-899X/1087/1/012007

[4] WADUD, Z., ADEEL, M., ANABLE, J., LUCAS, K. A disaggregate analysis of 'excess' car travel and its role in decarbonisation. *Transportation Research Part D: Transport and Environment* [online]. 2022, **109**, 103377. ISSN 1361-9209, eISSN 1879-2340. Available from: https://doi.org/10.1016/j.trd.2022.103377

[5] ZENG, W., MIWA, T., MORIKAWA, T. Prediction of vehicle CO2 emission and its application to eco-routing navigation. *Transportation Research Part C: Emerging Technologies* [online]. 2016, **68**, p. 194-214. ISSN 0968-090X, eISSN 1879-2359. Available from: https://doi.org/10.1016/j.trc.2016.04.007

[6] CHIU ,B., GUERRA, E. What predicts motorcycle ownership, mode choice, and use for utilitarian travel? A literature review. *Transport Reviews* [online]. 2023, **43**(6), p. 1165-1189. eISSN 1464-5327. Available from: https://doi.org/10.1080/01441647.2023.2205177

[7] LIU, J., WU, C., LE VINE, S., JIAN, S. Panel data analysis of Chinese households' car ownership and expenditure patterns. *Transportation Research Part D: Transport and Environment* [online]. 2023, **123**, 103915. ISSN 1361-9209, eISSN 1879-2340. Available from: https://doi.org/10.1016/j.trd.2023.103915

[8] RUSLAN, R., SUGIARTO, S., ANGGRAINI, R., SALEH, S. M. Forecasting private vehicle ownership and it effect to public transportation planning in Banda Aceh, Indonesia. *IOP Conference Series: Materials Science and Engineering* [online]. 2020, **917**, 12040. ISSN 1757-899X. Available from: https://doi.org/10.1088/1757-899x/917/1/012040

[9] RUSLAN, R., SUGIARTO, S., ANGGRAINI, R., SALEH, S. M. Investigation of effect socioeconomic characteristic on vehicle ownership in developing country using multinomial logistic regression: a case study in Banda Aceh city. *AIP Conference Proceedings* [online]. 2023, **2711**(1), 070016. ISSN 0094-243X, eISSN 1551-7616. Available from: https://doi.org/10.1063/5.0137018

[10] POTOGLOU, D., KANAROGLOU, P. S. Modelling car ownership in urban areas: a case study of Hamilton, Canada. *Journal of Transport Geography* [online]. 2008, **16**(1), p. 42-54. ISSN 0966-6923, eISSN 1873-1236. Available from: https://doi.org/10.1016/j.jtrangeo.2007.01.006

[11] RODRIGUEZ-VALENCIA, A., DE D. ORTUZAR, J., MESA-GARCIA, S. Understanding the differences between car and motorcycle ownership. The case of Bogota, Colombia. *Journal of Transport Geography* [online]. 2024, **114**, 103773. ISSN 0966-6923, eISSN 1873-1236. Available from: https://doi.org/10.1016/j.jtrangeo.2023.103773

[12] CELIK, A. K., KABAKUS, N., TORTUM, A. Influential factors of household car and vehicle ownership in urban areas of Turkey. *Transportation Research Record: Journal of the Transportation Research Board* [online]. 2023, **2677**, p. 218-240. ISSN 0361-1981, eISSN 2169-4052. Available from: https://doi.org/10.1177/03611981221145138

[13] NGOC, A. M., NISHIUCHI, H. Discrete/continuous model for motorcycle ownership and utilization across income groups in a Vietnamese medium-sized motorcycle-dependent city. *Transportation Research Record: Journal of the Transportation Research Board* [online]. 2023, **2677**, p. 438-450. ISSN 0361-1981, eISSN 2169-4052. Available from: https://doi.org/10.1177/0361198123116161
[14] J. MA, J., YE, X. Modeling household vehicle ownership in emerging economies. *Journal of the Indian Institute of Science* [online]. 2019, **99**, p. 647-671. ISSN 0970-4140, eISSN 0019-4964. Available from: https://doi.org/10.1007/s41745-019-00133-9
[15] YOO, S., YOSHIDA, Y. Consumer preferences and financial incentives in the Japanese automobile industry. *Transport Policy* [online]. 2019, **81**, p. 220-229. ISSN 0967-070X, eISSN 1879-310X. Available from: https://doi.org/10.1016/j.tranpol.2019.07.002
[16] TUAN, V. A. Dynamic interactions between private passenger car and motorcycle ownership in Asia: a cross-country analysis. *Journal of the Eastern Asia Society for Transportation Studies* [online]. 2011, **9**, p. 541-556. eISSN 1881-1124. Available from: https://doi.org/10.11175/easts.9.541
[17] CHEN, N., AKAR, G., GORDON, S. I., CHEN, S. Where do you live and what do you drive: built-environmental and spatial effects on vehicle type choice and vehicle use. *International Journal of Sustainable Transportation* [online]. 2020, **15**, p. 444-455. ISSN 1556-8318, eISSN 1556-8334. Available from: https://doi.org/10.1080/15568318.2020.1762950
[18] TUAN, V. A. Mode choice behavior and modal shift to public transport in developing countries - the case of Hanoi City. *Journal of the Eastern Asia Society for Transportation Studies* [online]. 2015, **11**, p. 473-487. eISSN 1881-1124. Available from: https://doi.org/10.11175/easts.11.473
[19] TU, M., CHIKARAISHI, M., HUONG, Q., ZHANG, J. Effects of perceived neighborhood walkability on mode choice of short-distance trips in Hanoi city. *Journal of the Eastern Asia Society for Transportation Studies* [online]. 2015, **11**, p. 1328-1345. eISSN 1881-1124. Available from: https://doi.org/10.11175/easts.11.1328
[20] DARGAY, J. M., GATELY, D., SOMMER, M. Vehicle ownership and income growth, worldwide: 1960-2030. *The Energy Journal* [online]. 2007, **28**(4), p. 143-170. ISSN 0195-6574, eISSN 1944-9089. Available from: https://doi.org/10.2307/41323125
[21] GIULIANO, G., DARGAY, J. Car ownership, travel and land use: a comparison of the US and Great Britain. *Transportation Research Part A: Policy and Practice* [online]. 2006, **40**(2), p. 106-124. ISSN 0965-8564, eISSN 1879-2375. Available from: https://doi.org/10.1016/j.tra.2005.03.002
[22] HANLY, M., DARGAY, J. M. Car ownership in Great Britain: panel data analysis. *Transportation Research Record Journal of the Transportation Research Board* [online]. 2000, **1718**(1), p. 83-89. ISSN 0361-1981, eISSN 2169-4052. Available from: https://doi.org/10.3141/1718-11
[23] WOLDEAMANUEL, M. G., CYGANSKI, R., SCHULZ, A., JUSTEN, A. Variation of households' car ownership across time: application of a panel data model. *Transportation* [online]. 2009, **36**(4), p. 371-387. ISSN 0049-4488, eISSN 1572-9435. Available from: https://doi.org/10.1007/s11116-009-9210-3
[24] SENBIL, M., ZHANG, J., FUJIWARA, A. Motorcycle ownership and use in metropolitan area of Jabotabek, Indonesia. In: Transportation Research Board 86th Annual Meeting: proceedings. 2007.
[25] LAI, W.-T., LU, J.-L. Modeling the working mode choice, ownership and usage of car and motorcycle in Taiwan. *Journal of the Eastern Asia Society for Transportation Studies* [online]. 2007, **7**, p. 869-885. eISSN 1881-1124. Available from: https://doi.org/10.11175/easts.7.869
[26] CHIOU, Y.-C., WEN, C.-H., TSAI, S.-H., WANG, W.-Y. Integrated modeling of car/motorcycle ownership, type and usage for estimating energy consumption and emissions. *Transportation Research Part A Policy and Practice* [online]. 2009, **43**(7), p. 665-684. ISSN 0965-8564, eISSN 1879-2375. Available from: https://doi.org/10.1016/j.tra.2009.06.002
[27] CIRILLO, C., LIU, Y. Vehicle ownership modeling framework for the state of Maryland: analysis and trends from 2001 and 2009 NHTS data. *Journal of Urban Planning and Development* [online]. 2013, **139**(1), p. 1-11. ISSN 0733-9488, eISSN 1943-5444. Available from: https://doi.org/10.1061/(ASCE)UP.1943-5444.0000128
[28] WEN, C.-H., CHIOU, Y.-C., HUANG, W.-L. A dynamic analysis of motorcycle ownership and usage: a panel data modeling approach. *Accident Analysis and Prevention* [online]. 2012, **49**, p. 193-202. ISSN 0001-4575, eISSN 1879-2057. Available from: https://doi.org/10.1016/j.aap.2011.03.006
[29] KARLAFTIS, M., GOLIAS, J. Automobile ownership, households without automobiles, and urban traffic parameters: are they related? *Transportation Research Record Journal of the Transportation Research Board* [online]. 2002, **1792**(1), p. 29-35. ISSN 0361-1981, eISSN 2169-4052. Available from: https://doi.org/10.3141/1792-04
[30] HAUSMAN, J., MCFADDEN, D. Specification tests for the multinomial logit model. *Econometrica / Econometric Society Journal* [online]. 1984, **52**(5), p. 1219-1240. ISSN 0012-9682, eISSN 1468-0262. Available from: https://doi.org/10.2307/1910997

DEVELOPMENT OF PEDESTRIAN LEVEL OF SERVICE (PLOS) FOR JAYWALKING PEDESTRIANS AT UNSIGNALISED INTERSECTIONS ON URBAN ARTERIALS USING ANN & CLUSTERING: A CASE STUDY IN INDIA

Ampereza Ankunda, Malaya Mohanty*, Satya Ranjan Samal

KIIT Deemed to be University Bhubaneswar, Odisha, India

*E-mail of corresponding author: malaya.mohantyfce@kiit.ac.in

Malaya Mohanty 0000-0002-6116-782X, Satya Ranjan Samal 0000-0001-8675-453X

Resume

In a developing country like India where jaywalking is prevalent than using designated crosswalks, pedestrian safety is a major concern. Development of pedestrian level of service (PLOS) is essential for monitoring pedestrian safety for these manoeuvres. The present research incorporates a new methodology to evaluate pedestrian LOS for jaywalkers. The study is conducted in a smart city of Bhubaneswar in India. The pedestrian crossing speeds ranged from 0.6 to 1.4 m/s. Artificial Neural Networks (ANN) are used to determine the pedestrian crossing speeds from vehicular and pedestrian counts whose outputs are close to the field data. A 2-step K-means clustering technique is employed to determine the Pedestrian LOS ranges based on pedestrian crossing speeds. Urban planners, transportation engineers, and legislators can use the methodology to determine PLOS levels to create the pedestrian-friendly infrastructure.

Article info

Received 31 July 2024
Accepted 7 November 2024
Online 27 November 2024

Keywords:

pedestrian safety
PLOS
jaywalking
ANN
clustering
unsignalized intersection

Available online: https://doi.org/10.26552/com.C.2025.010

ISSN 1335-4205 (print version)
ISSN 2585-7878 (online version)

1 Introduction

Globally, numerous pedestrians lose their lives or suffer serious injuries in vehicular crashes every year. Accidents primarily take place in populated regions. The interaction between the moving vehicles and pedestrians is the cause of this. These road crashes are very expensive for both the victim and society. Every country's traffic and transport infrastructure have a big impact on how it develops [1]. Therefore, ensuring pedestrian safety and welfare is a key component of urban planning and transportation management. A useful tool for evaluating and regulating the quality of walking conditions in this situation is the idea of pedestrian level of service (PLOS), which encourages safe and effective pedestrian movement [2].

According to [3], the time taken by the low priority movements (here, pedestrians) to cross an unsignalized intersection serves as a performance indicator for them. The time difference between an actual and ideal operating time for these pedestrians is usually termed as delay, and it is a popular quality of service statistics for junctions. Prior studies have found a connection between traffic conflicts and service delays [3]. Secondly, in developed countries, unsignalized crossings are often managed by signs that determine the priority of different movements, which reduces the probability of conflicts. However, in developing countries like India, where the roads are already burdened by mixed traffic movements with no lane discipline, the traffic flow scenario at unsignalized intersections paint a grimy picture. The majority of unsignalized junctions lack a stop or yield sign, and even those that do, are frequently ignored by vehicles travelling through them [1]. In addition, the pedestrians who cross these intersections do not normally use the designated cross walks and frequently jaywalk. According to [4], LOS is the quantitative stratification of a performance measure or set of performance measurements that reflect service quality. The standard practice establishes six service levels, ranging from A to F, which represent the highest and worst service quality, respectively [5].

There have been much early research focusing on pedestrian safety, and development of Pedestrian LOS/

PLOS, which also has recently come up in [4]. Many studies have focused developing PLOS for sidewalks or at midblock sections [6-11], whereas crosswalks have found very little attention. Even in [12], a speed-based PLOS is established, however, considering speeds of pedestrian above 1.2 m/s as LOS A may not be a correct range, as the average speeds of pedestrians in various countries range from 0.53 m/s in Malta to 1.73 m/s in Denmark [13]. Thus, for every country, and for every type of pedestrian facilities, these ranges need to be different. Authors of [14] developed a new methodology to determine the Pedestrian Crossing Level of Service (PCLOS) for urban areas. Their methodology utilised the geometric infrastructures like kerbs, islands, zebra crossing to assess the PCLOS and not the vehicle and pedestrian behaviour and dynamics. In [15] is studied the perception of pedestrians in general to determine PLOS and didn't limit to any specific traffic infrastructure. A similar perception-based study for pedestrian was also conducted in [16] in Greece. The PLOS on sidewalks, considering Random Forest model, was determined in [17]. Many studies have also attempted to assess pedestrian safety with the help of surrogate safety measures like Anticipated Time to Collision (ACT), Post Encroachment Time (PET), Time to Collision (TTC), etc. [18-20], but the studies have largely been regarded as a substitute for actual investigation. Further, these studies mostly have revolved around highways and expressways. In [21] is developed a pedestrian fatality prediction model using the logistic regression and boosted trees for a city in India, however the factors attributed was just the perpetrator vehicle category. The volume on the road or speed was not considered much, as it was based on crash data only. Cafiso et al. in [22] developed a pedestrian risk index (PRI) to identify the severity of pedestrian-vehicle collision effects. In comparison to sidewalks and walkways, the pedestrian speeds are much higher at crosswalks. According to [23], pedestrians should wait 90 seconds before attempting an illegal crossing manoeuvre. These values are too high, mainly when the pedestrians are of relatively younger age (teenagers or adolescents) and are going to work or attend classes. The PET interaction threshold that was chosen at 20 seconds by [24] also seems very high in today's traffic scenario. A study by authors of [25] detailed that the unauthorised crossing/jaywalking is quite serious near intersections. The past studies reflect that the parameters covered to assess the LOS and safety of pedestrians are usually the geometric features or the volume of pedestrians. Secondly, crosswalks have not been studied much as jaywalking is common in developing countries like India, and therefore it is difficult to assess their safety or determine their LOS. Moreover, the pedestrian and vehicular dynamics are not considered much in past studies.

Therefore, the present study is focused on development of a PLOS model for crosswalks at unsignalized intersections that uses motorised traffic volume, pedestrian volume, and pedestrian speeds as factors influencing the pedestrian safety. The outcomes of this research could have significant implications for urban planners, transportation engineers, and policymakers. By integrating the PLOS into decision-making processes, cities can prioritize resources effectively, implement targeted safety improvements, and create pedestrian-friendly environments that encourage active transportation and enhance overall quality of life.

2 Data collection, extraction and methodology

The location of the study was chosen to be KIIT road, Bhubaneswar, India. This location was chosen for the study because of the high number of pedestrians ranging from students to faculty members and staff who must cross the major urban arterial to access various facilities. Further, Bhubaneswar is a smart tier-2 city, which represents majority of the cities of the country. The KIIT University is a major university [26] in the city, that is ranked within top 20 in India and ranked 147 in Asia [27] and does not have a boundary infrastructure. Rather, it has many satellite campuses across both sides of the major urban arterial road. The road is a 4-lane undivided road with bicycle lanes on both sides. Figure 1 represents the map location, with the camera locations for the study. Data was collected from 8:00 am to 7:00 pm. Data was collected with the help of two cameras, which were placed diagonally opposite (as shown in Figure 1) each at an angle to KIIT road to give a wide field of view. Figures 2a and 2b show the positions A and B at which the data was collected. The cameras are placed facing directions A and B. Various traffic parameters like vehicle counts and pedestrian speeds were then extracted using Kinovea video editing software to draw to the different findings. Counting of pedestrians was done manually. The methodology used for the study is shown in Figure 3.

3 Results and analysis

The results section of the study has been divided into subsection for easier and clear understanding.

3.1 Pedestrian dynamics

The present study deals with the safety aspects of pedestrians at unsignalized intersection. Therefore, firstly, the various traffic parameters related to pedestrian flow have been analysed. The number of pedestrians who were crossing KIIT road at the KIIT Times Square was determined by doing pedestrian counts. The pedestrian counts were done from 8:00 am to 7:00 pm on working days. The pedestrians who were walking on sidewalks were not counted since the study

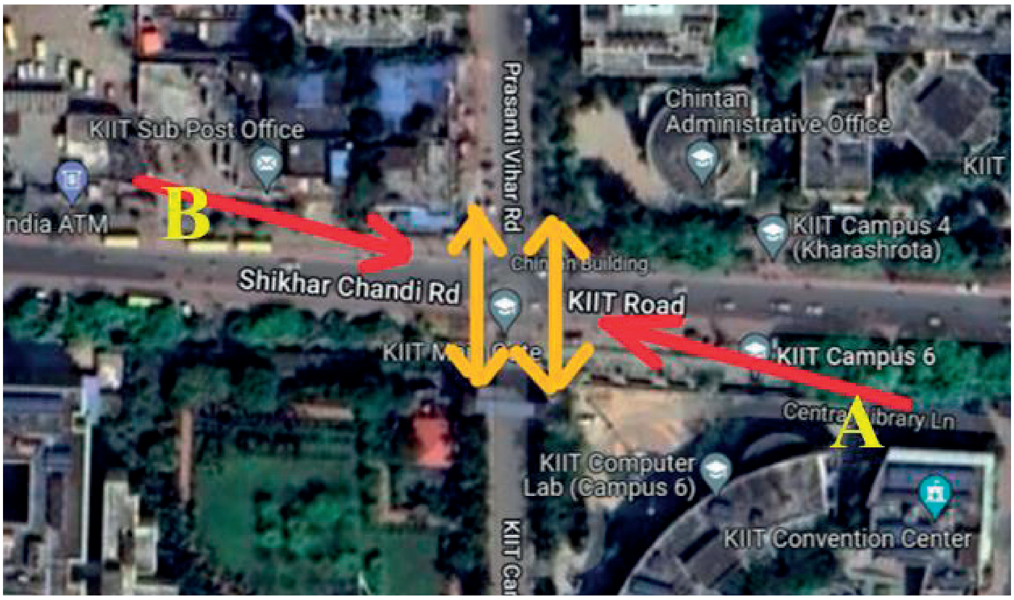

***Figure 1** Map view showing camera positions A and B*

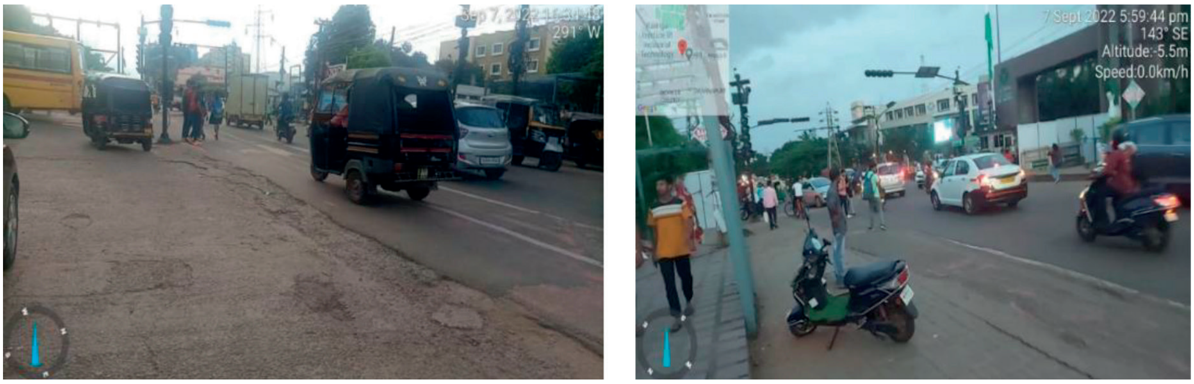

(a) *(b)*

***Figure 2** Camera positions at A and B as shown in Figure 1*

Choice of study area and Data collection

↓

Determining the number of Pedestrians crossing

↓

Measuring the Speed of Pedestrians while crossing

↓

Obtaining the classified motorised traffic volumes

↓

Using ANN to determine ped. speeds from ped. and vehicle volumes and validating the model

↓

Determining the Pedestrian Level of service using 2-step K-means clustering

***Figure 3** Methodology for the study*

Table 1 *Descriptive statistics of number of pedestrians crossing the road*

No. of Pedestrians Crossing per hour	
Mean	753
Minimum	426
Maximum	1,188
Sum	8,280
Count Duration/day	11 hours

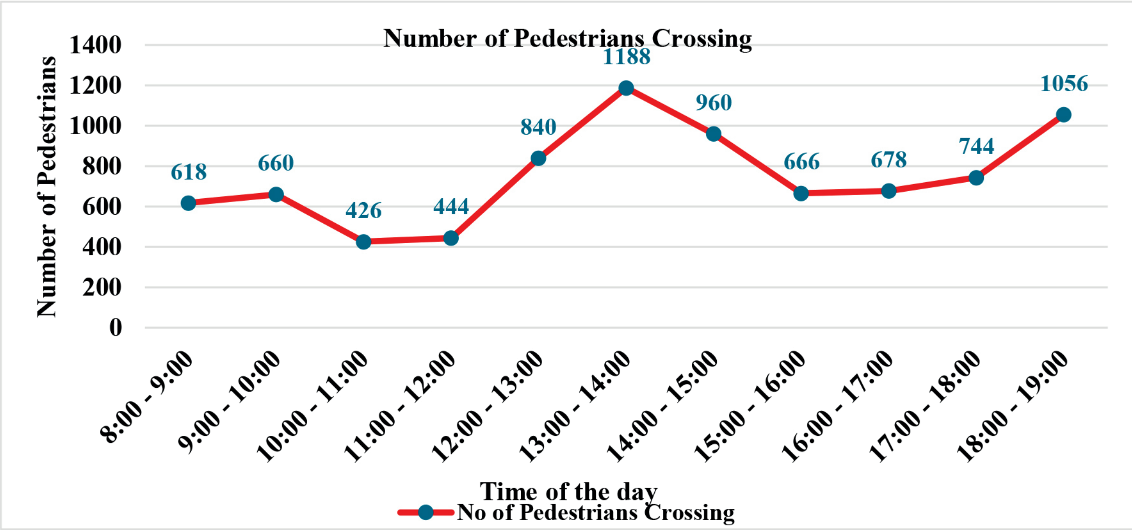

Figure 4 *Variation in average pedestrian volume over the day*

focuses on the behaviour of pedestrians crossing the main road either using or not using crosswalks. Table 1 showcases the descriptive statistics of pedestrians crossing the road per hour for a day.

The average total number of pedestrians crossing the KIIT Times Square was 8280 for the period of 11 hours in a single day. The average number of pedestrians crossing the road is 753 pedestrians per hour. The highest number of pedestrians crossing per hour recorded is 1188 and the lowest number is 426. The trend of the pedestrian flow is presented in Figure 4.

From Figure 4 can be noted that there are three peaks of pedestrian crossing the road of which first one is a low peak (9-10 AM) and next two are higher peaks (1-2 PM, and 6 -7 PM). The morning small peak is caused by the high number of students and university staff who are entering the university for morning classes and work. The second peak is observed at lunch time when the classes end for lunch break resulting in high number of pedestrians. The third peak is in the evening, which coincides with the closing of university and other offices nearby resulting in a peak period. The second peak at lunch time is the highest of the three peaks since most people get their lunch in the time window of 1 to 2 PM, while the start of classes/offices and leaving from work has a higher time window (like 8-10 AM and 5-7 PM). Next, a comparison was drawn between the individual and group crossing by pedestrians. Individual pedestrian crossing is when a single pedestrian moves from one end of the road to the other end of the road without anyone else moving with him/her at that same time. Group pedestrian crossing is when more than one person/ a group of people are moving from one end of the road to another end at the same time. In the present study, a group of pedestrians crossing the road is regarded as a single entity. This is because when people are crossing in a group, any vehicle - pedestrian crash would involve all of them. The number of group pedestrians crossing were counted for the different times of the day and the number of individuals in those groups was also noted as shown in Figure 5. It is observed that individual crossings are comparatively higher than the group crossings.

The highest number of group crossing is 204 groups (6:00 PM - 7:00 PM) and the lowest is 48 groups (8:00 AM-9:00 AM). In the morning, students are coming from their different residences and thus they cross the road individually. However, in the evening, students come from the university in groups and thus the higher number of group crossings is in the evening than in the morning.

Next, the speed of pedestrians crossing from direction A and direction B (as explained in "Data Collection and Extraction" section) was obtained from dividing the width of the road to the time taken by pedestrians to cross it. The average speed of pedestrians at different times of the day is shown in Table 2. Since, the difference between the group and individual

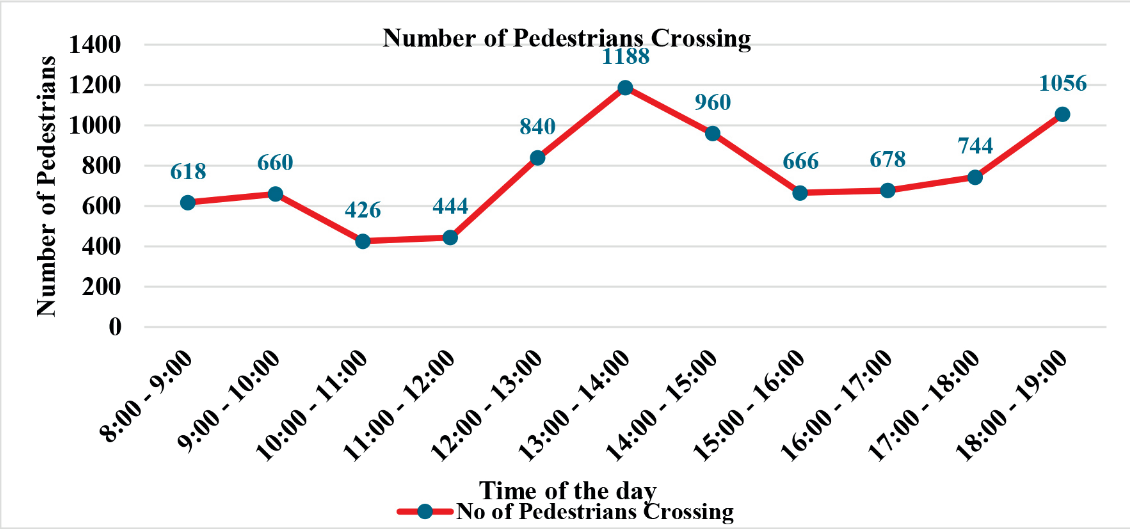

Figure 5 *Single and group pedestrian crossing the road*

Table 2 *Average speed of pedestrians while crossing the road*

Time of the Day	Average Speed at A (m/s)	Average Speed at B (m/s)
8-8.30 AM	0.86	1.09
8.30-9 AM	0.84	0.93
9-9.30 AM	0.87	1.18
9.30-10 AM	0.68	0.80
10-10.30 AM	1.03	1.28
10.30-11 AM	1.33	0.85
11-11.30 AM	0.91	1.22
11.30-12 PM	1.09	1.38
12-12.30 PM	1.29	1.13
12.30-1 PM	0.94	0.85
1-1.30 PM	0.90	0.93
1.30-2 PM	0.94	0.78
2-2.30 PM	1.04	1.02
2.30-3 PM	0.95	0.85
3-3.30 PM	0.93	0.93
3.30-4 PM	0.98	0.93
4-4.30 PM	0.86	1.02
4.30-5 PM	0.77	1.29
5-5.30 PM	0.83	1.11
5.30-6 PM	0.89	1.07
6-6.30 PM	1.24	1.04
6.30-7 PM	0.68	0.78

speeds of pedestrians are statistically insignificant, therefore all the obtained speeds have been considered for analysis. The variation trends of the speeds across the day is shown in Figure 6. The speeds are seen to vary during different times of the day with different peaks. For example, at position A, the speed of pedestrians are high between 10:30 AM -11:00 AM, 12:00 - 12:30 PM and 6:00 - 6:30 PM. At position B, high speed of pedestrians was observed in between 11:30 AM - 12:00 noon and 4:30 - 5:00 PM. According to [28], the average normal optimum crossing speeds of pedestrians is 1.2 m/s. The same optimum speed is also reported in IndoHCM [4] and few other studies. Considering this optimum speed, at maximum time intervals, from Figure 6 can be observed, that the speeds of pedestrians are less than optimum speed (below the red line), which shall lead to dissatisfaction among the pedestrians decreasing the PLOS for the facility. Speed has always been one of the

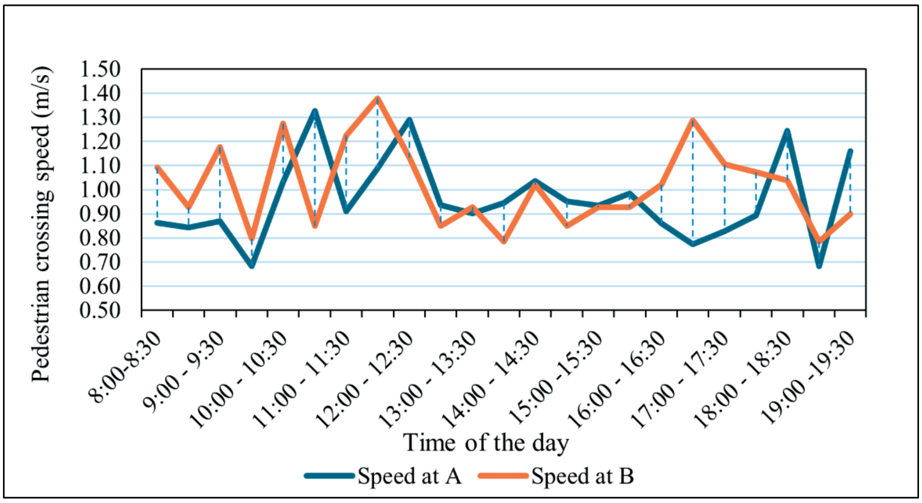

Figure 6 *Variation in average speeds of pedestrians while crossing the road*

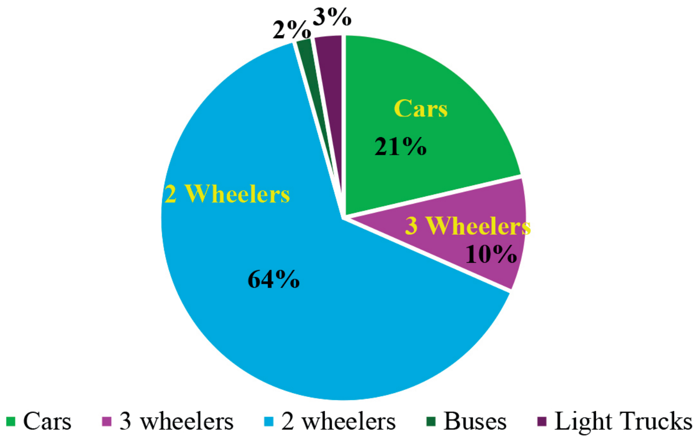

Figure 7 *Vehicular composition in Traffic stream*

most important parameters to be used for assessing various road user characteristics. However, speed is not the easiest parameter to measure. Volume is an easier parameter to measure than speed. Secondly, although it is commonly noticed from pedestrian flows and speeds that they are inversely related, but the vehicular dynamics needs to be assessed as it is common for pedestrians to be affected by vehicles, mainly when they are crossing the road. Therefore, in the next section of results and analysis, vehicular dynamics is evaluated and analysed to determine its effect on pedestrian speeds.

3.2 Vehicular dynamics

The studied road network is mainly used by 5 categories of vehicles, which include 2-wheelers, 3-wheelers, cars, light trucks, and buses. The percentage composition of these 5 categories is shown in Figure 7.

It can be observed from Figure 7, that 2-wheelers make up the highest percentage of composition of traffic with 64% share, followed by cars with 21%, 3-wheelers with 10%, light trucks with 3% and buses making up 2% of the traffic volume. It was observed that the vehicular volume affects the pedestrian crossing speeds along with the pedestrian volume. Secondly, the pedestrian crossing speeds can be used as one of the fundamental parameters for establishing the PLOS.

Therefore, pedestrian crossing speeds have been predicted in the present study using the volume of pedestrians crossing the road at a given point and the vehicular traffic volume using that same road at that said time. The PLOS is defined as the level of comfort provided to pedestrians as they are using different facilities on the road [4]. Although, the PLOS is calculated from the total delay faced by pedestrians in IndoHCM [4] guidelines, however, for crossing and jaywalking pedestrians it is difficult to assess the delay. Secondly, speed is the fundamental parameter, which leads to assessment of delay. Moreover, the delay ranges for PLOS would vary for different lane configurations. Therefore, indirectly, the speed with which the pedestrians are crossing the road is a simpler measure of their LOS. However, to calculate speeds, a definite section of road of known distance is required along with the time taken to cross the roadway. With heavy cross vehicular volumes and lower speeds of pedestrians, it becomes a tedious task to determine their speeds. Therefore, in the present study, Artificial Neural Network (ANN) has been utilized to determine the speeds of crossing pedestrians by considering their volume, and the vehicular volume on the road.

3.3 Pedestrian speed prediction using ANN

As mentioned earlier, in the present study, ANN has been used to predict pedestrian speeds while crossing the road. In the design of the system, the Pedestrian crossing volume and traffic volume have been used as the model parameters. Although, there are other numerous factors that affect the speed of pedestrians while crossing the roads, such as weather, age, gender, number of lanes, speeds of vehicles, etc., the purpose of this study was to find the easiest method that can be used to estimate pedestrian speeds and thus volumes of vehicles and pedestrians have been considered, which can be easily obtained on any road at any time. Secondly, the model used to predict the speeds of pedestrians while crossing the road gives highly accurate predicted results that are very close to the actual values with very small errors. In addition, this model predicted some pedestrian speeds with 100% accuracy. JMP Pro software made use of a variety of neural network validation approaches, including Holdback and K-fold methods. Holdback approach was found to offer improved prediction and validation for pedestrian crossing speeds. The ANN model was run with 1, 2, and 3 hidden layers, with the first two representing a shallow network and using TanH, Linear, and Gaussian activation functions, respectively. The three hidden layers employed in the model are shown in Figure 8. The method with the lowest Root Average Squared Error (RASE) has been selected for the prediction of the pedestrian crossing speeds.

Table 3 shows RASE of both the training and validation data for different ANN validation techniques and functions. The RASE for training shows how well the model fits the data used, while the RASE for validation shows how well the model would perform when given data it has not seen before. The lower the RASE, the more accurate the predictions will be. Thus, from Table 3, the activation function (Gaussian) and validation technique (Holdback) with a lower RASE (0.04) were used in ANN to model the data. 30% of the data was utilized for validation, while 70% was used for training. Figures 9a and 9b show the screenshots of ANN results graphs that when the pedestrian volume at A is 216 and the total vehicle volume is 1,639, the pedestrian crossing speed at A is predicted to be 0.88 m/s. Similarly, when the pedestrian volume at B is 276 and the total vehicle volume is 1,639, the pedestrian crossing speed at B is predicted to be 1.00 m/s. Table 4 presents the actual vs. predicted speeds of crossing pedestrians.

From Table 4 can be noted that the developed model gives very good results. With more training in ANN the model might give near 100% accuracies since even with first training of data sets, the results have been very precise. Table 5 shows the average, maximum and minimum errors between predicted and field values. It can be noted that the model generates an average

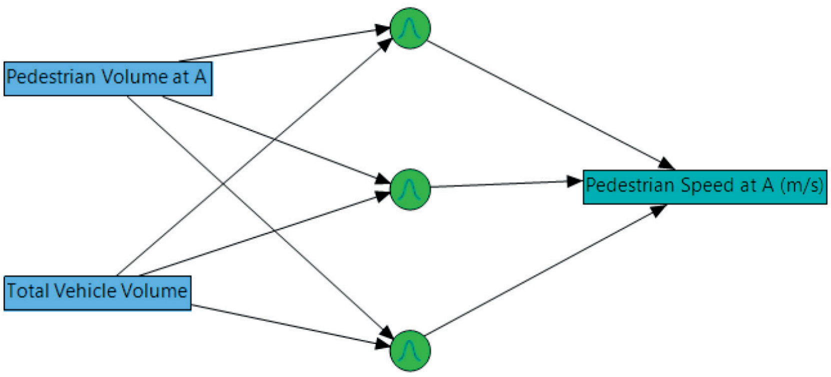

Figure 8 *Three hidden layers used for the model in ANN*

Table 3 *RASE for training and validation data*

Validation Technique	Activation function	Root Average Squared Error (Training data)	Root Average Squared Error (Validation data)
Holdback	TanH	0.19	0.08
	Linear	0.2	0.16
	Gaussian	0.2	0.04
K fold	TanH	0.11	0.19
	Linear	0.12	0.27
	Gaussian	0.06	0.15

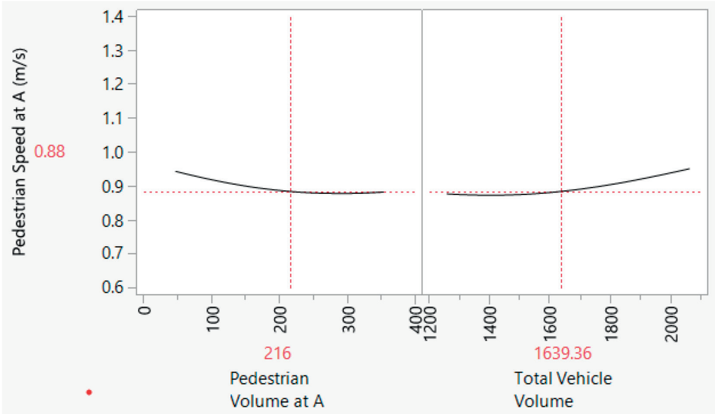

(a)

(b)

Figure 9 *Screenshots of dynamic result graphs from ANN modelling*

Table 4 *Actual speeds of pedestrians while crossing the road and the Predicted pedestrian crossing speeds at both A and B*

Actual Pedestrian Speed at A (m/s)	Predicted Pedestrian Speed at A (m/s)	Actual Pedestrian Speed at B (m/s)	Predicted Pedestrian Speed at B (m/s)
0.86	0.88	1.09	1.01
0.84	0.87	0.93	1.04
0.87	0.94	1.18	1.00
0.68	0.91	0.80	1.02
1.03	0.90	1.28	1.04
1.33	0.94	0.85	1.03
0.91	0.92	1.22	1.04
1.09	0.90	1.38	1.04
1.29	0.92	1.10	1.04
0.94	0.96	0.88	1.04
0.90	0.94	0.91	1.03
0.94	0.90	0.77	0.81
1.04	0.92	1.00	1.03
0.95	0.89	0.87	1.03
0.93	0.87	0.96	0.96
0.98	0.91	0.93	1.01
0.86	0.88	1.06	0.96
0.77	0.91	1.29	1.04
0.83	0.88	1.11	1.02
0.89	0.88	1.07	1.02
1.24	0.87	1.04	0.96
0.68	0.89	0.79	1.03

***Table 5** Error in predicted vs field speeds at A and B*

Parameter	Error at A (m/s)	Error at B (m/s)
Average	0.12	0.14
Max	0.39	0.34
Min	0.01	0.00

error of 0.12 m/s at A and 0.14 m/s at B. It is noted that some of the speeds are predicted by the model with 100% accuracy as there is a minimum error of 0.00 m/s at B. The least error at A is 0.01 m/s. These results are very accurate, and this developed model can be used with confidence to predict pedestrian speeds by just utilising vehicular and pedestrian volumes. Next, these speeds have been utilised to perform clustering to develop a Pedestrian LOS based on their crossing speeds at unsignalized intersections. The delay ranges shall vary for different types of roads with different lane configuration, however speed ranges for PLOS will more or less remain the same at least for the surveyed city along with cities with similar demographic structure.

3.4 Development of PLOS using the pedestrian crossing speeds and clustering technique

The speeds of pedestrians while crossing the road have been utilised to develop the Pedestrian LOS for the crossing behaviour. In the present study, it was possible to determine the Pedestrian level of service on the road without necessarily calculating the speed or delay. Only the volume counts of pedestrian and vehicles can help in assessing the LOS for a particular crossing point on road. Clustering technique aims to group the data in such a way that each group contains data points that are like one another and different from those found in other groups. K-means, K-medoid, and Hierarchical Agglomerative are the three popular methods of clustering to group/classify data points. The K-means clustering has been employed in this study to define the pedestrian speed ranges for different PLOS levels, since the K-means is an unsupervised classification method majorly effective for large data sets [29-31]. Further, past studies have shown that the k-means clustering should undeniably be utilised for data sets larger than 500. SPSS software was employed for performing clustering.

The K-mean method of clustering aims to form uniform clusters based on the diversity present within a cluster. Objects are thrown into different clusters at random to start the clustering process. Then, to reduce the within-cluster diversity, which is essentially the square of the distance between each item and the centre of its allocated cluster, they are gradually moved to other clusters with the help of repeated iterations. Since, 1.2 m/s has been established by various guidelines and researchers [4, 13, 32-33] as the average pedestrian speed in India, therefore, for urban areas, LOS C would start with pedestrian speeds of 1.2 m/s or higher. Therefore, in the present study, 2-step clustering is used; first for the speed data above 1.2 m/s and other for speed data less than 1.2 m/s. Before performing the cluster analysis, silhouette values are calculated to get the optimum number of clusters. Having silhouette value between 0.71 and 1.00 indicates the presence of strong clustering membership [29]. Figure 10 shows that the average silhouette value for speeds below and above the optimum average pedestrian crossing speed (1.2 m/s) is the highest for 3 number of clusters. Next the K-mean clustering is conducted by providing 3 number of clusters to be developed, each for speeds > 1.2 m/s and < 1.2 m/s. Additionally, the clustering is kept going until either convergence or a preset number of iterations are reached [34]. An essential component of the K-means clustering method is convergence. Simply put, when the cluster centers stop changing, the clusters have converged [35]. Multiple iterations are used to attain this convergence. For both groups (<1.2 m/s, >1.2 m/s), convergence have been attained after 3 and 2 iterations, respectively. Table 6 shows the change in clusters/iterations to achieve convergence and Table 7 presents the final cluster centers.

From Table 7, the ranges of PLOS are defined by considering the cluster centers of two consecutive clusters and then dividing the difference between them by 2. For example, for speed below 1.2 m/s, the cluster centers 1 and 2 are 0.67 and 0.94 m/s respectively. The difference between them is 0.94 - 0.67 = 0.27 m/s. If it is divided into 2 groups, the division comes at 0.67 + (0.27/2) = 0.81 m/s. Therefore, the range is < 0.81 m/s or 0-0.81 m/s. In similar ways, other ranges are also obtained. Thereafter, based on these values, the PLOS for crossing pedestrians is developed whose ranges are provided in Table 8. Any speeds above 1.2 m/s is considered good in terms of pedestrian service levels, whereas speeds below 1.03 m/s (less than LOS D) can be harmful for pedestrians considering they might be subjected to high level of discomfort and impatience leading to possible conflict scenarios.

4 Conclusion

Assessment of pedestrian safety is an important aspect at unsignalized intersections. In developing countries like India, most of the pedestrians are observed to jaywalk rather than using the designated cross

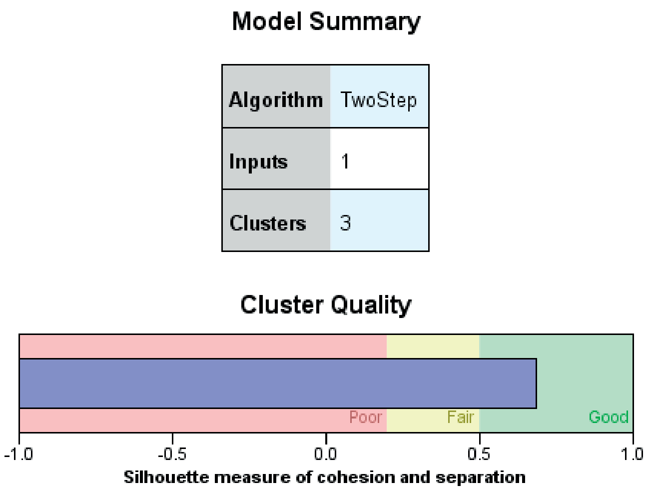

Silhouette plot for speeds below 1.2 m/s

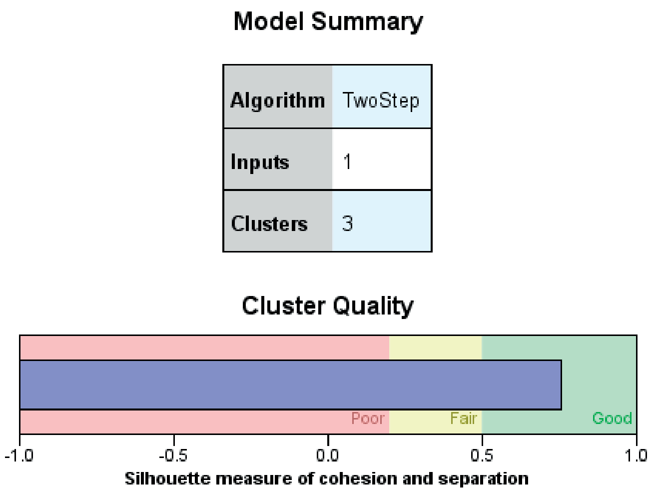

Silhouette plot for speeds above 1.2 m/s

Figure 10 *Average silhouette values for 3 clusters of speeds below and above 1.2 m/s*

Table 6 *Convergence of cluster centers*

	Convergence for speeds < 1.2 m/s		
	Change in Cluster Centers		
Iteration	1	2	3
1	0.210	0.114	0.022
2	0.032	0.003	0.032
3	0.000	0.000	0.000
	Convergence for speeds > 1.2 m/s		
Iteration	Change in Cluster Centers		
	1	2	3
1	0.105	0.231	0.013
2	0.000	0.000	0.000

Table 7 *Cluster centers and ranges*

	Pedestrian Speed below 1.2 m/s			Pedestrian Speed above 1.2 m/s		
Number of clusters	1	2	3	4	5	6
Cluster centers	0.67	0.94	1.11	1.39	2.08	1.69
			Cluster boundaries			
0	0.81	1.03	1.2	1.74	1.89	> 1.89
Number of clusters	1	2	3	4	5	6
Final Cluster ranges	0-0.81	< 0.81-1.03	< 1.03-1.2	< 1.2-1.74	< 1.74-1.89	> 1.89

Table 8 *PLOS ranges for crossing pedestrians*

Pedestrian Speed (m/s)	Pedestrian Level of Service
< 0.81	F
< 0.81 - 1.03	E
< 1.03 - 1.2	D
< 1.2 - 1.74	C
< 1.74 - 1.89	B
> 1.89	A

walks. At unsignalized intersections where no signals are provided for pedestrian crossing, development of a Pedestrian LOS is imperative as it can help assess the traffic scenario at the intersection from pedestrians' safety and comfort's point of view.

In the past many research and guidelines have established ranges of speeds, density, and delays at various pedestrian facilities for determination of PLOS. But there have been 2 major drawbacks. Firstly, the ranges developed by a guideline like HCM, 2000 does not hold true for other countries where the traffic conditions are different, and secondly, calculation of speeds and delays are not a straightforward calculation. In the present study, a new methodology along with introduction of ML and AI in form of ANN and clustering makes sure, the PLOS determination is not going to be a tedious work. Only volume counts of crossing pedestrians and moving vehicles can be used to assess the speed of pedestrian crossing and then the PLOS can be determined.

The present study has been conducted at a busy unsignalized intersection in the smart city of Bhubaneswar where both vehicular and pedestrian traffic is high. Considering that the area is a big university housing of more than 25000 students and 10000 staffs along with many IT hubs established in the vicinity, the traffic volume remains on the higher side. Firstly, the pedestrian dynamics were studied by observing their volume, trend of flow, and crossing speeds at different times of the day. Next, the classified vehicular volume on the main road throughout the day is also observed. It was observed that while the pedestrian flows showed a peak during lunch time (1-2 PM) along with two other regular morning and evening peaks, vehicular flow usually remained on the higher side, except for a few time intervals like 8-9 AM and 3-4 PM. The comparison of single and group of pedestrians crossing the road yielded similar results in terms of their speed. Thereafter, the vehicular and pedestrian volume were utilised as independent variables in ANN to determine the pedestrian crossing speeds. The results showed very accurate results with minimum and average errors of 0.00 m/s and 0.13 m/s respectively. These speeds were subjected to a 2-step clustering for developing the PLOS for the crossing manoeuvre at unsignalized intersection. Since, 1.2 m/s is observed to the average pedestrian crossing speed, not only from this study but in the past research, as well, therefore, speeds > 1.2 m/s were considered as LOS C, the design PLOS for crossing behaviour. Thereafter, speeds above 1.2 m/s and below 1.2 m/s were subjected to clustering and the ranges of PLOS from A to F were defined. It was observed that pedestrian speeds below 1.03 m/s might result in discomfort and inconvenience leading to forced crossing, which may cause conflict situations. The biggest advantage of this method to assess PLOS is that it does not consider the delays, which change based on the number of lanes on the road and the pedestrian speeds, which is directly obtained from the vehicular and pedestrian counts. The methodology used in this research can be adapted for cities globally to develop a standardized Pedestrian Level of Service (PLOS). The findings could have a significant value for urban planners, transportation engineers, and policymakers worldwide. By integrating the PLOS into planning and decision-making, cities can more effectively allocate resources, implement targeted safety measures, and create pedestrian-friendly environments that encourage active transportation and enhance the overall quality of urban life. Furthermore, various other factors, like pedestrian safety, can be incorporated into the present methodology to improve the designed PLOS levels.

Acknowledgment

The authors received no financial support for the research, authorship and/or publication of this article.

Conflicts of interest

The authors declare that they have no known competing financial interests or personal relationships that could have appeared to influence the work reported in this paper.

References

[1] MOHANTY, M., DEY, P. P. Quantification of LOS at uncontrolled median openings using area occupancy through cluster analysis. *Arabian Journal for Science and Engineering* [online]. 2019, **44**(5), p. 4667-4679. ISSN 2193-567X, eISSN 2191-4281. Available from: https://doi.org/10.1007/s13369-018-3509-3

[2] ZEGEER, C. V., STEWART, J. R., HUANG, H. H., LAGERWEY, P. A., FEAGANES, J., CAMPBELL, B. Safety effects of marked versus unmarked crosswalks at uncontrolled locations. Georgetown Pike McLean, VA: The Federal Highway Administration, 2005.

[3] CHANDRA, S., AGRAWAL, A., RAJAMMA, A. Microscopic analysis of service delay at uncontrolled intersections in mixed traffic conditions. *Journal of Transportation Engineering* [online]. 2009, **135**(6), p. 323-329. ISSN 2473-2907, eISSN 2473-2893. Available from: https://doi.org/10.1061/(asce)0733-947x(2009)135:6(323)

[4] Indian highway capacity manual (Indo-HCM). New Delhi: CSIR-Central Road Research Institute, 2017.

[5] RAJ, J., VEDAGIRI, P. Modeling level of service of urban roads based on travellers' perceptions. *European Transport - Trasporti Europei* [online]. 2022, **89**, p. 1-17. ISSN 1825-3997. Available from: https://doi.org/10.48295/et.2022.89.1

[6] BENHADOU, M., EL GONNOUNI, A., LYHYAOUI, A. Pedestrian level of service for sidewalks in Tangier City. *International Journal of Electrical and Computer Engineering (IJECE)* [online]. 2024, **14**(1), p. 1048-1057. ISSN 2088-8708, eISSN 2722-2578. Available from: http://doi.org/10.11591/ijece.v14i1.pp1048-1057

[7] KUCHU, J. Development of composite pedestrian level of service model in urban milieu at midblock sections. *Periodica Polytechnica Transportation Engineering* [online]. 2024, **52**(1), p. 40-51. ISSN 0303-7800, eISSN 1587-3811. Available from: https://doi.org/10.3311/PPtr.20798

[8] JAHAN, M. I., MAZUMDAR, A. A. B., HADIUZZAMAN, M., MASHRUR, S. M., MURSHED, M. N. Analyzing service quality of pedestrian sidewalks under mixed traffic condition considering latent variables. *Journal of Urban Planning and Development* [online]. 2020, **146**(2), 04020011. ISSN 0733-9488, eISSN 1943-5444. Available from: https://doi.org/10.1061/(ASCE)UP.1943-5444.0000563

[9] DANDAN, T. A. N., WEI, W. A. N. G., JIAN, L. U., YANG, B. I. A. N. Research on methods of assessing pedestrian level of service for sidewalk. *Journal of Transportation Systems Engineering and Information Technology* [online]. 2007, **7**(5), p. 74-79. ISSN 1570-6672. Available from: https://doi.org/10.1016/S1570-6672(07)60041-5

[10] LOO, B. P., LIAN, T., FRANK, L. D. Walking (in) convenience: an in-depth study of pedestrian detours to daily facilities. *Journal of the American Planning Association* [online]. 2024, 90(4), p. 742-757. ISSN 0194-4363, eISSN 1939-0130. Available from: https://doi.org/10.1080/01944363.2024.2310613

[11] HAYATI, N. N., SULISTYANINGTYAS, G., NAWIR, D., ISHAK, S. Z. Walkability assessment and pedestrian way planning on Mercedes Benz Road Corridor, Cicadas, Bogor Regency. *IOP Conference Series: Earth and Environmental Science* [online]. 2024, **1294**(1), 012002. ISSN 1755-1315. Available from: https://doi.org/10.1088/1755-1315/1294/1/012002

[12] National Research Council. Highway capacity manual 2000. Transportation Research Board Special Report 209, 16-9. 2000.

[13] BOSINA, E., WEIDMANN, U. Estimating pedestrian speed using aggregated literature data. *Physica A: Statistical Mechanics and its Applications* [online]. 2017, **468**, p. 1-29. ISSN 0378-4371, eISSN 1873-2119. Available from: https://doi.org/10.1016/j.physa.2016.09.044

[14] AHMED, T., MOEINADDINI, M., ALMOSHAOGEH, M., JAMAL, A., NAWAZ, I., ALHARBI, F. A new pedestrian crossing level of service (PCLOS) method for promoting safe pedestrian crossing in urban areas. *International Journal of Environmental Research and Public Health* [online]. 2021, **18**(16), 8813. eISSN 1660-4601. Available from: https://doi.org/10.3390/ijerph18168813

[15] GEORGIOU, A., SKOUFAS, A., BASBAS, S. Perceived pedestrian level of service in an urban central network: the case of a medium size Greek city. *Case Studies on Transport Policy* [online]. 2021, **9**(2), p. 889-905. ISSN 2213-624X, eISSN 2213-6258. Available from: https://doi.org/10.1016/j.cstp.2021.04.009

[16] AMPRASI, V., POLITIS, I., NIKIFORIADIS, A., BASBAS, S. Comparing the micro simulated pedestrian level of service with the users' perception: the case of Thessaloniki, Greece, coastal front. *Transportation Research Procedia* [online]. 2020, **45**, p. 572-579. ISSN 2352-1457, eISSN 2352-1465. Available from: https://doi.org/10.1016/j.trpro.2020.03.055

[17] PAUL, D., MORIDPOUR, S., VENKATESAN, S., WITHANAGAMAGE, N. Evaluating the pedestrian level of service for varying trip purposes using machine learning algorithms. *Scientific Reports* [online]. 2024, **14**(1), 2813. eISSN 2045-2322. Available from: https://doi.org/10.1038/s41598-024-53403-7

[18] VENTHURUTHIYIL, S. P., CHUNCHU, M. Anticipated collision time (ACT): a two-dimensional surrogate safety indicator for trajectory-based proactive safety assessment. *Transportation Research Part C: Emerging Technologies* [online]. 2022, **139**, 103655. ISSN 0968-090X, eISSN 1879-2359. Available from: https://doi.org/10.1016/j.trc.2022.103655

[19] JOHNSSON, C., LAURESHYN, A., DAGOSTINO, C. Validation of surrogate measures of safety with a focus on bicyclist-motor vehicle interactions. *Accident Analysis and Prevention* [online]. 2021, **153**(3), 106037. ISSN 0001-4575, eISSN 1879-2057. Available from: https://doi.org/10.1016/j.aap.2021.106037

[20] LU, C., HE, X., VAN LINT, H., TU, H., HAPPEE, R., WANG, M. Performance evaluation of surrogate measures of safety with naturalistic driving data. *Accident Analysis and Prevention* [online]. 2021, **162**, 106403. ISSN 0001-4575, eISSN 1879-2057. Available from: https://doi.org/10.1016/j.aap.2021.106403

[21] MOHANTY, M., SARKAR, B., GORZELANCZYK, P., PANDA, R., GANDUPALLI, S. R., ANKUNDA, A. Developing pedestrian fatality prediction models using historical crash data: application of binary logistic regression and boosted tree mechanism. *Communications - Scientific Letters of the University of Zilina* [online]. 2023, **25**(2), p. D45-D53. ISSN 1335-4205, eISSN 2585-7878. Available from: https://doi.org/10.26552/com.C.2023.036

[22] CAFISO, S., DI GRAZIANO, A., PAPPALARDO, G. In-vehicle stereo vision system for identification of traffic conflicts between bus and pedestrian. *Journal of Traffic and Transportation Engineering (English Edition)* [online]. 2017, **4**(1), p. 3-13. ISSN 2095-7564, eISSN 2589-0379. Available from: https://doi.org/10.1016/j.jtte.2016.05.007

[23] QIAN, Y., LIU, H. The influence of urban crossroad facilities on pedestrian safety in Shanghai, China. In: ICTCT Extra-Workshop in Beijing, China: proceedings. 2007.

[24] FU, T., MIRANDA-MORENO, L., SAUNIER, N. Pedestrian crosswalk safety at nonsignalized crossings during nighttime: use of thermal video data and surrogate safety measures. *Transportation Research Record: Journal of the Transportation Research Board* [online]. 2016, **2586**(1), p. 90-99. ISSN 0361-1981, eISSN 2169-4052. Available from: https://doi.org/10.3141/2586

[25] KATHURIA, A., VEDAGIRI, P. Evaluating pedestrian vehicle interaction dynamics at un-signalized intersections: a proactive approach for safety analysis. *Accident Analysis and Prevention* [online]. 2020, **134**, 105316. ISSN 0001-4575, eISSN 1879-2057. Available from: https://doi.org/10.1016/j.aap.2019.105316

[26] NIRF India Rankings - National Institutional Ranking Framework, Ministry of Education, Government of India [online]. 2023. Available from: https://www.nirfindia.org/2023/Ranking.html

[27] World University Rankings - Times Higher Education [online]. 2023. Available from: https://www.timeshighereducation.com/world-university-rankings/kiit-university

[28] FENG, S., DING, N., CHEN, T., ZHANG, H. Simulation of pedestrian flow based on cellular automata: a case of pedestrian crossing street at section in China. *Physica A: Statistical Mechanics and its Applications* [online]. 2013, **392**(13), p. 2847-2859. ISSN 0378-4371, eISSN 1873-2119. Available from: https://doi.org/10.1016/j.physa.2013.03.008

[29] BOORA, A., GHOSH, I., CHANDRA, S. Assessment of level of service measures for two-lane intercity highways under heterogeneous traffic conditions. *Canadian Journal of Civil Engineering* [online]. 2017, **44**(2), p. 69-79. ISSN 0315-1468, eISSN 1208-6029. Available from: https://doi.org/10.1139/cjce-2016-0275

[30] MOHANTY, M., PANDA, R., GANDUPALLI, S. R., ARYA, R. R., LENKA, S. K. Factors propelling fatalities during road crashes: a detailed investigation and modelling of historical crash data with field studies. *Heliyon* [online]. 2022, **8**(11), e11531. Available from: https://doi.org/10.1016/j.heliyon.2022.e11531

[31] MOHANTY, M., SARKAR, B., PATTANAIK, M. L., SAMAL, S. R., GORZELANCZYK, P. Development of congestion severity index for uncontrolled median openings utilising fundamental traffic parameters and clustering technique: a case study in India. *International Journal of Intelligent Transportation Systems Research* [online]. 2023, **21**(3), p. 461-472. ISSN 1348-8503, eISSN 1868-8659. Available from: https://doi.org/10.1007/s13177-023-00365-1

[32] IRC:103. Guidelines for pedestrian facilities. New Delhi: Publication of Indian Road Congress, 2012.

[33] SANGEETH, K., LOKRE, A. Factors influencing pedestrian speed in level of service (LOS) of pedestrian facilities. *Transportation Research Interdisciplinary Perspectives* [online]. 2019, **3**, 100066. eISSN 2590-1982. Available from: https://doi.org/10.1016/j.trip.2019.100066

[34] SARSTEDT, M., MOOI, E. *A concise guide to market research*. 2. ed. Berlin, Heidelberg: Springer, 2014. ISBN 978-3-662-51981-3, eISBN 978-3-642-53965-7.

[35] JAIN, A. K. Data clustering: 50 years beyond K-means. *Pattern Recognition Letters* [online]. 2010, **31**(8), p. 651-666. ISSN 0167-8655, eISSN 1872-7344. Available from: https://doi.org/10.1016/j.patrec.2009.09.011

EVALUATION OF NANOMODIFIED ASPHALT WITH $CaCO_3$: RHEOLOGICAL AND MIXTURE PERFORMANCE

Ahmed Mahir Mohammed[1,*], Alaa H. Abed[2]

[1]Civil Engineering Department, University of Baghdad, Baghdad, Iraq
[2]Civil Engineering Department, AL-Nahrin University, Baghdad, Iraq

*E-mail of corresponding author: ahmed.m.886@coeng.uobaghdad.edu.iq

Ahmed Mahir Mohammed 0009-0001-4585-323X, Alaa H. Abed 0000-0002-6569-4598

Resume

The impact of using three contents of 1, 3 and 5 % of nano CaCO3 on the composition of asphalt binder and the mechanical properties of Hot Mix Asphalt (HMA) wearing course was studied. Laboratory tests were performed to examine the physical and rheological characteristics of nanomodified asphalt binder. In addition, Superpave Indirect Tensile Test (IDT) was conducted to evaluate the mechanistic characteristics and moisture susceptibility of the HMA. The test findings pointed that the nano modified asphalt with 5% nano $CaCO_3$, decreased the temperature sensitivity due to asphalt stiffening and improved resistance to permanent deformation. Additionally, HMA mixture performance exhibits a substantial increase in moduli value at temperatures varying from 5 to 40 ^{o}C and increased flexibility at lower testing temperatures as compared to the neat HMA mixture.

Article info

Received 2 September 2024
Accepted 15 November 2024
Online 11 December 2024

Keywords:

nanomaterial
asphalt
$CaCO_3$
IDT
DSR
TSR

Available online: https://doi.org/10.26552/com.C.2025.012

ISSN 1335-4205 (print version)
ISSN 2585-7878 (online version)

1 Introduction

Researchers and agencies have recently focused on a trend of growing attention to the development of longer pavement life that sustains heavy traffic loads along with environmental impact. Nanomaterial has recently been incorporated into the asphalt as the key solution to overcome and survive the pavement lifecycle against the common distress that occurs in high-temperature climates as permanent deformation, fatigue, and thermal cracking besides stripping and reveling action that easily extracts asphalt film from aggregate leading to early premature failure within the pavement. Researchers worldwide have extensively used various types of nanomaterials, including TiO_2.SiO_2, ZnO, Fe_2O_3, and $CaCO_3$ that has been investigated in this study. Due to the rapid progress in nanomaterial technology, nano $CaCO_3$ is currently being employed to prepare the modified asphalt as a dependable and cost-effective material. The Nano-$CaCO_3$ is identified as economical material for producing modified asphalt; it has a white powder consisting of particles that have an average size ranging from 10 to 100 nanometers is produced using two methods: (a) the mineral carbonation process, which involves using industrial wastes such as CaO and $CaCl_2$ as a source of calcium in a packed bed reactor [1], and (b) utilizing the CO_2 exhaled during the cement manufacturing process at a cement plant [2]. Thus, employing nano $CaCO_3$ as a modifier additive not only reduces CO_2 emissions but also proves to be a cost-efficient approach to improving the rheological properties of the asphalt binder. It is composed of roughly 98.5 % calcium carbonate. Combined with asphalt, it enhances the performance of HMA mixtures by establishing a stable system that improves temperature susceptibility, particularly at high temperatures.

A study conducted by Hao et al. [3] revealed that adding 6 % nano $CaCO_3$ to asphalt concrete improved dynamic and residual stability. This enhancement was observed in both high-temperature and water stability. A separate group of scientists that was investigating to assess the rheological, physical, and performance properties of hot mix asphalt (HMA) that was improved by the addition of nano $CaCO_3$ found that higher nano concentration results in reduced penetration, increased stiffness and viscosity, heightened susceptibility to permanent deformation, and enhanced anti-aging effects [4-7]. Zhang et al. [8] conducted a study demonstrating the positive impact of incorporating up to 5 % nano-$TiO_2/CaCO_3$ on the mechanical properties of bituminous materials. This inclusion resulted in a decrease in penetration, while simultaneously increasing the softening point and viscosity. As a result, the sensitivity of the bituminous materials was reduced.

Additionally, it improves the durability of the bituminous material against deformation and wear caused by repeated stress at moderate temperatures. Adding $TiO_2/CaCO_3$ increased the asphalt stiffness modulus while raising its viscosity. The unique characteristic of nano $CaCO_3$ is its capacity to improve the durability of modified asphalt binder at elevated temperatures by strengthening it through its dispersing properties. Xing et al. [9] established that reducing particle sizes leads to a higher density of particles, hence enhancing the yield stress of the modified asphalt via the Orowan mechanism. According to the literature, nano $CaCO_3$ has improved different elements of asphalt performance, including its sensitivity to temperature, susceptibility to moisture, resistance to cracking fatigue, aging, adhesion, and dispersion in asphalt binder. Adding nano $CaCO_3$ to HMA mixtures increased rutting while decreasing susceptibility to high temperatures. When 4 % $CaCO_3$ is added, increasing the viscosity of the asphalt binder improves the tensile and compressive strengths of the HMA, leading to a 55.8 % improvement in fatigue life [10]. Zhai et al. [11] have investigated the impact of different concentrations (3 %, 4 %, 5 %, 6 %, and 7 %) of nano $CaCO_3$ modified asphalt in SBR polymer.

The study aimed to assess the performance of the HMA mixture using various tests, including Wheel track, static creep, overlay, and beam bending tests. The results demonstrated a significant improvement in the ability to resist rutting by incorporating 5 % $CaCO_3$/SBR. This improvement can be attributed to the increased surface area of nanoparticles, which enhanced viscosity and adhesion. As a result, the micromechanical properties, including adhesion, dissipated energy, anti-cracking resistance, and flexural deformation, were greatly enhanced compared to using asphalt modified only with SBS.

In a recent study conducted by Yarahmadi et al. [12], it was found that utilizing Nano $CaCO_3$ may successfully decelerate the progression and spread of fatigue fractures in Stone Matrix Asphalt (SMA) mixes. The performance of the SMA combination was enhanced at elevated temperatures and stress levels. The indirect tensile strength (ITS) test findings demonstrated that the addition of nanotechnology-enhanced materials to the SMA mixes enhanced its ability to withstand moisture damage and perform well when exposed to water. Li et al. [13] examined how adding nano

Table 1 *Doura Asphalt physical test*

Property	Units	Result
Penetration at 25 oC, 100 gm, 5 sec	0.1 mm	46
Softening Point	oC	49
Specific gravity at 25 oC	----	1.03
Flash point	oC	288
Ductility	cm	114
Residue from thin-film oven test AASHTO T 179		
Retained penetration, % of original	0.1 mm	61
Ductility at 25 oC, 5 cm/min	cm	87

Table 2 *Doura Asphalt Rheological test*

Property	Result	Temp.	M320
Original Test on Binder			
Rotational Viscosity, Pa.s.	0.63	135 °C	Max. 3
	0.16	165 °C	--------
Dynamic Shear Rheometer, G*/sin δ, kPa	2.34	64 °C	Min. 1
	0.84	70 °C	
	Tests on RTFO Residue		
	1.68	70 oC	Min 2.2
Tests on PAV Residue			
Dynamic Shear Rheometer, G*.sin δ, kPa	4266	25 °C	
	3452	28 °C	Max. 5000
Creep Stiffness, S, MPa	241	-12 °C	Max. 300
Creep Slope, m value.	0.322	-12 °C	Min. 0.3

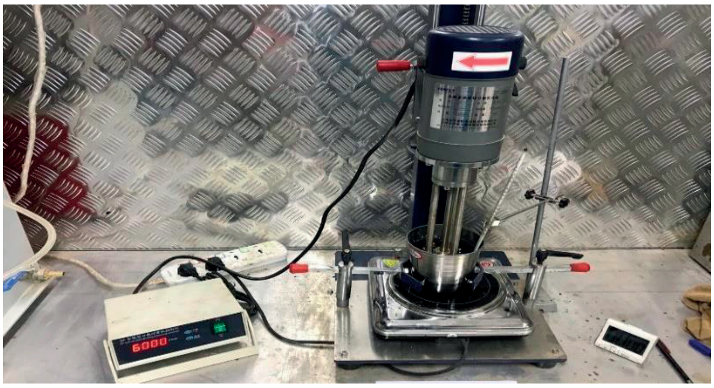

Figure 1 *Mixing of NCC with Asphalt*

$CaCO_3$/ SBR and ZnO/SBR composite modifiers affects the rutting resistance and viscosity of AK-70 asphalt binder to investigate various concentrations of nano CaCO3 (4 %, 5 %, 6 %), Nano ZnO (1 %, 3 %, 5 %), and SBR (3 %, 4 %, 5 %) evaluated using Dynamic Shear Rheometer (DSR) and Rationale viscosity (RV) tests. The results indicated that the modified asphalt with composites exhibited increased viscosity and improved resistance to rutting compared to the neat asphalt. Vasilievici et al. [14] investigated the impact of a 5 % Polystyrene ratio on the stiffness of the asphalt binder D50/70, including nano $CaCO_3$, utilizing dynamic mechanical analysis. Polystyrene was shown to increase the stiffness of the nano $CaCO_3$ asphalt binder.

This research hypothesis shows the impact of using three contents of 1, 3 and 5 % of nano $CaCO_3$ types of nanomaterials on the composition of asphalt binder and the mechanical properties of HMA wearing. Laboratory tests including physical asphalt test and RV, DSR, Bending Beam Rheometer (BBR), Rolling Thin Film Oven (RTFO), and Pressure Aging Vessel (PAV), were performed to examine the physical and rheological characteristics of the binders. Additionally, Superpave IDT was conducted to evaluate the mechanistic characteristics and moisture susceptibility of the HMA.

2 Material selection

2.1 Asphalt

The 40-50 penetration grade of asphalt yielding to PG (64-16) from Doura petroleum refinery was used in this study, physical and rheological properties of which are described in Tables 1 and 2.

2.2 Nano $CaCO_3$

The study employed nano $CaCO_3$ (NCC) as an asphalt modifier. The NCC is a white substance powder that cannot be dissolved and has an average particle size of 15 to 40 nanometers with a purity level of approximately 97.5 %; it was imported from Sky-Spring Company, United States.

2.3 Blending of nanomodified asphalt

A dry mixing technique was developed in this study, involving high-speed stirring to distribute the nanomaterials evenly throughout the asphalt binder matrix. The NCC was introduced into a sole asphalt PG (64-16) at different concentrations, specifically 1, 3, and 5 % by weight of the neat asphalt. The dry mixing approach employs a high-speed shear mixer (HSM) to disperse the nanomaterials evenly. Next, the nanomaterial is introduced, and the HSMs exhibit a unique tip design that sets them apart from traditional mixers.

Figure 1 illustrates the shear mixing action that occurs over a specific duration. The initial batch of asphalt material, weighing 500 ± 2 g, was heated to a temperature of 160 °C. It was then manually stirred for 20 minutes. The nano additive was added gradually, at a rate of 2 to 4 g per minute. This process continued until all the nanoparticles were thoroughly dispersed within the binder. The specific conditions used a speed of 6000 rpm and 45 minutes as a blending time. The mixing uniformity is sufficient to prevent asphalt aging. After completion, the asphalt was poured into metal cans and allowed to cool at room temperature for further testing.

3 Testing protocols

3.1 Physical and rheological asphalt test

Both neat and nanomodified asphalt at varying percentages were introduced into physical routine tests, including penetration test ASTM D5, softening point ASTM D36, ductility ASTM D113, storage stability ASTM D7173. Finally, asphalt temperature sensitivity is measured using the penetration Index (PI) [15]:

$$PI = \frac{1952 - 500\log_{10}P25 - 20SP}{50\log_{10}P25 - SP - 120} \tag{1}$$

Asphalt viscosity was determined using RV according to AASHTO TP 48 at 135 °C. On the other hand, the DSR was utilized at 10 rad/sec frequency, employ ing 8 mm and 25 mm diameter and the gaps were 1 and 2 mm, respectively. The failure temperatures of asphalt were determined by observing the point at which G*/sinδ went below 1 kPa. The aging process involved using the Rolling Thin Film Oven (RTFO) for the short-term aging and the Pressure Aging Vessel (PAV) for the long-term aging was employed to assess the high-temperature rating for modified asphalt and their ability to withstand both high and moderate-temperature environments and repeated loading circumstances. Finally, BBR was utilized to determine low-temperature characteristics of neat and modified asphalt based on AASTHO T313.

4 Discussion and analysis

4.1 The physical response

Figure 2 indicated that with increasing the nano content from 1 to 5 %, the penetration value decreases by about 7, 16 and 20 % as compared to neat asphalt, which can be attributed to the dispersion of the NCC inside the asphalt, which leads to increased stiffness and resistance to penetration. This behavior is an indication that the NCC has acquired the high-temperature viscoelastic characteristics as a result of nanoparticle's higher surface area, which might lead to the asphalt's reduced sensitivity towards temperature [6].

Similar trends are also noted in Figure 3; hence, nanomodified asphalt had reduced ductility value by 6, 13, and 21 % as nano content increased from 1 to 5 %, respectively, compared to the neat asphalt.

On the other hand, the modification of the neat asphalt presents sensitivity towards the temperature variation; for this, the softening point suffers a change in falling to temperature of 4 °C at 1 % NCC content, reaching 8 °C at 5 % NCC, as shown in Figure 4.

The drop in penetration value and the increase in softening point imply an increase in specimen stiffness and a decrease in temperature susceptibility, resulting in improved resistance to rutting at high temperatures.

The penetration test results are consistent with research conducted by Hao et al. [3]. The rise in softening point is a positive indication as bitumen with a higher softening point tends to be more resistant to permanent deformation [16]. The PI values gets higher with the increment of modifier content, which indicates the enhancement of modified bitumen against high-temperature susceptibility. Figure 5 flows that the PI value increased to - 0.82, - 0.59, and - 0.28 for nano content range 1 to 5 %. Nanomodified asphalts with NCC having high PI values are more resistant to low-temperature cracking and permanent deformation.

The final comment adheres to the storage stability of nanomodified asphalt since it relates to the agglomeration issue and is presented in Figure 6; the

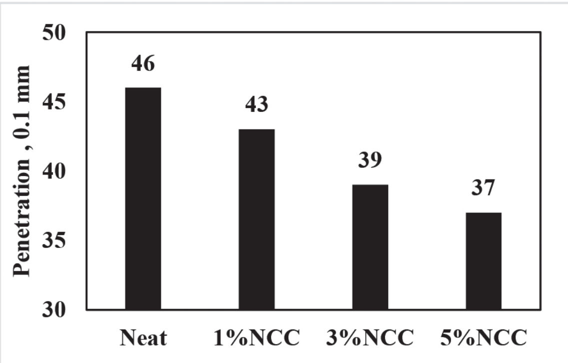

Figure 2 *Penetration value of neat and NCC modified asphalt*

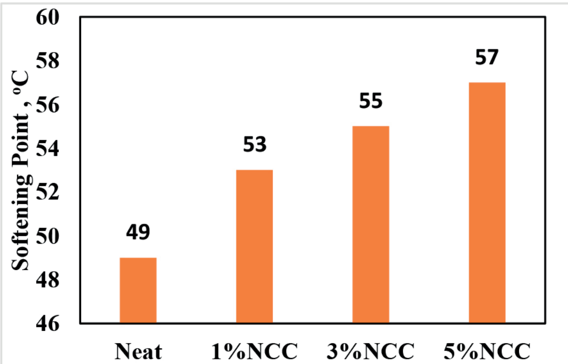

Figure 4 *Softening point value of neat and NCC modified asphalt*

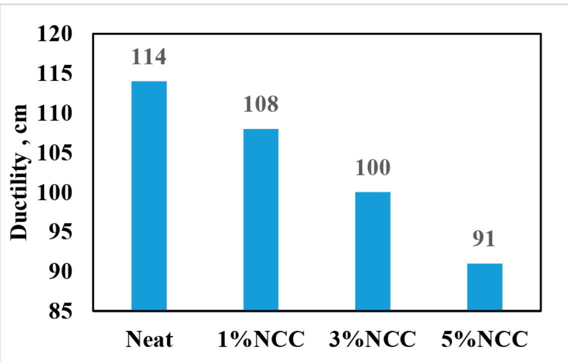

Figure 3 *Ductility value of neat and NCC modified asphalt*

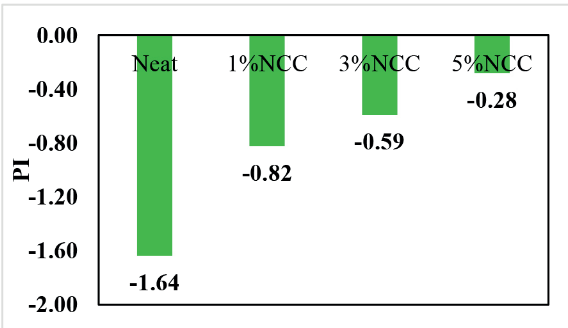

Figure 5 *PI value of neat and NCC modified asphalt*

used HSM with 6000 rpm has significantly approved that with the increasing content, the difference between softening reading will not reach beyond the critical value of 2.5 °C, thus, ensuring a good dispersion for the NCC modified blends.

The result obtained from physical testing indicated an improvement related to the modification of the asphalt binder by stiffening the asphalt within the penetration grade; the use of 5 % Nano content had the greatest impact on the properties of the asphalt with NCC. While the penetration index and softening point rise with the amount of nanomaterial, asphalt ductility is decreased due to the material's decreased temperature sensitivity, improving resistance to low-temperature cracking and permanent deformation.

4.2 The rheological response

A DSR was used to find the Superpave PG system's upper critical temperature (T_{crit}). The neat and nanomodified bitumen samples, both unaged and RTFOT-aged, were exposed to DSR oscillatory shear at 10 rad/s (1.59 Hz), corresponding to field traffic traveling at around 90 km/h. Initial temperature values were established at 64 °C for unaged samples and 70 °C for samples undergoing RTFOT aging, with a six-degree increment.

Using the G*/sinδ values, the highest critical temperatures for each sample were calculated and employed in the PG system. The DSR standards' rutting, and fatigue requirements are displayed in Table 3, Figure

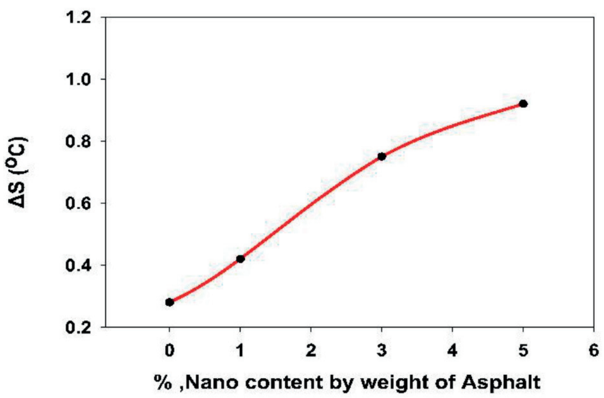

Figure 6 *Storage Stability of neat and NCC modified asphalt*

Table 3 *Criteria required for PG - DSR limit*

Item	Property	Limits	Concern
Original	G*/sinδ	≤ 1.1 kPa	
RTFO	G*/sinδ	2.2 kPa ≤	Rutting
PAV	G*/sinδ	5000 kPa≥	Fatigue

Table 4 *Rutting and upper critical temperature for neat and nanomodified asphalt*

Binder	Temp. °C	G*/sinδ, kPa		T_{crit}
		Original	RTFO	
	64	2.341	3.48	
Neat	70	0.842	1.68	64
	76	0.452	0.589	
	64	2.51	3.81	
1% NCC	70	1.10	1.84	64
	76	0.53	0.77	
	64	3.07	4.25	
3% NCC	70	1.97	2.85	70
	76	0.61	1.30	
	64	5.42	5.28	
5% NCC	70	3.37	3.49	70
	76	1.06	1.89	

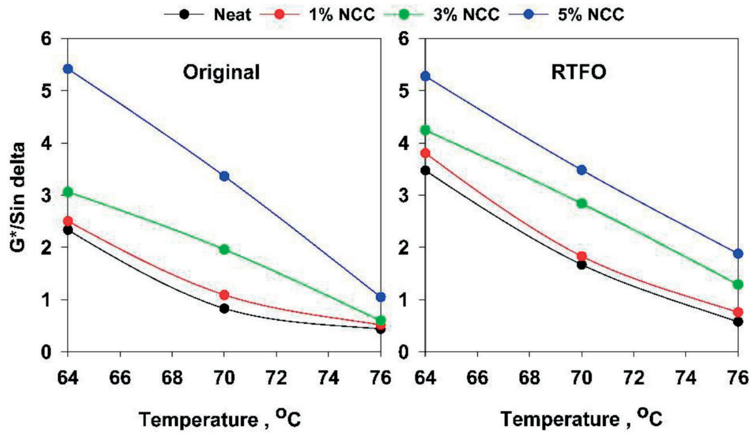

Figure 7 *Result of DSR-rutting parameter G*/sinδ for neat and NCC modified asphalt*

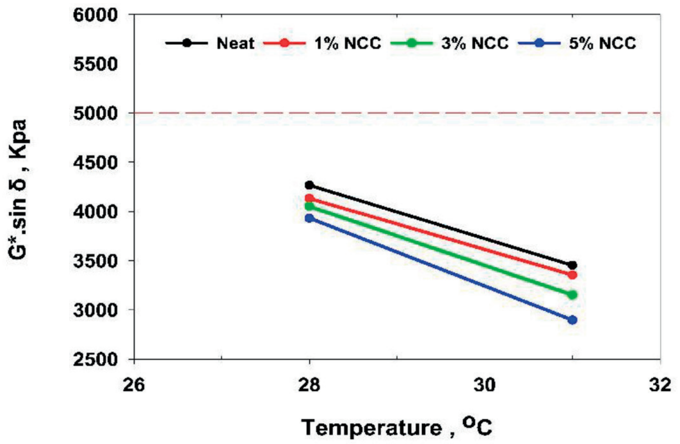

Figure 8 *Result of DSR-fatigue parameter G*.sinδ for neat and NCC modified asphalt*

7, while Table 4 lists the upper critical temperatures for each sample. The upper critical temperature (T_{crit}) serves as a means of evaluating the rutting performance of a specific bitumen sample. A higher G*/sinδ number indicates greater resistance of a sample to permanent deformation.

The results indicate that adding the NCC at concentrations of 3 % and 5 % has positively affected by shifted PG by one grade to a temperature of 70 °C. Modifications in the upper PG grading are linked to the enhancement of high-temperature performance caused by the augmentation of the materials' hardness or stiffness. As a result, they become more resilient to external forces and demonstrate superior resistance to rutting. At a temperature of 70 °C, the RTFO nanomodified asphalt demonstrates improved resistance to rutting. This is achieved by raising the value of G*/sin δ, which reaches 2.85 and 3.49 kPa when the nano range is between 3 and 5 %.

In comparison, neat asphalt at the same temperature only reaches 1.68 kPa. It is worth noting that the G*/sinδ values for un-aged and RTFO-aged samples were constant at the same temperature. Therefore, it can be inferred that the NCC modified RTFO aged samples do not undergo rapid hardening or oxidation, which is often due to aging. Meanwhile, the optimum content of NCC at 5 % relatively moves asphalt specification when tested at PG +6 °C, i.e., 64 °C, indicating less susceptibility to fatigue damage than other Nano types. It is shown that for all Nano types, the 1 % has the lowest stiffness value, which could be attributed to the low amount that did not disperse uniformly in the asphalt. It can be concluded that, 5 % NCC nano modified asphalt is almost satisfying and improves the rutting of asphalt. The improvement in these characteristics suggests that nanomodified asphalt is more resistant to permanent deformation, and rutting at high temperatures will perform better in hot regions where the pavement permanently deforms. An increase in this characteristic also suggests that bitumen will perform better when it is manufactured and used (short-term aging stage). The fatigue factor G*.sin δ was examined at moderate temperatures (25 and 28 °C) to assess the durability against fatigue cracking. The maximum allowable value for G*.sinδ, as per the long-term aging (PAV) criterion, is 5000 kPa. Consequently, a lower value of G*.sinδ is considered a favorable attribute regarding resistance to fatigue cracking. Figure 8 presents the fatigue factor values obtained following the PAV process. The NCC-modified asphalt exhibited a somewhat lower G*.sinδ due to the increased loss in moduli. It is evident that increasing the nano content from 1 to 5 % results in

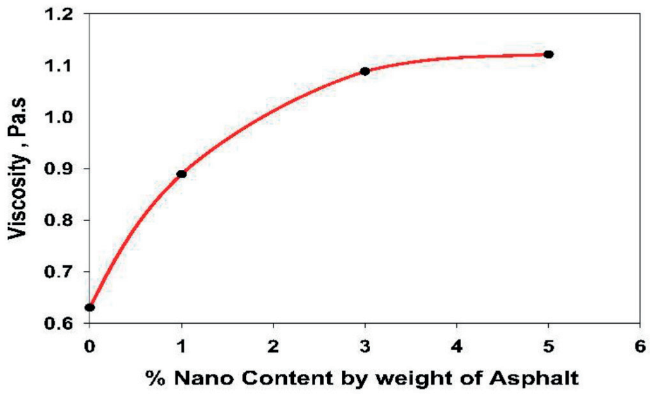

Figure 9 *Viscosity values for neat and NCC modified asphalt*

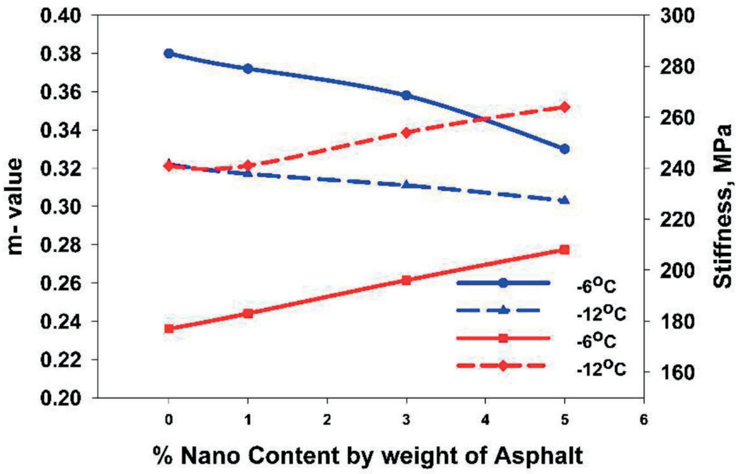

Figure 10 *BBR results stiffness and m-value for neat and NCC modified asphalt*

a drop in the value of G*.sinδ. This decrease occurs at an average rate of approximately 4, 7, and 12 % when tested at temperatures of 25 and 28 °C. This suggests a potential antioxidant effect of nano NCC following PAV [17-18]. Nanoparticles exhibit significant performance potential due to their size and high specific area, and their use is expanding to enhance the asphalt binder's performance characteristics. The effectiveness of asphalt binders modified with metal oxide nanoparticles against the buildup of microcracks and fatigue, as well as its relationship to oxidative aging, is one of the topics that has hardly ever been the focus of prior studies.

According to Figure 9, increasing the NCC content from 1 to 5 % leads to an enhancement in asphalt viscosity. This results in the growth of the binder film thickness and the coating of aggregates in the heated mixture. A viscosity value of 1.121 Pa s was observed using a 5 % concentration of NCC. Consequently, the viscosity of all the nanomaterials increased as the Nano content increased at a temperature of 135 °C. Specifically, a 5 % increase in NCC resulted in a 43 % increase in asphalt viscosity.

The asphalt needs to retain a low stiffness level to mitigate the risk of low-temperature cracking in colder pavement conditions. By raising the Nano content to 5 % at temperatures of -6 and 12 °C, the m-value would be marginally reduced for any content below 8 % compared to pure asphalt. This reduction indicates a decreased capacity for stress relaxation. Figure 10 demonstrates that the inclusion of NCC particles leads to a decrease in the m-value when compared to pure asphalt at both temperatures. The stiffness of the NCC-modified asphalt has exhibited a modest alteration at temperatures of -6 and -12 °C compared to clean asphalt. This alteration is shown in Figure 10 and characterized by an increase in creep stiffness of around 3.6 % and 10 % when the NCC content is raised from 1 % to 5 %. However, adding the NCC to the asphalt has not significantly enhanced its performance at low temperatures and had a negligible impact on low-temperature cracking. This finding aligns with previous studies conducted by [10] and [19].

The physical and rheological properties of nanomodified asphalt with varying levels of NCC content indicate an enhancement in asphalt performance compared to regular asphalt. However, these enhancements are quite small, especially when it comes to a low-temperature examination, which includes BBR and fatigue factor. Consequently, after analyzing the test findings, a certain nano content was selected for each kind to study the HMA mixture. The data indicates that there is a 3 to 5 % rise in modified asphalt. Nevertheless, the incorporation of 5 % Nano content exhibited the

Table 5 *Physical properties of coarse aggregate*

Property	Result		Limits
	5-12 mm	5-9 mm	
Bulk Specific gravity, ASTM C127	2.627	2.618	--------
Apparent Specific gravity, ASTM C127	2.674	2.674	
Absorption, %, ASTM C127	0.66	0.797	
Fractured Face, %, ASTM D 5821	93	95	Min. 90
Consensus Properties			
Coarse Aggregate Angularity, %, ASTM D 5821	97	98	Min. (95/90)
Flat, elongated particles, %, ASTM D 4791	1.2	0.8	Max. 10
Source Properties			
Abrasion %, ASTM C131	21	15	Max .30
Soundness, %, ASTM C88	3.71	2.81	Max .12

Table 6 *Physical properties of fine aggregate*

Property	Result		Limit
	Crusher Sand	River Sand	
Bulk Specific gravity, ASTM C127	2.576	2.545	--------
Apparent Specific gravity, ASTM C127	2.635	2.656	
absorption, %, ASTM C127	0.854	1.647	
Consensus Properties			
Angularity, %, ASTM D1252	60	49	Min. 45
Sand Equivalent, %, ASTM D2419	78	53	Max. 45
Source Properties			
Deleterious. materials, %, ASTM C142	0.58	0.92	Max .10

most significant impact on the characteristics of the asphalt. Therefore, rising the Nano content in asphalt to 5 % may meet the requirement specification, and the asphalt can resist rutting. Ultimately, adding 5 % nano content improves the properties of asphalt binders and will be further explored as the optimal nano content to improve the IDT and moisture damage, as presented in the further manuscript sections.

5 HMA

5.1 Mixing design

An aggregate maximum size of 12.5 mm, crushed quartz sourced from north of Baghdad. The Al-Nibaie quarry serves as the origin of this aggregate for their physical, source, and consensus properties were listed in Tables 5 and 6. Aggregates were prepared to establish a Job Mix Formula (JMF) for the combined aggregate blended with different blending ratios for each raw material, as graphically shown in Figure 11.

Duplicate specimens that have 150 mm in diameter and 115 mm in height were prepared at target design asphalt content of 4.5 % by weight of the mixture and varying percentages of 0.5 % above and below target asphalt as well as 1.0 %. The final volumetric properties and optimum asphalt content are listed in Table 7 for the neat and NCC modified mixture.

5.2 Specimen fabrication and test procedure

In this study, the effect of different percentages was identified to evaluate the Resilient Modulus, Creep, and tensile strength of HMA mixtures at a temperature of 5, 15, 25 and 40 °C with the aid of DTM 50. A cylinder of dimensions 150 mm diameter and 165 mm height was initially designed for air void content (4 %) and fabricated using Superpave Gyratory Compactor (SGC).

The specimen had at least 6 mm sawed off both sides, and four samples were created by sawing specimens to 150 mms diameter by 50 mm thickness, as presented in Figures 12 and 13. The Superpave IDT tests include resilient modulus (Mr), creep (D_t), and tensile-strength tests (TS), which adhere to the test

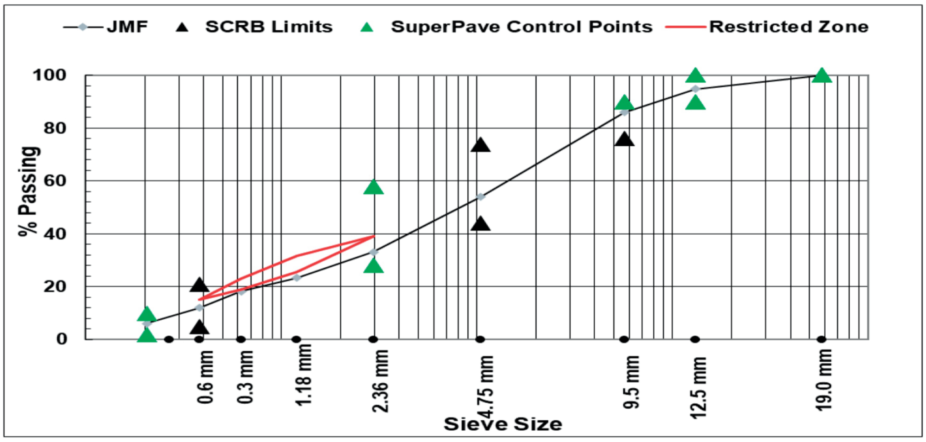

Figure 11 *HMA mix design gradation*

Table 7 *volumetric properties of HMA*

Property	Neat Asphalt	5% NCC modified Asphalt	Requirement
OAC, %	5.0	5.2	4.0-6.0
VA, %	4.0		4.0
VFA, %	74.4	72.92	65-75
VMA, %	15.23	14.73	Min 14.0
DP, %	1.03	1.04	0.8-1.6
% G_{mm} at $N_{initial}$	87.11	86.61	≥ 89%
% G_{mm} at N_{design}	96.13	96.23	96%

OAC = Optimum Asphalt Content, VA= Air Voids, VFA = Void Filled Asphalt, VMA = Voids in Mineral Aggregate, DP= Dust to Binder Ratio

Figure 12 *IDT preparation and cutting*

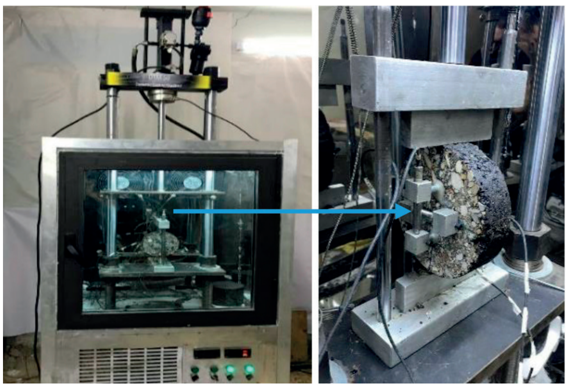

Figure 13 *Configuration of IDT using DTM 50*

procedures established by Roque and Buttlar 1992 ,1994 [20-22] to assess the cracking resistance.

The cylindrical samples underwent a test, where a repeated peak load was applied, causing horizontal deformations within the 0.038 to 0.089 mm range. Each load cycle has a 0.1 s load application interval followed by 0.9 s of rest. The computer continuously recorded the load and deformation. The specific methodologies for estimating the Mr can be located in the works of Roque and Buttlar [20-22] using:

$$M_r = \frac{P \times GL}{\Delta H \times t \times D \times C_{CMPL}} \quad (2)$$

where GL is the gauge length equal to ¼ diameter, P is the maximum load applied, t and D are the thickness and diameter, respectively, ΔH is the Horizontal Deformation and C_{CMPL} is a non-dimensional factor. The creep compliance was adopted on the same specimen with a static load of 100 s, and the recorded stress and strain were applied to find creep compliance as follows:

$$D_j = \frac{\Delta H \times t \times D \times C_{compliance}}{P \times GL}. \quad (3)$$

where D_j (GPa) is the creep compliance at time t, $C_{compliance}$ is the correction factor. Finally, the destructive test was conducted to find the TS at a static rate of 50.8 mm/min within DTM 50 following Equation:

$$TS = \frac{2P(C_{SX})}{\pi . t . D}. \quad (4)$$

Hence, C_{SX} is a factor corresponding to the stress correction and P is the maximum recorded load. To study the role of NCC as anti-stripping to prevent the negative impact of moisture damage, the AASHTO T283 procedure was followed. Specimens of a diameter of 101 mm and a thickness of 63 mm are made using OAC % for Marshall testing. Compaction levels range from 43 to 54 blows per each face for neat and nanomodified asphalt to achieve target air voids of 7 ± 0.5 %. The samples were divided into two groups, each consisting of three samples. One group was unconditioned, while the other group was conditioned. The control groups was kept in a water bath at 25 °C for 2 hours before testing. ITS was measured by applying a compressive force to the specimen, using a Marshall testing apparatus at a 50.8 mm/min rate until the specimen fractured. The second set of conditioned samples is placed in a vacuum chamber for the ITS testing. The specimens underwent the vacuum pressure treatment to get the targeted saturation level, which should fall within the 70 to 80 % range. Then the samples that have undergone vacuum saturation were stored in a freezer at -18 °C for at least 16 hours. Afterwards, the samples were taken from the freezer and placed in a water bath for 24 hours at 60 °C. after which they were transported to the water bath maintained at 25 °C and left there for 2 hours. The ITS test is performed on the conditioned samples mentioned above, and the maximum load is documented. The ITS of the samples is calculated by determining the maximum loads for both conditioned and unconditioned samples using:

$$TSR\,\% = \frac{2000 \times P}{\pi \times t \times D}, \quad (5)$$

where: ITS value for each specimen is in kPa, P is the peak load at failure, and t and D are thickness and diameter in mm, respectively.

$$TSR\,\% = \frac{Condition\ specimen}{Un - condition\ speimen} \times 100. \quad (6)$$

A total of 24 samples were employed in this study for both neat and nanomodified asphalt. The moisture susceptibility of a combination, as defined by AASHTO M 320-2002, was regarded as satisfactory if its TSR value was equal to or higher than 80 %.

5.3 IDT testing result

The results of the Resilient modulus test between the nanomodified HMA mixture and the neat asphalt mixes are compared in this section. Three duplicates were conducted at different temperatures. Table 8 displays the peak load, Poisson ratio, maximum horizontal deformation, and moduli value for both mixtures. Nanomodified asphalt enhances the moduli values, exhibiting a consistent upward trend. The addition of nanoparticles in asphalt, specifically NCC, results in a higher modulus value compared to the neat asphalt. The NCC has been found to increase the modulus Mr value at temperatures of 15, 25, and 40 °C by 11.2 %, 16.6 %, and 8.0 % respectively. At 5 °C, there is a slight effect of 4 %.

The NCC has a positive impact on these Mr value. This is because the nanoparticles have a large specific surface area, which enhances viscosity, adhesion, and strength, ultimately improving the modulus value at higher and intermediate temperatures. Figure 14 illustrates the disparity in Mr values between the neat and 5 % NCC modified asphalt at different temperatures.

The inclusion of 5 % NCC has had a significant effect on the moduli value, particularly at temperatures of 25 and 40 °C. This is because nanomaterials possess distinct features that increase viscosity and result in stiffer HMA mixes. These factors likely contribute to the observed improvement in Mr characteristics. To summarize, the aforementioned improvements led to increased Mr values, which are displayed in Table 8.

This suggests that adding 5 % nanomodified asphalt to the mixtures improved their ability to withstand stress and strain, while also reducing the non-linear behavior of the HMA mixtures. The decrease in non-linearity further reinforces the resilience of flexible pavements against permanent deformation.

The creep compliance quantifies the correlation

***Table 8** Mr value, load, Poisson, and horizontal deformation of neat and nanomodified*

Temp. °C	Item	Peak load, N	Deformation, (µm)	*Poisson,* V	Mr, MPa
5	Neat	2257	19.08	0.260	15223
	5% NCC	2143	18.87	0.259	15862
15	Neat	1875	27.89	0.297	9670
	5% NCC	2019	26.16	0.292	10889
25	Neat	1461	36.58	0.361	5362
	5% NCC	1548	34.58	0.348	6430
40	Neat	555	75.00	0.405	1199
	5% NCC	578	73.08	0.389	1303

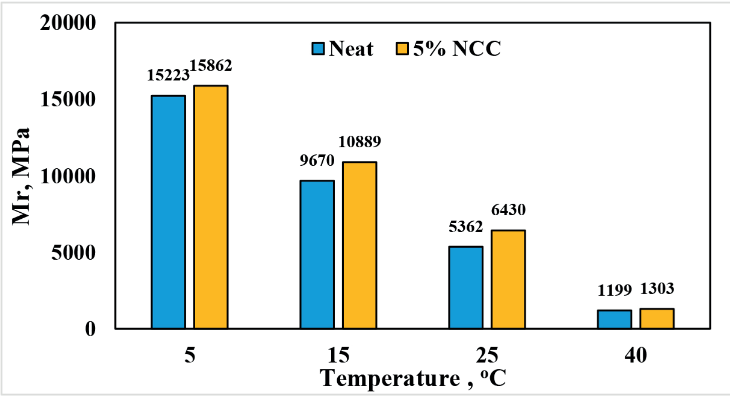

***Figure 14** Effect of NCC nanomodified asphalt on Mr at varying temperatures*

***Table 9** IDT Creep test parameter*

Type	Temp, (°C)	D_1 (1/GPa)	m-value	D(t), (1/GPa)
Neat	5	0.0823	0.475	0.587
	15	0.286	0.546	3.63
	25	0.448	0.625	7.96
	40	0.6304	0.704	16.57
5% NCC	5	0.079	0.465	0.551
	15	0.353	0.515	3.46
	25	0.436	0.617	7.76
	40	0.598	0.680	14.32

between the tension and the strain that occurs over time. Assessing the extent of damage that has occurred in HMA is of the utmost importance. The experimental research conducted in [23] suggests that the creep strain rate is primarily governed by the two crucial parameters: the m-value and the D_1 value. There is a clear difference between these two concepts. The m-value controls the pace at which the creep strain occurs in the long-term section of the creep compliance curve, whereas the D_1 value mainly affects the early portion. The m-value is more significant in terms of the rate at which irrecoverable strain accumulates. Conversely, a drop in the m-value indicates a decrease in the amount of accumulated damage. The utilization of the power law was employed to demonstrate the creep compliance fitting for both neat and NCC nanomodified asphalt. Enhancing the creep performance of HMA mixture is achieved through the utilization of nanomaterial to modify the asphalt binder.

The addition of nanoparticles to asphalt resulted in increased flexibility at lower testing temperatures of 5 and 15 °C, as well as altered creep values at intermediate and higher temperatures of 25 and 40 °C. These changes are anticipated to improve the resistance of HMA mixtures to rutting and thermal cracking. Furthermore, they provide a dependable validation of the results obtained in previous research studies carried out by [24-25]. Figure 15 illustrates a comparison of the data presented in Table 9. The creep parameters, specifically the m-value and D1, of nanomodified asphalt mixes are lower than those of mixtures containing the neat binder. The addition of NCC resulted in a modest drop in the D_1 and m-value compared to the plain mixture. This can be due to the reduced deformation of

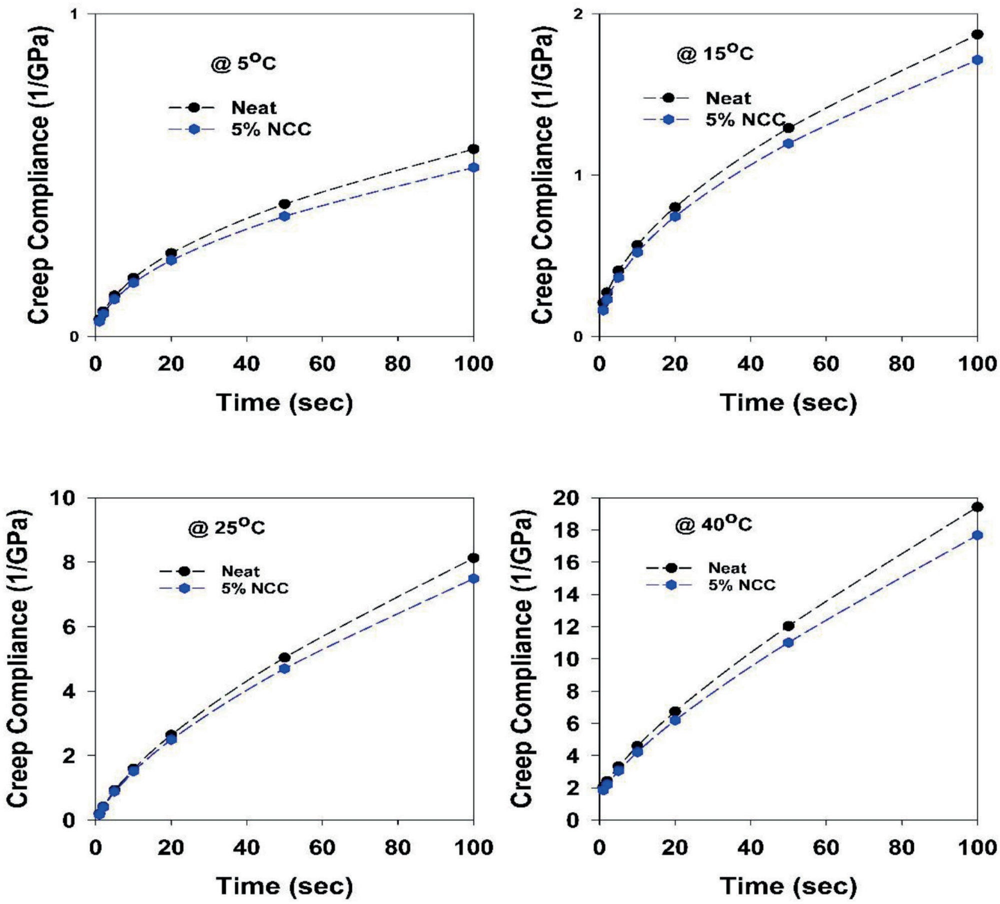

Figure 15 *Effect of NCC nanomodified asphalt on creep at varying temperatures*

the nano modified mixes, which is corroborated by the stiffening effect of NCC.

The tensile stress exhibits the anticipated trends, indicating that the strength value diminishes as the temperature increases. At lower temperatures of 5 and 15 °C, the ratings for all the mixtures show an increase in TS value for NS and NT modified mixtures. However, there appears to be little variation in NCC, which corresponds to neat asphalt. Conversely, the thermal susceptibility (TS) value of nanomodified mixes is greater than that of neat HMA mixtures at temperatures ranging from 25 to 40 °C. This suggests that the addition of 5 % nanomodified asphalt positively affects the strength of HMA at higher temperatures.

The NCC-modified HMA mixture had a greater TS value compared to the neat HMA mixture at lower temperatures of 5 and 15 °C. The behavior is expected to vary as a result of the temperature sensitivity of the NCC mixture. This sensitivity causes the viscosity of the asphalt binder to rise, which in turn enhances the tensile strengths of HMA by 12 % at 25 °C and 22 % at 40 °C. Nevertheless, FS exhibits a consistent upward tendency of no more than 9 % across all the temperatures for the plain mixture. Based on the previous investigation, the use of nanomodified asphalt binder has the potential to improve the tensile strength and failure strain as compared to neat asphalt.

This improvement is particularly significant at temperatures of 25 and 40 °C, with even greater enhancement observed at lower temperatures. As a result, this would lead to an increase in the fracture energy value, enabling HMA mixtures to absorb a greater amount of energy. The improved energy dissipation capacity of HMA mixtures will boost their resistance to fatigue and fracture failure, hence leading to a prolonged lifespan of asphalt pavements. Conversely, the changed mixture showed significant improvement at lower temperatures, while its influence was less pronounced at mid to higher temperatures compared to the neat asphalt. Figure 16 and Table 10 present a comparison of the TS and FS values for both neat and nanomodified asphalt.

5.4 Moisture damage

Pavements that are consistently exposed to water might lead to premature moisture damage. Moisture damage, indicated by the reduction in the bonding strength between the aggregate and asphalt binder when water is present, is a significant issue that affects asphalt pavements. Figure 17 demonstrates that the ITS

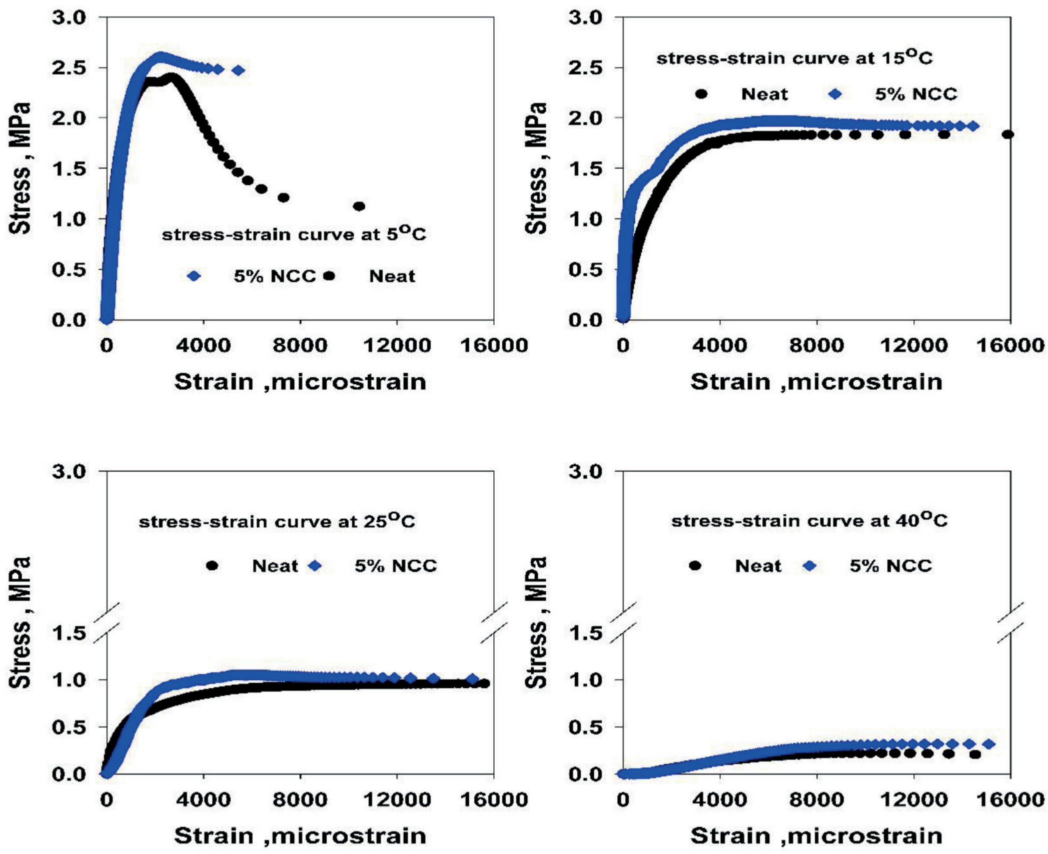

Figure 16 *Effect of NCC nanomodified asphalt on Tensile Strength at varying temperatures*

Table 10 *TS and FS value for neat and nanomodified asphalt at varying temperature*

		Neat		
Temp, °C	5	15	25	40
TS, (MPa)	2.35	1.79	0.92	0.21
FS (10^3 micro)	1.66	4.51	7.06	10.78
		5% NCC		
Temp, °C	5	15	25	40
TS, (MPa)	2.47	1.84	1.04	0.26
FS (10^3 micro)	1.84	4.92	7.54	11.16

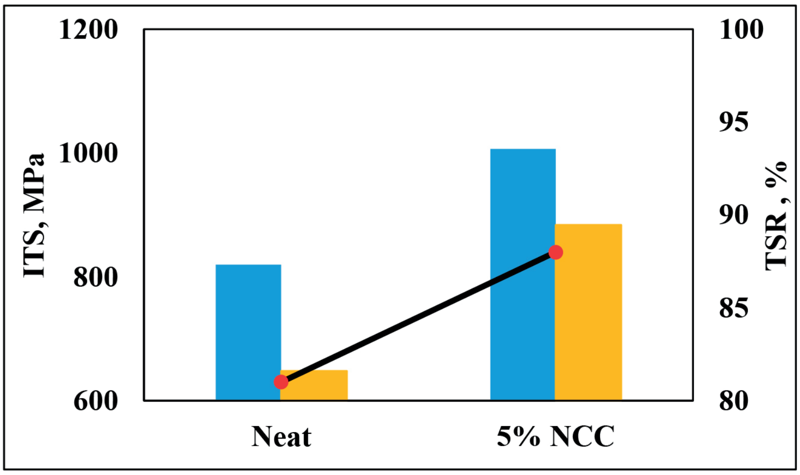

Figure 17 *TSR and ITS result for neat and NCC nanomodified asphalt*

and TSR values of HMA for condition and un-condition samples. The predictability of this result arises from the fact that water reduces the cohesive force between the aggregate and asphalt binder. As a result, conditioned samples show decreased resistance when subjected to loading. Therefore, all of the testing results met the parameters specified by AASHTO T283 for a minimum of 80 % TSR.

The influence of nanomaterial on the ITS and TSR of the HMA combination is more significant compared to neat asphalt. As anticipated, the NCC modified mixes exhibited improved ITS values compared to neat asphalt. The ITS values of conditioned and unconditioned samples have been modified by 5 % using the NCC. Unconditioned and conditioned mixtures led to a 19 % and 27 % enhancement in ITS values, respectively, when compared to asphalt. This phenomenon occurs as a result of the beneficial impact of NCC particles, which increases the stiffness of the asphalt. Consequently, the HMA mixture samples exhibit improved resistance to damage caused by moisture.

As a result, the TSR values experienced a substantial increase to 88 % as compared to the original asphalt. Moreover, this enhancement can be attributed to the fact that NCC modified asphalt has formed a strong connection with the aggregate due to the presence of extremely minimal dispersion forces. Due to the presence of a "polar surface," most aggregates have an electrical charge that largely attracts the lower active polarity of asphalt binder, which is composed mainly of high molecular weight hydrocarbons. Therefore, the NCC mitigates the moisture-induced harm in HMA by improving the bond between asphalt and aggregate and creating a robust nano network structure, as stated in reference [6].

It is important to mention that earlier research [3, 4, 23, 25] have reached a consensus on NCC contribution to moisture damage. Overall, the incorporation of nanomodified into asphalt has resulted in increased tensile stress resistance, greater adhesion within the asphalt matrix, enhanced resistance to water intrusions into HMA mixes and improved TSR value. The greater effect was demonstrated by NCC, which resulted in a TSR increase of up to 88 %, compared to neat asphalt with 81 %. Demonstrating the function of these nanoparticles as additives that prevent or reduce damage caused by moisture to some level, based on the specific surface area of these nanomaterials and the increased stiffness they provide to asphalt binder.

6 Conclusion

The conclusions drawn from this study are as follows:

1. The incorporation of 5 % NCC content had the most significant impact on the characteristics of the asphalt. This led to a decrease in its sensitivity to temperature due to the stiffening of the asphalt within the specified penetration grade. Additionally, it improved the resistance to permanent deformation, as indicated by higher values of softening point and penetration index. Furthermore, it enhanced the ability of the asphalt to withstand low-temperature cracking by reducing its ductility.
2. Asphalt viscosity increases by 43 %, hence improving the performance of the asphalt binders at high temperatures.
3. The DSR test findings showed that the rutting factor value in the RTFO test was observed while using 5 % NCC as an additive. This resulted in a better $G^*/\sin\delta$ value of 3.49 kPa compared to neat asphalt, which maintained a value of 1.68 kPa.
4. The BBR testing result indicated that the NCC had minor effect at low temperatures.
5. Nanomodified asphalt mixture exhibits a substantial increase in moduli value compared to the neat mixture, with enhancements of approximately 4 %, 11.2 %, 16.6 %, and 8.0 % for NCC at temperatures ranging from 5 to 40 °C, furthermore affected the creep, tensile stain and strength at moderate to high temperatures.
6. Nanomodified asphalt mixtures with 5 % NCC present the higher TSR value up to 88 % leading to prevent and reduce damage caused by moisture.

Acknowledgment

The authors received no financial support for the research, authorship and/or publication of this article.

Conflicts of interest

The authors declare that they have no known competing financial interests or personal relationships that could have appeared to influence the work reported in this paper.

References

[1] BATUECAS, E., LIENDO, F., TOMMASI, T., BENSAID, S., F. DEORSOLA, A., FINO D. Recycling CO2 from flue gas for CaCO3 nanoparticles production as cement filler: a life cycle assessment. *Journal of CO2 Utilization* [online]. 2021, **45**, 101446. eISSN 2212-9839. Available from: https://doi.org/10.1016/j.jcou.2021.101446

[2] POUDYAL, L., ADHIKARI, K., WON, M. Nano calcium carbonate (CaCO3) as a reliable, durable, and environment-friendly alternative to diminishing fly ash. *Materials* [online]. 2021, **14**(13), 3729. eISSN 1996-1944. Available from: https://doi.org/10.3390/ma14133729

[3] HAO, X. H., ZHANG, A. Q., YANG, W. Study on the performance of nano calcium carbonate modified asphalt concrete AC-13. *Advanced Materials Research* [online]. 2012, **450-451**, p. 503-507. ISSN 1662-8985. Available from: https://doi.org/10.4028/www.scientific.net/AMR.450-451.503

[4] RAUFI, H., TOPAL, A., KAYA, D., SENGOZ, B. Performance evaluation of nano-CaCO3 modified bitumen in hot mix asphalt. In: 18th IRF World Road Meeting 2017: proceedings. 2017. p. 14-17.

[5] MOHAMMED, A. M., ABED A. H. Enhancing asphalt binder performance through nano-SiO2 and nano-CaCO3 additives: rheological and physical insights. *Case Studies in Construction Materials* [online]. 2023, **19**, e02492. eISSN 2214-5095. Available from: https://doi.org/10.1016/j.cscm.2023.e02492

[6] MOHAMMED, A. M., ABED, A. Improving local asphalt pavement with nano-CaCO3. *E3S Web of Conferences* [online]. 2023, **427**, 3020. eISSN 2267-1242. Available from: https://doi.org/10.1051/e3sconf/202342703020

[7] ALBAYATI, A. H., WANG, Y., AL-ANI, A. F. Enhancing asphaltic mixtures with calcined nano montmorillonite: a performance assessment. *Case Studies in Construction Materials* [online]. 2024, **20**, e02713. eISSN 2214-5095. Available from: https://doi.org/10.1016/j.cscm.2023.e02713

[8] ZHANG, L., GAO, X., WANG, W., WANG, H., ZHENG, K. Laboratory evaluation of rheological properties of asphalt binder modified by nano-TiO2/CaCO3. *Advances in Materials Science and Engineering* [online]. 2021, **2021**(1), 5522025. ISSN 1687-8434, eISSN 1687-8442. Available from: https://doi.org/10.1155/2021/5522025

[9] XING, X., PEI, J., SHEN, CH., LI, R., ZHANG, J., HUANG, J., HU, D. Performance and reinforcement mechanism of modified asphalt binders with nano-particles, whiskers, and fibers. *Applied Sciences* [online]. 2019, **9**(15), 2995. eISSN 2076-3417. Available from: https://doi.org/10.3390/app9152995

[10] MOGHADAS NEJAD, F., GERAEE, E., AZARHOOSH, A. R. The effect of nano calcium carbonate on the dynamic behaviour of asphalt concrete mixture. *European Journal of Environmental and Civil Engineering* [online]. 2020, **24**(8), p. 1219-1228. ISSN 1964-8189, eISSN 2116-7214. Available from: https://doi.org/10.1080/19648189.2018.1456486

[11] ZHAI, R., GE, L., LI, Y. The effect of nano-CaCO3/styrene-butadiene rubber (SBR) on fundamental characteristic of hot mix asphalt. *Road Materials and Pavement Design* [online]. 2020, **21**(4), p. 1006-1026. ISSN 1468-0629, eISSN 2164-7402. Available from: https://doi.org/10.1080/14680629.2018.1532924

[12] YARAHMADI, A. M., SHAFABAKHSH, G., ASAKEREH, A. Laboratory investigation of the effect of nano $CaCO_3$ on rutting and fatigue of stone mastic asphalt mixtures. *Construction and Building Materials* [online]. 2022, **317**, 126127. ISSN 0950-0618, eISSN 1879-0526. Available from: https://doi.org/10.1016/j.conbuildmat.2021.126127

[13] LI, Z., GUO, T., CHEN, Y., LIU, Q., CHEN, Y. The properties of nano-CaCO3/nano-ZnO/SBR composite-modified asphalt. *Nanotechnology Reviews* [online]. 2021, **10**(1), p. 1253-1265. ISSN 2191-9097. Available from: https://doi.org/10.1515/ntrev-2021-0082

[14] VASILIEVICI, G., BOMBOS, D., BOMBOS, M., GABOR, R., NICOLAE, C. Asphalt nanocomposite based on calcium carbonate. *Materiale Plastice*. 2013, **50**(3), p. 220-224. ISSN 0025-5289, eISSN 2668-8220.

[15] WANG, W., CHENG, Y., TAN, G., LIU, Z., SHI, C. Laboratory investigation on high-and low-temperature performances of asphalt mastics modified by waste oil shale ash. *Journal of Material Cycles and Waste Management* [online]. 2018, **20**, p. 1710-1723. ISSN 1438-4957, eISSN 1611-8227. Available from: https://doi.org/10.1007/s10163-018-0737-2

[16] SENGOZ, B., ISIKYAKAR, G. Analysis of styrene-butadiene-styrene polymer modified bitumen using fluorescent microscopy and conventional test methods. *Journal of Hazardous Materials* [online]. 2008, **150**(2), p. 424-432. ISSN 0304-3894, eISSN 1873-3336. Available from: https://doi.org/10.1016/j.jhazmat.2007.04.122

[17] MOHAMMED, A. M., ABED, A. H. Rutting and fatigue behavior of neat and nanomodified asphalt mixture with SiO2 and TiO2. *Alexandria Engineering Journal* [online]. 2024, **109**, p. 994-1009. ISSN 1110-0168, eISSN 2090-2670. Available from: https://doi.org/10.1016/j.aej.2024.09.083

[18] ALBAYATI, A. H., AL-KHEETAN, M. J., MOUDHAFAR, M. M., MOHAMMED, A. M. Nanomaterials in asphalt cement: exploring their single and combined effects on the physical and rheological properties. *Results in Engineering* [online]. 2024, **24**, 103225. eISSN 2590-1230. Available from: https://doi.org/10.1016/j.rineng.2024.103225

[19] YAO, H., YOU, Z., LI, L., LEE, CH. H., WINGARD, D., YAP, Y. K., SHI, X., GOH, S. W. Rheological properties and chemical bonding of asphalt modified with nanosilica. *Journal of Materials in Civil Engineering* [online]. 2013, **25**(11), p. 1619-1630. ISSN 0899-1561, eISSN 1943-5533. Available from: https://doi.org/10.1061/(ASCE)MT.1943-5533.0000690

[20] BUTTLAR, W. G., ROQUE, R. Development and evaluation of the strategic highway research program measurement and analysis system for indirect tensile testing at low temperatures. *Transportation Research Record*. 1994, **1454**, p. 163-171. ISSN 0361-1981.

[21] ROQUE, R., BIRGISSON, B., TIA, M., KIM, B., CUI, Z. Guidelines for use of modifiers in superpave mixtures: executive summary and volume 1 of 3 volumes: evaluation of SBS modifier. Gainesville: University of Florida, 2004.

[22] ROQUE, R., BUTTLAR, W. G. The development of a measurement and analysis system to accurately determine asphalt concrete properties using the indirect tensile mode (with discussion). *Journal of the Association of Asphalt Paving Technologists*. 1992, **61**. ISSN 0270-2932.

[23] CAO, Y., LIU, Z., SONG, W. Performance and overall evaluation of nano-alumina-modified asphalt mixture. *Nanotechnology Reviews* [online]. 2022, **11**(1), p. 2891-2902. ISSN 2191-9097. Available from: https://doi.org/10.1515/ntrev-2022-0485

[24] ZANGENA, S. A. Performance of asphalt mixture with nanoparticles. In: *Nanotechnology in eco-efficient construction*. PACHECO-TORGAL, F., DIAMANTI, M. V., NAZARI, A., GRANQVIST, C. G., PRUNA, A., AMIRKHANIAN, S. (Eds.). Elsevier, 2019. ISBN 978-0-08-102641-0, p. 165-186.

[25] ALBAYATI, A. H., AL-ANI, A. F., BYZYKA, J., AL-KHEETAN, M., RAHMAN, M. Enhancing asphalt performance and its long-term sustainability with nano calcium carbonate and nano hydrated lime. *Sustainability* [online]. 2024, **16**(4), 1507. eISSN 2071-1050. Available from: https://doi.org/10.3390/su16041507

OBSERVATIONAL STUDY OF PEDESTRIAN BEHAVIOR AT SIGNALIZED CROSSWALKS

Damian Frej

Department of Automotive Engineering and Transport, Kielce University of Technology, Kielce, Poland

*E-mail of corresponding author: dfrej@tu.kielce.pl

Damian Frej 0000-0003-1899-4712

Resume

The pedestrian behavior at five signalized crosswalks in Kielce, was analyzed in this study with a particular focus on the increasing use of mobile phones and other electronic devices while crossing the street. Compared to previous ITS studies, which showed that 7% of pedestrians used phones, the current study reveals a significant increase in this phenomenon, with percentages ranging from 14 to 60%. The highest levels of phone usage and risky behaviors were observed at the intersection of Aleja Solidarnosci and Swietokrzyska Street. The results also indicate a decrease in the number of cases of crossing on a red light but an increase in the number of pedestrians crossing during the flashing green signal. The study results point to the need for targeted educational campaigns and the adaptation of infrastructure to address the new challenges associated with mobile device use by pedestrians.

Article info

Received 31 August 2024
Accepted 7 November 2024
Online 13 December 2024

Keywords:

pedestrian behavior
road safety
phones
traffic lights
risky behaviors

Available online: https://doi.org/10.26552/com.C.2025.013

ISSN 1335-4205 (print version)
ISSN 2585-7878 (online version)

1 Introduction

A pedestrian, as a road user, plays a key role in urban dynamics. Pedestrians, who travel without any transportation means, are vulnerable and dependent on both the infrastructure and adherence to traffic rules. Unlike drivers or cyclists, they are completely exposed, making them the most at risk in road traffic [1-3]. Crossing streets is often necessary in cities, highlighting the need for pedestrian-friendly solutions that do not reduce the road capacity [4-5]. Modern urban planning aims to balance the pedestrian safety with transportation efficiency [6-7]. A growing concern is the distraction caused by mobile devices. Studies show that using a phone while crossing significantly increases accident risk by impairing focus and decision-making [8-9].

Pedestrian crossings vary in safety. Collision-prone crossings require more caution, while non-collision crossings, such as overpasses or tunnels, provide the greater safety but may be less convenient [10-12]. Enforcing pedestrian right-of-way is crucial, and in many countries, penalties for violations are strict, helping to improve the compliance. However, pedestrian accidents remain high in Poland due to improper behavior by both drivers and pedestrians [13]. The lack of awareness of the risks, such as using phones or headphones while crossing, exacerbates the problem [14].

Improving pedestrian safety requires both better infrastructure and societal change. Solutions like well-marked crossings, better lighting, and technologies to minimize distractions, such as phone-blocking apps, are vital. In Europe, consistent efforts in education, enforcement, and technology have led to significant accident reductions [15-17]. Examples include smart crossings with pedestrian detection systems, illuminated crosswalks, speed bumps, and safety islands. These innovations, along with the driver alert systems and traffic monitoring cameras, are key to improving safety [18-19].

2 Pedestrian accidents in Poland

Between 2019 and 2023, the number of pedestrians who died as a result of road accidents in the European Union remained relatively high, despite the introduction of new safety measures. In 2019, approximately 3,900 pedestrians died in the EU, and by 2023, this number had decreased slightly to around 3,700, indicating

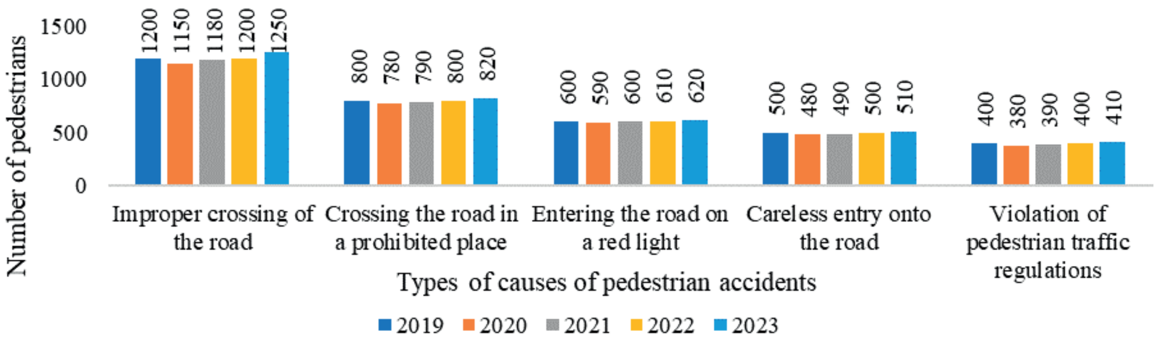

Figure 1 *Statistics of accidents caused by pedestrians in 2019-2023*

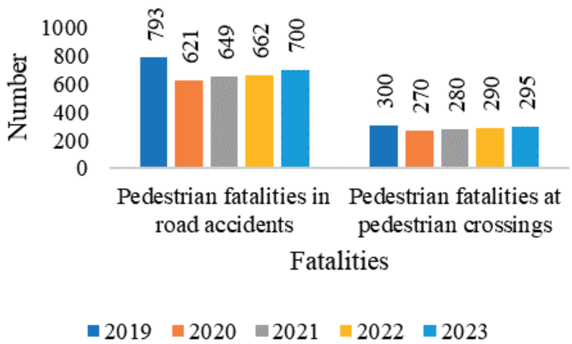

Figure 2 *Pedestrian fatalities in 2019-2023*

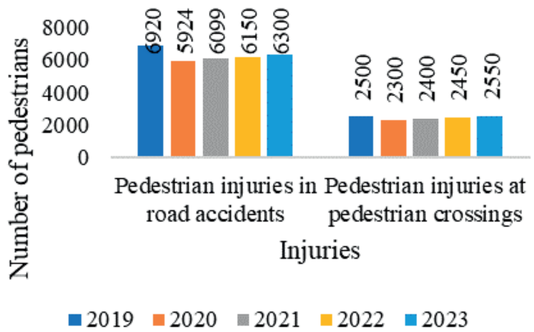

Figure 3 *Number of injured pedestrians in 2019-2023*

a small but noticeable downward trend [20]. The number of pedestrian accidents at crosswalks was around 20,000 in 2019 and decreased to approximately 19,000 by 2023, suggesting that engineering and technical solutions are gradually yielding positive results [21].

In Poland, the pedestrian safety situation is particularly concerning. In 2019, there were 7,549 road accidents involving pedestrians, resulting in 793 deaths and 6,920 injuries. In 2020, despite the pandemic, the number of accidents dropped, but in 2023 it rose again to 7,000, indicating an urgent need for intensified efforts to improve the pedestrian safety at crosswalks [22]. Key issues in Poland include insufficient enforcement of pedestrian right-of-way laws and low driver awareness of the dangers posed by improper behavior near the crosswalks.

An analysis of pedestrian-caused accidents shows that improper road crossing cases decreased in 2020, but rose in subsequent years, reaching 1,250 incidents in 2023 [23]. A similar increase was observed in accidents caused by pedestrians crossing at unauthorized locations and entering the road at red lights [24-25]. The statistics of pedestrian-caused accidents from 2019 to 2023 are presented in Figure 1.

The analysis shows that although there were decreases in pedestrian-caused accidents in some years, the overall trend indicates an increase, especially in cases of improper road crossing, crossing at unauthorized locations, and entering the road on a red light. These trends highlight the need for ongoing education and infrastructure improvements.

Pedestrian fatalities peaked at 793 in 2019, dropped to 621 in 2020 due to COVID-19 traffic reductions, but rose again to 700 by 2023, marking a 5.7% increase [20-21]. Fatalities at crosswalks followed a similar pattern, decreasing from 300 in 2019 to 270 in 2020, and rising to 295 in 2023, a 1.7% increase [22-23].

Pedestrian injuries fell from 6,920 in 2019 to 5,924 in 2020, but rose to 6,300 by 2023, reflecting a 2.4% increase [24]. Injuries at crosswalks also fluctuated, dropping to 2,300 in 2020 but increasing to 2,550 in 2023, a 4.1% rise [25]. Figures 2 and 3 present the numerical data on pedestrian fatalities and injuries from 2019 to 2023.

The data indicate that while the pandemic contributed to a reduction in pedestrian accidents and casualties in 2020-2021, there has been a gradual increase since 2021. The rise in casualties at pedestrian crossings underscores the need for continued road safety education and infrastructure improvements. Pearson correlation analysis (using STATISTICA 13) revealed significant relationships between the pedestrian behavior and accidents. The strongest correlation (0.998) was found between the crossing at unauthorized locations and improper road crossing, suggesting that these behaviors often occur together. A high correlation (0.995) also exists between the pedestrian injuries and fatalities, indicating that an increase in one often accompanies an increase in the other.

Careless road entry and injuries at pedestrian crossings show a correlation of 0.980, highlighting the impact of distractions on accident rates. Violations of pedestrian traffic regulations and unauthorized crossings are similarly correlated (0.976), as is the relationship between careless entry and improper crossing (0.974). These findings suggest that distractions, such as mobile phone use, play a significant role in pedestrian-involved accidents.

However, there is a lack of precise data quantifying pedestrian distractions, such as phone use or listening to music, during accidents. Current road safety data collection methods are insufficient in this area, relying on subjective testimony. Introducing more advanced monitoring technologies, such as street cameras or surveys, could provide better insights into the impact of distraction on pedestrian safety and lead to more effective preventive measures.

3 Methodology

The main objective of the study was to analyze the pedestrian behavior at signaled intersections, with particular emphasis on the impact of the use of mobile devices on their decisions and safety. The study aimed to measure the frequency with which the pedestrians use mobile phones or other electronic devices when crossing the road, and to assess how this behavior affects the overall road safety. The results of the study were to be used as a basis for making recommendations for potential infrastructure improvements and educational initiatives to improve pedestrian safety.

A review of the existing literature revealed that the study lacks a detailed analysis of the impact of mobile use on pedestrian decisions. Most studies to date have focused on pedestrians' general traffic light compliance, but have not taken into account the impact of different types of mobile device use (e.g., holding the phone, talking, active screen use) on their behaviour. In addition, few studies have looked at high-traffic intersections, where pedestrians and drivers have to manage limited time and space, further complicating safety issues. The increasing number of accidents involving pedestrians using mobile devices highlights the urgent need to understand these behaviors and identify the factors that influence pedestrian decisions. The aim of this study was to fill this gap and provide practical information for improving road safety policies and adapting infrastructure to changing pedestrian behaviour.

3.1 Location and context of the study

Five high-traffic intersections, representing commercial, educational and residential areas, were selected for the study, which allowed the analysis of pedestrian behaviour in different contexts. Each intersection was equipped with traffic lights, which made it possible to analyse the pedestrian behaviour according to the different phases of the traffic lights.

3.2 Observation procedure

The observations were carried out by a team of nine researchers who were divided into three groups. Two groups were on opposite sides of each crossing, recording pedestrian behavior, with a focus on mobile device use and traffic light response. The third group documented the length of traffic light phases and the pedestrian crossing time. Each crossing was observed through 51 signaling cycles, with sessions running on different days and times of the day to ensure comprehensive data collection.

3.3 Data collection tool

A detailed observation checklist (observational questionnaire) was used as a tool to classify the pedestrian behavior according to traffic lights and mobile device use. The checklist included variables such as:

- Traffic light compliance: Entrance to the crossing at a green, flashing green or red light.
- Mobile Usage: A type of interaction with a device, including holding a phone, using headphones, talking on the phone, or actively using a screen.
- Other factors: use of personal transport devices (e.g., bicycles, scooters) and red light cases.

3.4 Data analysis

After the data collection was completed, quantitative and statistical analysis was carried out using the STATISTICA 13 software. The analysis included both quantitative summaries and statistical assessments of factors influencing pedestrian decisions. Particular attention was paid to pedestrians using mobile devices, and the results were compared to the available literature. Pearson correlation analysis was used to detect relationships between behaviours (e.g., crossing red lights and using mobile devices) and demographic variables. These results are expected to form the basis for future actions to improve the road safety.

Although the study provides valuable information on pedestrian behaviour at signalled crossings in Kielce, it is limited to one city, which may affect the generalizability of the results. In addition, direct observation, despite the use of a checklist, could introduce subjectivity of the researchers. Future research could consider using automated monitoring technologies to mitigate the impact of this bias.

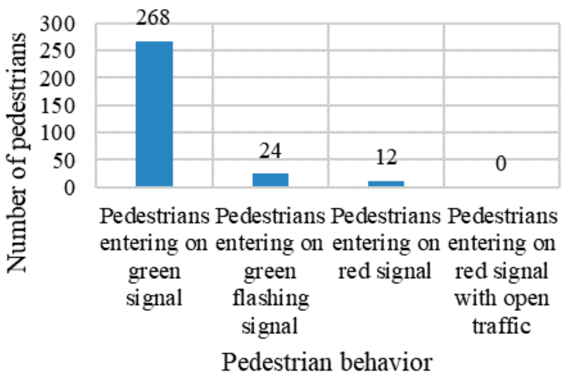

Figure 4 *Number of pedestrians who used the crossing at the intersection of Warszawska Street and Aleja Tysiaclecia Panstwa Polskiego during 51 cycles*

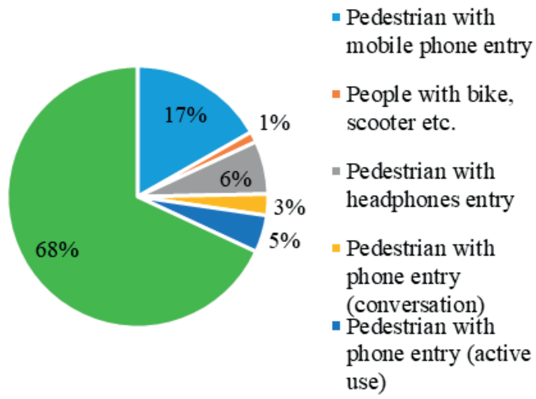

Figure 5 *Pedestrian behaviour at the intersection of Warszawska Street and Aleja Tysiaclecia Panstwa Polskiego during 51 cycles*

4 Observational studies of pedestrians

A significant gap in the literature on the impact of various forms of mobile device use (e.g., talking on the phone, active use of the screen) on pedestrian behaviour was addressed in this study. Most previous studies have focused only on pedestrians' compliance with traffic lights, without a detailed analysis of the impact that different types of mobile device use have on decision-making. Additionally, previous studies have rarely looked at the context of high-traffic intersections, where limited time and space increase the risk of collisions. The results of this study are expected to provide practical guidelines for improving the road infrastructure and shaping pedestrian safety policy. The ability to identify the riskiest pedestrian behaviors related to the use of mobile devices allows for the design of more precise educational and infrastructural activities. As a result, the recommendations resulting from this study could contribute to development of preventive measures that will effectively reduce the number of accidents involving pedestrians, supporting the creation of more friendly and safer urban spaces.

4.1 Pedestrian crossing at the intersection of Warszawska Street and Aleja Tysiaclecia Panstwa Polskiego

The first examined site, is a signalized pedestrian crossing located at the intersection of Warszawska Street and Aleja Tysiaclecia Panstwa Polskiego. This intersection is a significant part of the road network in the city of Kielce. In the immediate vicinity of the studied site, there is a university, numerous service points, shops, and public transport stops, which generate significant pedestrian traffic across various age groups. The study at this intersection was conducted on March 13, 2023. During 51 signal cycles, 304 people used the crossing, of which 268 began crossing on a green signal, 24 entered on a flashing green signal, and 12 started crossing on a red signal with closed vehicle traffic. None of the pedestrians began crossing on a red signal with open vehicle traffic.

The data collected from the intersection of Warszawska Street and Aleja Tysiaclecia Panstwa Polskiego during 51 signal cycles are presented in Figure 4, which shows the number of pedestrians using the crossing. In addition, Figure 5 illustrates pedestrian behavior at the same intersection, detailing how they responded to traffic signals and their use of mobile devices. These figures provide a comprehensive overview of pedestrian activity and highlight the key behavioral patterns observed during the study.

The data presented in Figure 4 shows that among all the pedestrians using the crossing during the study, 68% did not use any additional devices such as headphones or mobile phones. It was recorded that 51 pedestrians had a phone, 20 people were using headphones, 8 people were talking on the phone, and 14 people were actively using a phone while crossing the street. Additionally, only 4 pedestrians with a bicycle or scooter used the crossing during the study. The average duration of the green signal, based on 20 measurements, was 22.43 seconds, while the average duration of the red signal was 76.65 seconds. The average time it took for a pedestrian to cross the street was 23.43 seconds. It is important to note that the duration of the green signal is shorter than the average time needed to cross the pedestrian crossing, which may impact the pedestrian safety.

Based on the data presented in Figure 5, it is evident that among all the pedestrians who used the crossing, 68% (or 207 people) did not use any additional devices such as headphones or mobile phones. At the same time, 17% of pedestrians (52 people) used a mobile phone while crossing, and 6% (18 people) were using headphones. Additionally, 5% of pedestrians (15 people) were engaged in a phone conversation, and 3% (9 people) were actively using their phone, such as looking at the screen, while crossing the street. It is also noteworthy that only 1% of pedestrians (4 people) used the crossing with a bicycle, scooter, or similar means of transport. These data indicate that while the majority of pedestrians avoid using electronic devices while crossing the street, a significant portion is still distracted by various devices, which may affect their safety.

4.2 Pedestrian crossing at the intersection of Swietokrzyska Street and Warszawska Street

The next examined site, is a signalized pedestrian crossing located at the intersection of Swietokrzyska Street and Warszawska Street. This intersection is characterized by high vehicle traffic, primarily due to transit traffic heading toward the S74 expressway. The increased pedestrian traffic in this area is associated with the nearby high school, shopping mall, and other facilities that generate high foot traffic among various age groups. The study at this intersection was conducted on May 22, 2023.

During the 51 signal cycles at the analyzed crossing, 326 people used the crossing. Among them, 288 started crossing on a green signal, 29 on a flashing green signal, and 9 decided to cross on a red signal with vehicle traffic stopped. The analysis of pedestrian activity at the intersection of Swietokrzyska Street and Warszawska Street over 51 signal cycles is depicted in Figure 6, which shows the number of pedestrians using the crossing. Figure 7 provides further insights into pedestrian behavior at this intersection, detailing how they interacted with traffic signals and the extent of mobile device use. These figures illustrate key patterns and behaviors observed during the study at this location.

Detailed data on this is presented in Figure 6. It is noteworthy that none of the pedestrians attempted to cross on a red signal with open vehicle traffic, indicating an awareness of the risks associated with such behavior. It should also be noted that the average duration of the green signal, based on 20 measurements, is 36.92 seconds. The average duration of the red signal is 62.80 seconds. The average time it took for a pedestrian to cross the pedestrian crossing was 19.29 seconds. It is also important to note that in this case, the duration of the green signal is longer than the average time needed for a pedestrian to cross.

Based on the data presented in Figure 7 it is evident that among all the pedestrians who used the crossing during the study, 41% (or 134 people) did not use any additional devices such as headphones or mobile phones. On the other hand, 13% of pedestrians (42 people) used a mobile phone, 10% (32 people) were using headphones, 4% (12 people) were engaged in a phone conversation, and 2% (7 people) were actively using their phone, such as looking at the screen, while crossing the street. Additionally, as many as 30% of pedestrians (98 people) used the crossing with a bicycle, scooter, or other similar means of transport. These data highlight that a significant portion of pedestrians are still distracted by various devices or use alternative means of transport, which may affect their safety at the crossing.

4.3 Pedestrian crossing at the intersection of Warszawska Street and Swietokrzyska Street

The third test was carried out at the crossing located at the intersection of Warszawska and Swietokrzyska streets., A significant intensity of both vehicular and pedestrian traffic, especially during the rush hours, was observed in this case, the same as for the previous research facility.. The survey took place on May 22, 2023. During the 51 signal cycles, 326 people used the crossing. Among them, 225 started crossing on a green signal, 4 entered the crossing on a flashing green signal, and 2 attempted to cross on a red signal, but with vehicle traffic stopped. It is noteworthy that none of the pedestrians attempted to cross on a red signal with open vehicle traffic, which may indicate a high level of awareness among pedestrians regarding

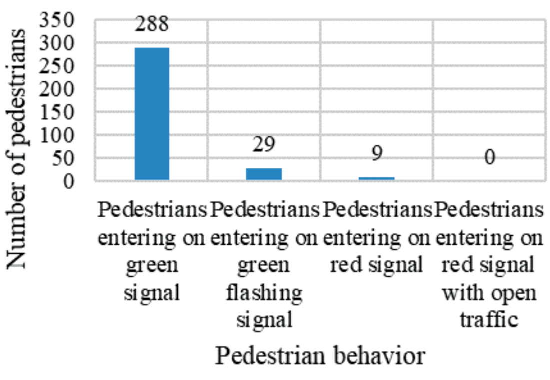

Figure 6 *Number of pedestrians who used the crossing at the intersection of Swietokrzyska Street and Warszawska Street during 51 cycles*

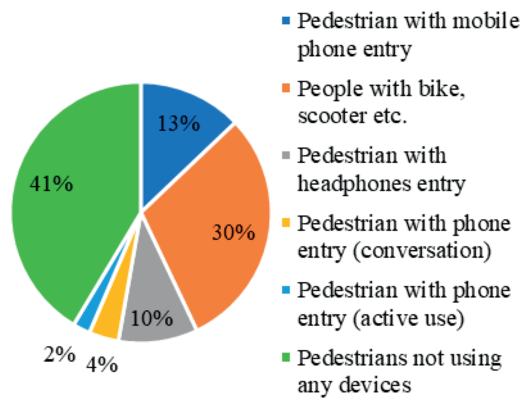

Figure 7 *Behaviour of pedestrians at the intersection of Swietokrzyska Street and Warszawska Street during 51 cycles*

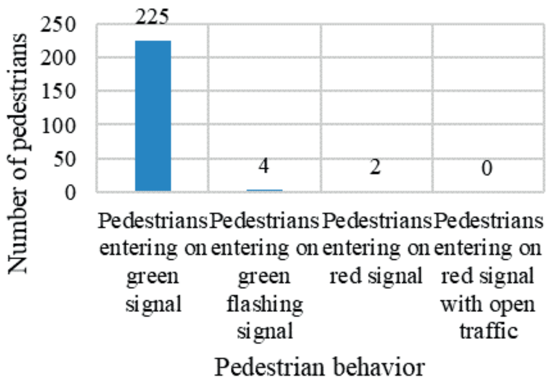

Figure 8 *Number of pedestrians who used the crossing at the intersection of Warszawska Street and Swietokrzyska Street during 51 cycles*

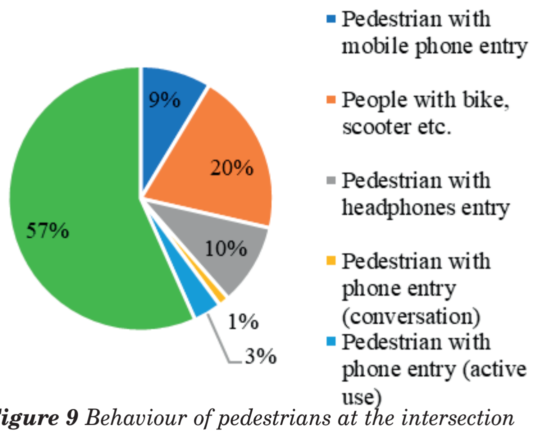

Figure 9 *Behaviour of pedestrians at the intersection of Warszawska Street and Swietokrzyska Street during 51 cycles*

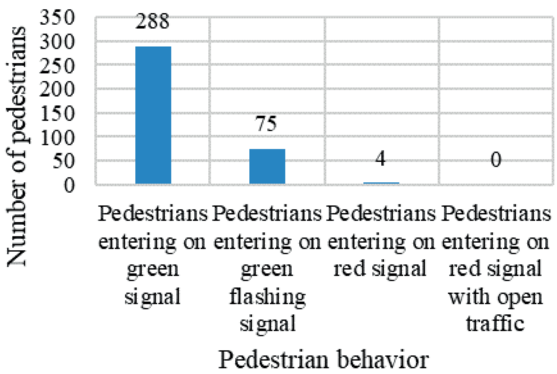

Figure 10 *Number of pedestrians who used the crossing at the intersection of Swietokrzyska Street and Solidarnosci Avenue during 51 cycles*

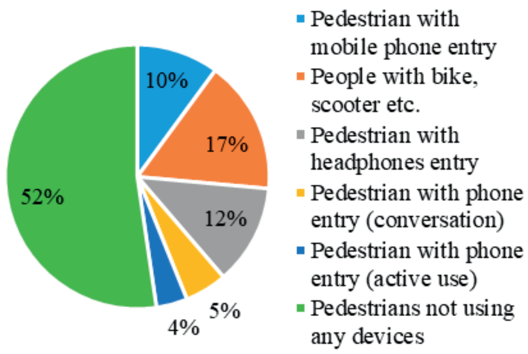

Figure 11 *Behaviour of pedestrians at the intersection of Swietokrzyska Street and Solidarnosci Avenue during 51 cycles*

the road safety rules. Figure 8 presents the number of pedestrians using the crossing at the intersection of Warszawska Street and Swietokrzyska Street during 51 signal cycles. Figure 9 summarizes pedestrian behavior at this intersection, focusing on their responses to traffic signals and mobile device use. These figures highlight key patterns observed during the study.

It should be noted that the average duration of the green signal, based on 20 measurements, is 30.41 seconds. The average duration of the red signal is 69.24 seconds. The average time it took for a pedestrian to cross the pedestrian crossing was 11.24 seconds. It is also important to note that in this case, the duration of the green signal is longer than the average time needed for a pedestrian to cross.

Based on the data presented in Figure 9, it is evident that among all the people who used the crossing during the study, 57% (or 186 people) did not use any additional devices such as headphones or mobile phones. It is also worth noting that 9% of pedestrians (30 people) used a mobile phone, 10% (33 people) were using headphones, 1% (3 people) were engaged in a phone conversation, and 3% (9 people) were actively using their phone, for example, looking at the screen, while crossing the street. Additionally, 20% of pedestrians (65 people) used the crossing with a bicycle, scooter, or other similar means of transport. These data highlight that while the majority of pedestrians avoid using electronic devices while crossing the street, a significant portion is still distracted or uses alternative means of transport, which may affect their safety.

4.4 Pedestrian crossing at the intersection of Swietokrzyska Street and Solidarnosci Avenue

Another survey was conducted on May 25, 2023 at the intersection of Swietokrzyska Street and Solidarnosci Avenue. This crossing plays a vital role in pedestrian traffic in the area due to its strategic location, proximity to large residential areas and the vicinity of a shopping mall, which attracts significant numbers of pedestrians during the day. During the 51 signal cycles, a total of 367 people crossed the street. The vast majority, 288 pedestrians, used the crossing on a green signal. Meanwhile, 75 people chose to cross during the flashing green signal, which may indicate a sense of urgency or an attempt to save time. Only 4 people took the risk of crossing on a red signal, but only when vehicle traffic was stopped. Importantly, no one attempted to cross on a red signal when vehicle traffic was open, indicating the pedestrians' sense of responsibility in this area.

Figure 10 shows the number of pedestrians using the crossing at the intersection of Swietokrzyska Street and Solidarnosci Avenue during 51 signal cycles. Figure 11 illustrates pedestrian behavior at this intersection, highlighting their responses to traffic signals and use of mobile devices. These figures capture key behavioral trends from the study.

It should be noted that the average duration of the green signal, based on 20 measurements, is 65.30 seconds. The average duration of the red signal is 34.45 seconds. The average time it took for a pedestrian to cross the street was 6.80 seconds. It is also important to note that in this case, the duration of the green signal is longer than the average time needed for a single pedestrian to cross. Based on the data, it is evident that among all the people who used the crossing during the study, 52% (or 191 people) did not use any additional devices such as headphones or mobile phones. However, 10% of pedestrians (37 people) used a mobile phone, 12% (45 people) were using headphones, 4% (14 people) were actively using their phone (for example, looking at the screen), and 5% (19 people) were engaged in a phone conversation while crossing the street. Additionally, 17% of pedestrians (63 people) used the crossing with a bicycle, scooter, or other similar means of transport. These data indicate that while the majority of pedestrians avoid using electronic devices while crossing the road, a significant number of users still engage in activities that may distract them from their surroundings, potentially affecting their safety.

4.5 Pedestrian crossing at the intersection of Solidarnosci Avenue and Swietokrzyska Street

The fifth survey was also carried out on May 25, 2023 and included a pedestrian crossing located at the intersection of Solidarnosci Avenue and Swietokrzyska Street. During the 51 signal cycles, a total of 270 people used the crossing. The vast majority, 261 pedestrians, crossed the street on a green signal. Additionally, 8 people chose to cross during the flashing green signal, which may indicate a sense of urgency or an attempt to save time. Only 1 person attempted to cross on a red signal, but only when vehicle traffic was stopped. It is noteworthy that no one attempted to cross on a red signal with open vehicle traffic, suggesting that pedestrians in this area adhere to safety rules.

Figure 12 presents the number of pedestrians who used the crossing at the intersection of Solidarnosci Avenue and Swietokrzyska Street during 51 signal cycles. Figure 13 highlights pedestrian behavior at this intersection, focusing on their responses to traffic signals and mobile device use. These figures provide key insights into pedestrian activity and behavior observed during the study.

It should be noted that the average duration of the green signal, based on 20 measurements, is 45.64 seconds. The average duration of the red signal is 55.52 seconds. The average time it took for a pedestrian to cross the street was 5.90 seconds. It is also important to note that in this case, the duration of the green signal is longer than the average time needed for a single pedestrian to cross. Based on the data obtained from the study, it is evident that among all the people who used the crossing during the study, 40% (or 108 people) did not use any additional devices such as headphones or mobile phones. On the other hand, 26% of pedestrians (69 people) used a mobile phone, 9% (24 people) were using headphones, 5% (13 people) were engaged in a phone conversation, and 7% (18 people) were actively using their phone, for example, looking at the screen, while crossing the street. Additionally, 13% of pedestrians (36 people) used the crossing with a bicycle, scooter, or other similar means of transport. These data indicate that while a significant portion of pedestrians avoid using electronic devices while crossing the road, a notable number of people still engage in activities that may distract them from their surroundings, potentially affecting their safety.

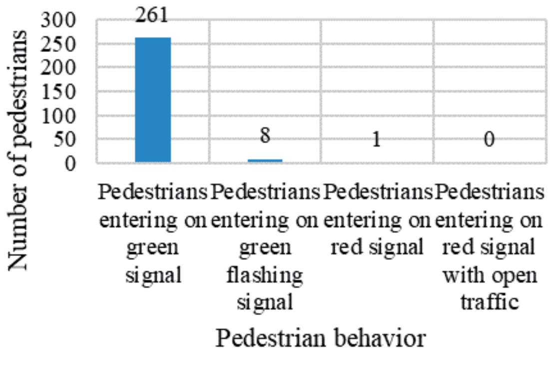

Figure 12 *The number of pedestrians who used the crossing at the intersection of Solidarnosci Avenue and Swietokrzyska Street during 51 cycles*

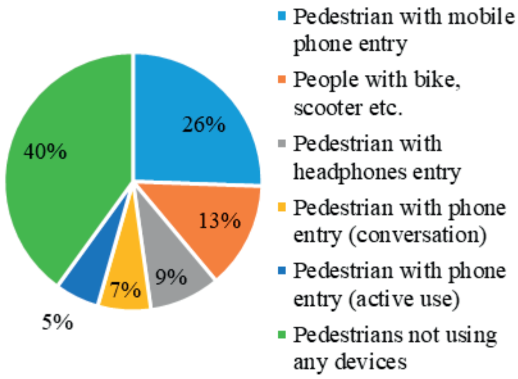

Figure 13 *Behaviour of pedestrians at the intersection of Solidarnosci Avenue and Swietokrzyska Street during 51 cycles*

5 Results of observational studies

The statistical analysis, with a significance level of p = 0.0001 (Table 1), clearly confirms the significant impact of the type of intersection on pedestrian behavior. The study results indicate that at the intersection of Aleja Solidarnosci and Swietokrzyska Street, the highest number of pedestrians used mobile phones - 69 people, accounting for 26% of all pedestrians at this location. This is the highest percentage among all the locations studied. This same intersection also stands out with the highest number of pedestrians actively using their phones 15 people (6%) - and the most people talking on the phone -18 people (7%).

At the intersection of Swietokrzyska and Warszawska Streets, 42 people (15%) were observed using mobile phones, which is also a significant percentage. At this location, 12% of pedestrians used headphones, which is noticeably higher than at other intersections. Conversely, at the intersection of Warszawska and Swietokrzyska Streets, as many as 34% of pedestrians were pushing a bicycle or scooter, the highest percentage of this user group compared to other locations. Additionally, at the intersection of Swietokrzyska Street and Aleja Solidarnosci, 12% of pedestrians used headphones, suggesting greater distraction in this area. This location also recorded the highest percentage of people talking on the phone-5%.

Overall, the analysis of all studied locations reveals that 15% of pedestrians used a mobile phone while crossing. It is also noteworthy that 10% of all pedestrians used headphones, which can significantly limit their ability to respond to their surroundings. One in four pedestrians, or 16% of those surveyed, was pushing a bicycle or scooter, which requires particular attention in the context of road safety.

The most important conclusion from the analysis, however, is that 52% of pedestrians did not use any device that could distract them. This suggests that the majority of pedestrians, despite the widespread availability of mobile devices, try to maintain focus while crossing the road. Nevertheless, the high percentage of pedestrians using mobile devices at certain intersections indicates the need for preventive and educational measures to raise awareness of the risks associated with distraction in road traffic.

The statistical significance coefficient of p = 0.0001 (Table 2), which is lower than the established significance level of 0.05, clearly indicates that the type of intersection has a significant impact on how pedestrians use signalized crosswalks.

The analysis shows that at all the intersections studied, the vast majority of pedestrians crossed the road when the green light was on - 1,330 such instances were recorded, accounting for 89% of all observed situations. The highest percentage of pedestrians adhering to the traffic signal was observed at the intersections of Warszawska Street and Aleja Solidarnosci, where 97% of pedestrians crossed on the green light. Conversely, at the intersection of Swietokrzyska Street and Aleja Solidarnosci, it was noted that 20% of pedestrians (75 people) chose to cross during the flashing green light. This may suggest that pedestrians at this location are inclined to take risks to cross before the light changes to red.

The most instances of crossing on a red light were recorded at the intersection of Warszawska Street and Aleja Tysiaclecia Panstwa Polskiego, where 12 people (4% of all pedestrians at this location) engaged in this risky behavior. This may be due to the short duration of the green light, which could prompt pedestrians to take risks to cross the road more quickly. Importantly,

Table 1 *Summary of pedestrian behaviour at individual intersections*

Crossroads		Pedestrian with a phone	Pedestrian with headphones	Pedestrian with a bike, scooter	Pedestrian talking on the phone	Pedestrian actively using the phone	Pedestrian not using any device
1	n	51	20	4	8	14	207
	%	17	7	1	3	5	68
2	n	42	32	48	12	7	135
	%	15	12	17	4	3	49
3	n	20	23	96	3	8	131
	%	7	8	34	1	3	47
4	n	37	45	60	19	14	192
	%	10	12	16	5	4	52
5	n	69	24	36	18	15	108
	%	26	9	13	7	6	40
Sum	n	219	144	244	60	58	773
	%	15	10	16	4	4	52
Chi-square	χ^2 = 188.06		df = 20			p = 0.0001	

Table 2 Summary of pedestrian behaviour in terms of compliance with traffic lights

Crossroads		Pedestrians entering on green signal	Pedestrians entering on green flashing signal	Pedestrians entering on red signal	Pedestrians entering on red signal with open traffic
1	n	268	24	12	0
	%	88%	8%	4%	0%
2	n	288	29	9	0
	%	88%	9%	3%	0%
3	n	225	4	2	0
	%	97%	2%	1%	0%
4	n	288	75	4	0
	%	78%	20%	1%	0%
5	n	261	8	1	0
	%	97%	3%	0%	0%
Sum	n	1330	140	28	0
	%	89%	9%	2%	0%
Chi-square		χ^2 = 97.501	df=12		p=0.0001

Table 3 Percentage Breakdown of Pedestrian Crossing Behavior, %

Parameter	Crossroads 1	Crossroads 2	Crossroads 3	Crossroads 4	Crossroads 5
Pedestrian with phone	17	15	7	10	26
Pedestrian with headphones	7	12	8	12	9
Pedestrian with bike, scooter	1	17	34	16	13
Pedestrian talking on phone	3	4	1	5	7
Pedestrian actively using phone	5	3	3	4	6
Pedestrian not using any devices	68	49	47	52	40

Table 4 Percentage of pedestrian behaviour in terms of compliance with traffic lights, %

Parameter	Crossroads 1	Crossroads 2	Crossroads 3	Crossroads 4	Crossroads 5
Pedestrians entering on green signal	88	88	97	78	97
Pedestrians entering on green flashing signal	8	9	2	20	3
Pedestrians entering on red signal	4	3	1	1	0
Pedestrians entering on red signal with open traffic	0	0	0	0	0

none of the intersections studied had any cases where pedestrians crossed on a red light with open vehicle traffic, suggesting that pedestrians in Kielce are aware of the dangers associated with such behavior.

The percentage breakdown of pedestrian behavior at crosswalks is presented in Table 3. It is noteworthy that the highest percentage of pedestrians crossing the intersection with a mobile phone in hand was recorded at Intersection 5, where it reached 26%. For pedestrians using headphones, the highest percentage was observed at Intersections 2 and 4, both at 12%. Pedestrians with a bicycle or scooter most frequently crossed at Intersection 3, accounting for 34%. It is important to note that pedestrians using bicycles or scooters made up only 1% of all the pedestrians at Intersection 1. Pedestrians talking on the phone constituted no more than 7% of the total, while those actively using a mobile phone represented no more than 6%. Additionally, it is noteworthy that at Intersection 5, only 40% of all pedestrians observed at the crosswalk were not using any distraction devices.

The percentage breakdown of pedestrian behavior in relation to compliance with the traffic signals is presented in Table 4. It is noteworthy that over 88% of pedestrians crossing at the crosswalks correctly adhered to the traffic signals, crossing only when the green signal was displayed. During the observations, as many as 20% of all the pedestrians at the crosswalk on Intersection 4 entered the crosswalk during the flashing green signal. For the other crosswalks, this percentage did not exceed 9%. In the observational study, none of the pedestrians entered the crosswalk during the red signal with open vehicle traffic. During the study, only at the crosswalk at Intersection 5 did no pedestrians enter during the red signal. At the other crosswalks, the percentage of such incidents ranged from 1 to 4%.

6 Discussion

The results of the conducted studies in Kielce indicate various pedestrian behaviors at different signalized intersections, as clearly confirmed by the statistical significance coefficient of p = 0.0001 (Table 2). This result, which is lower than the accepted significance level of 0.05, suggests a significant impact of the type of intersection on how pedestrians use the crosswalks.

In article [26], the authors analyze a 2018 study on pedestrian safety at crosswalks in Poland, which led to new regulations in 2021 requiring drivers to stop when a pedestrian approaches. The study found that only 45% of drivers yielded to pedestrians at unmarked crossings, while 55% of pedestrians had to wait. Seniors waited longer, and drivers in residential areas were more likely to yield. Risky behaviors like crossing on red lights (7%) and outside crosswalks (8%) were noted, with vehicle speeds often exceeding legal limits, highlighting the need for further safety measures.

Independent research for this study showed a significant rise in pedestrian mobile device use at signalized crosswalks, reaching 14-60% depending on location, with the highest rate at Aleja Solidarnosci and Swietokrzyska in Kielce. The findings underline the need for education and infrastructure changes to reduce risks associated with pedestrian distractions.

In article [27], the authors examine the impact of approaching trams on pedestrian behavior in Wroclaw and Poznan. Pedestrians were more likely to break rules to catch a tram, influencing others to do the same. Predictable traffic signals improved compliance. Similarly, research in Kielce showed traffic intensity influenced risky pedestrian behaviors, with up to 20% crossing during the flashing green lights. In article [28], the authors evaluated behaviors at crosswalks in Poland, identifying factors contributing to pedestrian accidents and proposing infrastructural solutions. Independent research found that 89% of pedestrians in Kielce followed traffic rules, but 15% using phones increased accident risks.

In article [29], a study in Auckland, New Zealand, explored motivations for risky road crossings at undesignated locations, finding habits and attitudes as key factors. Women acted based on personal beliefs, while men were more influenced by peers. Polish research emphasized education on responsible mobile device use, noting distracted pedestrians often took risks like stepping onto the road during the flashing green lights. In article [30], the authors reviewed the eye-tracking studies to understand the pedestrian decision-making during crossings. They highlighted the need for further research on the impact of autonomous vehicles. Polish findings showed that the mobile device use reduced pedestrian attention in 26% of cases at a busy intersection, stressing the importance of education.

In article [31], research in Belgium examined children crossing roads near schools, finding that holding an adult's hand reduced risky behaviors. The study highlights the need for parental education and infrastructural changes like raised crosswalks. Polish research linked mobile device use to decreased attention, especially in younger pedestrians. In article [32], the authors analyzed the pedestrian phone use at signalized intersections, showing that it leads to reduced awareness, slower walking speeds, and risky behaviors. Independent research in Kielce confirmed a rise in phone use, with 26% of pedestrians distracted at the busiest intersections, emphasizing the need for educational initiatives and technological solutions to improve safety.

7 Conclusion

The studies conducted in 2023 at five pedestrian crossings in Kielce showed a significant increase in the number of pedestrians using mobile phones and other electronic devices while crossing the street. Compared to earlier studies conducted by ITS, where the percentage of pedestrians using phones was 7%, the current studies revealed a dramatic increase in this phenomenon. At some crossings, the percentage of pedestrians engaging in risky behaviors related to mobile device use ranged from 14% to as high as 60%, representing a two- to nine-fold increase. This high percentage can be attributed to the growing popularity of smartphones and associated devices such as wireless headphones.

A key finding from the studies is that at the intersection of Aleja Solidarnosci and Swietokrzyska Street, the highest percentage of pedestrians using mobile phones (69 people) and actively using phones while crossing the street (15 people) was recorded. At the intersection of Warszawska Street and Aleja Tysiaclecia Panstwa Polskiego, 12 instances of crossing on a red light were observed, which may be related to the short duration of the green light relative to the time needed to cross the intersection. The analysis results indicate that pedestrians using mobile phones often enter the crossing without proper attention, which can lead to dangerous situations on the road. This phenomenon is consistent with previous studies, which suggest that mobile device use significantly impairs the ability to accurately assess the road conditions.

It is also noteworthy that, compared to previous ITS studies, the percentage of red-light crossings has decreased from 7% to a range of 0.3 to 4%. This indicates a greater awareness of the dangers associated with crossing on a red light. However, there has been an increase in the number of pedestrians entering the crossing during the flashing green signal, often ending up on a red light. This behavior pattern was observed in 2 to 26% of pedestrians, highlighting the need to continue educational efforts to raise pedestrian awareness.

A new aspect studied in 2023 was the percentage of pedestrians using bicycles, electric scooters, or other personal transport devices while crossing, which ranged from 13% to 30%. Previous ITS studies did not include this aspect, underscoring the need to consider new forms of mobility in the road safety improvement strategies.

Based on the analysis of data from 2020-2023, it was found that the number of pedestrian-involved accidents in Poland has decreased, but the percentage of incidents involving pedestrians stepping onto crosswalks remains stable at around 19-20%. Despite the overall improvement, the issue of inappropriate pedestrian behavior, including mobile phone use, remains a significant challenge. The increase in risky pedestrian behaviors can be partially attributed to the psychological effects of extending pedestrian priority, which may lead to a false sense of security.

Therefore, there is an urgent need to strengthen educational efforts aimed at pedestrians, emphasizing their responsibility for their own safety, especially in the context of mobile device use. Additionally, adapting the road infrastructure, including traffic signals, to the real needs of pedestrians could significantly reduce the risk of accidents and improve overall road safety. Planned further studies focused on unsignalized crossings should aim to better understand pedestrian behavior and assess the risks associated with mobile device use, providing valuable insights for future road safety improvement strategies.

The authors plan further studies on pedestrian behavior, extending the analysis to three European Union countries: Poland, the Czech Republic, and Slovakia. The planned research will include observations of pedestrian behavior at different times of the day, specifically in the morning when people go to work, at midday when most people take lunch breaks, and in the afternoon when many return home. Additionally, the studies will be conducted on both working days and non-working days, allowing for an analysis of how various temporal and social factors influence the pedestrian behavior. This broader scope will provide a more comprehensive understanding of the relationship between the pedestrian behavior and situational context, offering valuable insights for developing effective strategies to improve safety at pedestrian crossings.

Acknowledgment

The authors received no financial support for the research, authorship and/or publication of this article.

Conflicts of interest

The authors declare that they have no known competing financial interests or personal relationships that could have appeared to influence the work reported in this paper.

References

[1] ELVIK, R. Rewarding safe and environmentally sustainable driving: systematic review of trials. *Transportation Research Record: Journal of the Transportation Research Board* [online]. 2014, **2465**(1), p. 1-7. ISSN 0361-1981, eISSN 2169-4052. Available from: https://doi.org/10.3141/2465-01

[2] HOOGENDOORN, R. G., HARMS, I. M., HOOGENDOORN, S. P., BROOKHUIS, K. A. Dynamic maximum speed limits: perception, mental workload, and compliance. *Transportation Research Record: Journal of the Transportation Research Board* [online]. 2012, **2321**(1), p. 46-54. ISSN 0361-1981, eISSN 2169-4052. Available from: https://doi.org/10.3141/2321-07

[3] HOSSAIN, A., SUN, X., ZAFRI, N. M., CODJOE, J. Investigating pedestrian crash patterns at high-speed intersection and road segments: findings from the unsupervised learning algorithm. *International Journal of Transportation Science and Technology* [online]. 2024, **14**, p. 186-201. ISSN 2046-0430, eISSN 2046-0449. Available from: https://doi.org/10.1016/j.ijtst.2023.04.007

[4] TIWARI, G., MOHAN, D., FAZIO, J. Conflict analysis for prediction of fatal crash locations in mixed traffic streams. *Accident Analysis and Prevention* [online]. 1998, **30**(2), p. 207-215. ISSN 0001-4575, eISSN 1879-2057. Available from: https://doi.org/10.1016/S0001-4575(97)00082-1

[5] JOHANSSON, C., LEDEN, L. Short-term effects of countermeasures for preventing traffic accidents in residential areas. *Accident Analysis and Prevention* [online]. 2007, **39**(3), p. 500-509. ISSN 0001-4575, eISSN 1879-2057. Available from: https://doi.org/10.1016/j.aap.2006.08.017

[6] DAVIES, D. G., HALLIDAY, M. E., MAYES, M., POCOCK, R. L. Pedestrian risk exposure: the traffic and environmental factors in the analysis of child pedestrian casualties [online]. TRL Report 182:1-83. Transport Research Laboratory, 2016. Available from: https://trl.co.uk/reports/TRL182

[7] ROSEN, E., SANDER, U. Pedestrian fatality risk as a function of car impact speed. *Accident Analysis and Prevention* [online]. 2009, **41**(3), p. 536-542. ISSN 0001-4575, eISSN 1879-2057. Available from: https://doi.org/10.1016/j.aap.2009.02.002

[8] HATFIELD, J., MURPHY, S. The effects of mobile phone use on pedestrian crossing behaviour at signalized and unsignalized intersections. *Accident Analysis and Prevention* [online]. 2007, **39**(1), p. 197-205. ISSN 0001-4575, eISSN 1879-2057. Available from: https://doi.org/10.1016/j.aap.2006.07.001

[9] NASAR, J. L., TROYER, D. Pedestrian injuries due to mobile phone use in public places. *Accident Analysis and Prevention* [online]. 2013, **57C**, p. 91-95. ISSN 0001-4575, eISSN 1879-2057. Available from: https://doi.org/10.1016/j.aap.2013.03.021

[10] THOMPSON, L. L., RIVARA, F. P., AYYAGARI, R. C., EBEL, B. E. Impact of social and technological distraction on pedestrian crossing behaviour. *Injury Prevention* [online]. 2012, **19**(4), p. 232-237. ISSN 1353-8047, eISSN 1475-5785. Available from: https://doi.org/10.1136/injuryprev-2012-040601

[11] PETERMEIJER, S. M., CIELER, S., DE WINTER, J. C. Comparing spatially static and dynamic vibrotactile take-over requests in the driver seat. *Accident Analysis and Prevention* [online]. 2017, **99**(A), p. 218-227. ISSN 0001-4575, eISSN 1879-2057. Available from: https://doi.org/10.1016/j.aap.2016.12.001

[12] DANELSON, K. A., GOLMAN, A. J., KEMPER, A. R., GAYZIK, F. S., GABLER, H. C., DUMA, S. M., STITZEL, J. D. Finite element comparison of human and Hybrid III responses in a frontal impact. *Accident Analysis and Prevention* [online]. 2015, **85**, p. 125-156. ISSN 0001-4575, eISSN 1879-2057. Available from: https://doi.org/10.1016/j.aap.2015.09.010

[13] FINLEY, M. D., THEISS, L. Field evaluation of pilot vehicles and portable traffic control signals with and without a flagger. *Transportation Research Record: Journal of the Transportation Research Board* [online]. 2017, **2617**(1), p. 1-8. ISSN 0361-1981, eISSN 2169-4052. Available from: https://doi.org/10.3141/2617-01

[14] RETTING, R. A., FERGUSON, S. A., MCCARTT, A. T. A review of evidence-based traffic engineering measures designed to reduce pedestrian-motor vehicle crashes. *American Journal of Public Health* [online]. 2003, **93**(9), p. 1456-1463. ISSN 0090-0036, eISSN 1541-0048. Available from: https://doi.org/10.2105/AJPH.93.9.1456

[15] Pedestrian safety, urban space and health: an overview - Transport Research Laboratory [online] [accessed 2024-08-31]. TRL Report 594. 2017. Available from: https://trl.co.uk/reports/TRL594

[16] Global status report on road safety 2018 - World Health Organization [online] [accessed 2024-08-31]. 2018. Available from: https://www.who.int/publications/i/item/9789241565684

[17] JACOBSEN, P. L. Safety in numbers: More walkers and bicyclists, safer walking and bicycling. *Injury Prevention* [online]. 2003, **9**(3), p. 205-209. ISSN 1538-9588, eISSN 1538-957X. Available from: https://doi.org/10.1136/ip.9.3.205

[18] TUMAS, P., SERACKIS, A., NOWOSIELSKI, A. Augmentation of severe weather impact to far-infrared sensor images to improve pedestrian detection system. *Electronics* [online]. 2021, **10**(8), 934. eISSN 2079-9292. Available from: https://doi.org/10.3390/electronics10080934

[19] IFTIKHAR, S., ZHANG, Z., ASIM, M., MUTHANNA, A., KOUCHERYAVY, A., ABD EL-LATIF, A. A. Deep learning-based pedestrian detection in autonomous vehicles: substantial issues and challenges. *Electronics* [online]. 2022, **11**(21), 3551. eISSN 2079-9292. Available from: https://doi.org/10.3390/electronics11213551

[20] Road safety in the European Union: Trends, statistics and main challenges - European Commission [online] [accessed 2024-08-31]. 2024. Available from: https://ec.europa.eu/transport/road_safety/road_safety_data_en

[21] Pedestrian fatalities in the EU 2019-2023 - European Transport Safety Council (ETSC) [online] [accessed 2024-08-31]. 2024. Available from: https://etsc.eu/pedestrian-safety/

[22] Road accidents in Poland in 2019-2023: statistical report - Polish Police/Wypadki drogowe w Polsce w latach 2019-2023: raport statystyczny - Policja Polska (in Polish) [online] [accessed 2024-08-31]. 2024. Available from: https://policja.pl/wypadki-drogowe-raport

[23] Accident statistics on national roads managed by (Accident statistics on national roads managed by GDDKiA)Statystyki wypadkow na drogach krajowych zarzadzanych przez (Statystyki wypadkow na drogach krajowych zarzadzanych przez GDDKiA) (in Polish) [online] [accessed 2024-08-31]. 2024. Available from: https://www.gov.pl/web/gddkia/statystyki-wypadkow-na-drogach-krajowych-zarzadzanych-przez-gddkia

[24] Annual report on road safety in Sweden 2023 - Vision Zero Initiative [online] [accessed 2024-08-31]. 2024. Available from: https://www.visionzeroinitiative.com

[25] FREJ, D., JASKIEWICZ, M., POLIAK, M., ZWIERZEWICZ, Z. Smartphone use in traffic: a pilot study on pedestrian behavior. *Applied Sciences* [online]. 2022, **12**(24), 12676. eISSN 2076-3417. Available from: https://doi.org/10.3390/app122412676

[26] KRUSZYNA, M., RYCHLEWSKI, J. Influence of approaching tram on behaviour of pedestrians in signalised crosswalks in Poland. *Accident Analysis and Prevention* [online]. 2013, **55**, p. 185-191. ISSN 0001-4575, eISSN 1879-2057. Available from: https://doi.org/10.1016/j.aap.2013.03.015

[27] DABROWSKA-LORANC, M., SICINSKA, K., ZIELINSKA, A. Road users' behaviour study in areas of zebra crosswalks. *Transport Problems* [online]. 2021, **16**(3), p. 185-198. ISSN 1896-0596, eISSN 2300-861X. Available from: https://doi.org/10.21307/tp-2021-052
[28] BUDZYNSKI, M., GOBIS, A., GUMINSKA, L., JELINSKI, L., KIEC, M., TOMCZUK, P. Assessment of the influence of road infrastructure parameters on the behaviour of drivers and pedestrians in pedestrian crossing areas. *Energies* [online]. 2021, **14**(12), 3559. eISSN 1996-1073. Available from: https://doi.org/10.3390/en14123559
[29] SOATHONG, A., CHOWDHURY, S., WILSON, D., RANJITKAR, P., Investigating the motivation for pedestrians' risky crossing behaviour at urban mid-block road sections. *Travel Behaviour and Society* [online]. 2021, **22**, p. 155-165. ISSN 2214-367X, eISSN 2214-3688. Available from: https://doi.org/10.1016/j.tbs.2020.09.005
[30] LEVEQUE, L., RANCHET, M., DENIEL, J., BORNARD, J. C., BELLET, T. Where do pedestrians look when crossing? A state of the art of the eye-tracking studies. *IEEE Access* [online]. 2020, **8**, p. 164833-164843. eISSN 2169-3536. Available from: https://doi.org/10.1109/ACCESS.2020.3021208
[31] RIAZ, M. S., CUENEN, A., POLDERS, E., AKRAM, M. B., HOUDA, M., JANSSENS, D., AZAB, M. Child pedestrian safety: study of street-crossing behaviour of primary school children with adult supervision. *Sustainability* [online]. 2022, **14**(3), 1503. eISSN 2071-1050. Available from: https://doi.org/10.3390/su14031503
[32] FREJ, D. P. Phone use by pedestrians - pilot studies. *The Archives of Automotive Engineering/Archiwum Motoryzacji* [online]. 2024, **104**(2), p. 5-18. eISSN 2084-476X. Available from: https://doi.org/10.14669/AM/175257

ANALYSIS OF HYBRID SPECTRUM SENSING IN COGNITIVE RADIO USING HYBRID APPROACHES

Haribhau Ashok Shinde*, Sandeep Garg

Department of Electronics and Communication, Oriental University, Indore, Madhya Pradesh, India

*E-mail of corresponding author: haribhau88@gmail.com

Haribhau Ashok Shinde 0009-0008-4367-7202, Sandeep Garg 0000-0002-7140-2352

Resume

Cognitive radio (CR) technology enables dynamic spectrum access to meet the growing demand for wireless communication. This study investigates spectrum sensing methods, specifically energy detection (ED) and matched filter detection (MFD), within hybrid strategies. A novel hybrid MFD method was developed and evaluated via MATLAB simulations, analyzing factors like sample size, signal-to-noise ratio (SNR), and false alarm probability. Results reveal that ED has a higher miss-detection rate compared to MFD and the proposed hybrid method, which performs particularly well under low sample counts and SNR conditions. This research enhances spectrum sensing techniques in cognitive radio systems, paving the way for more reliable wireless communication networks.

Available online: https://doi.org/10.26552/com.C.2025.003

Article info

Received 23 May 2024
Accepted 18 September 2024
Online 8 October 2024

Keywords:

cognitive radio
spectrum sensing
energy detection
primary user
sensing detection

ISSN 1335-4205 (print version)
ISSN 2585-7878 (online version)

1 Introduction

The CR is a viable approach for more effective spectrum usage, notably in the worldwide wireless network market. It addresses the challenge of limited radio channels, primarily allocated to licensed users like television, radio, and cellular network providers. The CR technology allows DSA, allowing secondary users (SU) to use underutilized spectrum lacking interference. This approach not only alleviates spectrum scarcity but optimizes wireless communication networks, as well, driving innovation and improving connectivity across various applications. As demand for wireless communication grows, CR adoption and advancement are crucial for sustainable and efficient spectrum management [1-2].

Mitola developed cognitive radio in 1999-2000 to enable unlicensed users to reuse licensed spectrum. This technology, known as dynamic spectrum access (DSA) [3], uses an intelligent radio system called Cognitive Radio (CR) to identify frequencies, identify available spectrum gaps, and adjust transceiver features based on the radio environment data [4]. The CR addresses spectrum scarcity by allowing unlicensed users to access the channel of a licensed user when the primary user is not present [5-6]. The CR adapts to the current spectrum background, identifies gaps, and communicates opportunistically within these gaps with minimal interference [7].

The CR, although being a wireless technique, offers the ability to increase the spectrum space for wireless communication (WC). It differs from traditional wireless technology by taking advantage of multidimensional electromagnetic (MDEM) potential. This phenomenon opens up new opportunities in the MDEM space. Furthermore, multidimensional spectrum (MSD) options include frequency, time, location, code, power, angle of arrival, and polarization of wireless transmissions [8]. The CR can effectively address the spectrum shortage issue in VANET. The CR-based VANET, also known as CR-VANET, is an assuring mechanism that addresses road security, crowding, and infotainment concerns. It also serves as a foundation for next-generation transportation systems, particularly automobiles that are autonomous [9]. The increasing number of vehicles on the road has highlighted the need for Intelligent Transportation Systems (ITS) to prevent collisions, monitor traffic, and assure road safety. The VANET technology enables vehicle-to-vehicle (V2V) communication, making it suitable for new vehicular applications. The vehicle nodes have onboard modules for detecting, transmitting, and receiving communications. The vehicle's on-board system makes decisions depending on traffic conditions, vehicle speed, and other factors to prevent accidents. Furthermore, CR-enabled vehicular networks are expected to improve communication efficiency compared to existing VANETs [10].

Three crucial tasks are carried out by a cognitive radio when it is used in broadcasting environments: spectrum sensing (SS), spectrum analysis, and spectrum decision [11]. The SS is a vital factor of the CR network, involving the detection of unoccupied spectrum spaces to establish communication channels for SUs without interfering with the transmissions of primary users (PU) [12]. The spectrum sensing stage of the CR life cycle is the most sensitive [13]. This procedure continuously scans the frequency spectrum for vacancies using a chosen bandwidth or channel. Spectrum holes are the vacancies that are present in the channel. We increase the spectrum's usage by making use of these gaps in the spectrum [14]. Therefore, the spectrum sensing approach must operate effectively to identify these spectrum gaps so that CR technology may use them to support the new devices that need to communicate. Two types of bands are assumed by CR technology: licensed bands and unlicensed bands. Those who possess a band within the spectrum are referred to as main (PU) users since they are granted permission to use the band whenever they like. The second-class users are those users who attempt to utilise any available bandwidth. Although the principal users don't always use their licenced band, the secondary users can still communicate by utilising these bands. SS techniques might be utilized to find these shortfalls in these licensed bands. To identify gaps and make the most use of the channels that are not being used by the principal users, the spectrum sensing algorithm's performance becomes vital [15]. Different signal properties, including ED, MFD [16], cyclo stationary detection, and so on, are used in traditional spectrum sensing techniques [17-18]. The most often utilized SS technology is ED [19-20]. Greater reliability is achieved with matched filtering, although needs previous awareness of the signal of the PU [21-22]. Therefore, CFD-based SS achieves well in the negative SNR zone as related to matched filter and ED-based approaches, given that CFD sensing has some understanding of PUs [23].

Though every spectrum sensing methodology has advantages and disadvantages, no single approach is always the best choice. To tackle this obstacle, scholars have suggested hybrid spectrum sensing methodologies that merge various sensing approaches to capitalize on their complimentary benefits. Improved detection robustness, adaptability to a variety of environmental circumstances, and dependability are possible with hybrid spectrum sensing.

Hybrid techniques are included in cognitive radio systems by employing different fusion procedures to integrate the outputs of individual sensing methods. Compared to independent methods, hybrid spectrum sensing can perform better by cleverly merging the outputs of ED and matching filter feature detection. They assess how well various fusion strategies perform in terms of improving detection precision, lowering false alarm rates, and simplifying calculation. We illustrate the potential advantages of combined spectrum sensing to improve the effectiveness of spectrum usage and facilitate smooth cohabitation with main users through simulations and performance evaluations. Our results give useful insights for constructing robust and adaptable spectrum sensing techniques and advancing modern spectrum sensing for CR systems. The primary contributions to the analysis are as follows:

1. The hybrid spectrum sensing method combines techniques for matching filter detection and ED. This hybrid strategy is intended to maximize the benefits of each method while correcting for their unique limits, resulting in improving overall SS performance.
2. Performance of the suggested hybrid technique will be thoroughly evaluated using MATLAB simulations in a variety of scenarios with varying SNR levels, false alarm probability, and sample counts.
3. Furthermore, it suggests hybrid spectrum sensing strategies that enhance detection robustness and adaptability to varying environmental conditions by combining several sensing techniques.

The review of the literature for several types of research related to ED and matched filter detection was summarized in Section 2; the system model, its types and the suggested technique were explained in Section 3, and Section 4 provides graphs illustrating the stimulation and effect, a conclusion in section 5, and the list of references for this work is given in the part that follows.

2 Literature review

The ED method's low implementation complexity makes it a well-liked signal-sensing strategy in spectrum sensing. Nevertheless, uncertainty arises because noise variance uncertainty is frequently computed. This study [24] suggests an ED-based sensing technique that integrates signal samples from several antennas to produce a decision threshold independent of noise variation. According to simulation data, this method outperforms the ED method without noise variance estimations, approaching 1 even at SNRs of -15 dB. However, the noise characteristics could vary depending on the environment or operating conditions, the method claim to be noise-independent might not always hold true.

In cognitive radio, spectrum sensing is essential, and ED is the most commonly utilized kind. Because of their predetermined thresholds, conventional double-threshold ED approaches have a poor detection probability. An adaptive double-threshold cooperative spectrum sensing method is presented [25], which aggregates detection results using the "or" condition and the average energy of prior sensing moments. When compared to alternative double-threshold methods, this method considerably enhances detection performance. However, it might function well in a steady environment, and some sudden changes in the environment could cause it to malfunction. It might not respond fast enough to cope with the signal's frequent shifts.

The utilization of wireless systems has risen due to the growing need for apps on tablets, mobile phones, IoT, and WSNs. To enhance throughput in wireless networks, it is necessary to comprehend spectrum scarcity [26]. By borrowing spectrum from cognitive networks, networks can work together to achieve lower error rates at lower SNR values and longer sharing procedures. However, the evaluation, which evaluates ED probability with false alarm rates and signal-to-noise ratio, may not fully capture the performance and efficacy of spectrum-sharing mechanisms in cognitive networks.

In the present research [27], a novel ED method for cognitive radio system spectrum detection is introduced. Using Newton's method with forced convergence, the three-event ED (3EED) approach approximates the optimum decision threshold with high accuracy. The method represents a breakthrough in tracking primary users' actions, outperforming conventional ED (CED) in spectrum sensing. However, false positives and false can still occur despite the efforts to reduce the chance of decision errors. Careful consideration should be given to how these faults may affect the overall performance of the system.

The 5G technology uses more energy but also demands higher receiver sensitivity. 5G technology is anticipated to provide large data traffic volumes and minimum latency [28]. It also highlights the potential advantages of cognitive radio and 5G by implying that MIMO can increase radiated energy and spectrum efficiency. However, when cognitive spectrum sensing and power harvesting are used together, there may be mismatches with current devices and infrastructure, necessitating major upgrades or changes.

The paper [29] focuses on applying a novel method based on matched filter identification to find effective channels in cognitive radio networks at low SNR. The ED in different SNR conditions is compared with the matching filter detection with 10 samples using MATLAB. The findings indicate that matched filter detection performs better in terms of sensing since it has a higher chance of detection at low SNRs (-30 dB) than ED (-10 dB). However, not all situations or signal types will lend themselves to matched filter detection. Various elements, like multipath propagation, interference types, and signal modulation, may affect its effectiveness.

Dynamic spectrum allocation is required due to the growing number of wireless applications and consumers. A radio system called Cognitive Radio takes advantage of its environment to determine vacant spectrum to increase efficiency. For systems based on Cognitive Radio, spectrum sensing is essential. This work [30] employs simulations to assess several spectrum sensing techniques and determines the best way based on real-world application results. However, system efficiency might be decreased by false positives or lost opportunities to utilize the available spectrum.

As a result, the method's noise characteristics can change based on the surroundings and how it is used, therefore its claim that its noise-independent is not necessarily valid. It is possible that spectrum-sharing processes in cognitive networks are not fully captured by the assessment of ED probability and false alarm rates. There is still a chance of false positives and false negatives, which could impact system performance. Mismatches may arise when cognitive spectrum sensing and power harvesting are combined, requiring updates or modifications.

3 System model

Spectrum sensing is the process of detecting available frequency bands in wireless communication. It allows cognitive radios to opportunistically access unused spectrum, enhancing efficiency.

a) Energy detection

A secondary user tracks the energy content in a particular frequency band to verify its occupancy using energy-detecting technology. When the primary users are present in the spectrum, energy levels rise significantly over the noise floor. To determine the spectrum occupancy, when detecting energy, the incoming signal energy is compared to a predetermined threshold [31].

b) Cyclostationary (CS) detection

Cyclostationary detection is the most important spectrum sensing technique for advanced radio that is available. It is a promising algorithm because it can identify the spectrum at low SNR without being affected by noise. By calculating the mean and autocorrelation of the signal, it takes advantage of the periodicity characteristics of the data. The identification of PU without a discernible interference between PU and SU is another important feature of CS. The CS algorithm has been used recently to identify the spectrum under different circumstances [32].

c) Matched filter detection

It is a viable method for spectrum sensing in CR networks, particularly when comprehensive prior information of the primary user signal's parameters is available, including its center frequency, bandwidth, modulation scheme, and the wireless channel's response. This technique entails comparing the received signal with pilot samples obtained previously from the same radio transmitter. By leveraging these stored pilot signals, the matched filter computes a test statistic, enabling precise detection of the primary user's presence [33].

3.1 Mathematical model for current spectrum sensing methods

The efficiency of this algorithm is dependent on several factors, including noise uncertainty, sample size, and SNR ratio. One of the two hypotheses H_0 or H_1 is chosen by spectrum sensing using Equation (1) and (2) by the signal that is received.

$$H_0 : x(n) = w(n), \tag{1}$$

$$|H_1 : x(n) = y(n) + w(n). \tag{2}$$

In this study, a spectrum sensing technique is employed to ascertain the presence or absence of a PU within a particular frequency band. The hypothesis H_0 suggests the absence of the primary user, while H_1 signifies the presence of the primary user's signal. In addition, $x(n)$ is the n^{th}sample of the signal received by the secondary user and $y(n)$ is the transmitted signal. The detection statistic S is then compared with a predefined threshold λ, and the detector's performance is assessed using the probability of detection (P_d) and the probability of false alarm (P_{fa}).

P_{fa} is a probability of H_0, and is provided by Equation (3),

$$P_{fa} = P_r\left(S > \lambda / H_0\right). \tag{3}$$

P_d denotes a probability of H_1, and is given by,

$$P_d = P_r\left(S > \lambda / H_1\right). \tag{4}$$

The possibility that a sensing algorithm may detect a PU presence even in the absence of PUs is known as the false alarm probability. A low false alarm probability makes it more likely that SUs will use the sensed spectrum, which raises the secondary network's feasible throughput. The number of times the sensing approach properly determines the existence of PU is known as the probability of detection. The PU controls how well the system performs. Enhancing PU spectrum utilisation can maximise PU priority by recognising more PUs and minimising interference through longer sensing distances and interference-prevention limits.

A successful sensing approach achieves a high probability of detection while maintaining a low probability of false alarms.

Another challenging task is figuring out the threshold that will be utilized to compare to the probability. As a result, practical conditions must be followed when doing theoretical analysis and numerical computations.

Techniques for spectrum sensing are based on the problem of binary hypothesis testing. The theoretical formulation is in equation (5):

$$x(n) = \left\{\begin{cases} w(n) & under\ H_0 \\ y(n) + w & under\ H_1 \end{cases}\right. . \tag{5}$$

a) Energy detection

Energy detection is highly preferred for its simplicity and its capability to operate without prior knowledge of the primary signals [34-35]. The detection statistic for ED was derived by computing the average energy of N experimental samples, y(n), as equation (6):

$$S = \frac{1}{N}\sum_{n=1}^{N} |x(n)|^2 . \tag{6}$$

Equation (7) defines the average signal-to-noise ratio:

$$SNR = \frac{P}{\sigma_n^2} \tag{7}$$

and σ_n^2 denotes the noise variance.

The received signal power is defined in equation (8):

$$P = \lim_{N \to \infty} \frac{1}{N}\sum_{n=1}^{N} |y(n)|^2 . \tag{8}$$

The probability of a false alarm was determined as equation (9),

$$P_{fa} = \left(\frac{\lambda - \sigma_n^2}{\sqrt{2\sigma_n^2 / N}}\right). \tag{9}$$

The probability of detection is determined by equation (10),

$$P_d = \left(\frac{\lambda - (P + \sigma_n^2)}{\sqrt{2(P + \sigma_n^2)^2 / N}}\right). \tag{10}$$

Equations (9) and (10) are substituted to give the criteria for the chance of false alarm in Equations (11) and (12).

$$\lambda = Q^{-1}(P_{fa}) \cdot \sqrt{2\sigma_n^4 / N} + \sigma_n^2 , \tag{11}$$

$$\lambda = Q^{-1}(P_d) \cdot \sqrt{2(P + \sigma_n^2)^2 / N} + P + \sigma_n^2 . \tag{12}$$

From Equation (7), (11), (12), it is possible to determine the correlation between N, SNR, P_{fa}, and P_d using equation (13):

$$P_d = Q\left(\frac{Q^{-1}(P_{fa}) \cdot \sqrt{2 / N} - SNR}{\sqrt{2 / N} \cdot (SNR + 1)}\right). \tag{13}$$

Further, the probability of missing a recognition is equation (14):

$$P_{mr} = 1 - P_d . \tag{14}$$

b) Matched filter detection

As explained in [36], the Matched filter is used for coherent detection. This method is extensively employed in spectrum sensing due to its ability to optimize the SNR. When the characteristic unknown signal aligns with those of a known signal, it is inferred that a PU is present in the spectrum. By correlating the received signal with a reference pilot signal, y_p, the presence of the PU can be detected using equation (15):

$$S = \frac{1}{N}\sum_N x(n) * y_p(n). \quad (15)$$

Corresponding to Neyman-Pearson criteria, P_d and P_{fa} are, stated as

$$P_d = Q\left(\frac{(\lambda - E)}{\sqrt{E\sigma_n^2}}\right), \quad (16)$$

$$P_{fa} = Q\left(\frac{\lambda}{\sqrt{E\sigma_n^2}}\right), \quad (17)$$

where:

$$E = \sum_{n=1}^{N} y(n)^2, \quad (18)$$

where E represents the energy signal.

By manipulating Equations (16) and (17), the following formulas can be used to get the thresholds:

$$\lambda = Q^{-1}(P_d) \cdot \sqrt{E\sigma_n^2} + E, \quad (19)$$

$$\lambda = Q^{-1}(P_{fa}) \cdot \sqrt{E\sigma_n^2}, \quad (20)$$

$$P_d = Q\left(Q^{-1}(Pfa) - \sqrt{\frac{E}{\sigma_n^2}}\right). \quad (21)$$

3.2 Model of the hybrid matched filter detection technique

Figure 1 illustrates the block diagram for the recommended "Hybrid Matched Filter Detection". This approach integrates the conventional Matched Filter Detection methodology with the double Matched Filter Detection (MFD). Given its hybrid nature, it manifests two distinct responses contingent upon the probability of a false alarm. When the probability of a false alarm is below 0.5, the second part of the detector, representing a double-matched filter detector, is activated. This innovative double-matched filter detector functions by multiplying the thresholds and detection statistics derived from two standard-matched filter detectors. Conversely, when the probability of a false alarm equals or exceeds 0.5, a standard-matched filter detector is employed.

Equation (22) is the detection statistics of the detector for $P_{fa} < 0.5$

$$S = \frac{1}{N}\sum_N x(n) * y_p(n) \cdot \frac{1}{N}\sum_N y(n) * y_p(n). \quad (22)$$

Equation (15) provides the detection statistics of the detector corresponding to P_{fa} >= 0.5. The detector's cutoff for $P_{fa} < 0.5$ is provided by equation (23):

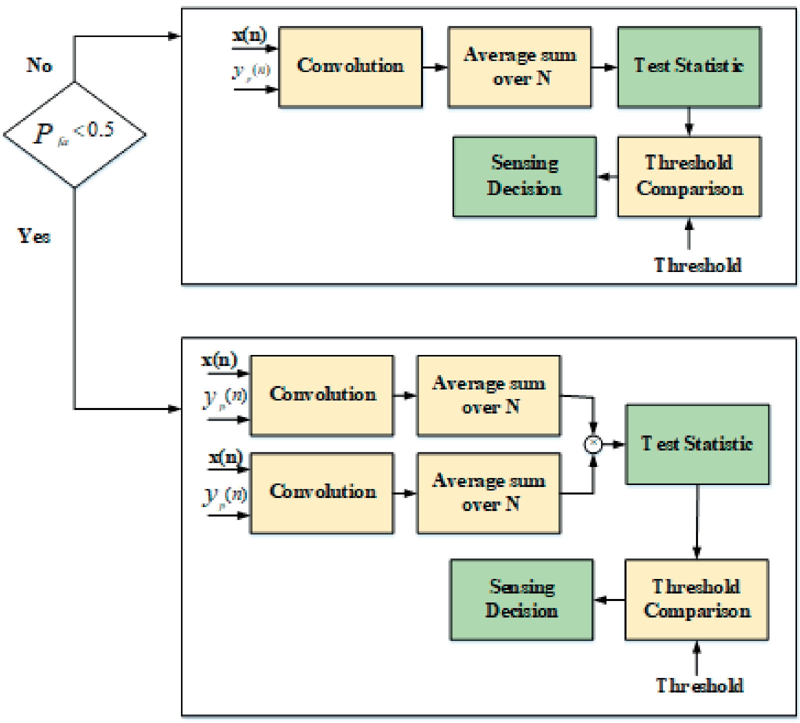

Figure 1 *The hybrid matched filter detection technique's proposed model*

$$\lambda = \left(Q^{-1}(P_{fa}) \cdot \sqrt{E\sigma_n^2}\right)^2. \tag{23}$$

Equation (20) gives the threshold of the detector corresponding to P_{fa} >= 0.5.

When the false alarm probability is less than 0.5, the double-matched filter detector works better than the conventional matched filter detector. The probability of missed detections rises with the false alarm probability, up to 0.5 or higher, however, there comes a tipping point where the double-matched filter detector is outperformed by the conventional matched filter detector.

The probability of miss-detection was calculated utilizing a flowchart in Figure 2, with variables N_t, N_d, and P_{fa} representing Monte-Carlo simulations, iterations, and false alarm probability, respectively. The approach for both the ED and MFD involves setting the sample count, SNR, and several Monte Carlo runs. The loop was implemented to cover false alarm probabilities in increments of 0.01 from 0 to 1, with another cycle increasing the number of Monte Carlo simulations. A new variable, i, was used to determine the number of Monte-Carlo simulations completed and remaining. The transmitted signal and additive white Gaussian noise are randomly generated for each Monte-Carlo simulation utilizing the randn function with a mean of zero, allowing signals to have both positive and negative values.

This is how the detection statistic is computed: Equation (6) is utilized for the Energy Detection, and the detection statistic's outcome is always positive. The Matched Filter Detection uses Equation (15), and the result could be positive or negative.

When calculating the risk of false threshold for ED, Equation (11) is taken into account, but for Matched Filter Detection, Equation (20) was employed. One finding is that the value in the equation's second component is always higher than the value in the first portion. When these values are added together, as per Equation (11), the threshold for Energy Detection always yields a positive result. On the other hand, a null, positive, or negative threshold can be used for Matched Filter Detection. This phenomenon is explained by the Q^{-1} function's fluctuating behaviour.

- it is positive for a P_{fa} < 0.5;
- it is negative for a P_{fa} > 0.5;
- it is zero for a P_{fa} = 0.5.

To ascertain whether the detection statistic surpasses the threshold, confirmation is required. If the detection statistic is smaller than the threshold, it can be used to interpret whether the variable i equals N_t. This requirement is satisfied when every Monte-Carlo simulation for every value of the false alarm chance has been finished. $1 - N_d/N_t$ provides the likelihood of miss-detection. The false alarm likelihood simulation terminates at that point.

The variable i will be increased and a new Monte-Carlo simulation will begin by randomly generating the signals if the variables i and N_t differ. We shall increase the variable N_d if the detection statistic exceeds the threshold. The next step is to confirm that, as previously mentioned, the variable i equals N_t. In the last step, the completion of all the Monte Carlo simulations for the present false alarm probability is confirmed. If this is the case, it is possible to determine the probability of miss-detection for the current false alarm probability; if not, one must run additional Monte-Carlo simulations until all the false alarm probabilities have been run and a plot is produced. The Double MFD scenario's method for determining the chance of miss-detection is quite parallel to the MFD method. The alterations are in the MFD's threshold and squared values of the detection statistic.

The Double MFD's detection statistic and threshold are established as follows:

- The detection statistic is calculated using Equation (22) and the outcome is always positive.
- The threshold is calculated using Equation (23) and is always positive, except P_{fa} = 0.5, where the value is zero.

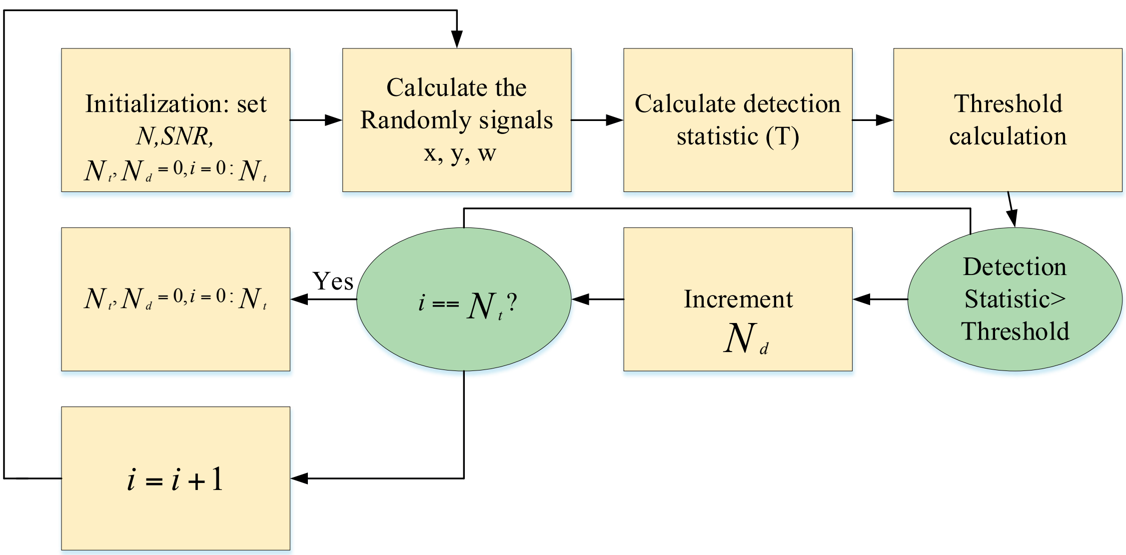

Figure 2 *The algorithm that computes the miss-detection probability*

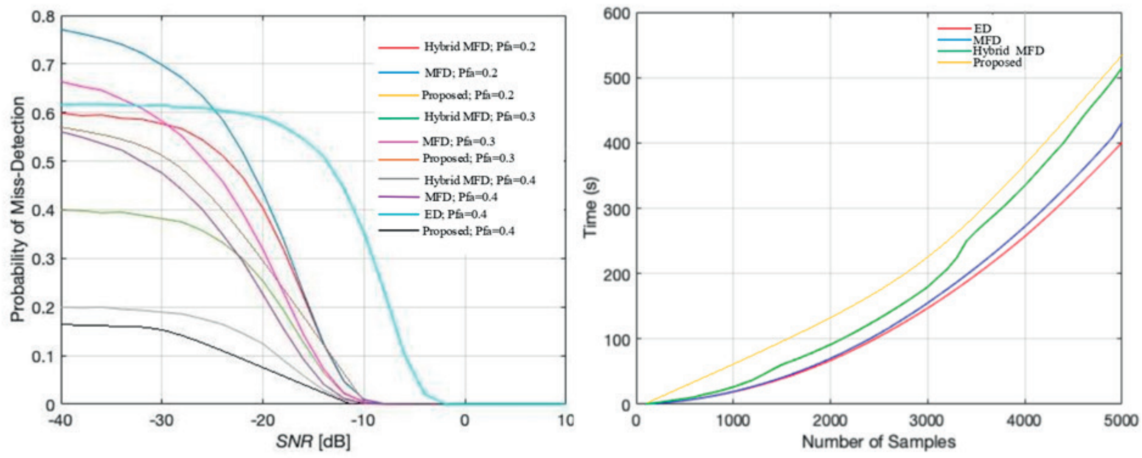

(a) (b)

***Figure 3** Comparison between techniques for the probability of miss-detection vs SNR for* (a) Pfa = 0:3, (b) N=100

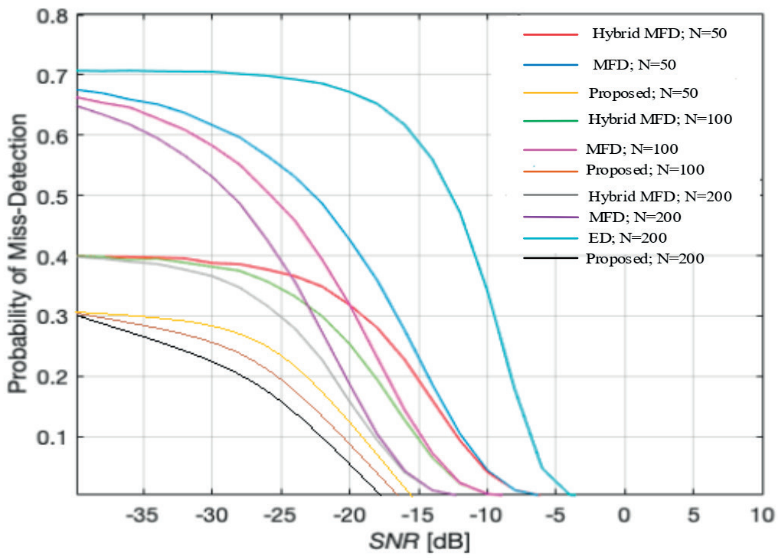

***Figure 4** Comparison of the time vs number of samples with P_{fa} = 0:3 and SNR D -25 dB*

4 Stimulation and results

MATLAB is used to simulate and analyse various strategies while changing the parameters to assess the impact of the number of samples, chance of false alarm, and SNR on the probability of miss-detection. Figures 3 and 4 display the consequence for the probability of miss-detection as a function of SNR when comparing different spectrum sensing approaches. P_{fa} = 0.3 is taken into account in Figure 3.

In Figure 3, we consider N = 100 while varying the probability of false alarm (except the ED sensing approach, which only took P_{fa} = 0.4 into account). Compared to the MFD, the Hybrid MFD (or HMFD) in Figure 3 exhibits a lower probability of missed detection for N = 50, N = 100, and N = 200, up to the SNR of -10 dB, -12 dB, and -16 dB, correspondingly. Under these SNR settings, the proposed hybrid technique performs better.

When comparing Figure 4's P_{fa} = 0.2, P_{fa} = 0.3, and P_{fa} = 0.4 values to the MFD, the probability of miss-detection decreases until the SNR reaches -14 dB, -12 dB, and -10 dB, in that order. Increasing SNR is analogous to the HMFD and MFD behaviours. As an indicator of computational difficulty, Figure 4 contrasts the approach simulation running time for a given N across several spectrum sensing techniques. Figure 4 takes into account SNR of -25 dB and P_{fa} of 0.3. O(N^{-2}) is the computational complexity for all spectrum sensing methods under consideration. As N increases in Figure 4, so does the running time. The disparity between the three spectrum sensing methods increases with increasing N. MFD and HMFD need 431 and 515 seconds, respectively, to mimic 5000 samples, also the ED sensing approach requires 401 seconds. Compared to the traditional sensing method the proposed hybrid sensing takes 520 seconds to complete the task. In contrast to current methods like ED, MFD, and

HMFD the suggested HMFD sensing methodology will undoubtedly enable the SUs to identify spectrum gaps more effectively in a variety of situations, all the while gaining unhindered access to major licensed bands.

5 Conclusion

The study's findings highlight the critical role of efficient spectrum sensing in cognitive radio (CR) technology to meet the burgeoning demand for wireless communication in transportation systems. By exploring energy detection (ED) and matched filter detection (MFD) methods, and developing a novel hybrid-matched filter detection approach, the research addresses the need for reliable spectrum access in vehicular communication networks. The MATLAB simulations revealed that ED, although simpler, has a higher miss-detection rate compared to MFD and the hybrid MFD method. Notably, the hybrid MFD method demonstrated superior performance, especially in challenging conditions characterized by low sample counts, low signal-to-noise ratios (SNR), and false alarm probabilities slightly below 0.5. This advanced method ensures more accurate detection of primary users, thereby preventing interference and ensuring seamless communication. The enhanced spectrum sensing techniques proposed in this study not only improve the reliability and efficiency of cognitive radio systems but significantly contribute to safer and more connected vehicular environments, as well. As transportation systems increasingly rely on robust wireless communications, the advancements in CR technology underscore a pivotal step towards achieving dynamic, resilient, and high-performance communication networks essential for modern transportation infrastructures.

Acknowledgment

The authors received no financial support for the research, authorship and/or publication of this article.

Conflicts of interest

The authors declare that they have no known competing financial interests or personal relationships that could have appeared to influence the work reported in this paper.

References

[1] SHABIR, A., KANWAL, K., AYESHA, H., ALMAS, A., RAZA, S., JAFFAR, S. A hybrid cognitive radio reporting scheme for wireless regional area networks. *Journal of Computing and Biomedical Informatics* [online]. 2024, Special Issue on Intelligent Computing of Applied Sciences and Emerging Trends (ICASET). ISSN 2710-1606, eISSN 2710-1614. Available from: https://jcbi.org/index.php/Main/article/view/444

[2] LIU, S., WU, J., HE, J. Dynamic multichannel sensing in cognitive radio: hierarchical reinforcement learning. *IEEE Access* [online]. 2021, **9**, p. 25473-25481. eISSN 2169-3536. Available from: https://doi.org/10.1109/ACCESS.2021.3056670

[3] SINGHAL, C., PATIL, V. HCR-WSN: Hybrid MIMO cognitive radio system for wireless sensor network. *Computer Communications* [online]. 202, **169**, p. 11-25. ISSN 0140-3664, eISSN 1873-703X. Available from: https://doi.org/10.1016/j.comcom.2020.12.025

[4] KHAMAYSEH, S., HALAWANI, A. Cooperative spectrum sensing in cognitive radio networks: A survey on machine learning-based methods. *Journal of Telecommunications and Information Technology* [online]. 2020, **3**, p. 36-46. ISSN 1509-4553, eISSN 1899-8852. Available from: https://doi.org/10.26636/jtit.2020.137219

[5] NASSER, A., CHAITOU, M., MANSOUR, A., YAO, K. C., CHARARA, H. A deep neural network model for hybrid spectrum sensing in cognitive radio. *Wireless Personal Communications* [online]. 2021, **118**(1), p. 281-299. ISSN 0929-6212, eISSN 1572-834X. Available from: https://doi.org/10.1007/s11277-020-08013-7

[6] MOHANAKURUP, V., BAGHELA, V. S., KUMAR, S., SRIVASTAVA, P. K., DOOHAN, N. V., SONI, M., AWAL, H. 5G cognitive radio networks using reliable hybrid deep learning based on spectrum sensing. *Wireless Communications and Mobile Computing* [online]. 2022, **2022**, 1830497. eISSN 1530-8677. Available from: https://doi.org/10.1155/2022/1830497

[7] ARSHID, K., JIANBIAO, Z., HUSSAIN, I., PATHAN, M. S., YAQUB, M., JAWAD, A., AHMED, F. Energy efficiency in cognitive radio network using cooperative spectrum sensing based on hybrid spectrum handoff. *Egyptian Informatics Journal* [online]. 2022, **23**(4), p. 77-88. ISSN 1110-8665, eISSN 2090-4754. Available from: https://doi.org/10.1016/j.eij.2022.06.008

[8] OYEWOBI, S. S., DJOUANI, K., KURIEN, A. M. A review of industrial wireless communications, challenges, and solutions: A cognitive radio approach. *Transactions on Emerging Telecommunications Technologies* [online]. 2020, **31**(9), e4055. ISSN 2161-3915, eISSN 2161-3915. Available from: https://doi.org/10.1002/ett.4055

[9] HOSSAIN, M. A., NOOR, R. M., YAU, K. L. A., AZZUHRI, S. R., Z'ABA, M. R., AHMEDY, I. Comprehensive survey of machine learning approaches in cognitive radio-based vehicular ad hoc networks. *IEEE Access* [online]. 2020, **8**, p. 78054-78108. eISSN 2169-3536. Available from: https://doi.org/10.1109/ACCESS.2020.2989870

[10] AKTER, S., MANSOOR, N. A spectrum aware mobility pattern based routing protocol for CR-VANETs. In: 2020 IEEE Wireless Communications and Networking Conference WCNC: proceedings [online]. IEEE. 2020. eISBN 978-1-7281-3106-1, eISSN 1558-2612, p. 1-6. Available from: https://doi.org/10.1109/WCNC45663.2020.9120760

[11] MOHAMED, A. R., EL-BANNA, A. A., MANSOUR, H. A. Multi-path hybrid spectrum sensing in cognitive radio. *Arabian Journal for Science and Engineering*. 2021, **46**(10), p. 9377-9384. ISSN 2193-567X, eISSN 2191-4281.

[12] MAHENDRU, G., SHUKLA, A. K., PATNAIK, L. M. An optimal and adaptive double threshold-based approach to minimize error probability for spectrum sensing at low SNR regime. *Journal of Ambient Intelligence and Humanized Computing* [online]. 2022, **13**(8), p. 3935-3944. ISSN 1868-5137, eISSN 1868-5145. Available from: https://doi.org/10.1007/s12652-021-03596-w

[13] FALIH, M. S., ABDULLAH, H. N. DWT based energy detection spectrum sensing method for cognitive radio system. *Iraqi Journal of Information and Communication Technology* [online]. 2020, **3**(3), p. 1-11. ISSN 2222-758X, eISSN 2789-7362. Available from: https://doi.org/10.31987/ijict.3.3.99

[14] USMAN, M. B., SINGH, R. S., MISHRA, S., RATHEE, D. S. Improving spectrum sensing for cognitive radio network using the energy detection with entropy method. *Journal of Electrical and Computer Engineering* [online]. 2022, **2022**(1), 2656797. ISSN 2090-0147, eISSN 2090-0155. Available from: https://doi.org/10.1155/2022/2656797

[15] MUSUVATHI, A. S. S., ARCHBALD, J. F., VELMURUGAN, T., SUMATHI, D., RENUGA DEVI, S., PREETHA, K. S. Efficient improvement of energy detection technique in cognitive radio networks using K-nearest neighbour (KNN) algorithm. *EURASIP Journal on Wireless Communications and Networking* [online]. 2024, **2024**(1), 10. ISSN 1687-1472, eISSN 1687-1499. Available from: https://doi.org/10.1186/s13638-024-02338-8

[16] SARKAR, S., MURALISHANKAR, R., GURUGOPINATH, S. Vasicek and Van Es entropy-based spectrum sensing for cognitive radios. *IET Networks* [online]. 2024, **13**(1), p. 1-12. ISSN 2047-4954, eISSN 2047-4962. Available from: https://doi.org/10.1049/ntw2.12096

[17] SOLANKI, S., DEHALWAR, V., CHOUDHARY, J., KOLHE, M. L., OGURA, K. Spectrum sensing in cognitive radio using CNN-RNN and Transfer learning. *IEEE Access* [online]. 2022, **10**, p. 113482-113492. eISSN 2169-3536. Available from: https://doi.org/10.1109/ACCESS.2022.3216877

[18] GENG, Y., HUANG, J., YANG, J., ZHANG, S. Spectrum sensing for cognitive radio based on feature extraction and deep learning. *Journal of Physics: Conference Series* [online]. 2022, **2261**(1), 012016. ISSN 1742-6596. Available from: https://doi.org/10.1088/1742-6596/2261/1/012016

[19] LORINCZ, J., RAMLJAK, I., BEGUSIC, D. Analysis of the impact of detection threshold adjustments and noise uncertainty on energy detection performance in MIMO-OFDM cognitive radio systems. *Sensors* [online]. 2022, **22**(2), 631. eISSN 1424-8220. Available from: https://doi.org/10.3390/s22020631

[20] BANI, K., KULKARNI, V. Hybrid spectrum sensing using MD and ED for cognitive radio networks. *Journal of Sensor and Actuator Networks* [online]. 2022, **11**(3), 36. eISSN 2224-2708. Available from: https://doi.org/10.3390/jsan11030036

[21] SHRESTHA, R., TELGOTE, S. S. (2020, October). A short sensing-time cyclostationary feature detection based spectrum sensor for cognitive radio network. In: 2020 IEEE International Symposium on Circuits and Systems ISCAS: proceedings [online]. IEEE. 2020. ISBN 978-1-7281-3320-1, eISSN 2158-1525, p. 1-5. Available from: https://doi.org/10.1109/ISCAS45731.2020.9180415

[22] KUMAR, A., GAUR, N., CHAKRAVARTY, S., ALSHARIF, M. H., UTHANSAKUL, P., UTHANSAKUL, M. Analysis of spectrum sensing using deep learning algorithms: CNNs and RNNs. *Ain Shams Engineering Journal* [online]. 2024, **15**(3), 102505. ISSN 2090-4479, eISSN 2090-4495. Available from: https://doi.org/10.1016/j.asej.2023.102505

[23] VADIVELU, K., GNANAMANOHARAN, E., TAMILSELVAN, S. Detection of spectrum sensors for maximizing eigenvalue and hardware efficiency in cognitive radio networks using machine learning. *International Journal of Intelligent Systems and Applications in Engineering* [online]. 2024, **12**(2s), p. 540-552. ISSN 2147-6799. Available from: https://ijisae.org/index.php/IJISAE/article/view/3654

[24] LUO, J., ZHANG, G., YAN, C. An energy detection-based spectrum-sensing method for cognitive radio. *Wireless Communications and Mobile Computing* [online]. 2022, **2022**, 933336. eISSN 1530-8677. Available from: https://doi.org/10.1155/2022/3933336

[25] YU, S., LIU, J., WANG, J., ULLAH, I. Adaptive double-threshold cooperative spectrum sensing algorithm based on history energy detection. *Wireless Communications and Mobile Computing* [online]. 2020, **2020**, 794136. eISSN 1530-8677. Available from: https://doi.org/10.1155/2020/4794136

[26] SAAD, M. A., MUSTAFA, S. T., ALI, M. H., HASHIM, M. M., ISMAIL, M. B., ALI, A. H. Spectrum sensing and energy detection in cognitive networks. *Indonesian Journal of Electrical Engineering and*

Computer Science [online]. 2020, **17**(1), 464-471. ISSN 2502-4752, eISSN 2502-4760. Available from: http://doi.org/10.11591/ijeecs.v17.i1.pp464-471

[27] MARTIAN, A., AL SAMMARRAIE, M. J. A., VLADEANU, C., POPESCU, D. C. Three-event energy detection with adaptive threshold for spectrum sensing in cognitive radio systems. *Sensors* [online]. 2020, **20**(13), 3614. eISSN 1424-8220. Available from: https://doi.org/10.3390/s20133614

[28] JANG, W. M. Simultaneous power harvesting and cyclostationary spectrum sensing in cognitive radios. *IEEE Access* [online]. 2020, **8**, p. 56333-56345. eISSN 2169-3536. Available from: https://doi.org/10.1109/ACCESS.2020.2981878

[29] TEJESH, K., BHARATHI, P. S. Effective channel detection at low SNR in cognitive radio network using matched filter approach and compare with energy detection-based approach. *Revista Geintec - Gestao, Inovacao e Tecnologias*. 2021, **11**(2), p. 1349-1361. ISSN 2237-0722.

[30] CHAUHAN, N., SHAH, A., BHATT, P., DALAL, P. Simulation based analysis of non-cooperative spectrum sensing techniques in cognitive radio. *Test Engineering and Management*. 2020, **83**, p. 5149-5162. ISSN 0193-4120.

[31] RAGHAVENDRA, Y. M., ASHA, M., MANJULA, G., LATHA, M., SWARANALAKSHMI., HARSHITHA, R. Optimization of energy and spectrum sensing using orthogonal frequency division multiple access. *International Research Journal on Advanced Engineering Hub (IRJAEH)* [online]. 2024, **2**(04), p. 861-869. eISSN 2584-2137. Available from: https://doi.org/10.47392/IRJAEH.2024.0121

[32] KUMAR, A., VENKATESH, J., GAUR, N., ALSHARIF, M. H., UTHANSAKUL, P., UTHANSAKUL, M. Cyclostationary and energy detection spectrum sensing beyond 5G waveforms. *Electronic Research Archive* [online]. 2023, **31**, p. 3400-3416. ISSN 2688-1594. Available from: https://doi.org/10.3934/era.2023172

[33] RAI, A., SEHGAL, A., SINGAL, T. L., AGRAWAL, R. Spectrum sensing and allocation schemes for cognitive radio [online]. In: *Machine Learning and Cognitive Computing for Mobile Communications and Wireless Networks*. SINGH, K. K., SINGH, A., CENGIZ, K., LE, D.-N. (eds.). Scrivener Publishing LLC, 2020, ISBN 9781119640363, eISBN 9781119640554, p. 91-129. Available from: https://doi.org/10.1002/9781119640554.ch5

[34] RAGHAVENDRA, L. R., MANJUNATHA, R. C. Cognitive radio spectrum sensing using hybrid MME and energy double thresholding optimized with weighted chimp optimization algorithm. *International Journal of Intelligent Systems and Applications in Engineering* [online]. 2023, **11**(9s), p. 245-257. ISSN 2147-6799. Available from: https://ijisae.org/index.php/IJISAE/article/view/3115

[35] KOCKAYA, K., DEVELI, I. Spectrum sensing in cognitive radio networks: threshold optimization and analysis. *EURASIP Journal on Wireless Communications and Networking* [online]. 2020, **2020**(1), 255. ISSN 1687-1472, eISSN 1687-1499. Available from: https://doi.org/10.1186/s13638-020-01870-7

[36] ABED, H. S., ABDULLAH, H. N. Improvement of spectrum sensing performance in cognitive radio using modified hybrid sensing method. *Acta Polytechnica* [online]. 2022, **62**(2), p. 228-237. ISSN 1210–2709, eISSN 1805–2363. Available from: https://doi.org/10.14311/AP.2022.62.0228

KOMUNIKÁCIE
COMMUNICATIONS

VEDECKÉ LISTY ŽILINSKEJ UNIVERZITY
SCIENTIFIC LETTERS OF THE UNIVERSITY OF ZILINA

VOLUME 27 Number 1

January 2025

Each paper was reviewed by at least two reviewers.
Individual issues of the journal can be found on: http://komunikacie.uniza.sk
The full author quidelines are available at:
https://komunikacie.uniza.sk/artkey/inf-990000-0400_Author-guidelines.php
Published quarterly by University of Žilina in EDIS - Publishing House of the University of Žilina.
Communications is currently indexed, abstracted and accepted by CEEOL, CLOCKSS, Crossref (DOI), digitálne pramene, DOAJ, EBSCO Host, Electronic Journals Library (EZB), ERIH Plus, Google Scholar, Index Copernicus International Journals Master list, iThenticate, JournalGuide, Jouroscope, Norwegian Register for Scientific Journals Series and Publishers, Portico, ROAD, ScienceGate, SCImago Journal & Country Rank, SciRev, SCOPUS, Web of Science database, WorldCat (OCLC).

Journal Komunikácie - vedecké listy Žilinskej univerzity v Žiline / Communications - Scientific Letters of the University of Žilina has been selected for inclusion in the Web of Science™. Articles published after 2022, beginning with 24(1), will be included in the product Emerging Sources Citation Index (ESCI).

Contact:
Komunikácie - vedecké listy Žilinskej univerzity v Žiline
Communications - Scientific Letters of the University of Žilina
University of Žilina
Univerzitná 8215/1
010 26 Žilina
Slovakia

E-mail: komunikacie@uniza.sk
Web: https://komunikacie.uniza.sk

ISSN (print version): 1335-4205
ISSN (online version): 2585-7878

Registered No. (print version): EV 3672/09
Registered No. (online version): EV 3/22/EPP
Publisher, owner and distribution:
University of Žilina, Univerzitná 8215/1,
010 26 Žilina, Slovakia

Company identification number IČO: 00 397 563
Frequency of publishing: four times a year
Circulation: 30 printed copies per issue
Print edition price: 100 Euro (price without VAT)

Publishing has been approved by:
Ministry of Culture, Slovak Republic

UNIVERSITY OF ŽILINA

In its over 70 years of successful existence, the University of Žilina (UNIZA) has become one of the top universities in Slovakia.

Scientific conferences

organized by University of Žilina

KOPES 2025
Colloquium of Czech and Slovak University Electrical Engineering Teachers
Date and venue: 21 – 23 January 2025, Zuberec (SK)
Contact: pavol.rafajdus@uniza.sk

Advanced Industrial Engineering Seminar
Date and venue: February – April 2025, Zilina (SK)
Contact: luboslav.dulina@fstroj.uniza.sk
Web: www.priemyselneinzinierstvo.sk

Workshop: Study water transportation and tourism
Date and venue: 5 – 6 February 2025, Bratislava (SK)
Contact: martin.jurkovic@uniza.sk

SETAC Europe 35th Annual Meeting
Innovation for Tomorrow: Progress in Safe and Sustainable Concepts
Date and venue: 11 – 15 May 2025, Vienna (AT)
Contact: europe-meeting@setac.org
Web: www.setac.org

TRANSCOM 2025
16th International Scientific Conference on Sustainable, Modern and Safe Transport
Date and venue: 21 – 23 May 2025, Horný Smokovec (SK)
Contact: transcom@uniza.sk
Web: transcom-conference.com

UNIVERSITY OF ŽILINA
Science & Research Department

Univerzitná 8215/1,
010 26 Žilina,
Slovakia

Ing. Janka Macurová
tel.: +421 41 513 5143
e-mail: janka.macurova@uniza.sk